Spin-Dependent Processes at Electrodes Detected by Simultaneously Performed EPR, Electrochemistry and EDMR

Thèse N° 9547

Felix BLUMENSCHEIN

Acceptée sur proposition du jury

Prof. P. Ricci, président du jury
Prof. J.-Ph. Ansermet, Dr. C. Roussel, directeurs de thèse
Prof. N. Alonso-Vante, rapporteur
Prof. C. Fontanesi, rapporteur
Dr G. Boero, rapporteur

2019

ÉCOLE POLYTECHNIQUE
FÉDÉRALE DE LAUSANNE

bee humble,
kind and bright

— the Bumblebee

With Tanja and Mara...

Acknowledgements

I am very grateful to many people, for their support, help, advice, discussions and also deflections. Without these people this thesis would not have been possible, of less quality and less fun.

First of all, I want to thank my two thesis advisors, Prof. J. P. Ansermet and Dr. Christophe Roussel, without whose support this work would not have been possible.

I want to thank Prof. J. P. Ansermet, for offering this interesting project, giving me the opportunity to join this amazing group and work in such an independent way. I did not often meet a person with such inspiring passion for physics and I can only admire his group leading approach. He is always interested and informed about each project, always finds time to discuss problems, results and ideas. He was incredibly patient and supporting in any way. I could even take part in his lectures via skype, when we had a problem with Mara's nursery. I also want to thank you for never giving up, your optimism motivated me to work hard and think outside the box.

I want to thank Dr. Christophe Roussel who took the challenge to take the person with the least possible amount of electrochemical knowledge under his wings. He introduced me to electrochemistry, helped me to develop the first cell concept and improve it to the most recent stage, and always helped me with my many questions - no matter how simple. His knowledge and intuition for chemical processes and interpretations were extremely valuable throughout the whole thesis.

I want to thank Prof. Ron Naaman and his group for preparing and providing the Al5 chiral electrode functionalization.

I also want thank the LSEN group, especially Karla Banjac, for providing the helicene chiral electrode functionalization.

I would also like to thank Prof. Nicolas Alonso-Vante, Prof. Claudio Fontanesi and Dr. Giovanni Boero for accepting to be part of my PhD exam jury and Prof. Paolo Ricci to preside it.

I want to thank Dr. Mika Tamski, whom I occupied probably most of all persons with my many questions and discussions, especially at the end of this thesis. Soon, the time of my head popping sharply up behind the screen and asking questions out of nowhere about the most random topics are over, thanks to the honey badger and pieter. Thank you for helping me in so many ways and thank your for all the cookies you baked!

Special thanks goes to Dr. Murari Soundararajan, who actually introduced me to CW EPR, who spent uncounted hours to help me with the setup, tackle LabVIEW bugs, discuss ideas, results, measuring concepts, evaluation schemes and detection methods. Already missing these productive discussions!

Acknowledgements

I also want to thank Alexia Geneviève, who worked for some time with us for her studies and somehow never left even though she's not working with us anymore. Thank you for the fun times, cakes, hot chocolate, whatever you call this pudding thing and keeping up the mood on long days! I also want to thank the rest of the group, members and people who already left, Dr. Marcin Bialek, Dr. Yoon Dongyoung, Hu Junfeng, Dr. Alexandre Dimitriades, Dr. Antonio Vetro and Dr. Sylvain Bréchet. This group was always fun and open to the most random discussions and problem tackling.

Je veux remercier aussi tous les techniciens, électriciens et les secrétaires. Spécialement je veux remercier Claude Amendola. Merci pour ta amabilité et serviabilité. Tes conseils regardant des questions techniques et faisabilité ainsi que l'aide avec des constructions, machines et aussi en les secteurs où je n'ai pas eu d'accès étaient très précieux. Bien sûr aussi, c'était un grand plaisir de parler avec toi des choses comme nos projets matière alpine, nature et enfants.

I also want to thank my whole family. Always having a back-up and plan B option is not self-evident. Especially, I want to thank my partner Tanja and our little baby Mara. Without you life would be boring and without joy. Tanja, thank you so much for your unconditional support and getting along with my stressed me. Couldn't think of anyone better to simultaneously each of us working on a PhD and having a baby. To many more days in the nature, travels, relaxing days, fun and joy! Mara, oerre arr ayye, degn dagn dugn dei, eign ugn eign, kleiner Quatschkopf!

Lausanne, 1st July 2019   *Felix Blumenschein*

Abstract

The electrically detected magnetic resonance (EDMR) results presented in this thesis demonstrate a spin dependence of the charge transfer between an electrode and an electrolyte. These results were found using simultaneous detection of continuous wave electron paramagnetic resonance (CW EPR), EDMR and cyclic voltammetry. The electrochemical cell was located inside a microwave cavity and the electrolyte was saturated with methyl viologen radicals.

Electrodes were either spin polarized using optical spin-pumping in p-GaAs or electrodes functionalized with chiral self-assembled monolayers. Sample preparation and characterization are presented in depth. The measurement and evaluation schemes for combined cyclic voltammogram sweeps and stepwise magnetic field scans are discussed. The resulting detection of spin dependent charge transfer at a spin polarized electrode/electrolyte interface is demonstrated and quantified. The magnitude of this effect is compared with the one observed when using chiral molecules. This brings confirmation of a chirality induced spin selectivity (CISS) effect, based on an experiment in which the spins are excited selectively by magnetic resonance.

Keywords

EDMR, CW EPR, electrochemistry, impedance electrochemistry, spin dependence, electrode/electrolyte interface, methyl viologen radical, helicene, alanine peptide, p-GaAs, optical spin pumping, CISS, chirality, self-assembled monolayers.

Zusammenfassung

In dieser Doktorarbeit wurde der spinabhängige Ladungstransport zwischen Elektroden und Elektrolyt untersucht. Die Messung der elektrisch detektierten Resonanz erfolgt in einem eigens entwickelten System, welches die zeitgleiche Messung von Elektronenspinresonanz, elektrisch detektierter magnetischer Resonanz und elektrochemischen Strömen ermöglicht.

Die Elektroden werden durch optisches Spinpumpen auf p-GaAs oder durch chirale Spinfilter spinpolarisiert. Die Vorbereitung der Proben sowie deren Charakterisierung wird ausführlich präsentiert. Die Kombinierbarkeit von elektrochemischen Messungen und Mikrowellen Resonatoren und deren gleichzeitige Messung wird demonstriert. Das entwickelte Messsystem sowie die Auswertungsweise für gleichzeitiges kontinuierliches Variieren der Spannung und quasi kontinuierliches variieren des Magnetfeldes wird gezeigt. Das Ergebnis der spinabhängigen Ladungstransporte an einer Elektrode/Elektrolyt Grenzfläche wird diskutiert, quantifiziert und in Relation gebracht. Dies bestätigt den durch Chiralität induzierten Spinfiltereffekt mittels selektiver Spinanregung durch magnetische Resonanz.

Schlüsselwörter

EDMR, CW EPR, Elektrochemie, Impedanz Elektrochemie, Spin Abhängigkeit, Elektrode/Elektrolyt Grenzfläche, Methyl Viologen Radikal, Helicene, Alaninpeptid, p-GaAs, Optisches Spin Pumpen, CISS, Chiralität, selbstorganisierende Monoschicht.

Contents

Contents

List of Figures

List of Tables

List of Abbreviations and Symbols

$\parallel$	WE surface in plane with B_0
$\perp$	WE surface perpendicular to B_0
$\lambda/4$ − **plate**	Lambda Quarter Wave Plate (phase retardance of parallel inciding light by 90° (quarter wave length)
2DEG	Two-Dimensional Electron Gas
AC	Alternating Current
Ag	Silver
Al n	$SHCH_2CH_2CO-(Ala-Aib)_n-COOH$ ($n = 5$ here usually)
Au	Gold
ACN	Acetonitrile
B	Magnetic Field [mT]
$\mathbf{B_0}$	External Magnetic Field [mT]
$\mathbf{B_1}$	MW Induced Magnetic Field Inside Cavity [mT]
$\mathbf{B_{mod}}$	External Magnetic Modulation Field [mT]
$\mathbf{B_{res}}$	Resonance Magnetic Field [mT]
BQ	Benzoquinone
CISS	Chirality Induced Spin Selectivity
CE	Counter Electrode
CV	Cyclic Voltammometry / Voltammogram
CW	Continuous Wave
$\mathbf{e^-}$	Electron
E	Energy
EC	Electrochemistry
EIS	Electrochemical Impedance Spectroscopy
EDMR	Electrically Detected Magnetic Resonance
EPR	Electron Paramagnetic Resonance

EPVD	Electron beam Physical Vapor Deposition
f	Frequency
FMR	Ferromagnetic Resonance
GaAs	Gallium Arsenide
GaN	Gallium Nitride
HOMO	Highest Occupied Molecular Orbital
I	Current
LCVR	Liquid Crystal Variable Retarder
LUMO	Lowest Unoccupied Molecular Orbital
MHD	Magneto Hydrodynamic
MV	Methylviologen
MV^0	Methylviologen (Neutral)
MV$^{+\bullet}$	Methylviologen Radical (Monochloride)
MV^{2+}	Methylviologen Dication (Dichloride)
MW	Microwave
OCP	Open Circuit Potential
p-GaAs	GaAs, p-Doped
ptp	Peak-to-Peak
Pt	Platinum
RE	Reference Electrode
Py	Permalloy
RF	Radio Frequency
SAM	Self Assembled Monolayers
SCR	Space Charge Region
SNR	Signal to Noise Ratio
SOMO	Singly Occupied Molecular Orbital
T$_1$	Spin-Lattice Relaxation Time
T$_2$	Spin-Spin Relaxation Time
TTL	Transistor Transistor Logic
U	Potential / Voltage
UME	Ultramicroelectrode
v	volume
w	weight
W	Probability Distribution
WE	Working Electrode

1 Introduction to Spin-Dependent Electrochemistry and Spinterface

The goal of this thesis is to show spin-dependent charge transfer between an electrode and electrolyte. Thinking of current and electronics, most people think of devices based on electric charge transport. However, the inclusion of the angular momentum of transferred charges is on the rise since already 1971, when the first observations of spin accumulation induced by current in a semiconductor was performed.[1] The study of charges coupled with an angular momentum, i.e. its spin and corresponding magnetic moment, is called spintronics.[2] The storage of information by means of spins is according to its orientation as up and down, representing the bits 1 and 0. If charge carriers have a spin, they might conceivably allow information transport. The actual jump start of spintronics came with the independent discovery of giant magneto resistance by Fert, Baibich et al. and Grünberg, Binasch et al. in 1988.[3,4] Most people actually do not realize how present spintronics is in modern society, starting with hard disc data storage read heads using GMR and TMR, data transfer mediated by MRAM or quantum information technologies.[5,6] Spin-OLEDs and quantum computing using resonant technologies are also under development.[7] The LPMN under Prof. Ansermet has been for long time working on some of these topics, more recently on spin dependent charge recombination in OLEDs[8] or opto-spintronics on InP.[9,10]

[1] M. I. Dyakonov, "Current-induced-spin-orientation-of-electrons-in-semiconductors_1971_Physics-Letters-A.pdf", Phys. Lett. A **35**, 459–460 (1971).

[2] A. Fert, "Origin, development, and future of spintronics (Nobel lecture)", Angewandte Chemie - International Edition **47**, 5956–5967 (2008).

[3] M. N. Baibich, et al., "Giant Magnetoresistance of (001)Fe/(001)Cr Magnetic Superlattices", Physical Review Letters **61**, 2472–2475 (1988).

[4] G. Binasch, et al., "Enhanced magnetoresistance in layered magnetic structures with antiferromagnetic interlayer exchange", Physical Review B **39**, 4828–4830 (1989).

[5] Y. Ando, "Spintronics technology and device development", Japanese Journal of Applied Physics **54**, 070101 (2015).

[6] V. K. Joshi, "Spintronics: A contemporary review of emerging electronics devices", Engineering Science and Technology, an International Journal **19**, 1503–1513 (2016).

[7] T. Takui, et al., eds., *Electron Spin Resonance (ESR) Based Quantum Computing*, Vol. 31, Biological Magnetic Resonance (Springer New York, New York, NY, 2016).

[8] F. Comandè, and J. P. Ansermet, "Pulsed magnetic resonance of Alq3 OLED detected by electroluminescence", Synthetic Metals **173**, 40–42 (2013).

[9] C. Caspers, et al., "Opto-spintronics in InP using ferromagnetic tunnel spin filters", New Journal of Physics **17** (2015) 10.1088/1367-2630/17/2/022004.

[10] D. Yoon, et al., "Nuclear polarization by optical pumping in InP:Fe above liquid nitrogen temperature", Solid State Nuclear Magnetic Resonance **70**, 48–52 (2015).

Spintronics is mostly referred to as the study of spin-polarized currents in solid devices. Regarding the applicability of spintronics, a long spin-diffusion length is essential.[11,12] The expansion to interfaces, sometimes called spinterface, is complex and often difficult.[13] However, the study of solid-liquid interface spintronics, i.e. spin dependent electrochemistry (EC), is of interest, because spin-polarized electrochemical currents also increase the energy efficiency in electrochemical processes and may represent a new way to probe mechanisms at electrode surfaces.[14,15] Probably the first spin dependent electrochemical experiment was performed by Chazalviel, who found experimental evidence for the dependence of electrochemical rate between a polarized p-GaAs/electrolyte interface on the relative spin orientation between electrode and redox species.[16] He reasoned that paramagnetic species can only accept electrons of opposite spin direction to be reduced to the diamagnetic form. He therefore applied independent spin polarization methods for the electrode and electrolyte by using optical spin pumping on a p-GaAs semiconductor and an external magnetic field to spin polarize methyl viologen radicals ($MV^{+\bullet}$), such as depicted in figure 1.1 a). Chazalviel's work is path paving, complex and elaborate in many ways. However, his method can not fully exclude magneto hydrodynamic (MHD) effects as source for his findings. MHD is two fold, Lorentz force interaction of electric current with external magnetic fields,[17] and Kelvin force interaction of paramagnetic radicals in solution.[18] Mostly Lorentz force induces a stirring effect, which in general increases the reaction rate by increasing the mass transport, called magnetoelectrolysis.[19] Lorentz force $\vec{F}_L$ is the cross product of current density $\vec{j}$ and magnetic field $\vec{B}_0$, $\vec{F}_L = \vec{j} \times \vec{B}_0$, which applies on charged species, e.g. $MV^{+\bullet}$ and MV^{2+} in the case of methyl viologen, and can only vanish for perfectly parallel alignment of current and field, $\vec{j} \parallel \vec{B}_0$. However, to secure parallel alignment is in most cases impossible. While Lorentz force is important for both, diamagnetic and paramagnetic redox species, Kelvin force is especially important for paramagnetic redox species and magnetic electrodes. Kelvin forces are induced by strong field inhomogeneities and can, depending on the electrode and field constellations accumulate paramagnetic species in specific regions or deflect redox species away from or to electrodes and thereby decrease or increase the current.

Another effect which can distort the electrochemical current behavior is the change of interface tunneling pathways induced by magnetic fields.[20] This can increase the electrochemical

[11] J. Fabian, and S. D. Sarma, "Spin relaxation of conduction electrons", 1708–1715 (1999).

[12] I. Žutić, et al., "Spintronics: Fundamentals and applications", Reviews of Modern Physics **76**, 323–410 (2004).

[13] M. Galbiati, et al., "Spinterface: Crafting spintronics at the molecular scale", MRS Bulletin **39**, 602–607 (2014).

[14] W. Mtangi, et al., "Role of the Electron Spin Polarization in Water Splitting", The Journal of Physical Chemistry Letters **6**, 4916–4922 (2015).

[15] C. Fontanesi, "Spin-dependent electrochemistry: A novel paradigm", Current Opinion in Electrochemistry **7**, 36–41 (2018).

[16] J. Chazalviel, "Spin-dependent electrochemical kinetics at a semiconducting photocathode", Journal of Chemical Physics **83**, 149–156 (1985).

[17] L. M. Monzon, and J. Coey, "Magnetic fields in electrochemistry: The Lorentz force. A mini-review", Electrochemistry Communications **42**, 38–41 (2014).

[18] L. M. Monzon, and J. Coey, "Magnetic fields in electrochemistry: The Kelvin force. A mini-review", Electrochemistry Communications **42**, 42–45 (2014).

[19] B. Ferreira Gomes, et al., "Strong magnetoelectrolysis effect during electrochemical reaction monitored in situ by high-resolution NMR spectroscopy", Analytica Chimica Acta **983**, 91–95 (2017).

[20] G. Saravanan, and S. Ozeki, "Magnetic field control of electron tunneling pathways in the monolayer of (ferrocenylmethyl)dodecyldimethylammonium bromide on a gold electrode", Journal of Physical Chemistry B **112**, 3–6 (2008).

reduction and oxidation current with increasing magnetic field. Saravanan and Ozeki explained the magnetic field dependence they observed by an increase of the tilt angle of functionalizing hydrocarbon chains which was induced by cooperative magnetic orientation.[1] As for the case of MHD, this effect becomes noticeable only for large magnetic field changes in the range of tesla.

The effect of MHD and functionalization tilt is almost constant if the magnetic field is changed only in a small range. Modestov and Kazarinov therefore performed a similar experiment as Chazalviel, however without external magnetic field. Instead he only used optical spin pumping on p-GaAs to produce an accumulation of spin polarized radicals, which again can't dimerize together due to the same spin polarization.[21]

An ideal option which includes external fields but avoids large field changes is resonance. Resonance describes the use of photon absorbance to overcome the electron Zeeman splitting inside a magnetic field. Photons of defined wavelength are only absorbed at or very near a resonance field, such that for a small variation of either magnetic field or photon wavelength the absorbance disappears. This allows magnetic field changes of only few millitesla to see a strong effect, thus without MHD. Resonance experiments have the additional advantage that any signal is clearly connected to the existence of a spin polarized paramagnetic system.

We use a similar approach as Chazalviel, however using resonant technique. The spin polarization induced current change is vanished at resonance if microwave power saturation is reached, figure 1.1 b). Magnetic field sweeps around resonance therefore directly compares on and off resonance, b) and a). The first experiments combining electrochemical measurements and resonance were performed in 1962,[22] and the first in-situ electrochemical electron spin resonance (EPR) experiment in 1974.[23] These experiments were concerned about e.g. radical production observation and not interface effects. However, the specific problems and several possible solutions of performing electrochemical measurements in cavities and performing cavity based resonance experiments on electrochemical samples are therefore well known. The biggest challenge is to keep the electrochemical cell influence on the cavity mode as small as possible.[24] Recent developed systems miniaturize therefore the electrochemical cell using ultra micro electrodes (UME) in combination with loop gap resonators, allowing even strongly polar solvents.[25] I have developed an oxygen tight, transparent, low cost system, described in chapter 3. One of the biggest challenges is to avoid current diffusion-limitation, i.e. exhaustion of the relevant reactants at the electrode surface. Chazalviel avoided diffusion limited currents by using a sophisticated flow through device. However, this method introduces various new problems, especially regarding oxygen tightness which is needed to ensure radical stability. The additional volume inside the cavity may also be a

---

[1] This effect increases not only the current, but also the peak to peak separation of reduction to oxidation peak.

[21] A. Modestov, and V. Kazarinov, "Electrochemical reduction of 2,6-diphenylpyrylium cations by spin-polarized electrons. The Hedvall effect", Chemical Physics Letters **206**, 401–404 (1993).

[22] L. H. Piette, et al., "Electron Paramagnetic Resonance and Electrochemistry. Studies of Electrochemically Generated Radical Ions in Aqueous Solution.", Analytical Chemistry **34**, 916–921 (1962).

[23] I. B. Goldberg, et al., "Simultaneous electrochemical-electron spin resonance measurements. III. Determination of rate constants for second-order radical anion dimerization", Journal of Physical Chemistry **78**, 295–299 (1974).

[24] K. R. Fernando, et al., "Cell for combined electrochemistry and ESR measurements at variable temperatures in a varian TE102 microwave cavity", Journal of Magnetic Resonance (1969) **68**, 551–555 (1986).

[25] M. A. Tamski, et al., "Electrochemical electron paramagnetic resonance utilizing loop gap resonators and micro-electrochemical cells", Phys. Chem. Chem. Phys. **17**, 23438–23447 (2015).

problem. To avoid using a flow device system, I scanned the voltage at fixed magnetic field, then varied the field. From the matrix of data points covering a field range around resonance, I extract line scans which constitute spectra at constant voltage, section 3.2.1. This approach requires electrodes of great stability. The detection mechanism I use is based on electrical detection, which is mostly sensitive to transport through the interface and therefore directly to the reduction and oxidation processes. The measurements require careful signal detection and analysis because the effect I was seeking has a relative strength estimated at 0.01 %, see section 2.3. I am able to show a relative current change for the reduction of $MV^{+\bullet}$ to MV^0 and for the oxidation of $MV^{+\bullet}$ to MV^{2+}. To my knowledge, this is the first time spin-dependent charge transfer at an electrode has been demonstrated using electron spin resonance of a radical in solution to address spins in a selective fashion, thus avoiding spurious MHD effects.

The use of magnetic resonance to detect spin effects in electrochemical currents is new. Nonetheless, it resembles work that has been done on organic light emitting diodes, in the framework of studies concerned with the physical origin of organic magneto-resistance (OMAR).[8] The question of spin effects in electrochemistry remained mostly unexplored until about ten years ago. What sparked an interest for this was the discovery that chiral molecules act as spin filters, what is now called chiral induced spin selectivity (CISS). CISS refers to the fact that mostly one spin direction is transferred through helical molecules. The CISS effect makes it therefore possible to inject spin polarized electrons into redox species using only organic systems.[15] Spin polarization obtained by simply driving electrons through helical molecules is very promising and allows new concepts regarding the experimental setups beyond the one of this work. Spin dependent electrochemistry actually experienced a renewed interest in combination with organic systems thanks to CISS. With increasing interest in CISS the scarcity of literature on spin-dependent electrochemistry completely changed. Spin dependent electrochemical experiments with chiral functionalized electrodes have been performed using additional magnetic materials such as Ni,[26–28] or without any magnetic materials.[29,30] A recent review by Naaman et al. sums up most aspects of CISS.[31] One of the big advantages of CISS is that the necessary chiral molecule monolayers can often be deposited as a self assembled monolayer (SAM). This allows large quantity electrode production by simply covering them with a solution.[32]

A big problem for effects at interfaces concern spin relaxation time, spin diffusion length and spin dependent trapping at interfaces.[33] It appears, that many CISS systems excel in avoiding at least the latter two by decreasing blocking most states due to their fully bonded end atoms and a certain

[26] P. C. Mondal, et al., "Chiral Conductive Polymers as Spin Filters", Advanced Materials **27**, 1924–1927 (2015).

[27] P. C. Mondal, et al., "Field and chirality effects on electrochemical charge transfer rates: Spin dependent electrochemistry", ACS Nano **9**, 3377–3384 (2015).

[28] T. J. Zwang, et al., "Helix-Dependent Spin Filtering through the DNA Duplex", Journal of the American Chemical Society **138**, 15551–15554 (2016).

[29] A. Kumar, et al., "Chirality-induced spin polarization places symmetry constraints on biomolecular interactions", Proceedings of the National Academy of Sciences **114**, 2474–2478 (2017).

[30] W. Mtangi, et al., "Control of Electrons' Spin Eliminates Hydrogen Peroxide Formation During Water Splitting", Journal of the American Chemical Society **139**, 2794–2798 (2017).

[31] R. Naaman, et al., "Chiral molecules and the electron spin", Nature Reviews Chemistry **3** (2019) 10.1038/s41570-019-0087-1.

[32] D. Mandler, "Chiral self-assembled monolayers in electrochemistry", Current Opinion in Electrochemistry **7**, 42–47 (2018).

[33] S. Steil, et al., "Spin-dependent trapping of electrons at spinterfaces", Nature Physics **9**, 242–247 (2013).
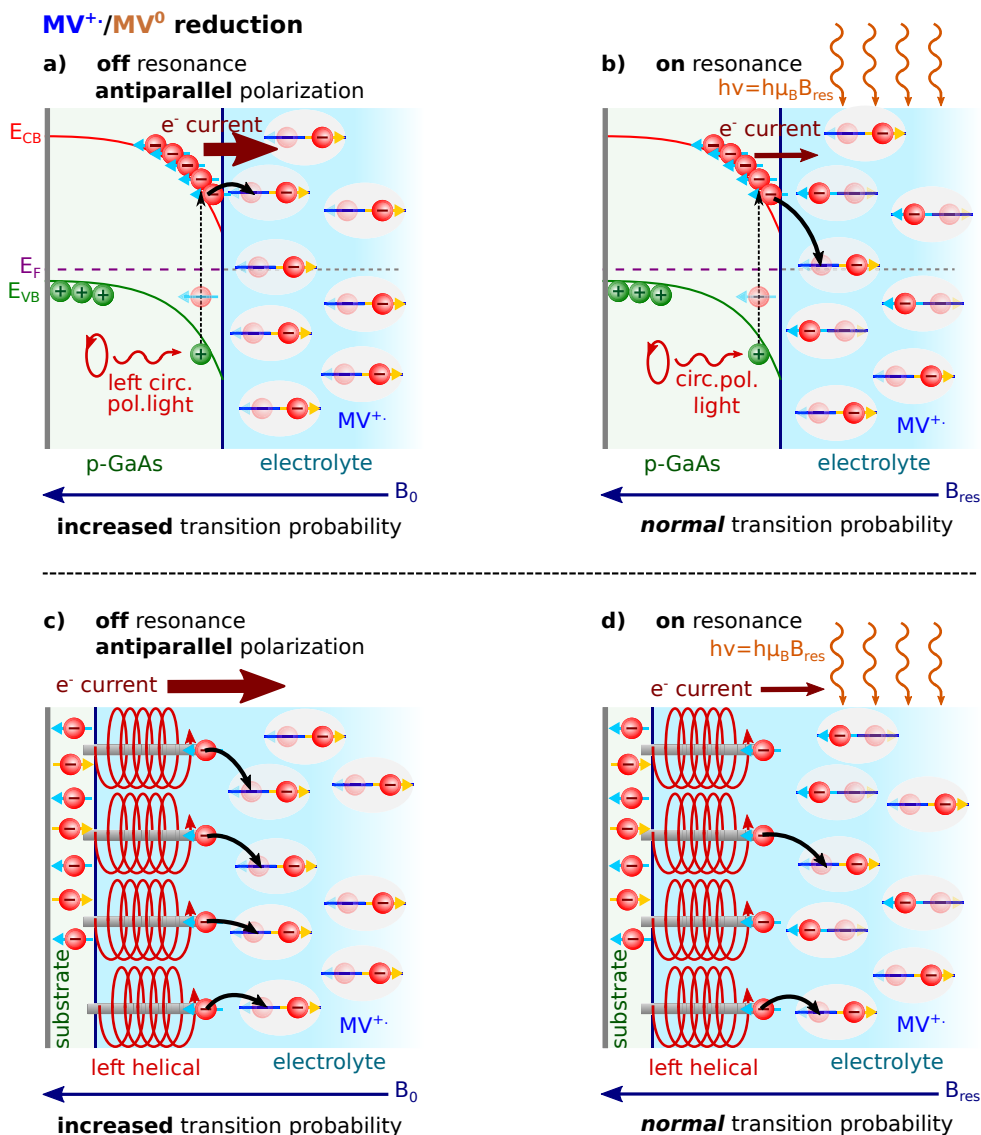
Figure 1.1 – Spin dependent electrode/electrolyte current change at resonance using molecular orbital Pauli exclusion. The spin polarization is exaggerated to 100 % for easier illustration. a) shows the increased current at B_0 for relative antiparallel spin orientation using optical spin pumping on p-GaAs. The resistance decrease vanishes at resonance, given microwave power saturation is reached, b). c) and d) are the corresponding illustrations using helical molecules for spin filtering, CISS.

chemical inertness. However, spin dependency is always shown as effect of current or voltage change comparing with and without magnetic field or chiral and non chiral molecules. To my knowledge, this is the first study of spin effects in CISS electrochemistry that relies on resonance. The experimental realization is simpler than with optical pumping. p-GaAs is replaced with electrodes covered with either [5]helicene or peptides consisting of 5 alanine groups (Al5). The resulting current change around resonance is similar, i.e. increased current for CISS transferred electrons of spin antiparallel to the radical spin, figure 1.1 c), normal current at resonance with microwave power saturation, d).

CISS effect is of much broader interest than creating spin effects at electrodes. It has been

argued that homochirality in biology is favorable for energy efficiency in organic systems.[29,34,35] The predominance of homochiral systems is in fact quite striking, such that e.g. amino acids are almost homochiral of L- and sugars of D-chirality ([36] p. 126), with "L" for levorotatory and "D" for dextrorotatory.[36,37]2 One demonstrated case of increased energy efficiency was the photoelectrochemical water splitting for hydrogen generation.[14,38]

The present thesis is structured in the following way. After this introduction, I will further describe the notions important to this topic in chapter 2. The spin dependent current effect depends on spin-polarization on two sides, the electrode and electrolyte. Therefore, optical spin pumping, chirality induced spin polarization and paramagnetic spin-polarization are explained. The important measuring concepts such as the electrochemical concepts (cyclic voltammetry, impedance spectroscopy and Mott-Schottky plots) and also EPR are described. The final goal of that is to derive a model explaining current decrease or increase in external magnetic fields, depending on the relative spin orientation of independently spin polarized electrode and electrolyte and the vanishing of this resistance change at resonance. Magnetic spin polarization, resonant and non resonant spin flip processes on radicals, electrochemical cathode descriptions, exclusion principle, electron hole recombination and two types of electrode spin polarization are therefore combined into a spin dependent current density model allowing a quantitative estimate. Chapter 3 is devoted to explain the setup, concepts, measuring scheme and evaluation method. The setup is characterized, the development, preparation and functioning of electrochemical cells and electrodes are discussed. Chapter 4 discusses the results of electrically detected magnetic resonance (EDMR) for optically pumped p-GaAs electrodes and chiral electrodes [5]helicene and two types of polyalanine SAM. These results are compared in chapter 5. This chapter ends by discussing several possible ways to continue and improve the setup and detection scheme. The appendix, A, discusses several other observations, problems and other developed systems.

Except from the EPFL logo, no figures were taken from other publications, books, works or persons. All figures in this thesis are generated with Inkscape, all plots either with Gnuplot or Matlab and molecule drawings with the LaTeX package *chemfig*. All 3D and surface plots are on purpose kept as separate-point plots and not the more common interpolated 3D surface substitute, to emphasize the stability and possible problems. In general, color coding is used to indicate affiliations, especially regarding figures with several subplots.

---

2 This goes so far that chemicals can be far cheaper for one chirality and that e.g. enzymatic decomposition of synthetic L-DNA is much slower than natural D-DNA due to missing enzymes.[37]

[34] R. A. Rosenberg, et al., "Chiral Selective Chemistry Induced by Natural Selection of Spin-Polarized Electrons", Angewandte Chemie - International Edition **54**, 7295–7298 (2015).

[35] D. Qi, et al., "Novel insights into the selection to electron's spin of chiral structure", Nano Energy **52**, 142–152 (2018).

[36] G. Pályi, et al., eds., *Progress in Biological Chirality* (Elsevier, 2004).

[37] G. Hayashi, et al., "Application of L-DNA as a molecular tag", Nucleic Acids Symposium Series **49**, 261–262 (2005).

[38] W. Zhang, et al., "Enhanced Electrochemical Water Splitting with Chiral Molecule-Coated Fe3O4Nanoparticles", ACS Energy Letters, 2308–2313 (2018).

2 On the Detection of Spin-Dependent Processes at Electrodes by MR

This section is intended to provide the theoretical concepts essential for the full understanding of the experimental methods, equipment, results and mechanisms used in this work for the detection of spin-dependent processes at electrodes by means of magnetic resonance (MR). Many of the topics covered below constitute entire fields of research and the corresponding models and experimental methods are vast. A full discussion of all aspects would go beyond the scope of this thesis. Also, common definitions and concepts such as band structure, density of states or space charge effects are presumed known.

Different fields of research also tend to use different expressions, descriptions, notions and abbreviations for the same thing. My intent is to use one denomination for each notion throughout all sections. Some descriptions and abbreviations might therefore be unusual for some readers, they are however always defined and explained within the text.

2.1 Electrochemistry

The basic idea of this thesis is the detection of spin dependent current between an electrode and an electrolyte. The field of research devoted to analyse current to voltage relations for the characterization of chemical changes at such an electrode/electrolyte interface is called electrochemistry (EC). An electrochemical reaction is defined as either a chemical reaction caused by a current supply or a spontaneous chemical reaction causing a current. In this thesis we concentrate mostly on the former case,[1] i.e. oxidation or reduction reactions of molecules in solution, called electrolyte, at electrodes due to an external current source. Reduction is hereby the process of a molecule accepting an electron from the electrode, while oxidation defines the electron donation from molecule to electrode. A redox reaction is reversible if the oxidized species Ox in solution can be reduced back to the reduced species Red by accepting n electrons and vice versa,

$$Ox + n \cdot e^- \underset{k_{Ox}}{\overset{k_{Red}}{\rightleftharpoons}} Red, \tag{2.1}$$

---

[1] The latter is at least present in the equilibration process and in the future a possible EDMR detection using OCP schematics is planned
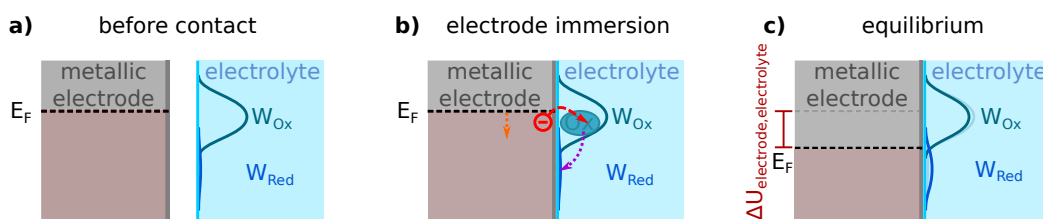
Figure 2.1 – Potential equilibriation of an electrode/electrolyte interface when immersing a metallic electrode into an electrolyte with mostly Ox and almost no Red species. An electron exchange between electrode and electrolyte occurs simply because the Fermi energy level E_F position and probability distribution (W) allow it. The subsequent E_F shift and W change induce a potential drop $\Delta U_{electrode,electrolyte}$.

k_{Red} being the reduction electron transfer rate constant and k_{Ox} being the oxidation electron transfer rate constant.[39] The insertion of an electrode into an electrolyte leads in general to an electron ($e = 1.6 \times 10^{-19}$ C) exchange between electrode and electrolyte, such as depicted in figure 2.1. This process is best described using the total distribution (W), which is the product of probability distribution and concentration of species in the electrolyte. W represents the probability to find an occupied state at defined energy and can equilibrate via the reaction defined by equation 2.1. W is very similar to the density of state distribution in physics, however with a significant difference: DOS may be filled or not, whereas W are generated. The electron exchange when immersing an electrode into an electrolyte can be explained using a thought experiment. To simplify the thought experiment, we assume a metallic electrode which possesses an easy band structure with conduction electrons available for any energy below the Fermi level E_F and we assume an electrolyte containing molecules almost only in their Ox state, i.e. large corresponding W_{Ox} and almost zero W_{Red}, figure 2.1 a). We also assume that E_F, before contact is made, is situated at a similar height as W_{Ox}. W_{Ox} is situated in general at larger energy compared to W_{Red} due to the additional electrons filling in general higher energy levels. Immersing the metallic electrode into the electrolyte, electrons will come from the electrode and reduce the Ox species of lower energy to Red, figure 2.1 b). This lowers E_F, slightly decreases W_{Ox} and increases W_{Red}. This process is reversible given W_{Red} of energies above E_F exist. The process continues until the reduction rate is equal to the oxidation rate. Looking at the probability, equilibrium is reached at the position of E_F such that the W_{Ox} surface below E_F is equal to the W_{Red} area above E_F, c). This equilibration process results in an interface potential drop $\Delta U_{electrode,electrolyte}$ between the electrode and electrolyte interface with corresponding potentials $U_{electrode}$ and $U_{electrolyte}$,

$$\Delta U_{electrode,electrolyte} = U_{electrode} - U_{electrolyte}.$$

Assuming different starting conditions in a), e.g. E_F lower at the center of W_{Red}, almost nothing would happen, since almost no Red are available below E_F. However, if we also assume a starting conditions with almost only Red but no Ox, the electrons could go from Red to a low E_F, increasing the W_{Ox} and rising E_F. $\Delta U_{electrode,electrolyte}$ is therefore one part to characterize the condition of a system.

To measure $\Delta U_{WE,electrolyte}$ at a so called working electrode (WE), is surprisingly complicated. A simple counter electrode (CE) will itself lead to another potential drop due to the CE/electrolyte interface, $\Delta U_{WE,CE} = (U_{WE} - U_{electrolyte}) - (U_{CE} - U_{electrolyte}) = (U_{WE} - U_{CE})$, called cell voltage,

---

[39] D. A. Brownson, and C. E. Banks, *Interpreting Electrochemistry* (2014), pp. 1–201.

such that the information about the interface potential drop at the WE is lost. It is therefore necessary to introduce a reference electrode (RE), whose relative potential U_{RE} does not change when dipping it into an electrolyte. If one is able to build such a RE, the potential drop between WE and electrolyte can be measured with a constant offset U_{RE},

$$\Delta U_{WE,RE} = (U_{WE} - U_{electrolyte}) - U_{RE}.$$

$\Delta U_{WE,RE}$ without external potential applied is the pure result of electrochemical equilibration between WE and electrolyte. The measurement of $\Delta U_{WE,RE}$ at a state of no current flux through the WE with volt-meter between WE and RE is called open circuit potential (OCP) measurement, U_{OCP}.

A common RE is the standard hydrogen electrode (SHE). SHE consists of a platinum (Pt) wire immersed into a $1\,\text{M}\,H^+$ aqueous solution with H_2 constantly bubbled at 1 bar and $25\,°C$. Interaction with the actual electrolyte is only possible through a salt-bridge, ensuring that the SHE internal electrochemical equilibrium is not changed by electrochemical processes with the sample electrolyte. The SHE is in electrochemistry defined as standard RE. Since potentials are always relative and compared to each other, the SHE is defined as a potential of zero $U_{RE=SHE} = 0\,V$ and all other RE are compared to it, such that

$$\Delta U_{WE,RE=SHE} = \Delta U_{WE,electrolyte}.$$

Electrochemical potentials are therefore typically reported relative to SHE or at least to the used RE which again can be measured versus SHE. If, as in this work, the use of rather bulky ideal RE as the SHE is not possible, often reference electrodes such as Ag/AgCl, or quasi RE as Pt or Ag wires are used.

The WE/electrolyte equilibrium potential $\Delta U_{WE,electrolyte}$ depends on the relative concentration of Ox and Red species and can also be calculated using the *Nernst* equation

$$\Delta U_{WE,electrolyte} = E_f^{0'}(Ox/Red) + \frac{RT}{nF}\ln\left(\frac{[Ox]}{[Red]}\right). \tag{2.2}$$

$[Ox]$ and $[Red]$ are the species concentration at the WE surface which are at equilibrium constant through the whole solution. $R = 8.314\,\text{J/(Kmol)}$ universal gas constant, $T[K]$ temperature, $F = 96485\,\text{C/mol}$ Faraday constant, n number of transferred electrons from equation 2.1. $E_f^{0'}(Ox/Red) = E^0(Ox/Red) + \frac{RT}{nF}\ln\left(\frac{a_{Ox}}{a_{red}}\right)$ is the formal potential with standard electrode potential $E^0(Ox/Red)$, a_{Ox} and a_{red} activity coefficients. $E_f^{0'}(Ox/Red)$ can be found measuring the OCP using same concentrations of Ox and Red, $\ln\left(\frac{[Ox]}{[Red]}\right) = 0 \implies U_{OCP} = \Delta U_{WE,electrolyte}^{equilibrium} = E_f^{0'}(Ox/Red)$.

Applying an additional external voltage, we move away from the so far described equilibrium state to dynamic electrochemistry. When the applied potential at the WE is more negative than $\Delta U_{WE,electrolyte}^{equilibrium}$, we start to reduce the Ox species as soon as E_F is risen such that the W_{Ox} area below E_F is larger than the area of W_{Red} above E_F (assuming same reduction and oxidation
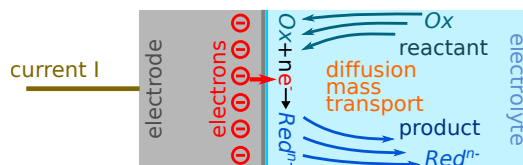
Figure 2.2 – Illustration of the electron exchange process at an electrode and bulk diffusion mass transport of reactants and products.

electron transfer rate constants),

$$Ox + n \cdot e^- \rightarrow Red. \tag{2.3}$$

Looking at the current I, we have to consider not only the interface but also the bulk sample solution as depicted in figure 2.2. The reactants have to diffuse from the bulk solution to the electrode surface, such that a flux $j_f [\mathrm{mol/(cm^2 s)}]$ reaches the electrode surface. Assuming immediate electron transfer between electrode and Red or Ox by tunneling electron transfer in the vicinity of typically $10\,\text{Å}$, the current can be approximated by

$$I = nAFj_f. \tag{2.4}$$

n amount of transferred electrons between electrode and electrolyte in equation 2.3, A electrode surface area. For slow transfer, equation 2.4 must take into account the electron-transfer rate constant.

A potentiostat with schematic similar as presented in figure 2.3 measures in a three electrode constellation the potential between WE and RE, while measuring the current between WE and CE.[40,41] A control amplifier connected to the CE in the potentiostat forces a current to flow through the electrolyte between WE and CE by controlling the applied potential between CE and
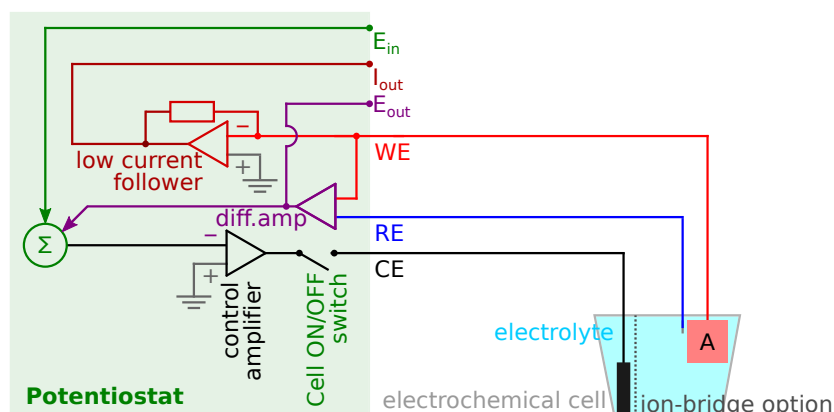
Figure 2.3 – Potentiostat schematic and electrochemical cell with a three electrode system. Potential and current are controlled using a control amplifier at the CE, while the potential is measured between WE and RE and current at the WE. A manual cell On/Off button allows manual circuit opening allowing true OCP measurements. A indicates the WE surface area of equation 2.4.

[40] Metrohm Autolab B.V., *Autolab Application Note* (https://www.ecochemie.nl/download/Applicationnotes/, 2011).

[41] Gamry Instruments Inc., *Application Note* (https://www.gamry.com/application-notes/, 2012).
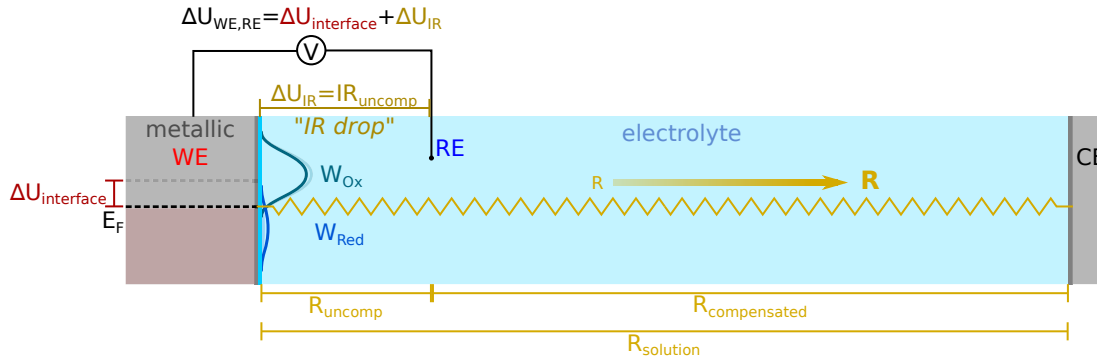
Figure 2.4 – Uncompensated electrolyte resistance potential drop of a three electrode system, also called IR drop. Continued from the equilibrium constellation in figure 2.1 c), i.e. no current flows and no potential is applied. In this constellation actually no IR drop exists, $\Delta U_{RI} = 0$. Only once an additional potential is applied, shifting E_F and forcing a current, the IR drop rises, $\Delta U_{RI} \neq 0$. The IR drop is minimized by moving the RE as close as possible to the WE and decreasing the electrolyte resistance using supporting electrolyte.

WE using the WE as ground. The current is measured at the WE using a low current follower. The resulting potential between WE and RE is measured with a differential amplifier. The differential amplifier information is fed to a summation point Σ which in turn controls the control amplifier at the CE: ultimately the CE potential is changed until the desired potential between RE and WE is reached. It is interesting that in this configuration the exact potential at the CE is not measured nor exactly known even though the applied potential is controlled by it. Also of interest is that only the current through the WE is measured and not the current between WE and CE. In general these currents are of course identical, however not momentarily. Electrochemical experiments are therefore typically designed in such a manner, that only the processes at the WE are of interest. When large currents are applied, a spatial separation of WE and CE or introduction of an ion-bridge between WE and CE is necessary. Most high end potentiostats deliver not only analog current I_{out} and potential E_{out} read out ports but also allow an additional direct potential contact to the summation point, E_{in} in figure 2.3. A manual cell On/Off button allows in this schematic a manual circuit opening for true OCP measurements. The CE should be of chemically inert material such as Pt or carbon to avoid surface change induced potential drift and minimize adsorption and desorption processes. What I call in this thesis an electrochemical sample typically consists of an electrode system as described which is plunged into the electrolyte situated in a vessel.

Besides the interface potential drop $\Delta U_{WE,electrolyte}$ also the so called uncompensated electrolyte between RE and WE produces a potential drop $\Delta U_{IR} = IR_{uncomp}$ due to its resistance R_{uncomp} when a current I flows, the so-called uncompensated electrolyte resistance potential drop or simply IR drop as depicted in figure 2.4. The potential measured between WE and CE includes a contribution due to this effect, namely,

$$\Delta U_{WE,RE} = \Delta U_{WE,electrolyte} + \Delta U_{IR}$$
$$= \Delta U_{WE,electrolyte} + IR_{uncomp}.$$

A process observed at a certain potential might therefore not correspond to this potential energy but to a smaller one. The IR drop should therefore be minimized. R_{uncomp} increases linearly with distance between WE and RE in the electrolyte. The IR drop can therefore be minimized by

placing the RE close to the WE. To keep the electrolyte resistance in general as small as possible, an additional salt, called supporting electrolyte is added to the solution. The supporting electrolyte itself is not electroactive in the potential range where it is used. After e.g. applying a potential to reduce Ox, Red species accumulate at the electrode surface. If only these species were present, they might create a space charge over a large distance from the electrode. This charge built-up would decrease the interface potential and therefore also oxidation or reduction current. The supporting electrolyte salt ions can be assumed to be very mobile and migrate to screen the Ox, Red, charge build-up. The supporting electrolyte is therefore added in large quantities, as much as several 100 mM, such that already the huge concentration difference to the redox species concentration of only few 1 mM reduces to a minimum the effect of a space charge build-up.[42,43]

The electrolyte typically consists of a suitable solvent such as water or organic solvent (acetonitrile (ACN) in my case), the electroactive compound (methyl viologen (MV) in my case), and a supporting electrolyte, i.e. inorganic or organic salt (TBAP in my case). The potential range of stable reactions, i.e. no solvent, redox species or electrode decomposition, is called potential window.

It has to be made clear, that an actual current of electrons or holes occurs only at the electrode/electrolyte interface and inside the electric conductors. Inside the electrolyte, owing to the screening by the supporting electrolyte, the current is dominated by the diffusion of the supporting electrolyte ions. The reactant rate flux j_f of equation 2.4 at the WE surface can be calculated using the electron transfer rate constants k_{Red} and k_{Ox}. For the example of equation 2.1, the flux rate can be derived to

$$j_f = k_{Ox}[Red] - k_{Red}[Ox], \tag{2.5}$$

with

$$k_{Ox} = k^0 \exp\frac{\alpha F\left(U_{WE} - E_f^{0'}(Ox/Red)\right)}{RT},$$

$$k_{Red} = k^0 \exp\frac{-(1-\alpha)F\left(U_{WE} - E_f^{0'}(Ox/Red)\right)}{RT}.$$

These are called the *Butler-Volmer* equations which account for electrochemical interface kinetics. k^0 is the standard electrochemical rate constant, U_{WE} applied potential and $E_f^{0'}(Ox/Red)$ is the formal potential already introduced in equation 2.2. α is the charge transfer coefficient. The rate constants are potential dependent and especially for potentials of $U_{WE} < E_f^{0'}(Ox/Red)$ the relation $k_{Red} \gg k_{ox}$ is obvious due to the exponential function; respectively $k_{Red} \ll k_{Ox}$ for $U_{WE} > E_f^{0'}(Ox/Red)$. This explains the current behavior for a system with E_F close to the center of a W state distribution and within a small time scale. Including equation 2.5 into equation 2.4,

[42] N. Elgrishi, et al., "A Practical Beginner's Guide to Cyclic Voltammetry", Journal of Chemical Education **95**, 197–206 (2018).

[43] S. Creager, *Handbook of Electrochemistry - Chapter: Solvents and Supporting Electrolytes* (Elsevier, 2007), pp. 57–72.
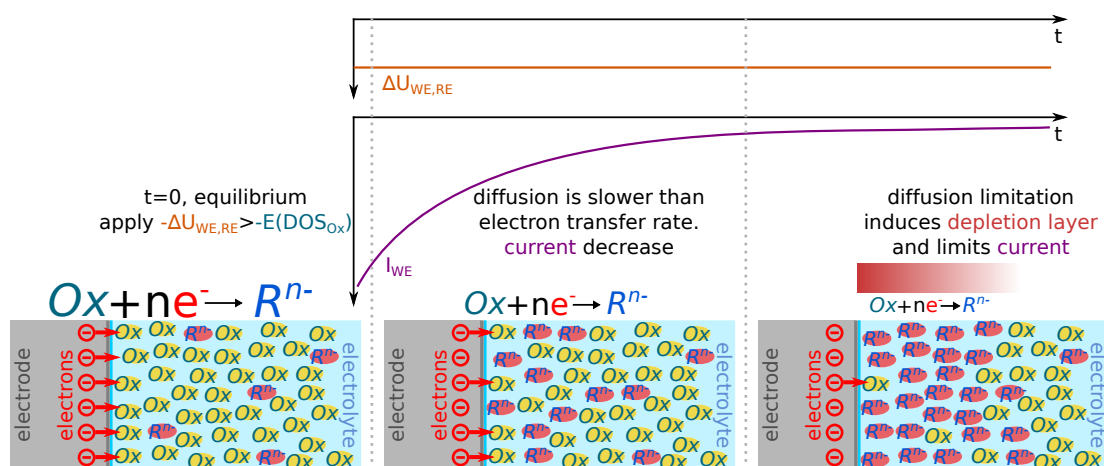
Figure 2.5 – Mass diffusion limited current I over time t for a chronoamperometric measurement. Time development from left to right. The reaction species available at the beginning are fast consumed for a system where the diffusion mass transport is slower than the electron transfer rate at the electrode/electrolyte interface. This eventually leads to a reactant depletion in the WE vicinity, the current is diffusion limited.

we become

$$j = nFk^0 \left(\exp \frac{\alpha F \left(U_{WE} - E_f^{0'}(Ox/Red) \right)}{RT} [Red] - \exp \frac{-(1-\alpha) F \left(U_{WE} - E_f^{0'}(Ox/Red) \right)}{RT} [Ox] \right).$$

However, if we apply a constant potential away from equilibrium for a certain time and measure the current, mass diffusion will play an increasing role such as depicted in figure 2.5. The measurement of current over time at constant potential is called chronoamperometric measurement. In this work the IUPAC convention is used, i.e. applying a negative potential at the WE leads to a cathodic reduction at the WE (electron going from WE to molecule) which is defined as negative current. Likewise, a positive potential leads to an anodic oxidation of *Red* at the WE (electron going from molecule to WE), defined as positive current. For figure 2.5 we assume again equation 2.3. We also assume that the diffusion mass transport is slower compared to the electron transfer rate and that the *Ox* species concentration is much larger than the *Red* species concentration. Applying a negative potential such that E_F is higher than the W_{Ox} center leads in this scenario to a fast consumption of the *Ox* species in the WE surface vicinity, i.e. *Ox* species depletion and *Red* species accumulation close to the WE surface due to a diffusion which is too slow of *Red* away from the WE and *Ox* from the bulk solution to the surface. This is called diffusion limitation and leads to a current decrease as depicted in figure 2.5 from left to right. The zone around the WE with low *Ox* species concentration is called depletion layer. The depletion induced current decay is proportional to the inverse square root of time t and can be described using the *Cottrell* equation, which is

$$j(t) = \pm \frac{nF[\text{reactant}]_{initial} \sqrt{D_{\text{reactant}}}}{\sqrt{\pi t}},$$

with initial reactant species (*Ox* or *Red*) concentration $[\text{reactant}]_{initial}$, diffusion coefficient D_{reactant} [cm^2/s], and positive sign in the case of the oxidation of *Red* reactant species, and

13
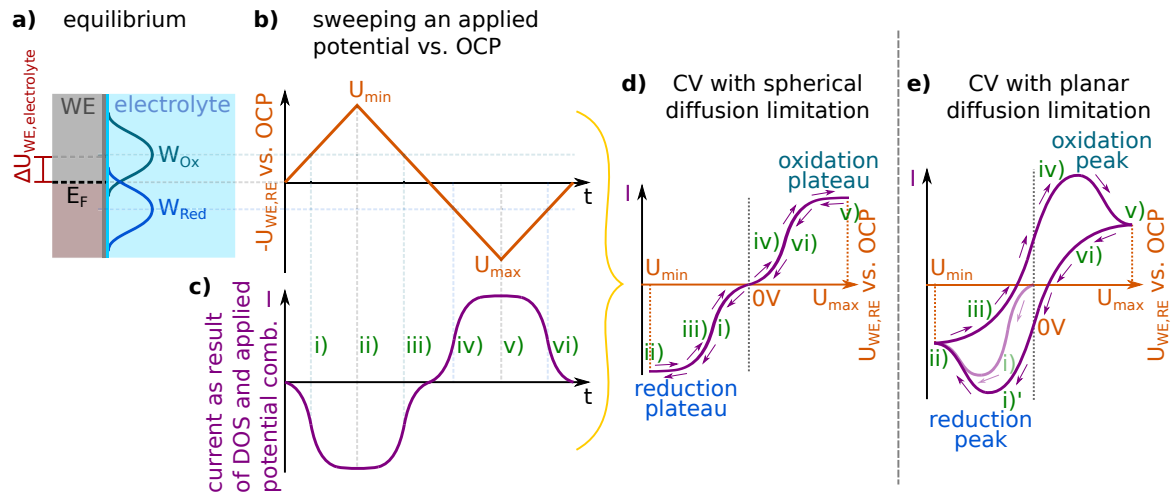
Figure 2.6 – Current development for a cyclic voltammogram (CV). a) shows the W distribution as discussed in figure 2.1 for equilibrium of a system with same Ox and Red concentration and E_F in their intersection. The potential is swept at constant rate v[V/s] and potential given relative to OCP, b). The resulting current in c) is a consequence of sweeping E_F according to b) through the W distribution in a). Important points are indicated and connected with dashed lines. Plotting the current over potential gives d). For more dominant mass diffusion limitation, i.e. planar mass diffusion, we get e).

negative sign for reduction of Ox reactant species.

If the potential is swept, we have to consider the relative position of the W distribution more closely. A continuous potential sweep at constant scan rate v[V/s] from a start to a minimum U_{min} (or maximum U_{max}), back through the starting potential to a maximum U_{max} (or minimum U_{min}) as depicted in figure 2.6 b) is called linear cyclic voltammogram (CV). A single continuous scan from U_{start} to e.g. U_{max} is called linear sweep voltammetry (LSV). We assume equation 2.3, equal concentrations of Ox and Red species and that at equilibrium, E_F is centered between the W_{Ox} and W_{Red} as depicted in subfigure a). An applied negative potential shifts E_F up, a positive potential down. For the beginning we assume very small diffusion mass transport limitation. Figure c) shows the resulting current versus time for the potential sweep in b). c) is simply derived looking at the combination of a) and b). We begin at OCP and start to scan in the negative potential direction versus OCP. Please note the minus in the potential axis in b). The current increases at the beginning in strength with negative sign according to the increasing W_{Ox} area below E_F: electrons tunnel from the WE to the spatially and energetically available Ox species. The current slope maximum is at the potential of W_{Ox} peak maximum, i). The current plateaus due to all W_{Ox} area being covered by E_F, i.e. the electron tunneling probability does not increase anymore. After reaching U_{min} at ii), we scan back to OCP and the current follows the reverse processes. Scanning to positive potentials vs. OCP, the current becomes positive due to electrons tunneling from Red species with energies larger or equal to E_F into the WE. The current therefore follows the W_{Red} area above E_F. Again the maximum current slope is at W_{Red} maximum. The resulting current over potential plot is presented as CV in d).

For many electrodes the diffusion limitation is however more predominant, which leads to a CV similar to e). Beginning at 0 V vs. OCP, we start with zero current. The current increases in strength until the diffusion limitation analog to figure 2.5 becomes dominant. The current decreases in strength due to the reactant depletion and product accumulation. The diffusion layer thickness
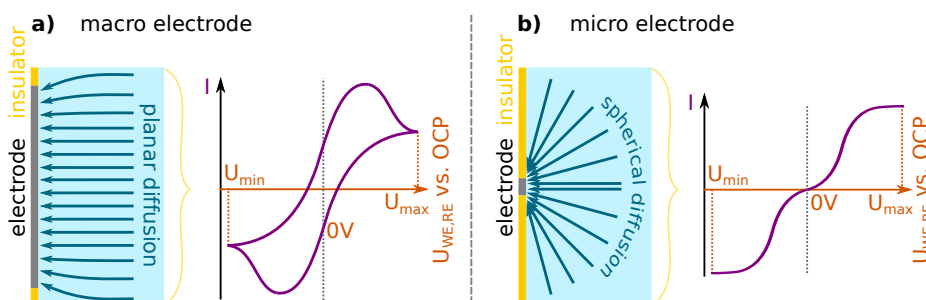
Figure 2.7 – Planar and spherical diffusion and resulting CV. Only reactant diffusion to the electrode is indicated. The same applies also for the product diffusion away from the electrode.

before sweeping through the reduction peak is typically of $\approx 10\,\mu m$. At the point of inverting the scanning direction, the diffusion layer thickness has increased to $\approx 40\,\mu m$.[39] Scanning back, iii), the OCP is shifted up due to a decreased W_{Ox} and increased W_{Red} in the WE surface vicinity (compare figure 2.1). This results in a current going through zero for potentials still negative. This schematic continues, such that going to U_{max} and back to $0\,V$ results in a negative current where no current occurred at the start. The second consecutive CV will therefore look different from the first CV. Obviously, the start does not have to be at OCP but at any potential. However, starting at OCP gives some additional information: if the system was already used for some prior experiments, the OCP is not equal to the original equilibrium position anymore but the system is still relaxing by diffusion, adsorption and desorption processes. OCP is at the equilibrium interface potential again, once OCP is not changing anymore. This can be double-checked by starting a CV at OCP: equilibrium is only reached if no current is flowing. The new equilibrium interface potential is in general not the same as the original one, which is due to changed surface and concentration states. Many text books suggest to start and end a CV at U_{max} or U_{min} which has other advantages, however does not cover the OCP information just described. Not only the OCP but also the current and shape of a CV is strongly dependent on its history, i.e. general age, amount and types of previous experiments.

To approximate a CV similar to 2.6 d), one has to minimize diffusion limitation by either strongly decreasing the amount of consumed products at the surface, such that the diffusion speed is sufficient, or increase the mass transport. The latter can only be achieved using a less viscous solvent or indirectly by artificially increasing the molecule flux using a flow-device or stirring. The former can be achieved using very small electrodes, e.g. commercial Pt ultra micro electrodes (UME) with a radius of $5\,\mu m$. The reason is, that the directions of diffusion are increased from only front, called planar diffusion, to also from the sides, convergent diffusion, such as depicted in figure 2.7 a) and respectively b). For spherical diffusion, the residual diffusion limitation defines the plateau height.

The identification and characterization of reduction and oxidation peaks or plateaus as indicated in figure 2.6 d) and e) provides information about the electrolyte thermodynamics, kinetics and allows analysis of coupled electrochemical processes or of adsorption processes. For example, electrochemists distinguish between reversible and irreversible redox systems, such as shown in figure 2.8. To do so, CVs covering the complete oxidation and reduction range are recorded at different scan rates. If the peak position does not change but only the peak height increases with scan rate, the system is identified as reversible. If not only the peak height but also relative
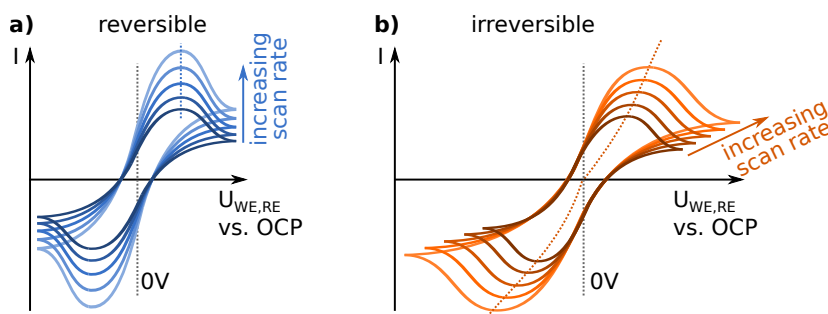
Figure 2.8 – Reversible and irreversible redox species CV for varying scan rates. Reversible systems are identified by reduction and oxidation peaks increasing in strength but shifting in potential. Irreversible systems also no shift in potential.

potential position changes to stronger values, the system is identified as irreversible. Perfectly reversible systems are characterized by a reduction to oxidation peak to peak separation of 60 mV per exchanged electron within one CV and an identical peak height of reduction and oxidation peak. For reversible processes E_F^0 is found in the center between oxidation and reduction. The reduction and oxidation peak current density strength increases according to the *Randles-Ševčik* equation,

$$j_{peak,reversible} = \pm 0.446 \cdot nF \cdot [\text{reactant}]_{bulk} \sqrt{\frac{nFD\nu}{RT}}.$$

Thus, the increase is linear with the square root of the scan rate $\nu [V/s]$. $D[cm^2/s]$ is the diffusion coefficient of the reduction (-) or oxidation process (+) and $[\text{reactant}]_{bulk}$ is the corresponding reactant species bulk concentration. Reversible processes are physically defined by rapid electron transfer kinetics in comparison to the mass transport rate. For irreversible processes this is not the case and the result is a peak position potential shift especially for fast scan rates. The shift to stronger potentials appears as if an additional, so called over-potential, has to be applied. However, the shift is delayed in time due to the slow electron exchange and therefore appears larger the faster the scan rate. The peak broadening can be assigned to the same effect.

The system described so far has to be further elaborated if we want to consider potential modulation,

$$U_t = U_0 \cdot \sin(2\pi f t).$$

The modulation amplitude U_0 is typically of some 1 mV and frequency f of typically some 1 Hz to some 1 MHz. For ease of discussion we assume no potential offset as depicted in subfigure 2.9 a). Assuming a response of alternating current (AC) I_t, the response frequency is equal to that of the excitation, but there is some delay in time, i.e. phase shift ϕ,

$$I_t = I_0 \cdot \sin(2\pi f t + \phi),$$

I_0 amplitude. The modulation over time displayed as average such in figure 2.9 b) is called
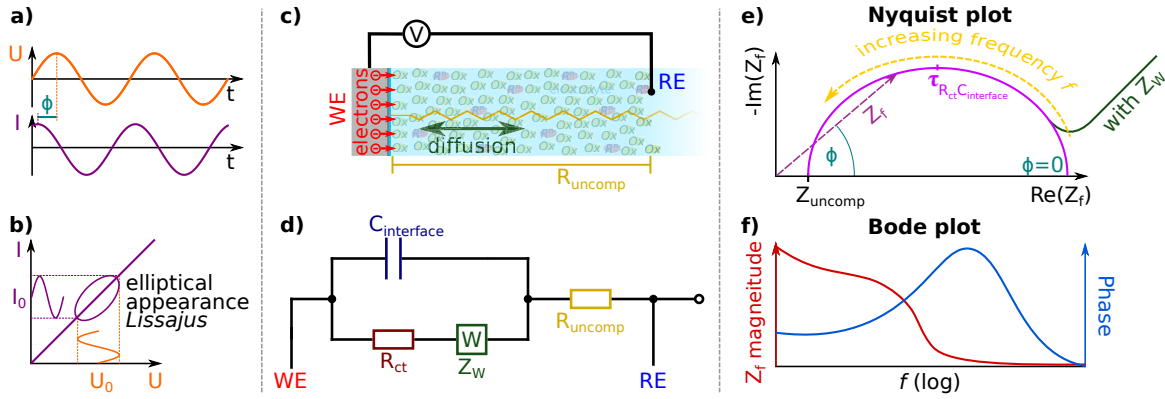
Figure 2.9 – Electrochemical impedance spectroscopy. a) and b) potential modulation technique for impedance measurement. d) displays an equivalent electric circuit with its components aligned in position with the corresponding electrochemical cell part in c). e) shows the resulting impedance as *Nyquist* plot, i.e. negative imaginary impedance part over real part. The pink half circle shaped line corresponds to the simplified *Randles* circuit without *Warburg* impedance Z_W. Adding Z_W increases the imaginary part again with a slope of 45 degres in direction of very slow frequencies, in green added line. f) represents the corresponding Bode plot representation, Z_W included.

Lissajous figure. The impedance is

$$Z = \frac{U_t}{I_t} = Z_0 \frac{\sin(2\pi f t)}{\sin(2\pi f t + \phi)}$$

with amplitude $Z_0 = \frac{U_0}{I_0}$. Using complex expressions for U_t and I_t,

$$\exp(\mathrm{i}2\pi f t) = \cos(2\pi f t) + \mathrm{i} \cdot \sin(2\pi f t)$$
$$\Rightarrow U_t = U_0 \cdot \exp(\mathrm{i}2\pi f t) \quad \text{and} \quad I_t = I_0 \cdot \exp(\mathrm{i}2\pi f t - \phi),$$

the impedance reduces to the time independent form

$$Z_f = \frac{E_t}{I_t} = Z_0 \exp(i\phi)$$
$$= Z_0 \big(\cos(\phi) + \mathrm{i} \cdot \sin(\phi)\big).$$

The electric behavior of electrochemical cells can be modeled using equivalent electric circuits such as presented in subfigure 2.9 d). The electric circuit elements are aligned with their corresponding electrochemical cell parts in c). The WE/electrolyte interface double layer can be described as charged capacitor with capacitance $C_{interface}$ which is placed parallel to the electrolyte charge transfer resistance R_{ct} and in series with the uncompensated electrolyte resistance R_{uncomp}, we get one of the simplest equivalent electric circuits, called *Randles* cell.[44] In this model, the capacitor discharging current is of the form

$$I_C(t) = I_0 \cdot \exp\left(\frac{1}{R_{uncomp} C_{interface}}\right),$$

---

[44] J. E. B. Randles, "Kinetics of rapid electrode reactions", Discussions of the Faraday Society **1**, 11 (1947).

with initial current I_0.[45] The so-called RC time constant $\tau_{R_uC} = R_{uncomp}C_{interface}$ defines the time t until the capacitor is charged down to e^{-1} of its original charge and is typically in the range of $100\,\mu$s and 1 ms, and therefore less important for standard chronoamperometric measurements but the more so for impedance measurements. Often the diffusion induced impedance Z_W is considered using a so called *Warburg* impedance element placed in series with R_{ct} and parallel to $C_{interface}$.[2] The systematic measurement and analysis of impedance is called electrochemical impedance spectroscopy (EIS). The plot of imaginary part over real part for the impedance measurement at a series of frequencies as depicted in figure 2.9 e)is called a *Nyquist* plot. The pink half circle is the result of a Randles circuit without Z_W. Impedance at low frequency is found on the right and at high frequency at the left. Starting at very small frequencies, I_t is able to follow U_t with almost no phase difference, hence Z consists almost only of the real part, $Z_0 \cos(\approx 0)$. The system struggles to follow for increasing f, ϕ increases and with it the imaginary part while the real part decreases, until the sinus maximum is reached at the cell-RC time constant frequency $f_{R_{ct}C} = \frac{1}{2\pi\tau_{2\pi R_{ct}C_{interface}}} = \frac{1}{R_{ct}C_{interface}}$. At even further increasing frequencies R_{ct} is bypassed by the increasingly important capacitance. For the inclusion of Z_W, the imaginary part does not vanish for very small f but the curve increases at a slope of 45 °. However, for large frequencies diffusion cannot manifest and the Warburg influence is negligible.[45] The huge disadvantage of Nyquist representation is the frequency information loss. Nyquist plots are therefore typically presented in combination with a *Bode* plot, i.e. Z_f magnitude and phase plotted over logarithmically scaled frequency as presented in f). Depending on the sample also the Z_f magnitude might be plotted on a logarithmic scale.[46] Finding the correct equivalent circuit for a measured system gives information about the system composition such as possible parallel existing interfaces and or surface processes.

2.1.1 Methyl Viologen

Several requirements have to be considered for the choice of a redox species for the detection of spin dependent charge transfer processes at an electrode/electrolyte interface. First of all, the redox species should possess a three stage oxidation schematic with the radical state being the center stage. This allows not only the observation of the radical reduction by spin polarized electrons from the electrode but also the effect of spin polarized electrons going from radical to spin polarized electrode by oxidation. Second, the molecule in solution has to be stable over several days which is necessary for the specific matrix scanning scheme discussed in section 3.2.1. Third, the actual radical state has to be stable in presence of electrodes, microwave and light at 830 nm. Light at 830 nm is necessary for optical spin pumping discussed in section 2.2.3 and microwave radiation at 9.4 GHz for CPR discussed in section 3.1.5. A majority of radical state is necessary to perform simultaneous CW EPR control experiments and is helpful for an optimal proportion of spin polarized processes. Fourth, the potential window should lay in the negative potential range, which is due to the use of p-GaAs for optical spin pumping and its easier decomposition by oxidation at positive potentials, see section 2.1.2. Fifth, no light absorbance at

---

[2] The common way of drawing equivalent electric circuits is in electrochemistry mostly opposite to d), i.e. RE on the left and WE on the right. This more common reading direction will also be used in the experimental part.

[45] A. J. Bard, and L. R. Faulkner, *Electrochemical Methods: Fundamentals and Applications*, Vol. 2 (Wiley, New York, 2001), p. 864.

[46] T. E. Keyes, and R. J. Forster, *Handbook of Electrochemistry* (Elsevier, 2007), pp. 591–635.

a) $\qquad$ MV^{2+} $\xrightarrow{+\ e^-}$ $MV^{+\bullet}$ $\xrightarrow{+\ e^-}$ MV^{0} $\qquad$ (2.6)

b)

c)
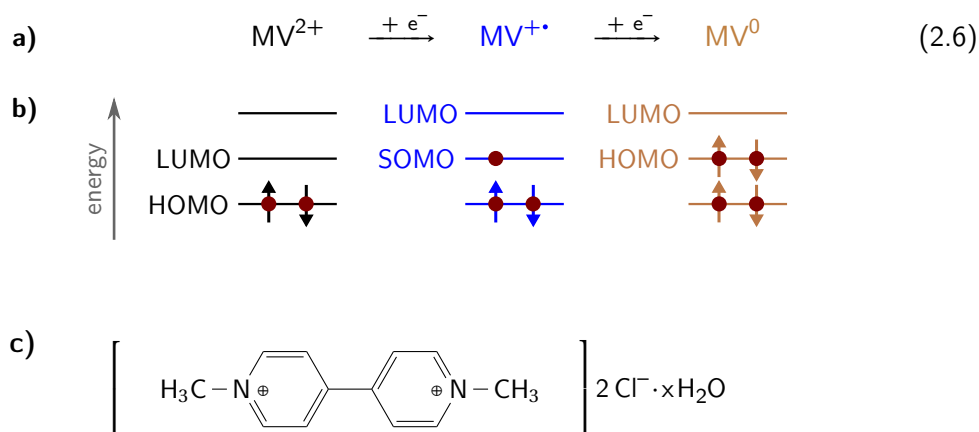
Figure 2.10 – Methyl viologen (dichloride) reduction path, corresponding molecule orbital occupation and molecule structure.

830 nm should occur which is especially important to avoid circular dichroism. Methyl Viologen (MV) has these properties. We also chose it because Chazalviel noted that MV was the only redox species for which a spin dependent process was observed. This is most likely due to the tendency of methyl viologen to enrich its radical state via to a comproportionation reaction which is described below.

Methyl viologen *1,1'-Dimethyl-4,4'-bipyridinium*, is mostly delivered as methyl viologen dichloride, $C_{12}H_{14}Cl_2N_2 \cdot xH_2O$, with its chemical structure depicted in figure 2.10 c). Dissolved in e.g. water or acetonitrile (ACN), the diamagnetic dication ground state MV^{2+} is transparent.[47] Reduction to $MV^{+\bullet}$ can either be achieved by electroreduction,[47] by chemical reduction using e.g. zinc,[48], direct photoreduction,[49] or by photochemical reduction with the aid of ruthenium(II) complexes[50] or other reactants[51]. The paramagnetic radical $MV^{+\bullet}$ is clearly recognizable by its strong blue color. Further reduction leads to the neutral MV^{0} with a red-brown color. The reduction scheme is depicted in figure 2.10 a). The corresponding highest occupied molecular orbital (HOMO), lowest unoccupied molecular orbital (LUMO) and singly occupied orbital (SOMO) are indicated in b) with arrows indicating the electrons spin orientation. The optical absorbance of $MV^{+\bullet}$ is mostly at 606 nm but also at 396 nm.[48] MV^{0} has optical absorbance at 396 nm and 378 nm when dissolved in ACN. Its presence is therefore hard to detect if $MV^{+\bullet}$ is present also.[50]

$MV^{+\bullet}$ reduction to MV^{0} is at least partly possible by the use of Zn, but takes very long (more than 10 hours) and the result is strongly changed in viscosity, indicating that various other processes

[47] P. M. S. Monk, *The Viologens: Physicochemical Properties, Synthesis, and Applications of the Salts of 4,4'-Bipyridine* (Wiley, Manchester, 1998), p. 311.

[48] J. Peon, et al., "Excited State Dynamics of Methyl Viologen. Ultrafast Photoreduction in Methanol and Fluorescence in Acetonitrile", The Journal of Physical Chemistry A **105**, 5768–5777 (2001).

[49] T. W. Ebbesen, et al., "Photoreduction of methyl viologen in aqueous neutral solution without additives", Nature **298**, 545–548 (1982).

[50] M. Suzuki, et al., "Photosensitized production of doubly reduced methylviologen followed by highly efficient methylviologen radical formation using self-assembling ruthenium(ii) complexes", Chemical Communications **1**, 1534–1535 (2002).

[51] H. Yoshikawa, and S.-i. Nishikiori, "Photoinduced Color Change of Methylviologen in Polycyano-Polycadmate Host Clathrates.", Chemistry Letters **5**, 142–143 (2000).

are taking place. Even though well visible in CVs, actual electroreduction of $MV^{+\bullet}$ to MV^0 in large quantities is in my experience almost impossible.[3] It is quite interesting, that for samples well sealed from oxygen the concentration is in general shifted to $MV^{+\bullet}$, independent of how long electrochemical experiments are performed. This is partly due to the comproportionation reaction following a dimerization process via the dimer $(MV)_2^{2+}$,[53]

$$MV^0 + MV^{2+} \rightleftharpoons (MV)_2^{2+} \rightleftharpoons 2\,MV^{+\bullet},$$
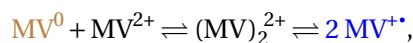
which continuously shifts the equilibrium to $MV^{+\bullet}$. However, at some point the MV^{2+} concentration should decrease so much, that the comproportionation process becomes unimportant. Another process must therefore play a role in shifting the concentration to $MV^{+\bullet}$ since a MV^0 accumulation is in general suppressed. This process is still unclear. The $(MV)_2^{2+}$ dimer has an absorption peak at 874 nm, which lies close to the applied light of 830 nm, but far enough such that no circular dichroism occurs. The dimer life time is in any case of only second range, such that its concentration is always very low.[53]

The biggest flaw of working with $MV^{+\bullet}$ is its extreme sensitive to oxygen and other chemicals. In fact, the high sensitivity at reaction rate constant of $7.7 \times 10^8\,dm^3/(mol \cdot s)$ for the $MV^{+\bullet}$ to MV^{2+} oxidation by oxygen through e.g. the path $MV^{+\bullet} + O_2 \xrightarrow{H_2O} 2\,MV^{2+} + H_2O_2 + 2\,OH^-$ led to the suggestion of using the loss of blue color as probe for even traces (< 1 ppm) of oxygen diffusion through e.g. polymers.[54,55] Also the presence of water can in combination with an electrolysis lead to $MV^{+\bullet}$ decay via H_2O_2.[56] Sample preparation therefore has to be carried out inside a glove-box and all chemicals are ordered in extra pure and dry standard.

2.1.2 p-GaAs as Working Electrode

For the detection of spin dependent interface charge transport, a spin polarization on the electrode is necessary. As discussed further down in section 2.2.3, a common and well documented classical means of obtaining spin polarization on III/V semiconductors is by by means of optical pumping. However, semiconductor electrodes come with some differences to the above described metallic electrodes. Due to the band structure it is not sufficient to solely consider the Fermi level E_F, but also the conduction band E_{CB} and valence band E_{VB}. Intrinsic semiconductors are not very conductive, such that some doping is necessary for the use as electrode. For n-type doping an additional donor level E_{DL} is introduced below E_{CB} with its height depending on the doping level, higher for higher doping. The Fermi level is shifted to the majority charge carrier band, i.e. lies between E_{CB} and E_{DL}. At room temperature the thermal energy is typically sufficient to bring

---

[3] MV^0 production is however not in general difficult, MV^0 can be produced in large quantities and even as pure crystals synthesized, [52].

[53] P. M. S. Monk, et al., "Evidence for the Product of the Viologen Comproportionation Reaction being a Spin-paired Radical Cation Dimer", J. Chem. Soc. Perkin Trans. II **1**, 2039–2041 (1992).

[54] P. B. Sweetser, "Colorimetric determination of trace levels of oxygen in gases with the photochemically generated methyl viologen radical-cation", Analytical Chemistry **39**, 979–982 (1967).

[55] C. Stradowski, "Methylviologen cation radical as probe of oxygen diffusion through polymer", Journal of Applied Polymer Science **41**, 2511–2512 (1990).

[56] N. Chitose, et al., "Effect of Formate Concentration on Radical Formation in the Radiolysis of Aqueous Methyl Viologen Solutions", The Journal of Physical Chemistry A **102**, 2087–2090 (1998).
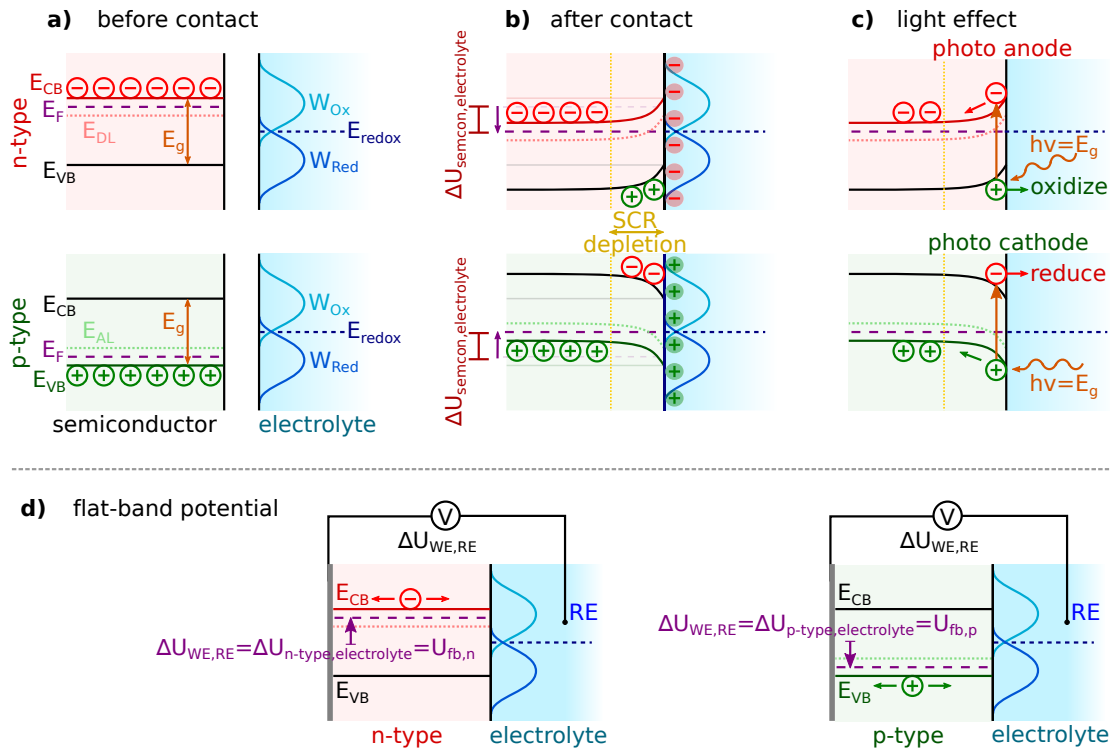
Figure 2.11 – Pinning induced surface band bending for an interface of doped semiconductor and electrolyte. The upper line in a)-c) corresponds to n-type doped semiconductors and the lower line to p-type. In a) the state before contact is depicted. Contacting the semiconductor with the electrolyte, the semiconductor Fermi level and electrolyte redox potential equilibrate by charge transfer, b). Pinning leads to a bending of conduction and valence band with subsequent depletion of majority carriers at the surface. Applying light at energy of the band gap E_g makes the n-type semiconductor act as a natural photo anode and p-type as natural photo cathode, d).

To overcome the depletion layer for the majority carriers, a potential has to be applied. The potential where the majority carrier current sets on, i.e. where the semiconductor bands are flat, is called flat-band potential, d).

most donor electrons into the conduction bands as depicted in figure 2.11 a), making n-type an electron majority charge carrier system. For a p-doped semiconductor this corresponds to an additional acceptor level E_{AL} above E_{VB}. At room temperature the E_{AL} level is filled with electrons from E_{VB}, such that E_{VB} is filled with conduction holes, making it a hole majority charge carrier system.

Before contacting a semiconductor with an electrolyte, the formal potential $E_f^{0'}(Ox/Red)$ of the Nernst equation 2.2, also called redox potential E_{redox}, is energetically typically higher than E_F, compare figure 2.11 a). Bringing the semiconductor in contact with the electrolyte, the semiconductor Fermi level equilibrates with E_{redox} by charge transfer resulting in an interface potential drop $\Delta U_{semcon,electrolyte}$. For the electrolyte we assume again same concentrations of Ox and Red species of equation 2.1. We also assume that the electrolyte volume is large and the semiconductor comparably small, such that contact with an electrode will shift W_{Ox} and W_{Red} only in a negligible way. It is therefore E_F moving down to E_{redox} for n-type by transferring electrons into the electrolyte, while E_{redox} is almost unchanged regarding before and after contact.[45] The semiconductor band structure moves with E_F in the bulk material. However, the bands

are pinned to their original level at the semiconductor edge.[57] For n-type this leads to band up bending from semiconductor bulk to surface as depicted in b). The resulting depletion of electron majority charge carriers and accumulation of hole minority charge carriers extends from the semiconductor surface up to several 100 nm into the semiconductor bulk in the space charge region (SCR) or depletion layer.[58] The SCR is compensated on the electrolyte side by an accumulation of mostly supporting electrolyte ions of negative charge. For p-type E_F is typically below E_{redox} and therefore moved up when contacting with the electrolyte, leading to a band down bending from semiconductor bulk to edge. This leads to an accumulation of electron minority charge carriers at the surface and of positively charged ions at the p-semiconductor/electrolyte interface in the electrolyte.

Shining light of energy $h\nu$ greater than the band gap produces electron hole pairs at the semiconductor surface which are separated due to the specific band bending and increases the surface minority charge carrier accumulation as depicted in figure 2.11 c).[59] This results in an additional semiconductor/electrolyte interface drop and therefore oxidation of *Red* at n-type, respectively reduction of *Ox* at p-type. Due to the nature of this process happening even without external potential applied, this makes n-type semiconductors natural photo anodes and p-type a natural photo-cathodes. The potential drop proportional to the light power, i.e. OCP shift, called photopotential, is in my observations of some 100 mV at a light power of 100 μW.

The use of light for optical electrode spin polarization is also the reason for the use of gallium arsenide (GaAS) in this thesis. GaAs has a convenient band-gap of $E_g = 1.42$ eV, i.e. red light at a wavelength of $\lambda = 870$ nm for which setup components are comparably easy to handle and readily available. Going to the three electrode system as described above in section 2.3, the GaAs is used as WE. The potential necessary to counteract the band bending until they are flat, i.e. until the interface potential drop is compensated, is called flat band potential U_{FB}. Without light U_{FB} is equal to $\Delta U_{semcon,electrolyte}$, as depicted in 2.11 d).

For the discussion of current in a three electrode system we start without light and consider the example of a p-GaAs WE, compare a) till d) in figure 2.12. The resulting current is plotted for a potential applied versus OCP. We assume no IR drop. At U_{FB} vs. OCP no current flows, since no charge separation exists, c). Going to more positive potentials, a majority charge carrier accumulation exists at the interface, such that the electrode acts as anode, d). For potentials more negative than U_{FB} no current exists due the increasing depletion layer at the interface, b) and a). Turning on irradiation, e)-h), electron hole pairs are created at the p-GaAs surface. For U_{FB} and potentials more positive nothing changes in comparison to c) and d) since this current majority charge carrier dominated and therefore resistance limited, given a doping large enough in comparison to the resistance, g) and h). However, for potentials more negative than U_{FB}, minority charge carriers are available at the interface, such that reduction of *Ox* by electrons at the photo cathode is enabled, f). Even though the interface conductance is here electron dominated, the p-GaAs bulk conductance is still dominated by hole majority carriers. The current is therefore limited by the amount of electron hole pairs created by light at the semiconductor surface, e). The

[57] N. Sato, *Electrochemistry at Metal and Semiconductor Electrodes* (Elsevier Science, Hokkaido, 1998), p. 412.

[58] A. W. Bott, "Electrochemistry of semiconductors", Current Separations **17**, 87–92 (1998).

[59] A. J. Bard, "Photoelectrochemistry and heterogeneous photo-catalysis at semiconductors", Journal of Photochemistry **10**, 59–75 (1979).

a) negative potential
$\Delta U_{WE,RE}=-xV$ vs. OCP — RE
E_{CB} — E_F — E_{redox} — E_{VB} — W_{Ox} — W_{Red}
depletion — p-type — electrolyte

b) OCP
$\Delta U_{WE,RE}=0V$ vs. OCP — RE
E_{redox} — SCR

c) flat band
$\Delta U_{WE,RE}=U_{FB}$ vs. OCP — RE

d) positive and > U_{FB}
$\Delta U_{WE,RE}=+xV$ vs. OCP — RE
oxidize — accumulation

current
photo cathode
increasing majority charge carrier **depletion**
a) b) c)
$\Delta U_{WE,RE}$ vs. OCP
R=const.
d) h)
U_{FB}
photo cathode ohmic range
g)
photo cathode power limited range
e) f)
dark and irradiation: majority charge carrier **accumulation**
→ quasi metallic behavior
dark anode

e) negative potential
$\Delta U_{WE,RE}=-xV$ vs. OCP — RE
reduce — $h\nu=E_g$
depletion — p-type — electrolyte

f) OCP
$\Delta U_{WE,RE}=0V$ vs. OCP — RE
reduce — $h\nu=E_g$ — SCR

g) flat band
$\Delta U_{WE,RE}=U_{FB}$ vs. OCP — RE
$h\nu=E_g$

h) positive and > U_{FB}
$\Delta U_{WE,RE}=+xV$ vs. OCP — RE
$h\nu=E_g$ — oxidize — accumulation

Figure 2.12 – Simplified potential dependent current discussion for a p-GaAs electrode without light in a)-d) and with light in e)-h). Without light a p-GaAs electrode acts purely as anode. With light a p-GaAs acts as anode for potentials above U_{FB} and as light power limited cathode for potentials below U_{FB}.

maximal light effect is reached at OCP, which in reverse is co-defined by the light power. Maximum possible photo cathodic current strength is therefore reached at OCP, assuming the electrolyte resistance is potential independent. As elaborated above, for most electrolytes the resistance is not constant, see e.g. figure 2.6. The light power can therefore be used to limit the maximal current and therefore suppress diffusion limitation. The offset from the dashed $R = const.$ line is due to over-potentials needed to compensate e.g. electrolyte space charge or adsorption. Another source of potential offset are surface states, i.e. additional orbitals localized on atoms at the surface where the lattice ends, e.g. dangling bonds defects due to the dissolution of only one species, e.g. only As in GaAs. Surface states often lay in the band gap and amount therefore to intermediate energy levels through which electrons can relax[60] and be "trapped", depending on the availability of holes, see figure 2.13 a) and b).[61] To compensate this, an over potential is necessary, i.e. the energy has to be increased so that surface state access becomes more unlikely in comparison to the distribution of states of surface species from the solution.

For n-doped GaAs everything is inversed, i.e. n-GaAs acts as cathode in dark and under illumi-

[60] J. Li, and L. Peter, "Surface recombination at semiconductor electrodes", Journal of Electroanalytical Chemistry and Interfacial Electrochemistry **193**, 27–47 (1985).

[61] R. Memming, *Semiconductor Electrochemistry 3. Electrochemical Systems* (Wiley-VCH Verlag GmbH & Co. KGaA, Weinheim, Germany, Apr. 2000).
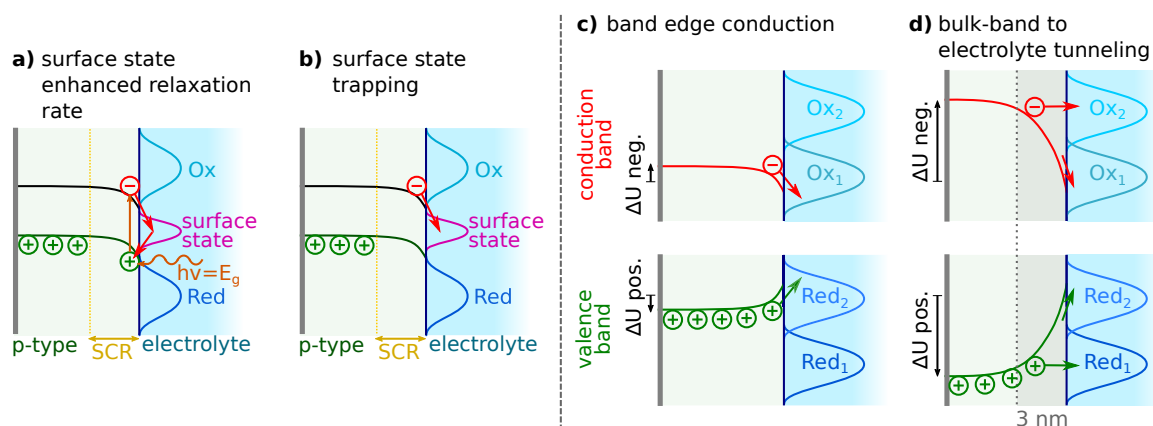
Figure 2.13 – Surface state relaxation, trapping and bulk band to electrolyte tunneling. Depending on the availability of charge recombination partners surface states can either act as intermediate energy levels through which electrons can relax more easily, a), or as traps, b). Assuming only electron transfer from the band edge to the electrolyte, many W could not be reached by electrons from the same semiconductor band. The access of W away from the band pinning energy is achieved by electrons from band regions up to some 10 Å in the semiconductor bulk, compare c) and d). Tunneling is indicated by horizontal arrows.

nation but as anode only under irradiation. The potential range of methyl viologen lies in the negative, compare section 2.1.1, which makes n-GaAs unsuitable for methyl viologen if photo current is the intent. Another reason for the use of p-doped GaAs is that in photo cathode potential range photo electron hole pairs created at the surface are separated and mixture with electrons from the bulk is suppressed. Optical spin pumping produces therefore an accumulation of mostly spin polarized electrons at the semiconductor/electrode interface, see section 2.2.3 below. The reduction is therefore dominated by electrons produced by optical spin pumping at the surface. For n-GaAs this is not the case, since in reduction range conductance is throughout the whole n-type GaAs sample of electron type. The electrons accumulated at the semiconductor/electrolyte interface are for n-GaAs therefore a mixture of not spin polarized bulk electrons and electrons due to optical spin pumping. The biggest flaw of p-GaAs is its dissolution at positive potentials: corrosion is mostly triggered by hole acceptance of atoms at the semiconductor surface and dissolution is more likely for the chemically more reactive species, here arsenide. The instability of p-GaAs at positive potentials is therefore due to its larger hole concentration worse than for n-GaAs.

Edge band pinning raises the question how certain radical states can be accessed. One could assume that charge carriers follow the band until the edge and only then tunnel to the electrolyte, such as depicted in figure 2.13 c). A radical state without overlap with the point of band pinning could not be accessed if only this mechanism would support charge transfer. However, these W can be accessed by charge tunneling from band ranges in the semiconductor bulk to electrolyte, as indicated in d) with horizontal arrows.[61] Tunneling of 10 Å is typically assumed as achieved by comparably large charge quantities, such that especially the steep band parts which come close to the edge are addressed by this process. Tunneling becomes more likely with increased charge carrier density because of the decreased SCR thickness. Memming finds for a doping of 1×10^{20} cm^{-3} a SCR thickness of 30 Å at 1 V applied, which is feasible by field assisted tunneling. The tunneling can lead to potential shift of redox peaks with respect to their expected potential. The conduction schematic of fixed band position at the edges is in any case extremely simplified.

In reality the combination of additional redox potentials, surface state or light induced flat band and band edge shift, quasi Fermi level or concentration dependent band shifting make prediction and analysis of CV for semiconductor/electrolyte interfaces difficult.[61]

2.2 Spin Polarization and Resonance

As will become clear in section 2.3, the magnitude of the spin effect on the current is strongly dependent on having a large spin polarization of both, the electrode and electrolyte. Regarding the spin-polarization on the electrode, we use optical spin pumping on III/V semiconductors (section 2.2.3) and the CISS effect (2.2.2). The electrolyte is spin polarized by an external magnetic field B_0 and is discussed in this section.

Electrons are spin one-half particles of negative charge. We will write the spin quantum number as m_s with $m_s = \pm\frac{1}{2}$. The resulting magnetic moment is antiparallel to its spin with z-component $(\mu_s)_z = -g\mu_B m_s$ (Landé factor g with $g_e = 2.0023$ for free electrons; Bohr magneton $\mu_B = \frac{e\hbar}{2m_e} = 9.2740 \times 10^{-24}$ J/T). Electrons will align inside an external magnetic field either antiparallel to B_0 ($m_s = -\frac{1}{2}$) with spin $|\downarrow\rangle$ or parallel to B_0 ($m_s = \frac{1}{2}$) with spin $|\uparrow\rangle$ and corresponding energy

$$E_{m_s} = m_s g \mu_B B_0,$$

compare figure 2.14. Paired electrons align parallel to each other due to the Pauli exclusion, resulting in an overall magnetization of zero. Samples such as radicals, paramagnetic centers or ferromagnets contain unpaired electrons and will experience a net magnetization: the B_0 induced Zeeman energy splitting of

$$\Delta E = E_{+\frac{1}{2}} - E_{-\frac{1}{2}} = g\mu_B B_0$$

leads according to the Maxwell-Boltzmann distribution to a higher population of the lower energy state $N_{-1/2}$ compared to the upper energy state $N_{+1/2}$, which is at equilibrium external perturbation at equilibrium

$$\frac{N^0_{+\frac{1}{2}}}{N^0_{-\frac{1}{2}}} = \exp\left(-\frac{E_{+\frac{1}{2}} - E_{-\frac{1}{2}}}{k_B T}\right) = \exp\left(-\frac{g\mu_B B_0}{k_B T}\right) \tag{2.7}$$

(temperature T [K], Boltzmann constant $k_B = 1.3806 \times 10^{-23}$ J/K).[62–65] The resulting spin-polarization

[62] J. E. Wertz, and J. R. Bolton, *Electron Spin Resonance: Elementary Theory and Practical Applications* (Springer Netherlands, Dordrecht, 1972), p. 497.

[63] D. M. Murphy, *Metal Oxide Catalysis - Chapter - EPR Spectroscopy of Polycrystalline Oxide Systems*, Vol. 1 (Wiley-VCH Verlag GmbH & Co. KGaA, Weinheim, Germany, 2009), pp. 1–50.

[64] G. R. Eaton, et al., *Quantitative EPR* (Springer Vienna, 2010), pp. 1–185.

[65] C. P. Slichter, *Principles of Magnetic Resonance*, Third Enlarged and Updated Edition, Springer Series in Solid-State Sciences (Springer Berlin Heidelberg, 1990), pp. 1–655.
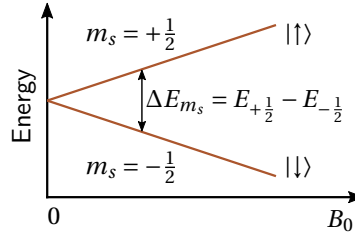
Figure 2.14 – Zeeman splitting of the electron spin state in an external magnetic field B_0.

P is defined as

$$P^0 \equiv \frac{N^0_{-\frac{1}{2}} - N^0_{+\frac{1}{2}}}{N^0_{-\frac{1}{2}} + N^0_{+\frac{1}{2}}} = \frac{\exp\left(-\frac{-\frac{1}{2}g\mu_B B_0}{k_B T}\right) - \exp\left(-\frac{+\frac{1}{2}g\mu_B B_0}{k_B T}\right)}{\exp\left(-\frac{-\frac{1}{2}g\mu_B B_0}{k_B T}\right) + \exp\left(-\frac{+\frac{1}{2}g\mu_B B_0}{k_B T}\right)}. \tag{2.8}$$

The population difference given by equation 2.7 can be increased by decreasing the temperature or increasing B_0. Chazalviel used samples containing organic electrolytes and was therefore bound to temperatures close to room temperature. He performed his experiments at large field ranges of $\pm 2.5\,\text{T}$.[16] This high field raises magneto hydrodynamic (MHD) effects, i.e. mostly Lorentz force acting on ions such as discussed in section 1. Large B_0 changes therefore introduce current changes. To avoid MHD problems, we use magnetic resonance experiments. The spin effect is hereby detected by sweeping the field across resonance which is about 1 mT broad, whereas Chazalviel's experiment and more recent papers described in section 1 rely on large changes of the magnetic field. In magnetic resonance experiments, the spin-polarization is disturbed by electromagnetic radiation of corresponding energy

$$h\nu = \Delta E_{m_s} = g\mu_B B_{res}, \tag{2.9}$$

called resonance condition (photon frequency ν, Planck constant $h = 6.626\,070\,15 \times 10^{-34}\,\text{Js}$). The resonant spin-flip stimulation at fitting external field $B_{res}(\nu)$ is a highly reliable method to detect spin-polarization. The Landé g-factor in equation 2.9 is material dependent, such that a shift of g from g_e can be used for material characterization. The concept of detecting electron spins by resonant absorption is called electron paramagnetic resonance (EPR).

2.2.1 CW EPR and Lock-In detection

Several methods for the detection of electron spin resonance are commonly used. This thesis is solely based on continuous wave (CW), cavity system EPR (no pulsed techniques, no coplanar waveguide systems, etc.). The basic cavity CW EPR setup consists of a cavity inside a sweepable external magnetic field B_0 and an electromagnetic wave source. Often frequencies around 9 GHz, i.e. X-band microwave (MW), are chosen. This choice is due to a relative low cost, component availability, ease of use and large community experience.[4] The basic detection concept is the perturbation of a standing wave inside the cavity. Therefore, waveguide impedance has to be matched with an iris, and MW frequency tuned to the cavity, until the standing wave inside is

---

[4] Though herein only called MW, it is often also referred to as radio frequency (RF).
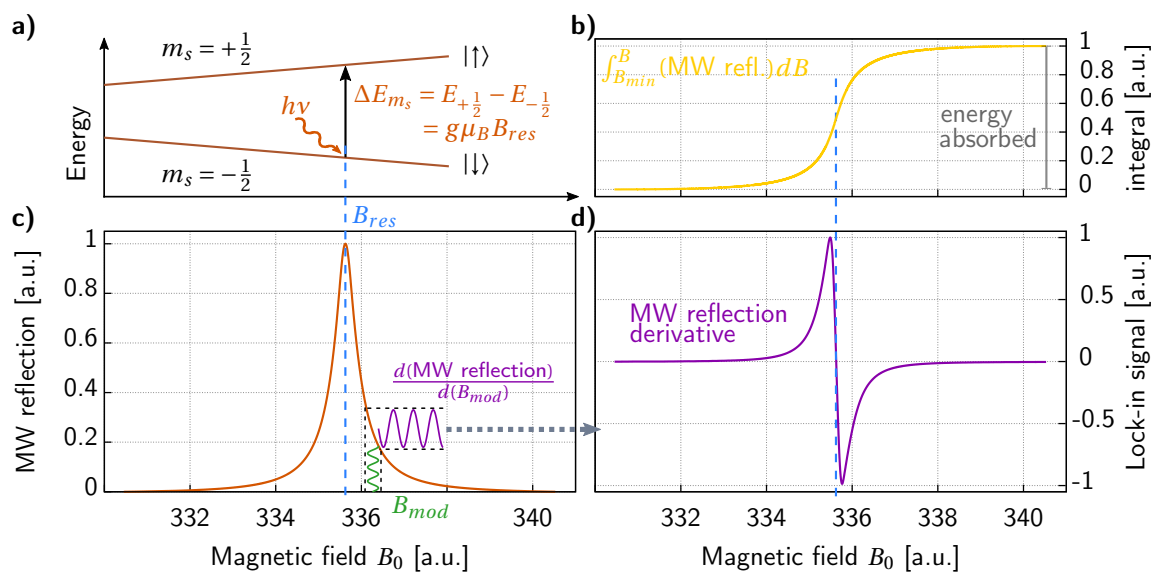
Figure 2.15 – Principle of the lock-in EPR signal. Around resonance the sample starts to absorb microwave, leading to a cavity system impedance change with subsequent MW reflection out of the cavity, c). By simultaneously modulating the magnetic field with B_{mod}, the lock-in actually measures the microwave reflection derivative, d). The presented derivative is an actual EPR spectrum of DPPH powder (recorded with a *MS400* spectrometer), while the absorption peak is an integration of the former. The second integral reflects the absorbed energy, proportional to the amount of spin-flips, b). All subplots are independently normalized. Subplot a) represents the electron energy system around B_{res} with the necessary photon energy to overcome the Zeeman splitting at B_{res}.

such, that virtually no MW is reflected out of the cavity. In this situation the cavity amplifies the applied MW power at the cavity center and the MW frequency is defined. The magnetic field is swept in a small range around resonance at e.g. $B_{res}(9.4\,\text{GHz}) = h\nu/g\mu_B \approx 337\,\text{mT}$ (equation 2.9 for g_e). At B_{res} the sample absorbs photons and the equilibrium population relation of equation 2.7 is disturbed. This absorbance changes the cavity impedance, which distorts the zero-reflection matching and tuning equilibrium, and leads to a subsequent MW back-reflectance out of the cavity. This absorption induced MW reflectance, detectable around resonance, is the CW EPR signal. It is proportional to the sample MW absorption, as depicted in figure 2.15 c). The integral of this absorption peak is directly proportional to the energy absorbed within one sweep cycle, i.e. the amount of spin-flips and therefore to the concentration of accessible spins, see figure 2.15 b). In combination with the cavity power amplification this is a highly sensitive and powerful system.

The maximum signal at B_{res} can be achieved by fully balancing the spin polarization down to zero (equation 2.7 and 2.8). At room temperature (294 K) and 335 mT this is rather small, spin population relation $N_{+1/2}/N_{-1/2} = 0.9985$ and spin polarization $P = 0.08\,\%$. As described, this can be increased by either decreasing the temperature[5] T or increasing the magnetic field[6] B_{res}. However, the temperature can only be changed in a small range for our samples in liquid state (negligible spin polarization increase at lowest temperature) and the magnetic field is defined by the cavity system.

---

[5] $N_{+1/2}/N_{-1/2} = 0.994$ and $P = 0.29\,\%$ for liquid nitrogen at 335 mT. $N_{+1/2}/N_{-1/2} = 0.897$ and $P = 5.43\,\%$ for liquid helium at 335 mT.

[6] $N_{+1/2}/N_{-1/2} = 0.9886$ and $P = 0.57\,\%$ at 2.5 T and room temperature. $N_{+1/2}/N_{-1/2} = 0.9597$ and $P = 2.06\,\%$ at 9 T and room temperature.
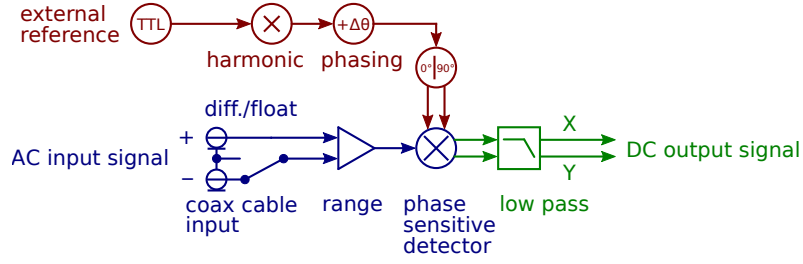
Figure 2.16 – Lock-in schematic drawing. A phase sensitive detector in combination with a low-pass filter reduces the noise around a reference frequency of a signal driven at the same modulation frequency. No phase-shift induced signal loss is possible by using two phase sensitive detectors shifted by 90°, X and Y.

Lock-in amplification is used to enhance the signal to noise ratio (SNR). In EPR, lock-in detection is accomplished by modulating one of the accessible signal influencing parameters, usually B_0 by B_{mod}. Lock-in detection can be thought of as phase-sensitive detection in combination with a low-pass filter to filter everything but the part proportional to the modulation frequency f_{mod}, i.e. bandwidth narrowing, compare schematic in figure 2.16.[66–68] Even though called lock-in amplification, this method is a noise filtering system to increase the signal to noise ratio (SNR). In the following, we explicit how lock-in detection acts as noise-filtering method.

Let us assume that a sine-like modulation with angular frequency ω_{mod} produces a sample response signal $V_{sig} \sin\left(\omega_{mod} t + \theta_{sig}\right)$ with amplitude V_{sig} and phase retardation θ_{sig}. This is the AC input signal at the lock-in. The original modulation is traced by the lock-in as separate reference input (often TTL) and is internally transferred to $V_{int} \sin\left(\omega_{int} t + \theta_{ref}\right)$ with phase retardation θ_{ref} to the reference input. The phase sensitive detector multiplies these two signals to

$$
V_{sig} \sin(\omega_{mod} t + \theta_{sig}) \cdot V_{int} \sin(\omega_{int} t + \theta_{ref})
$$
$$
= \underbrace{\frac{1}{2} V_{sig} V_{int} \cos\left([\omega_{mod} - \omega_{int}] \cdot t + \theta_{sig} - \theta_{ref}\right)}_{\text{DC for } \omega_{int} = \omega_{mod}} - \underbrace{\frac{1}{2} V_{sig} V_{int} \cos\left([\omega_{mod} + \omega_{int}] \cdot t + \theta_{sig} + \theta_{ref}\right)}_{\text{higher frequency for } \omega_{int} = \omega_{mod}}.
$$

The lock-in locks its internal reference to the external modulation, i.e. $\omega_{int} = \omega_{mod}$, and therefore $\omega_{mod} - \omega_{int} \approx 0$ will be DC and the high frequency part $\omega_{mod} + \omega_{int} \approx 2\omega_{mod}$ can be filtered by a consecutive low-pass filter down to

$$
\frac{1}{2} V_{sig} V_{int} \cos\left(\theta_{sig} - \theta_{ref}\right) \equiv X. \tag{2.10}
$$

This DC signal proportional to the sample modulation response amplitude V_{sig} can be maximized by phase-shifting θ_{ref} by $\Delta\theta$ such that $\cos\left(\theta_{sig} - \left(\theta_{ref} + \Delta\theta\right)\right) = 1$. $X = V_{sig}$ is directly proportional to V_{sig}. Signals and noise at other frequencies than the modulation frequency are suppressed. A lock-in is able to trace the modulation frequency accurately over long time. However, the signal itself may shift phase over time. Most lock-in systems therefore use a second phase sensitive detector which is shifted by 90° compared to the first phase sensitive detector

[66] P. Horowitz, and W. Hill, *The Art of Electronics*, 3rd edition (Cambridge University Press, 1989).

[67] Stanford Research Systems, *About Lock-In Amplifiers* (www.thinkSRS.com, 2011), pp. 1–9.

[68] Scientific Instrument Group, *Explore the Lock-in Amplifier* (www.signalrecovery.com, 1983), pp. 1–4.

$V_{int} \sin\left(\omega_{int} t + \theta_{ref} + 90 \deg\right)$, resulting in a signal of

$$\frac{1}{2} V_{sig} V_{int} \sin\left(\theta_{sig} - \theta_{ref}\right) \equiv Y, \tag{2.11}$$

see figure 2.16. In such a dual-phase lock-in system X and Y represent the sample modulation response amplitude as vector relative to the phase. If the phasing on the 'in phase' component X (equation 2.10) is not perfect, the lost signal part will be on the 'quadrature' component Y (equation 2.11). The magnitude

$$R = \left(X^2 + Y^2\right)^{\frac{1}{2}} = \frac{1}{2} V_{sig} V_{int}$$

therefore always contains the complete signal amplitude. However, the magnitude holds no in-channel sign information nor phase $\left(\theta \equiv \tan^{-1}\left(\frac{Y}{X}\right)\right)$ information. It is therefore necessary to always monitor X and Y or X and the magnitude to receive the full information. Additionally, in general simultaneous detection harmonics is possible, i.e. multiples of ω_{mod}.

The modulation can be realized by modulating either MW amplitude[7] or B_0. Typically magnetic field modulation at amplitude B_{mod} is used, such as indicated in green in figure 2.15. This graph also visualizes, why the EPR signal recorded with modulation lock-in technique produces a derivative of the actual absorption peak as signal, figure 2.15 d) and purple part. While B_{mod} should be held large for a strong signal X, equation 2.10, B_{mod} too large will lead to signal-broadening and resolution loss. The advantage of combining cavity impedance change with lock-in technology is, that the signal from microwaves reflected out of the cavity is only at resonance proportional to B_{mod}. This leads to a flat baseline of almost zero and is called transfer of modulation principle.[69] This is also the reason why MW amplitude modulation is less common.

To derive a model for the quantification of spin dependent current change at resonance in section 2.3, we need to come back to resonance and expand above started resonance description. The resonance system is a dynamic system, such that not only electrons with spin $|\downarrow\rangle$ transition absorption into $|\uparrow\rangle$, but also electrons with $|\uparrow\rangle$ relax $|\downarrow\rangle$ with corresponding transition probabilities $W_{-\frac{1}{2} \to +\frac{1}{2}}^{MW}$ and $W_{+\frac{1}{2} \to -\frac{1}{2}}^{MW}$, which can be described by Fermis golden rule (figure 2.17 orange part).[65] The total population $N \equiv N_{-\frac{1}{2}} + N_{+\frac{1}{2}}$ is constant. The amount of electrons with $m_s = -\frac{1}{2}$ and $m_s = +\frac{1}{2}$ change at the rate

$$\frac{dN_{-\frac{1}{2}}}{dt} = \left(N_{+\frac{1}{2}} \cdot W_{+\frac{1}{2} \to -\frac{1}{2}}^{MW}\right) - \left(N_{-\frac{1}{2}} \cdot W_{-\frac{1}{2} \to +\frac{1}{2}}^{MW}\right) = -\frac{dN_{+\frac{1}{2}}}{dt}. \tag{2.12}$$

It has been shown ([65] p. 5), that the transition induced by MW, i.e. an alternating field of strength B_1 at B_{res}, the resulting transition probability are in fact the same, $W_{-\frac{1}{2} \to +\frac{1}{2}}^{MW} = W_{+\frac{1}{2} \to -\frac{1}{2}}^{MW} \equiv W^{MW}$, such that equation 2.12 becomes

$$\frac{dN_{+\frac{1}{2}}}{dt} = W^{MW} \cdot \left(N_{-\frac{1}{2}} - N_{+\frac{1}{2}}\right) \equiv W^{MW} \cdot \Delta N. \tag{2.13}$$

---

[7] MW frequency modulation is not possible due to the frequency being coupled to the cavity system.

[69] J. S. Hyde, et al., "Microwave frequency modulation in CW EPR at W-band using a loop-gap resonator", Journal of Magnetic Resonance **185**, 259–263 (2007).
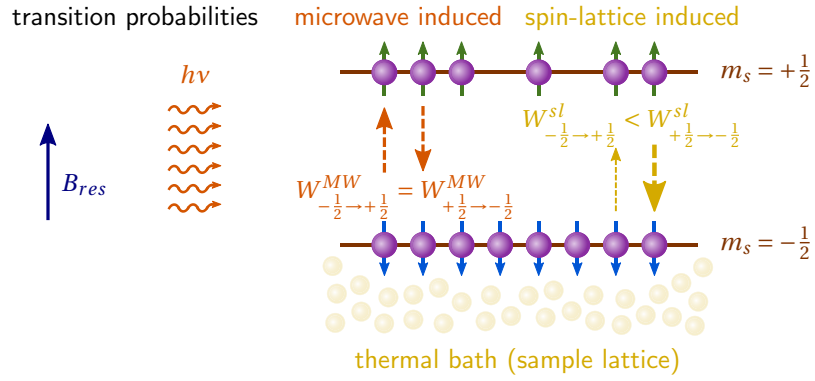
Figure 2.17 – Microwave and spin-lattice induced transition probabilities. The corresponding probabilities are indicated by the arrow thickness. The spin lattice relaxation is essential to maintain a population difference.

Under these assumptions the initial population difference will however eventually disappear until the population difference $\Delta N \equiv N_{-\frac{1}{2}} - N_{+\frac{1}{2}} = 0$, such that the EPR signal would decrease over a very short time.

A second source of spin-flips are the ensemble of spin-lattice relaxation mechanism. The equivalent temperature $T_{res} = \Delta E_{ms}/k_B$ needed for a spin-flip at 337 mT is only 0.46 K. This shows that from a purely energetic point of view, at room temperature there are plenty of fluctuations that could induce spin flips.[70] The induced spin transitions with transition probability rates $W^{sl}_{-\frac{1}{2}\to+\frac{1}{2}}$ and $W^{sl}_{+\frac{1}{2}\to-\frac{1}{2}}$ are indicated in figure 2.17 in yellow. The spin-lattice rate equation is

$$\frac{dN_{-\frac{1}{2}}}{dt} = \left(N_{+\frac{1}{2}} \cdot W^{sl}_{+\frac{1}{2}\to-\frac{1}{2}}\right) - \left(N_{-\frac{1}{2}} \cdot W^{sl}_{-\frac{1}{2}\to+\frac{1}{2}}\right) = -\frac{dN_{+\frac{1}{2}}}{dt}. \tag{2.14}$$

At steady state $dN_{-1/2}/dt = 0$ equation 2.14 becomes in combination with equation 2.7

$$\frac{N^0_{+\frac{1}{2}}}{N^0_{-\frac{1}{2}}} = \frac{W^{sl}_{-\frac{1}{2}\to+\frac{1}{2}}}{W^{sl}_{+\frac{1}{2}\to-\frac{1}{2}}} = \exp\left(-\frac{g\mu_B B_0}{k_B T}\right).$$

The relaxation rate $W^{sl}_{+\frac{1}{2}\to-\frac{1}{2}}$ is, due to $\exp\left(-\frac{g\mu_B B_0}{k_B T}\right) < 1$, faster than the rate $W^{sl}_{-\frac{1}{2}\to+\frac{1}{2}}$ and the overall process is therefore a spin lattice relaxation. Spin lattice relaxation is the reason for non disappearance of the population difference in contrast to the MW perturbation result in equation

[70] M. Stutzmann, et al., "Spin-dependent processes in amorphous and microcrystalline silicon: a survey", Journal of Non-Crystalline Solids **266-269**, 1–22 (2000).

2.13. With $N_{-\frac{1}{2}} = \frac{1}{2}(N + \Delta N)$ and $N_{+\frac{1}{2}} = \frac{1}{2}(N - \Delta N)$ we can calculate

$$
\begin{aligned}
\left(\frac{d(\Delta N)}{dt}\right)^{sl} &= \frac{d(N_{-\frac{1}{2}} - N_{+\frac{1}{2}})}{dt} \\
&\overset{2.14}{=} 2 \cdot \left(\left(N_{+\frac{1}{2}} \cdot W^{sl}_{+\frac{1}{2} \to -\frac{1}{2}}\right) - \left(N_{-\frac{1}{2}} \cdot W^{sl}_{-\frac{1}{2} \to +\frac{1}{2}}\right)\right) \\
&= N\left(W^{sl}_{+\frac{1}{2} \to -\frac{1}{2}} - W^{sl}_{-\frac{1}{2} \to +\frac{1}{2}}\right) - \Delta N\left(W^{sl}_{+\frac{1}{2} \to -\frac{1}{2}} + W^{sl}_{-\frac{1}{2} \to +\frac{1}{2}}\right) \\
&\equiv \frac{\Delta N^0 - \Delta N}{T_1}
\end{aligned}
\tag{2.15}
$$

$$
\left| \text{ with } \quad \Delta N^0 \equiv N\left(\frac{W^{sl}_{+\frac{1}{2} \to -\frac{1}{2}} - W^{sl}_{-\frac{1}{2} \to +\frac{1}{2}}}{W^{sl}_{+\frac{1}{2} \to -\frac{1}{2}} + W^{sl}_{-\frac{1}{2} \to +\frac{1}{2}}}\right) \quad \text{and} \quad T_1 \equiv \frac{1}{W^{sl}_{+\frac{1}{2} \to -\frac{1}{2}} + W^{sl}_{-\frac{1}{2} \to +\frac{1}{2}}}.
\right.
$$

With general solution

$$
N = \Delta N^0 + K \cdot e^{-t/T_1},
$$

where the constant K is defined by the sample initial condition (for a completely unmagnetized sample $K = -\Delta N^0$). T_1 is the time needed to fully magnetize an unmagnetized sample after placing it into B_0 and is called spin lattice relaxation time, as opposed to spin-spin relaxation time T_2. ΔN^0 is the population difference in equilibrium without external perturbations such as MW.

Also equation 2.13 can be transformed in this manner to

$$
\left(\frac{d(\Delta N)}{dt}\right)^{MW} = -2W^{MW}\Delta N,
\tag{2.16}
$$

such that the combined MW perturbation and spin-lattice relaxation give,

$$
\begin{aligned}
\left(\frac{d(\Delta N)}{dt}\right)^{total} &= \left(\frac{d(\Delta N)}{dt}\right)^{MW} + \left(\frac{d(\Delta N)}{dt}\right)^{sl} \qquad \left| \text{ equations 2.16 and 2.15} \right. \\
&= -2W^{MW}\Delta N + \frac{\Delta N^0 - \Delta N}{T_1}.
\end{aligned}
\tag{2.17}
$$

For the steady state, i.e. $\left(\frac{d(\Delta N)}{dt}\right)^{total} = 0$, equation 2.17 becomes

$$
\Delta N^{sl+MW} = \frac{\Delta N^0}{1 + 2W^{MW}T_1},
\tag{2.18}
$$

defining the population state in equilibrium after placing the sample in B_0 at B_{res} and turning on MW. The difference to the non-MW perturbed steady state population difference ΔN^0, i.e. *off*
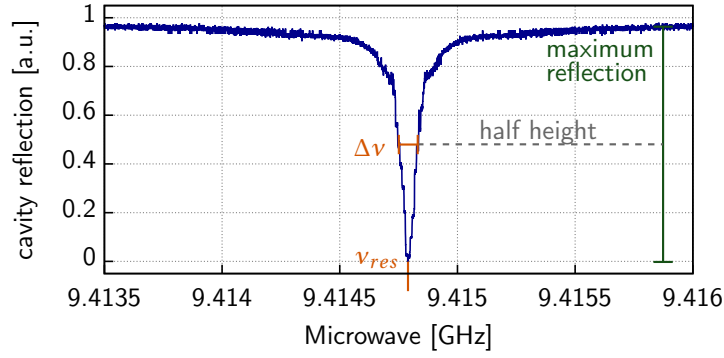
Figure 2.18 – Quality factor $Q = \frac{\nu_{res}}{\Delta\nu}$ definition illustrated on the example of an empty TE_{102} cavity. Higher Q for more narrow cavity resonance peaks and at higher frequencies.

resonance, is

$$\Delta N^0 - \Delta N^{sl+MW} = \Delta N^0 - \frac{\Delta N^0}{1 + 2W^{MW}T_1} = \frac{2W^{MW}T_1\Delta N^0}{1 + 2W^{MW}T_1}$$
$$\approx 2W^{MW}T_1\Delta N^0 \qquad (2.19)$$

$$\left| \text{ assuming } 2W^{MW}T_1 = \frac{2W^{MW}}{W^{sl}_{+\frac{1}{2}\to-\frac{1}{2}} + W^{sl}_{-\frac{1}{2}\to+\frac{1}{2}}} \ll 1 \right.$$

This MW absorption induced population difference change comparing on and off resonance defines the EPR signal strength. The larger $\Delta N^0 - \Delta N^{sl+MW}$, the stronger the cavity impedance change and induced MW reflected signal. W^{MW} in equation 2.19 is proportional to the square of the alternating magnetic field B_1. However, as indicated in equation 2.19, this is only true as long as $2W^{MW}T_1 \ll 1$. Beyond this point, the sample can no further linearly absorb additional MW power, which is called MW power saturation. The point of saturation is defined as $2W^{MW}T_1 \approx 1$ ([65] p. 9). At saturation the signal width increases in a form such that the lock-in signal peak-to-peak (ptp) separation ΔB_{ptp}, increases as

$$\Delta B_{ptp} = \sqrt{\frac{4}{3\gamma^2 T_2^2}(1 + \gamma^2 B_1^2 T_1 T_2)} \qquad (2.20)$$

with electron gyromagnetic ratio $\gamma \approx 1.761 \times 10^8\,\text{rad}/(\text{s}\cdot\text{mT})$.[64] T_2 is the spin-spin relaxation time, defining the relaxation time in the plane perpendicular to B_0 induced by mutual spin flips due to dipolar and exchange interaction. $\gamma^2 B_1^2 T_1 T_2 = 1$ is an equivalent description to $2W^{MW}T_1 = 1$ as point of saturation, such that far below MW power saturation equation 2.20 becomes

$$\Delta B_{ptp} \approx \frac{2}{\sqrt{3}\gamma T_2} \qquad \left| \text{ assuming } \gamma^2 B_1^2 T_1 T_2 \ll 1 \right. \qquad (2.21)$$

As described, the cavity is used in two ways: as high sensitivity tool and to concentrate the magnetic component of the MW power at the sample position, i.e. the cavity is used as resonator to store and focus the MW energy. By matching and tuning, the cavity system is optimized so that no MW is reflected back out of the cavity. This cavity resonance at frequency ν_{res} is defined by

the dimensions of the cavity and inserted sample.[8] A typical MW reflection pattern around ν_{res} is depicted in figure 2.18. The ability of a cavity to store energy is characterized by its quality factor Q

$$
\begin{aligned}
Q &\equiv \frac{2\pi \cdot \text{energy stored}}{\text{energy reflected within one EPR scan}} \\
&= \frac{2\pi \cdot \nu_{res,0} \cdot L}{R + R_{sample}} \\
&= \frac{\nu_{res}}{\Delta \nu},
\end{aligned}
\tag{2.22}
$$

where $\Delta \nu$ is the half height resonance width as depicted in figure 2.18 ([64] p. 81). The second and third line in equation 2.22 are equal but independent descriptions of Q. The $Q = \nu_{res}/\Delta \nu$ definition is the experimental method to find Q. The second line describes the cavity as actual RLC circuit, with unloaded resistance R, inductance L and unloaded resonance frequency $\nu_{res,0}$ with $\nu_{res} \neq \nu_{res,0}$. The additional sample resistance R_{sample} will decrease Q. Samples of large R_{sample}, are called lossy samples. Polar media such as H_2O interact with the MW electric field and therefore absorb power in the same manner as a microwave oven works, by electric field E_1 absorption. EPR on liquid samples are therefore in general performed using non-polar solvents.

The standing mode inside a cavity spatially separates the electric and magnetic field. A very typical cavity, and also the cavity used in this thesis, is a TE_{102} mode cavity. The resulting spatial separation of the microwave electric E_1 and magnetic field B_1 parts is such that maximum magnetic field and minimum electric field is at the cavity center, i.e. where the sample is situated, figure 2.19. The spatial separation of E_1 and B_1 minimizes sample heating by the MW, which is E_1 driven.

The efficiency of a resonator to convert the MW power to B_1 is proportional to the square root of the applied MW power $P[mW]$,

$$
B_1 = \frac{C'\sqrt{P}}{\sqrt{\Delta \nu}}
\tag{2.23}
$$

([64] p. 80). Especially for quantitative EPR measurements, it is vital to compare results not according to the used power but B_1, which is why results are usually plotted versus $\sqrt{P}$. The proportionality factor C' is the so called conversion efficiency.[9] The bandwidth $\Delta \nu[GHz]$ is defined as in figure 2.18 and indicates that C' includes Q. C' includes Q and several other influencing parameters. Although people mostly talk about Q, optimization of C' is the true goal. The actual value of C' is however more complex to find than Q. For typical Bruker cavities, C' varies between 1 to 10 $\sqrt{G \cdot Ghz/mW}$.[71] In general, C' can be increased by shrinking the resonator, which however cannot be considered in our case as our samples are three-electrode electrochemical cells.

The final signal intensity $V_S[V]$ is directly proportional to B_1, i.e. to the square root of applied power due to equation 2.23,

$$
V_S = \chi'' \eta Q \sqrt{P Z_0}
\tag{2.24}
$$

---

[8] This resonance has not to be confused with the EPR resonance as in equation 2.9.

[9] Also K or $C = \frac{C'}{\sqrt{\Delta \nu}}$ are common symbols.

[71] Bruker, *EPR resonators* (https://www.bruker.com/, 2009), pp. 1–26.
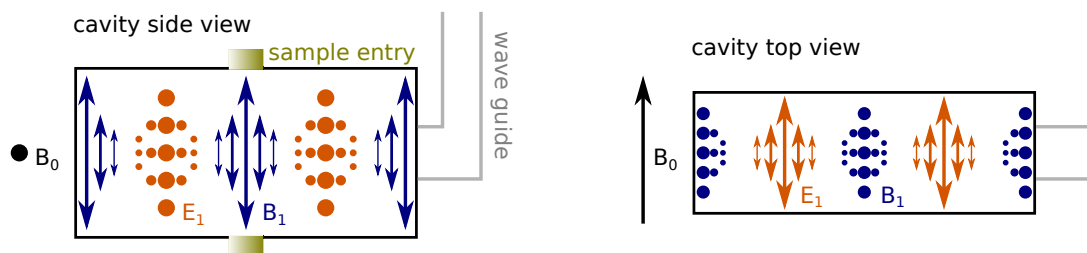
Figure 2.19 – Illustration of the electric E_1 (orange) and magnetic field B_1 (blue) distribution in a TE_{102} mode cavity. On the left as *side view*, i.e. along B_0. On the right as *top view*, i.e. along the sample axis.

with filling factor η, transmission line impedance Z_0, magnetic susceptibility χ'' [10] ([64] p. 63). The filling factor η is besides Q and C' another variable characterizing the used cavity system and describes the extent to which a sample covers the available B_1 inside a cavity,

$$\eta = \frac{\int\limits_{sample} \vec{B}_1(\vec{r})dV}{\int\limits_{cavity} \vec{B}_1(\vec{r})dV} \qquad (2.25)$$

([64] p. 89). B_1 is due to the cavity design typically maximal at the cavity center. η is therefore maximum for a large sample placed inside the center of a small cavity. For non lossy samples inside a $5\,\mathrm{mm}\varnothing$ quartz tube a typical value is $\eta = 0.01$ ([64] p. 89). For samples with large dielectric constant η will be chosen smaller.

The spin lattice relaxation time T_1 is an important sample characteristic in our experiment because we want to change the spin polarization by inducing electron spin resonance. T_1 values are typically found with pulsed EPR technique, wherein the actual magnetization relaxation can be observed directly. If no pulsed EPR system is available, T_1 can be found by saturation analysis.[72] However, here a fit including the EPR line-width and shape of EPR scans at a list of MW powers and inhomogeneous saturation line behavior approximation has to be made to find T_2. T_1 is then calculated from T_2 for which C' has to be known, equation 2.20 and 2.23. However, for an order of magnitude we can use equation 2.21 [11] and the knowledge, that generally $T_1 \geq T_2$, to approximate T_1 as

$$T_1 \geq \frac{2}{\sqrt{3}\gamma \Delta B_{ptp}}$$
$$\approx \frac{6.56 \times 10^{-7}\,\mathrm{mT}}{\Delta B_{ptp}}. \qquad (2.26)$$

This equation also gives the interpretation of broad line widths for short relaxation times and narrow line widths for long relaxation times.[62]

The line width may also be influenced by magnetic field inhomogeneities of B_0 , B_{mod} and B_1. If

---

[10] Imaginary component of the effective RF susceptibility.

[11] For an applied power far off MW power saturation.

[72] A. Lund, et al., "Relaxation-Time Determination from Continuous-Microwave Saturation of EPR Spectra", Radiation Research **172**, 753–760 (2009).

not enough care is taken on this, field inhomogeneity broadening dominate and render meaningless the estimate of T_1 deduced from the linewidth. Another source for line-broadening is sample induced field distortions. Broadening induced by sources effecting a constant magnetic field inhomogeneity is called inhomogeneous broadening, e.g. B_0 inhomogeneities or powder broadening. Broadening induced by sources effecting locally *fluctuating* magnetic field inhomogeneities is called homogeneous broadening, e.g. spin relaxations or anisotropy averaging in solutions. For solvent based samples, the homogeneous broadening increases with the concentration of active species.[73,74]

2.2.2 Chirality Induced Spin Selectivity

A rather recent and nice way to produce spin polarization is by means of chiral systems. In this work we concentrate on electrons going through one or few layers of chiral molecules. Electrons are hereby spin filtered by the spiral structure, called chirality induced spin selectivity, first described by Prof. Naaman and his group at the Weizmann Institute.[75,76] Measurements show spin polarization parallel to the helical axis, a polarization increase with the enantiomer length and dependency on the enantiomer helicity and electron propagation direction. Spin polarization of up to 11 % were observed by Gazzotti et al.,[77] other studies go up to 30 %,[78] and even 60 % (78 base pair oligo dsDNA/poly-Au),[79] depending on the chiral molecule length (all these experiments used additional Ni below the chiral molecules).
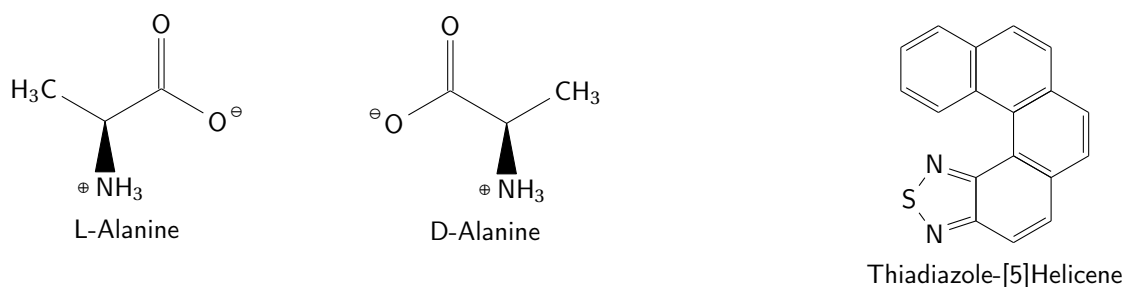
Figure 2.20 – Illustration of chirality and spirality at the example of Alanine and Thiadiazole-[5]Helicene. The two enantiomers L-Alanine (left-handed) and D-Alanine (right-handed) are mirror images of each other and can not be superimposed by any combination of movements due to one asymmetric carbon center. Alanine is in this configuration not spiral. However, a combination of several alanine molecules connected into a peptide can have a spiral structure. [n]Helicene is in this way chiral and spiral for $n > 1$, the rings separate spiral-like in out-of-plane direction. Displayed here is the used Thiadiazole-[5]Helicene.

[73] F. K. Kneubühl, "Line Shapes of Electron Paramagnetic Resonance Signals Produced by Powders, Glasses, and Viscous Liquids", The Journal of Chemical Physics **33**, 1074–1078 (1960).

[74] D. Freude, *Spectroscopy for Physicists - Chapter 3 - Paramagnetic Electron Resonance* (Uni Leipzig, 2006), pp. 1–14.

[75] K. Ray, et al., "Asymmetric scattering of polarized electrons by organized organic films of chiral molecules", Science **283**, 814–816 (1999).

[76] S. G. Ray, et al., "Chirality-induced spin-selective properties of self-assembled monolayers of DNA on gold", Physical Review Letters **96**, 1–4 (2006).

[77] M. Gazzotti, et al., "Spin-dependent electrochemistry: Enantio-selectivity driven by chiral-induced spin selectivity effect", Electrochimica Acta **286**, 271–278 (2018).

[78] P. C. Mondal, et al., "Spin-Dependent Transport through Chiral Molecules Studied by Spin-Dependent Electrochemistry", Accounts of Chemical Research **49**, 2560–2568 (2016).

[79] B. Gohler, et al., "Spin Selectivity in Electron Transmission Through Self-Assembled Monolayers of Double-Stranded DNA", Science **331**, 894–897 (2011).

The definition of "chiral" goes back to 1893, when Baron Kelvin wrote *"I call any geometrical figure, or group of points, "chiral", and say that it has chirality if its image in a plane mirror, ideally realized, cannot be brought to coincide with itself."* ([80] p. 27). This definition in the form of "handedness" is since common in chemistry. As depicted in figure, 2.20 spiral / helical molecules are always chiral but not all chiral molecules are helical. However, a peptide composed of several chiral but non-helical alanine molecules can be helical.

Even though called "chirally" induced, all theoretical approaches for CISS are developed on the concept of helical molecules. So far there is no literature describing CISS for non helical, but chiral molecules. Actually, there is no complete theoretical concept yet to fully describe and understand CISS. Yeganeh et al. use scattering processes combined with spin orbit coupling.[81] Gersten et al. show that the simple spin orbit coupling due to the movement in the curved force field of even DNA is not sufficient.[82] However, Gutierrez et al. use tight binding with spin orbit coupling with an external field of helical symmetry and Matityahu et al. use tight binding to probe spin orbit interactions on the bonds along the helix axis and electron hopping as main transport mechanism.[83,84] Díaz et al. develop a model based on coherent electron dynamics in the electric field created by the helical structure, raising a Rashba like effective spin-orbit coupling of electrons moving along the helical axis.[85] Maslyuk et al. demonstrate using DFT, that in any case the molecular helical geometry is crucial for the spin filtering.[86] Yang et al. developed a Landauer-Büttiker type analysis of linear-regime electron transmission and reflection derived from symmetry theorems to show that a spin-flip electron reflection process is inherent to CISS.[87]

I shortly present the results of Varela et al., because they best present the effect of relative orientation, movement and helicity. They developed a tight binding model using effective spin orbit coupling in an effective mass hamiltonian concept derived by Ando.[88,89] Varela et al. finds an energy gap for the transport of spin orientation depending on its spin orientation, propagation direction relative to the molecules helicity axis and molecule helicity. An excess energy is necessary for electrons moving along the helical molecule if its spin is antiparallel to its moving direction for right helical molecules. Favored are therefore electrons with spin parallel to its moving direction for right helical molecules. For left helical molecules this is inversed, i.e. antiparallel spin orienta-

[80] W. T. Baron Kelvin, "The molecular tactics of a crystal", Oxford: Clarendon Press, 74 (1894).

[81] S. Yeganeh, et al., "Chiral electron transport: Scattering through helical potentials", Journal of Chemical Physics **131** (2009) 10.1063/1.3167404.

[82] J. Gersten, et al., "Induced spin filtering in electron transmission through chiral molecular layers adsorbed on metals with strong spin-orbit coupling", The Journal of Chemical Physics **139**, 114111 (2013).

[83] R. Gutierrez, et al., "Modeling Spin Transport in Helical Fields: Derivation of an Effective Low-Dimensional Hamiltonian", The Journal of Physical Chemistry C **117**, 22276–22284 (2013).

[84] S. Matityahu, et al., "Spin-dependent transport through a chiral molecule in the presence of spin-orbit interaction and nonunitary effects", Physical Review B **93**, 1–10 (2016).

[85] E. Díaz, et al., "Coherent spin dynamics in a helical arrangement of molecular dipoles", AIMS Materials Science **4**, 1052–1061 (2017).

[86] V. V. Maslyuk, et al., "Enhanced Magnetoresistance in Chiral Molecular Junctions", The Journal of Physical Chemistry Letters **9**, 5453–5459 (2018).

[87] X. Yang, et al., "Spin-dependent electron transmission model for chiral molecules in mesoscopic devices", Physical Review B **99**, 024418 (2019).

[88] S. Varela, et al., "Effective spin-orbit couplings in an analytical tight-binding model of DNA: Spin filtering and chiral spin transport", Physical Review B **93**, 1–16 (2016).

[89] T. Ando, "Spin-orbit interaction in carbon nanotubes", Journal of the Physical Society of Japan **69**, 1757–1763 (2000).
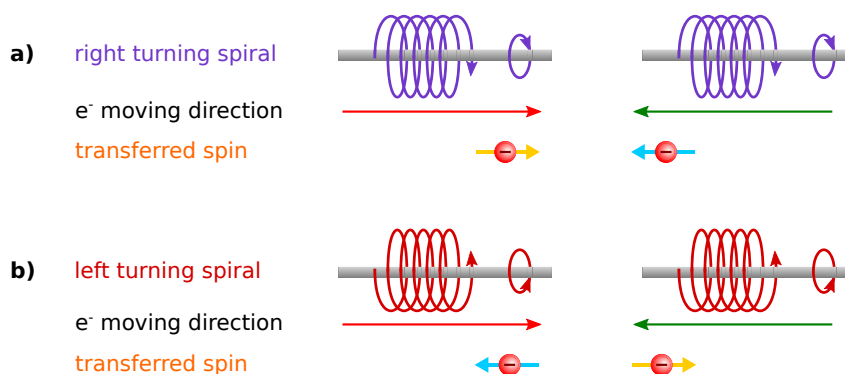
Figure 2.21 – Chirality induced spin selectivity, selection rule illustration. Right turning spirals transfer mostly electrons with spin parallel to their propagation direction along the helicity axis, a). Left turning spirals transfer mostly electrons with spin antiparallel to their propagation direction, b).

tion to its propagation direction is favored. Interestingly, this energy gap increases with stronger intrinsic spin orbit coupling but does not fall to zero for no intrinsic spin orbit coupling. Thus, the gap includes not only spin-orbit, but also a kinetic term induced by nearest neighbor p_z overlap.

Mentioned length dependency is quite strikingly shown by Kettner et al. with the example of Al5, Al6 and Al7, where they find a continuously increasing spin polarization from $P_{Al5} = 8\%$ to $P_{Al7} = 17\%$ (Ni substrate).[90] The helical systems used in this thesis were either a peptide of 5 alanine groups (Al5) or a helical chain of 5 benzene rings, called [5]helicene. Helicene in the form of thiadiazole-[5]Helicene such as depicted in figure 2.20 adopts its helical structure due to strong repulsion between its extremities. For [7]helicene, a spin polarization up to 8% was measured for single layer systems.[91] For [4]helicene, a spin polarization of 4% was measured for a multi layer system of uncontrolled orientation and up to 49% for uniformly absorbed helicene on an atomically flat highly oriented pyrolytic graphite substrate.[92] The polarization was found to be extremely dependent on the helicene layer quality and it stays unclear what the effect of multilayer system was. The [5]helicene used in this thesis is therefore expected to show a spin polarization better than 4%.

2.2.3 Optical Spin Pumping on p-GaAs

A very well known and often used system for spin polarization in solid state systems is by means of optical spin pumping. For GaAs as for most other III-V cubic zinc blende compound semiconductors, the gap at the Brioullin center is direct, conduction band E_{CB} is not degenerate s-type of Γ_6 symmetry and valence band E_{VB} is threefold degenerate p-type of Γ_8 symmetry, such as depicted in figure 2.22 a).[93] The valence degeneracy is lifted by spin-orbit coupling, leading to a Γ_7 symmetric split-off band Δ below E_{VB} and two other valence bands combined at E_{VB} in $\Gamma[000]$.

[90] M. Kettner, et al., "Spin Filtering in Electron Transport Through Chiral Oligopeptides", The Journal of Physical Chemistry C **119**, 14542–14547 (2015).

[91] M. Kettner, et al., "Chirality-Dependent Electron Spin Filtering by Molecular Monolayers of Helicenes", Journal of Physical Chemistry Letters **9**, 2025–2030 (2018).

[92] V. Kiran, et al., "Helicenes - A New Class of Organic Spin Filter", Advanced Materials **28**, 1957–1962 (2016).

[93] J. S. Blakemore, "Semiconducting and other major properties of gallium arsenide", Journal of Applied Physics **53**, R123 (1982).

a) GaAs band structure around E_g

b) spin selection

c) optical spin pumping: **right helicity σ⁻**

d) optical spin pumping: **left helicity σ⁺**
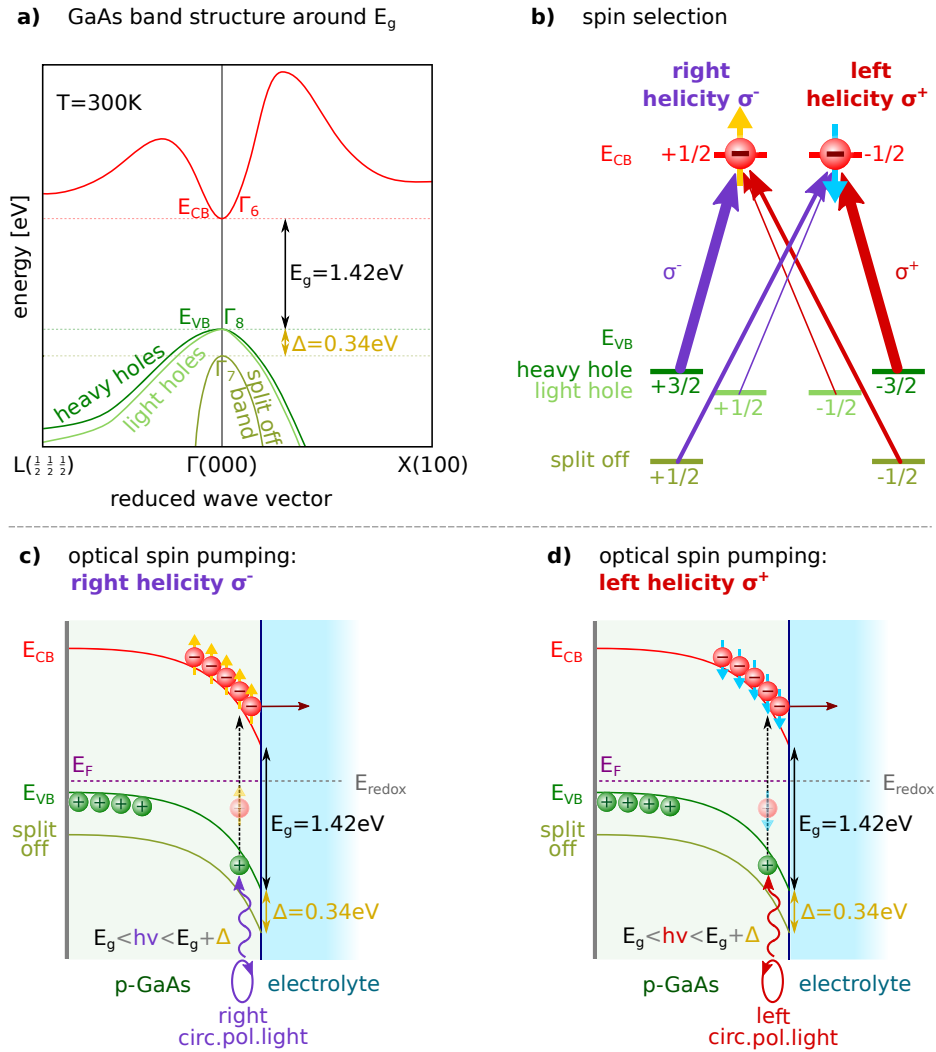
Figure 2.22 – GaAs band structure and optical spin pumping. The band structure in a) is shown in the wave vector region around the direct band gap. Circularly polarized light leads to a net spin polarization according to the light energy falling in between the three fold degenerated valence band system, b). Right circularly polarized light leads to an electron spin up polarization which is localized at the surface for a p-GaAs/electrolyte cathodic interface, c). For left circularly polarized light the optically pumped electron has spin down orientation, d).

The latter two valence bands are of Γ_8 type and correspond to heavy and light hole valence bands. Electron hole pairs produced with circularly polarized light of energy E_g from the heavy hole band possess due to the conservation of photon angular momentum, a spin orientation aligned with the light beam direction is obtained.[94] The photon angular momentum $\sigma\hbar$ can reach from $-1 \leq \sigma \leq +1$, where $\sigma = +1/2$ corresponds to perfectly left circularly polarized light (short σ^+) and $\sigma = -1/2$ to right circularly polarized light (short σ^-). Light of left helicity produces electrons of spin polarization antiparallel to the light propagation direction, such as depicted in figure 2.22 d), and right helicity produces a spin parallel to the light propagation direction, c).

This selection rule is strongest at $h\nu = E_g$, but valid in the range $E_g \leq h\nu \leq E_g + \Delta$. Spin polarization

---
[94] F. Meier, and B. Zakharchenya, *Optical Orientation - Modern Problems in Condensed Matter Sciences*, Vol. 8 (1984).

of up to $P = 0.5$ are possible with this so called optical spin pumping technique.[95] $P = 1$ could only be achieved for $h\nu \equiv E_g$. For energies above, parallel and antiparallel spin orientation are produced simultaneously due to the light hole band and for energies above $E_g + \Delta$ also from the split off band, compare figure 2.22 b).[96] Polarization can therefore be increased by keeping the wavelength close to E_g.

The biggest advantage of this type of spin polarization is the fast and easy polarization inversion, which can be obtained by switching the light helicity. However, $P = 0.5$ is rather optimistic and only realizable at low temperatures, since P decreases at room temperature due to the spin relaxation time T_1 and spin diffusion length. An actual spin polarization of less than $P = 0.1$ for p-GaAs is therefore more realistic. This was also the value reported by the first group to perform optical spin pumping on GaAs.[95]

The direct band gap of GaAs is of $E_g = 1.42\,\text{eV}$, the gap including the split off band is $E_g + \Delta = 1.76\,\text{eV}$.[12][93] A light source of $830\,\text{nm} \hat{=} 1.49\,\text{eV}$ is therefore very well suited to reach a good spin polarization since it lays relatively close to the heavy hole valence band. In combination with p-doping, optical spin pumping allows relatively easy to build spin polarizable electrochemical photo cathodes, such as depicted in figure 2.22 c) and d). The biggest advantage if used in negative potential range is here the accumulation of almost solely electrons produced by optical spin pumping at the interface. Regarding electrochemistry, this also allows current limitation by light power as an additional means to avoid diffusion limitation(section 2.1.2).

Less often discussed is the role of the resulting hole. The hole is also spin polarized, which is however dependent on the actual valence band from which the electron was pumped. Holes created in the heavy hole band posses a spin of $3/2$ parallel to the light propagation while holes created in light hole or split off band possess a spin of $-1/2$ (figure 2.22 b)).[97,98] Conversely, this means that also the electron hole recombination can be spin dependent.[99] The hole spin life time is typically $\tau_h < 6\,\text{ps}$, and for p-GaAs the holes resulting from pumping are mixed with the holes present due to doping which are the majority charge carrier.[99]

2.2.4 Electrically Detected Magnetic Resonance

The conduction of electrons into half filled orbitals and the recombination of electrons with holes underlay spin dependency as described in the following. Stutzmann et al. point out three possibilities of how the spin could affect the behavior of electrons and holes in semiconductors: interaction with another spin polarized electron, hole or paramagnetic center.[70] The discussion

---

12   $E_g + \Delta = 1.78\,\text{eV}$ according to Chazalviel.

[95]   C. Weisbuch, and C. Hermann, "Optical detection of conduction-electron spin resonance in GaAs, Ga1-xInxAs, and Ga1-xAlxAs", Physical Review B **15**, 816–822 (1977).

[96]   G. Lampel, "Nuclear dynamic polarization by optical electronic saturation and optical pumping in semiconductors", Physical Review Letters **20**, 491–493 (1968).

[97]   D. J. Lepine, "Spin-Dependent Recombination on Silicon Surface", Physical Review B **6**, edited by Intergovernmental Panel on Climate Change, 436–441 (1972).

[98]   A. K. Fumani, and J. Berezovsky, "Spin-Pumping Efficiency in Room-Temperature CdSe Nanocrystal Quantum Dots", The Journal of Physical Chemistry C **118**, 28202–28206 (2014).

[99]   H. Dersch, et al., "Recombination processes in a-Si:H: Spin-dependent photoconductivity", Physical Review B **28**, 4678–4684 (1983).
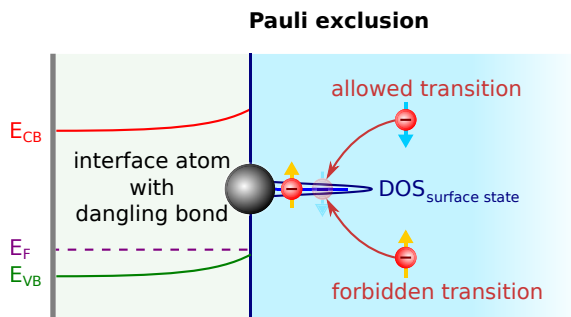
Pauli exclusion

Figure 2.23 – Dangling bond electron hole recombination. Dangling bonds exist e.g. on surface and interface atoms with unpaired electrons. The resulting surface states accept due to Pauli exclusion only electrons of spin polarization opposite to the unpaired electron spin. The hole is indicated as missing electron in semi transparent color.

with holes is a bit easier when thinking of them as what they actually are, i.e. missing electrons, and in this sense to discuss the transferred electron's spin and spin of the electron missing at this site. In this sense, none of the plots shown in this section depict holes with their actual spin but rather, a semi transparent missing electron (e.g. figure 2.23) or as hole with the acceptable spin (figure 2.24). Antipirallel spin orientation results in a total spin of 0 and only one possible magnetic quantum number, $m_s = 0$, called singlet state. For parallel orientation the total spin is 1 and therefore three possible magnetic quantum numbers, $m_s = -1, 0, +1$, called triplet. To combine two electrons in a covalent type of electron pair bond, an antisymmetric singlet spin state is necessary to comply with the Pauli exclusion principle. The tunneling of electrons into paramagnetic centers such as radicals is with the same argument allowed only for electrons of spin opposite to the paramagnetic center electron spin. Surface states able to accept electrons can be of dangling bonds type. Dangling bonds can be thought of as immobilized free radicals, i.e. unpaired electrons of partly bonded atoms such as the surface atoms depicted in figure 2.23. These surface state orbitals can trap or recombine only with electrons of antiparallel spin polarization due to the Pauli exclusion.

A current which relies on any of these processes will therefore depend on spin polarization. Since unpaired electrons are accessible with resonance, also the current will change at resonance. Such electrical detection of magnetic resonance (EDMR) is the experimental basis by which we seek to demonstrate spin effect at electrodes. The spin dependent recombination of electron hole pairs was one of the first suggestions to use electrical detection methods for resonance experiments.[97] The EDMR method suggested by Lepine measures the current going through a metal/n-Si interface and its subsequent change at resonance. He showed, that spin polarized electrons recombine spin dependently with holes via surface centers. The dangling bond and conduction electrons were spin polarized by an external magnetic field. Due to Pauli exclusion a conduction band electron can not fit into the same orbital if both electrons are spin polarized in the same direction. However, when applying microwave, the sample absorbs microwave at resonance, which disturbs the spin polarization, such that at resonance the recombination current increases. Solomon developed the system further to p-n junction, which depicts the recombination of electrons with holes at the interface.[100] Rong et al. described the effect for the case of Pt-related defects,

---

[100] I. Solomon, "Spin-dependent recombination in a silicon p-n junction", Solid State Communications **20**, 215–217 (1976).

which they could identify thanks to the specific hyperfine structure they observed.[101] Whatever the source, the result is the same, i.e. resonant detectable electron hole recombination. Spin dependent electron hole recombination is nowadays well described for solid states and connected to specific recombination centers. However, to the authors knowledge, spin dependent electron hole recombination at an electrode/electrolyte interface has not been examined yet.

EDMR experiments have also been performed on e.g. ferromagnetic samples,[102] thin film interfaces using photo currents,[103] polaron recombination,[104] exciton formation,[105] and electron hole recombination.[8,106] However, for electrochemical systems EDMR has not been applied yet for interface electron spin effects. In any case, EDMR can be extremely sensitive, Rong et al. point out a sensitivity many orders of magnitude better than conventional EPR methods.[13] However, this is only the case for very specific, rather simple sample types such as their p-n junction solid state samples. The sensitivity is strongly dependent on the sample quality, contacts and several electronic configuration questions, which are discussed in section 3.1. Finally, the sensitivity is strongly dependent on the relative current change, where down to 10^{-6} are common for solid state samples but relative changes of almost 10 percent are possible.[109] In our case the interface with an electrolyte introduces more noise than what is observed typically for pure solid state samples. Electrochemical systems can also undergo extreme changes and modify the electrode. The extreme sensitivity is therefore not necessarily valid for electrode/electrolyte interfaces. However, we were able to detect surface-selective EPR signals on surfaces of about 1 mm2 which contain roughly 10^{13} atomic sites.

Another problem is the transfer of modulation described in section 2.2.1. Most literature EDMR measurements are performed with magnetic field modulation for which the lock-in signal interpretation is similar to standard CW EPR.[110] We use potential modulation which has a non zero offset.[102] However, a constant offset does not represent a major problem for modern lock-in detectors. In our case the offset is however not constant and several work around approaches are presented in section 3.1.6.

---

[13] According to Stutzmann et al. down to 10^3 spins per 0.1 mT line width and possibilities up to single spin detection, which was in fact experimentally confirmed in 2004 by Xiao et al..[108]

[101] F. C. Rong, et al., "Electrically detected magnetic resonance of a transition metal related recombination center in Si $p-n$ diodes", Applied Physics Letters **60**, 610–612 (1992).

[102] S. T. Goennenwein, et al., "Electrically detected ferromagnetic resonance", Applied Physics Letters **90**, 3–5 (2007).

[103] W. Harneit, et al., "Room temperature electrical detection of spin coherence in C60", Physical Review Letters **98**, 1–4 (2007).

[104] T. Eickelkamp, "Electrically detected magnetic resonance in photoexcited fullerenes", Molecular Physics **95**, 967–972 (1998).

[105] J. A. Gómez, et al., "On the origin of exciton formation in dye doped Alq3 OLEDs", Applied Physics A **108**, 727–731 (2012).

[106] F. Comandè, and J.-P. Ansermet, "Time-resolved spin processes in Alq3 light-emitting diodes", Physical Review B **90**, 201201–1 –4 (2014).

[109] T. Aichinger, and P. M. Lenahan, "Giant amplification of spin dependent recombination at heterojunctions through a gate controlled bipolar effect", Applied Physics Letters **101**, 1–5 (2012).

[110] D. M. G. Leite, et al., "Electrically detected magnetic resonance modeling and fitting: An equivalent circuit approach", Journal of Applied Physics **115**, 034510 (2014).

2.3   Resonant Detection of Charge Transfer Spin Dependency

We can now connect all above sections by placing spin polarizable electrodes into an radical electrolyte solution situated in an external magnetic field, using either CISS or optical spin pumping on the electrode side and monitoring the current during MW resonant detection. The EDMR detection method as discussed in 2.2.4 measures the current change around resonance. In the following, an order of magnitude approximation is developed by combining radical spin polarization, resonant and non resonant spin flip processes on radicals, electrode spin polarization, electrochemical cathode description, exclusion principle and electron hole recombination.

A current flows between the electrodes and electrolyte when a potential is applied, reducing or oxidizing the radicals. The current density between electrode and electrolyte is according to equations 2.4 and 2.5

$$j = nF(k_{Ox}[Red] - k_{Red}[Ox]),$$

i.e. charge transfer rate k and electrolyte species concentration dependent. For better comparability with section 3.1.5, the electrolyte species concentration is changed from molar concentration $[Ox]$ to charge concentration $N^{Ox} = F[Ox]$, respectively from $[Red]$ to $N^{Red} = F[Red]$, and $n = 1$ due to the single electron transport processes or methyl viologen, i.e.

$$j = k_{Ox}N^{Red} - k_{Red}N^{Ox}.$$

Turning on the mechanisms for spin polarization described in section 2.2, electrons coming from the electrode are spin polarized by optical spin pumping or CISS, while the radical spin is independently spin polarized by B_0. For the beginning we concentrate solely on the transfer of spin polarized electrons from and to radicals and discuss oxidation of diamagnetic species only at the end of this section. For radicals, it is valid to assume that the charge transfer rate k is not only direction dependent, i.e. k_{Red} and k_{Ox} as discussed for section 2.3, but also spin dependent. The current density therefore has to be further developed in electron spin polarization dependency on both sides,

$$
\begin{aligned}
j_{e,sp} = &\left(k^{Ox}_{+\frac{1}{2},-\frac{1}{2}} N^{Red}_{-\frac{1}{2}} + k^{Ox}_{+\frac{1}{2},+\frac{1}{2}} N^{Red}_{+\frac{1}{2}} + k^{Ox}_{-\frac{1}{2},-\frac{1}{2}} N^{Red}_{-\frac{1}{2}} + k^{Ox}_{-\frac{1}{2},+\frac{1}{2}} N^{Red}_{+\frac{1}{2}} \right) \\
&- \left(k^{Red}_{+\frac{1}{2},-\frac{1}{2}} N^{Ox}_{-\frac{1}{2}} + k^{Red}_{+\frac{1}{2},+\frac{1}{2}} N^{Ox}_{+\frac{1}{2}} + k^{Red}_{-\frac{1}{2},-\frac{1}{2}} N^{Ox}_{-\frac{1}{2}} + k^{Red}_{-\frac{1}{2},+\frac{1}{2}} N^{Ox}_{+\frac{1}{2}} \right),
\end{aligned}
\tag{2.27}
$$

where e.g. $k^{Red}_{+\frac{1}{2},-\frac{1}{2}} N^{Ox}_{-\frac{1}{2}}$ describes the current density due to the reduction of Ox species with spin polarization $m_s = -\frac{1}{2}$ with electrons of spin polarization $m_s = +\frac{1}{2}$. The transfer rate double index of e.g. "$+\frac{1}{2}, -\frac{1}{2}$" indicates at first position the spin polarization of transferred electron and at second position the spin polarization of the electron already located at the acceptor to emphasize its dependency on the spin polarization on both sides, such as indicated in figure 2.24.

For simplification we start by considering only one charge transfer direction, say k_{Red}, which is at least in the range of redox peak maxima of a diffusion limited system a valid approximation.
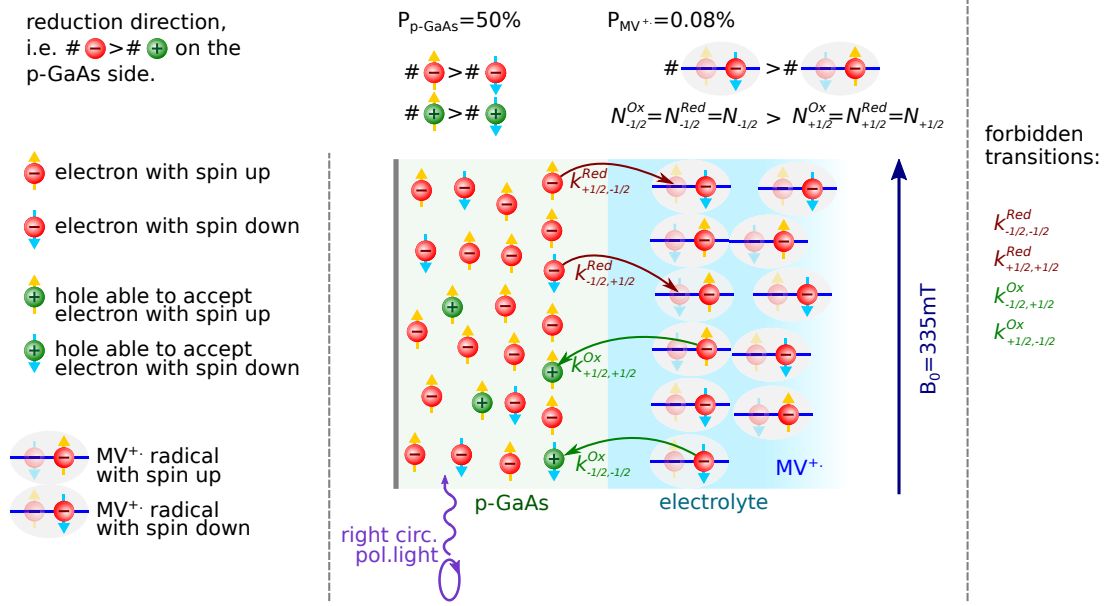
Figure 2.24 – Depiction of possible and allowed charge transfer reactions for a p-GaAs WE in contact with a MV$^{+\bullet}$ radical solution. # stands for concentration. Depicted are all possible processes, maximum possible spin polarization due to optical spin pumping on the p-GaAs side and external magnetic field B_0 on the electrolyte side. Due to the three types of valence bands, for simplicity holes are indicated with the spin direction of pumped electron. On the radical side the missing electron is indicated as semi transparent. Half the processes are forbidden transitions due to Pauli exclusions, as discussed in section 3.1.6. Note the different k indexes regarding reduction and oxidation direction. In this depiction the maximum possible spin-polarization of $P = 50\%$ is used for visibility reasons. In the further discussion the realisitc value of $P = 10\%$ is used.

Equation 2.27 for only reduction direction is

$$j_{e,sp}^{Red} = \left(k_{+\frac{1}{2},-\frac{1}{2}}^{Red} N_{-\frac{1}{2}}^{Ox} + k_{+\frac{1}{2},+\frac{1}{2}}^{Red} N_{+\frac{1}{2}}^{Ox} + k_{-\frac{1}{2},-\frac{1}{2}}^{Red} N_{-\frac{1}{2}}^{Ox} + k_{-\frac{1}{2},+\frac{1}{2}}^{Red} N_{+\frac{1}{2}}^{Ox} \right).$$

As introduced in section 1, discussed in section 2.2.4 and also pointed out by Chazalviel, spin polarized radicals can only accept electrons of opposite spin direction into the SOMO, which is due to the Pauli exclusion principle for the molecular orbital filling. The processes $k_{-\frac{1}{2},-\frac{1}{2}}^{Red} N_{-\frac{1}{2}}^{Ox}$ and $k_{+\frac{1}{2},+\frac{1}{2}}^{Red} N_{+\frac{1}{2}}^{Ox}$ are therefore negligible. We further assume MV$^{+\bullet}$ as radical, such that both, Red and Ox species are MV$^{+\bullet}$ at any point, such that $N_{+\frac{1}{2}}^{Red} = N_{+\frac{1}{2}}^{Ox} \equiv N_{+\frac{1}{2}}$ and $N_{-\frac{1}{2}}^{Red} = N_{-\frac{1}{2}}^{Ox} \equiv N_{-\frac{1}{2}}$. This is valid for large radical stock solutions combined with slow scan rates. For the sake of readability, the redox species marking Red of k and the second transfer rate index of k is skipped in the following, such that we're left with

$$\begin{aligned} j_{e,sp}^{Red} &= + k_{+\frac{1}{2},-\frac{1}{2}}^{Red} N_{-\frac{1}{2}}^{Ox} + k_{-\frac{1}{2},+\frac{1}{2}}^{Red} N_{+\frac{1}{2}}^{Ox} \\ &= k_{+\frac{1}{2}} N_{-\frac{1}{2}} + k_{-\frac{1}{2}} N_{+\frac{1}{2}}. \end{aligned} \tag{2.28}$$

Using the population difference representation $\Delta N = N_{-1/2} - N_{+1/2}$ and total population $N =$

$N_{-1/2} + N_{+1/2}$, equation 2.28 can be rewritten to

$$
\begin{aligned}
j_{e,sp} &= \left(\frac{k_{+\frac{1}{2}}}{2} N_{-\frac{1}{2}} + \frac{k_{+\frac{1}{2}}}{2} N_{-\frac{1}{2}} \right) + \left(\frac{k_{-\frac{1}{2}}}{2} N_{+\frac{1}{2}} + \frac{k_{-\frac{1}{2}}}{2} N_{+\frac{1}{2}} \right) \\
&= \left(\frac{k_{+\frac{1}{2}}}{2} \left(\Delta N + N_{+\frac{1}{2}} \right) + \frac{k_{+\frac{1}{2}}}{2} \left(N - N_{+\frac{1}{2}} \right) \right) + \left(\frac{k_{-\frac{1}{2}}}{2} \left(-\Delta N + N_{-\frac{1}{2}} \right) + \frac{k_{-\frac{1}{2}}}{2} \left(N - N_{-\frac{1}{2}} \right) \right) \\
&= \left(\frac{k_{+\frac{1}{2}} + k_{-\frac{1}{2}}}{2} \right) N + \left(\frac{k_{+\frac{1}{2}} - k_{-\frac{1}{2}}}{2} \right) \Delta N.
\end{aligned}
\tag{2.29}
$$

The current density with external field B_0 and off resonance at steady state is therefore

$$
j_{e,sp}^0 = \left(\frac{k_{+\frac{1}{2}} + k_{-\frac{1}{2}}}{2} \right) N^0 + \left(\frac{k_{+\frac{1}{2}} - k_{-\frac{1}{2}}}{2} \right) \Delta N^0.
$$

Turning on microwave, radicals absorb MW according to equation 2.9 at resonance, $h\nu = g\mu_B B_{res}$, leading to a population difference change from ΔN^0 to ΔN^{sl+MW}, such as discussed in section 2.2.1 on the derivation for equation 2.19. Comparing on-resonance and slightly off-resonance populations, the population difference changes according to equation 2.19 by

$$
\Delta N^0 - \Delta N^{sl+MW} \approx 2 W^{MW} T_1 \Delta N^0.
\tag{2.30}
$$

The current density at resonance is according to equation 2.29,

$$
j_{e,sp}^{res} = \left(\frac{k_{+\frac{1}{2}} + k_{-\frac{1}{2}}}{2} \right) N^{res} + \left(\frac{k_{+\frac{1}{2}} - k_{-\frac{1}{2}}}{2} \right) \Delta N^{res}.
$$

The current density change comparing on and off resonance is therefore

$$
j_{e,sp}^0 - j_{e,sp}^{res} = \left(\left(\frac{k_{+\frac{1}{2}} + k_{-\frac{1}{2}}}{2} \right) N^0 + \left(\frac{k_{+\frac{1}{2}} - k_{-\frac{1}{2}}}{2} \right) \Delta N^0 \right) - \left(\left(\frac{k_{+\frac{1}{2}} + k_{-\frac{1}{2}}}{2} \right) N^{res} + \left(\frac{k_{+\frac{1}{2}} - k_{-\frac{1}{2}}}{2} \right) \Delta N^{res} \right).
$$

The total population does not change, i.e. $N^0 = N^{res}$, and ΔN^{res} is given by $\Delta N^{sl+MW} \equiv \Delta N^{res}$. The current density change therefore simplifies to

$$
\begin{aligned}
j_{e,sp}^0 - j_{e,sp}^{res} &= \left(\frac{k_{+\frac{1}{2}} - k_{-\frac{1}{2}}}{2} \right) \Delta N^0 - \left(\frac{k_{+\frac{1}{2}} - k_{-\frac{1}{2}}}{2} \right) \Delta N^{sl+MW} \qquad \Big| \text{ using equation 2.30} \\
&\approx \left(\frac{k_{+\frac{1}{2}} - k_{-\frac{1}{2}}}{2} \right) \left(2 W^{MW} T_1 \Delta N^0 \right).
\end{aligned}
$$

The relative current density change comparing on and just off resonance is correspondingly

$$
\begin{aligned}
\frac{j_{e,sp}^0 - j_{e,sp}^{res}}{j_{e,sp}^0} &\approx \frac{\left(k_{+\frac{1}{2}} - k_{-\frac{1}{2}} \right) \left(2 W^{MW} T_1 \Delta N^0 \right)}{\left(k_{+\frac{1}{2}} + k_{-\frac{1}{2}} \right) N^0 + \left(k_{+\frac{1}{2}} - k_{-\frac{1}{2}} \right) \Delta N^0} \qquad \Big| \text{ using } \Delta N^0 = N_{-\frac{1}{2}}^0 - N_{+\frac{1}{2}}^0 \ll N^0 = N_{-\frac{1}{2}}^0 + N_{+\frac{1}{2}}^0 \\
&\approx 2 W^{MW} T_1 \frac{\Delta N^0}{N^0} \left(\frac{k_{+\frac{1}{2}} - k_{-\frac{1}{2}}}{k_{+\frac{1}{2}} + k_{-\frac{1}{2}}} \right).
\end{aligned}
\tag{2.31}
$$

This relative current change at resonance is proportional to the microwave induced spin flip probability W^{MW}, spin-spin relaxation time T_1, relative population difference off resonance $\Delta N^0 / N_0$ and relative spin dependent charge transfer rate $\left(k_{+\frac{1}{2}} - k_{-\frac{1}{2}} / k_{+\frac{1}{2}} + k_{-\frac{1}{2}} \right)$.

Chazalviel described the current density as product of chemical rate constant k_c, electrode charge carrier density of state D and electrolyte charger carrier concentration N. In other words, he wrote $k = k_c D$ for each spin. Thus, we can rewrite the electron transfer rate,

$$\frac{k_{+\frac{1}{2}} - k_{-\frac{1}{2}}}{k_{+\frac{1}{2}} + k_{-\frac{1}{2}}} \approx \frac{D_{+\frac{1}{2}} - D_{-\frac{1}{2}}}{D_{+\frac{1}{2}} + D_{-\frac{1}{2}}}.$$

Let us now proceed to estimate the size of the signal we might expect. As discussed in section 2.2.2 and 2.2.3, using CISS or optical spin pumping, at room temperature we can expect at best an electrode spin polarization of 10 %, i.e. at best $\frac{k_{+\frac{1}{2}} - k_{-\frac{1}{2}}}{k_{+\frac{1}{2}} + k_{-\frac{1}{2}}} \approx \frac{D_{+\frac{1}{2}} - D_{-\frac{1}{2}}}{D_{+\frac{1}{2}} + D_{-\frac{1}{2}}} \approx 0.1$. $\Delta N^0 / N^0$ is equal to the spin polarization P^0 in equation 2.8, i.e. at room temperature $\Delta N^0 / N^0 \approx 0.0008$. Assuming microwave power saturation is reached, we can use the definition of saturation for equation 2.19, $2W^{MW} T_1 = 1$. According to equation 2.31, in the best case we can therefore expect a relative current density change comparing on and slightly off resonance by

$$\frac{j_{e,sp}^0 - j_{e,sp}^{res}}{j_{e,sp}^0} \approx 10^{-4}.$$

However, if the assumption of $2W^{MW} T_1 = 1$ is made, then the assumption of $2W^{MW} T_1 \ll 1$ used for equation 2.19 is obviously not valid anymore, which ultimately leads to an additional multiplication factor of 1/3 for all equations ongoing from equation 2.30, i.e. $\frac{j_{e,sp}^0 - j_{e,sp}^{res}}{j_{e,sp}^0} \approx \frac{1}{3} 10^{-4}$.

This electrical detection method is not identical to the type of EDMR as described in section 2.2.4 The biggest difference is the weak dependence of the current on the applied potential discussed in section 2.2.4 for e.g. the electron hole recombination at p-n junctions. In this thesis, the resonant current change is strongly potential dependent due to its electrochemical nature (section 2.1). Also, Stutzmann et al. point out that all spin dependent transition rates are increased at resonance.[70] In the present work, this is not the case due to the independent spin polarization on both interface sides. A possibly observed effect is therefore not only potential, but also potential sweeping direction dependent and a current change at resonance is positive or negative depending on the spin polarization combination. To describe this dependency, below I discuss the case of an optically pumped p-GaAs electrode. As stated in the beginning of this section, only the reduction of radicals, i.e. $MV^{+\bullet}$, is considered for just derived order of magnitude estimation. However, it can be expanded to all four redox processes of methyl viologen redox species. Each of these four processes are discussed separately in the following.

Starting in potential sweeping in reduction direction, for the reduction of MV^{2+} to $MV^{+\bullet}$, no spin polarization on the electrolyte side is possible, i.e. $\Delta N^0 = 0$, and therefore no spin dependent current change is to be expected. For the reduction of the $MV^{+\bullet}$ radical to MV^0, a spin polarization exists in the described way above. With respect to section 2.2.4, $MV^{+\bullet}$ corresponds to a electron localized at the SOMO able to accept only electrons of opposite spin. The radical is spin polarized

by B_0 and the reducing electron is spin polarized in this example by optical spin pumping. For light antiparallel aligned with B_0, left circularly polarized light will produce electrons of spin antiparallel to the radical, compare section 2.2.3. The electron current is therefore increased in comparison to no B_0, such as depicted in figure 2.25 a). For right circularly polarized light the electron current will be decreased in comparison to no B_0. Resonance at MW power saturation corresponds to the population state of $B_0 = 0$, c). The relative electron current change with respect to equation 2.31 is therefore negative for parallel and positive for antiparallel spin orientation. When performing a full CV, the free radical electron of $MV^{+\bullet}$ is due to the reduction process $MV^{2+}/MV^{+\bullet}$ and therefore spin polarized by optical spin pumping, which would completely change the effect. However, the CV scan rate in this work is below $50\,mV/s$, such that due to spin relaxation considerations the $MV^{+\bullet}$ radical spin polarization is definitely predominantly due to the external magnetic field.

For the oxidation of MV^0 to $MV^{+\bullet}$, same as for the $MV^{2+}/MV^{+\bullet}$ reduction also no electrolyte spin polarization is possible and therefore no resonant electron current change. The oxidation of $MV^{+\bullet}$ to MV^0 is however very different from the $MV^{+\bullet}/MV^0$ reduction process, such that a spin dependent electron current change at resonance can only be expected if certain conditions are met: for the $MV^{+\bullet}/MV^{2+}$ oxidation an electrode spin polarized by B_0 comes from the $MV^{+\bullet}$ radical to the electrode into either conduction band, valence band or surface state. If the electron is conducted into the semiconductor conduction band, the exclusion principle does not apply and a spin dependent electron current change at resonance is unlikely. However, if the conductance is dominated by electrons recombining with either free spaces at dangling bond surface states such as described in section 2.2.4, or directly with valence band holes, a spin dependent electron current change at resonance can be expected. In both cases the spin polarization is due to optical spin pumping. However, the surface state could be spin polarized by either electrons relaxing from the conduction band or holes from the valence band. In conclusion this means that the oxidation of $MV^{+\bullet}$ at an p-GaAs electrode is only spin dependent, if the $MV^{+\bullet}$ *Red* species W overlaps with either valence band or a suitable dangling bond surface state, see figure 2.22 b) and 2.23. Spin polarized electron hole recombination can be increased if the oxidation process is still in the photo cathodic potential range, such as depicted in figure 2.25 d) - f). In the dark-anode potential range the depletion layer vanishes and the surface valence band is flooded with un-polarized holes, diminishing the optical spin pumping effect. As for the $MV^{+\bullet}/MV^0$ reduction, the electron current change at resonance is dependent on the relative spin orientation, however inversed: optical pumping of electrons with spin parallel (antiparallel) to the electrolyte leave a place which can only be filled by electrons of again parallel (antiparallel) orientation. Comparing to on resonance, f), the electron current is therefore increased for parallel spin orientation, e), and decreased for antiparallel spin orientation, d).

The possibility of surface state electron hole recombination should also be considered for the $MV^{2+}/MV^{+\bullet}$ reduction and $MV^0/MV^{+\bullet}$ oxidation nothing changes, since the corresponding electrode interface site is not spin polarized. For the $MV^{+\bullet}/MV^0$ reduction a surface state would act as intermediate state. Depending on the intermediate time and relaxation time combination, such intermediate state could therefore completely destroy expected spin effect, only slighty affect it or something in between. Electrically detected spin dependent current change at resonance is therefore also useful to analyze the nature of certain interface charge transfer mechanism.[15]

For the discussion of chiral functionalized surfaces, optical spin pumping is replaced by CISS.

MV$^{+\cdot}$/MV^0 reduction

Figure 2.25 – Spin dependent electrode/electrolyte electron current change at resonance for MV$^{+\cdot}$ reduction and oxidation at a p-GaAs WE. The spin polarizations are exaggerated to 100 %. Compared to no external magnetic field, at negative potential the electron conduction from the conduction band to MV$^{+\cdot}$ is due to Pauli exclusion increased for antiparallel polarization, a), and decreased for parallel spin polarization on electrode and electrolyte side, b). At resonance the electron current changes up to its normal value without B_0, c). In oxidation direction the process is inverted and only possible for electron hole recombination via surface states or valence band. For anti parallel polarization the electron current is decreased, d), and for parallel increased, e). This is due to the hole left by optical spin pumping, which can only be filled with electrons of spin polarization identical to the generated electron. At resonance the electron current changes up to its value without B_0, f). Field and light direction are turned by 90 deg compared to above graphs for better comparability with the actual experimental conditions later on.

The electrons are therefore spin filtered dependent on their propagation direction and molecule helicity, compare figure 2.21. The reduction direction scan discussion is similar to above, i.e. due to the electron spin filtering an effect is possible at MV$^{+\cdot}$/MV^0 but not for MV^{2+}/MV$^{+\cdot}$. As illustrated in figure 2.26, the electron current is increased for antiparallel spin orientation, a), and decreased for parallel spin orientation, b), compared to on resonance c). However, oxidation is here also conduction electron based. A possible electron current change at resonance for the oxidation
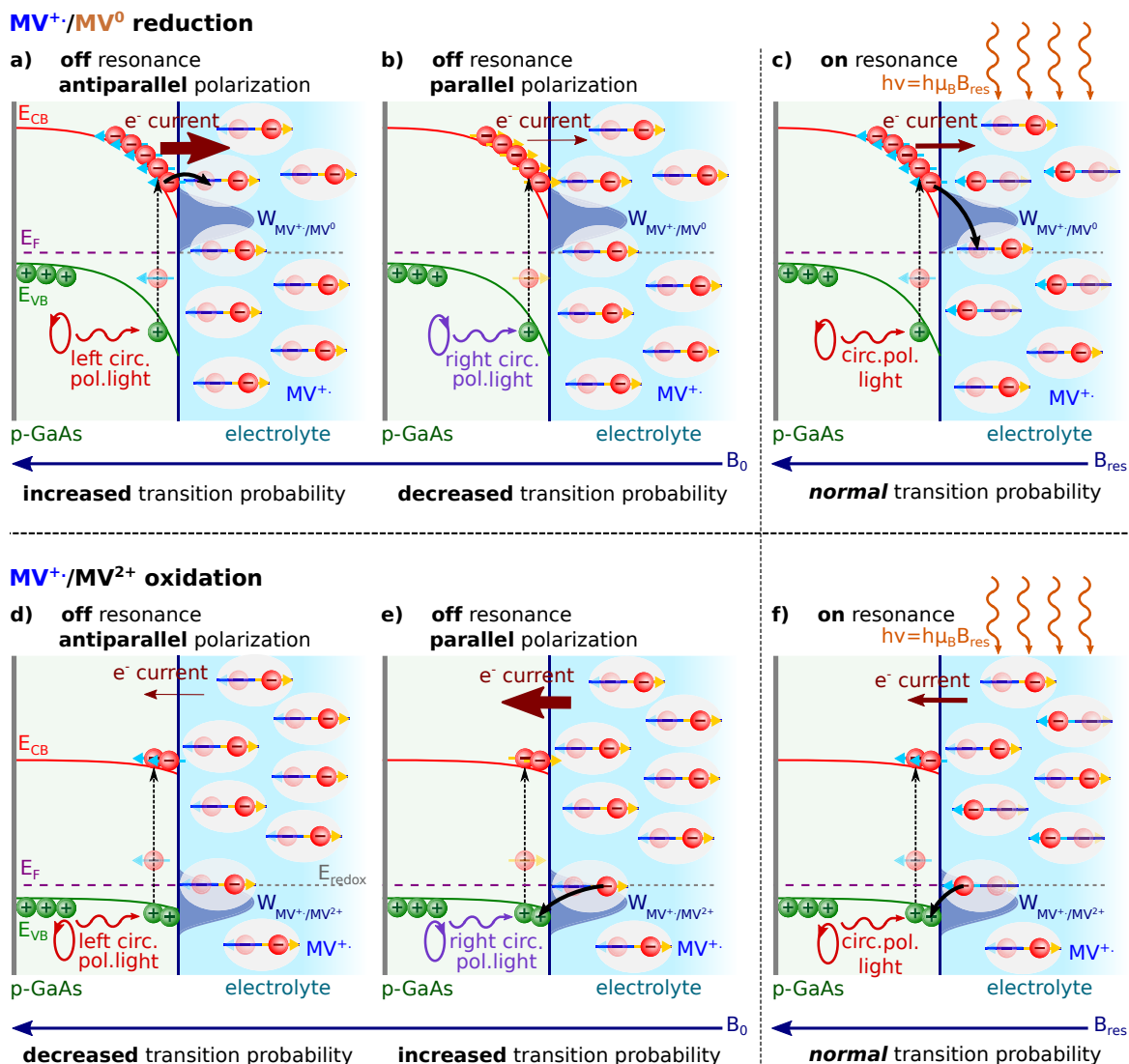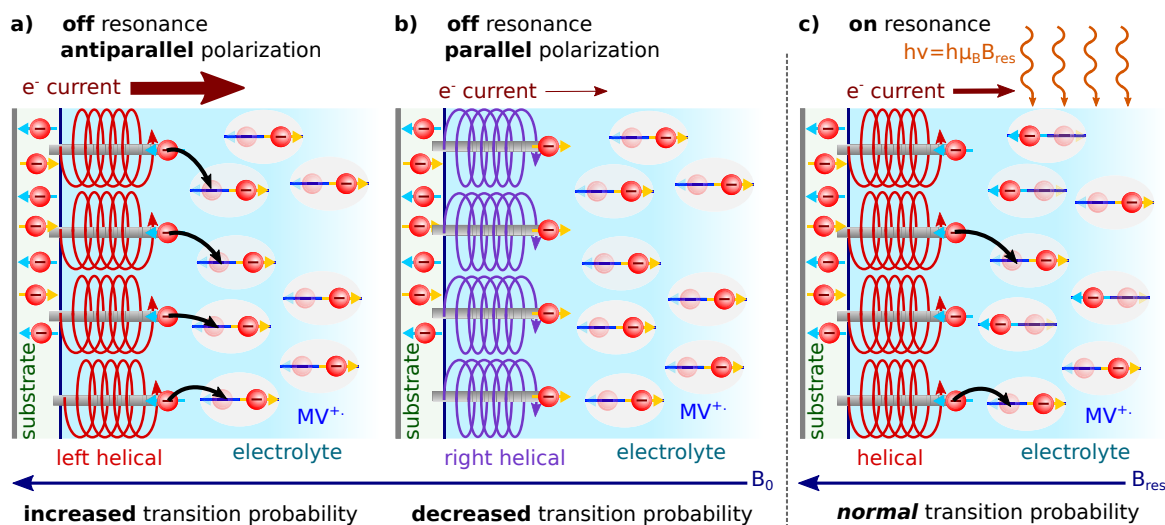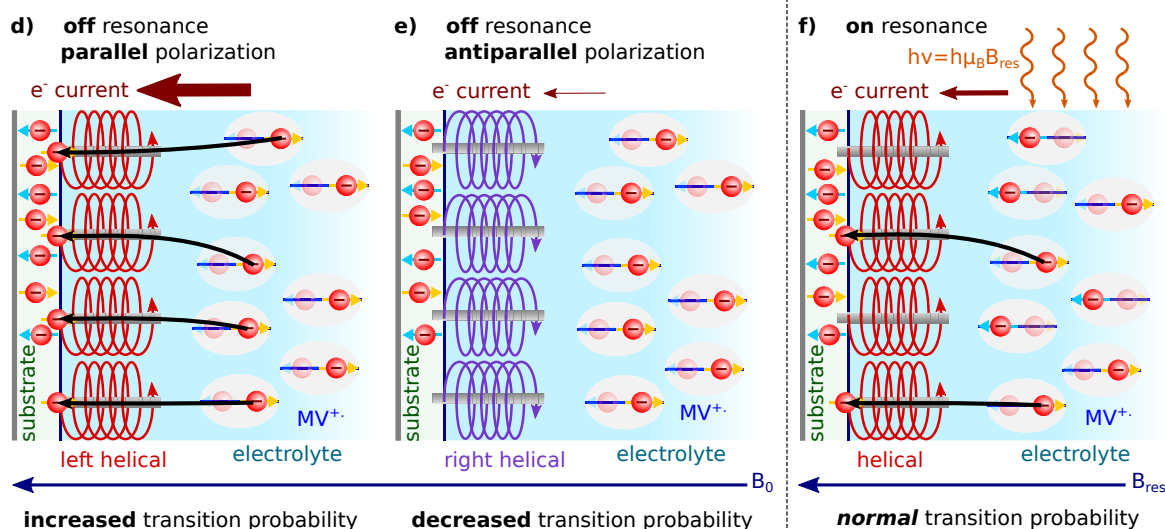
Figure 2.26 – Spin dependent electrode/electrolyte electron current change at resonance for $MV^{+\bullet}$ reduction and oxidation at spiral molecules. The spin polarizations are exaggerated to 100 %. Compared to no external magnetic field, at negative potential the electron conduction to $MV^{+\bullet}$ is due to Pauli exclusion increased for antiparallel polarization, a), and decreased for parallel spin polarization on electrode and electrolyte side, b). At resonance the electron current changes up to its normal value without B_0, c). In oxidation direction the spiral molecules dominate a possible effect due to the filtering. No electron hole recombination is necessary. For anti parallel polarization the electron current is increased, d), and for antiparallel decreased, e), compared to on resonance f). Parallel and antiparallel is here due to CISS also direction dependent.

direction would therefore also be based on the spin filtering effect and not pauli exclusion, with or without intermediate surface states. As expected for p-GaAs, here also the electron current is increased for parallel spin orientation, d), and decreased for antiparallel spin orientation, e), compared to off resonance, f). The expected effect size is identical to that of p-GaAs and the effect is reversed by inverting the molecules helicity.

For the maximum order of magnitude current change we can therefore consider the current at the $MV^{+\bullet}/MV^0$ and $MV^{+\bullet}/MV^{2+}$ peaks, which are used samples typically in the range of $1\,\mu A$ to $10\,\mu A$. The expected effect is therefore in the $0.1\,nA$ to $1\,nA$ range. This is a best case scenario, such that the actual current change might be much smaller. The development of a system able to detect in the sub nA range is discussed in section 3, specifically 3.1.6 and 3.2. Especially surface states and spin relaxation times might reduce the effect immensely or even completely suppress it. However, surface state recombination might even be necessary for the observation of a resonance effect for p-GaAs when the electrochemical process is an oxidation.

3 Methodology for Simultaneously Performed EPR, EC and EDMR

In the following, the experimental setup, detection method and evaluation scheme is described in detail. General characterization results, inter system dependencies, electrode and sample preparation are also discussed. The development and optimization of the setup described in this chapter, including the measurement methods, the detection and data evaluation strategies was the major part of this thesis. This rather long part is important to fully interpret and discuss the results, possible flaws, artifacts and systematic perturbations arising from the specificities of this setup and measuring protocol. All results presented in this thesis were performed in a temperature range of 20 °C to 24 °C and all electrochemical measurements were performed on an electrolyte of 2 mM MV$^{+\bullet}$ dissolved in ACN with 200 mM TABP as supporting electrolyte, in a 5 mm diameter NMR tube using a Pt wire tip quasi reference electrode of 0.125 mm and a Pt rod CE of 0.5 mm diameter.

3.1 Setup, Sample Preparation, Characterization and Calibration

The experimental system consists of three major parts: CW EPR setup, optical excitation part and electrochemical measuring system combined with EDMR. Each of these parts are discussed regarding their theory and literature respectively in sections 2.2.1, 2.2.3, 2.1 and 2.2.4. The complete setup schematic is depicted in figure 3.1. Each of these three parts is separately discussed in detail in sections 3.1.5, 3.1.3, 3.1.1 and 3.1.6, where also again the corresponding parts of figure 3.1 are separately depicted for reading comfort. Each of these parts is essential for the success of one full measurement and needs to be perfectly adjusted for every experiment with respect to its own function and how it interacts with other parts of the setup.

3.1.1 Electrochemical Base System

An electrochemical cell consists in this work of three electrodes (working electrode (WE), counter electrode (CE) and reference electrode (RE)) placed inside a glass container filled with electrolyte. The measurement scheme for any given sample is rather time consuming, requiring in the range of half a day up to several weeks. MV$^{+\bullet}$ is extremely sensitive to oxygen[55] and water.[56] We therefore rely on electrochemical cells which are outstandingly well sealed and show excellent chemical stability and inertness. Oxygen tightness was controlled in situ, which is necessary due
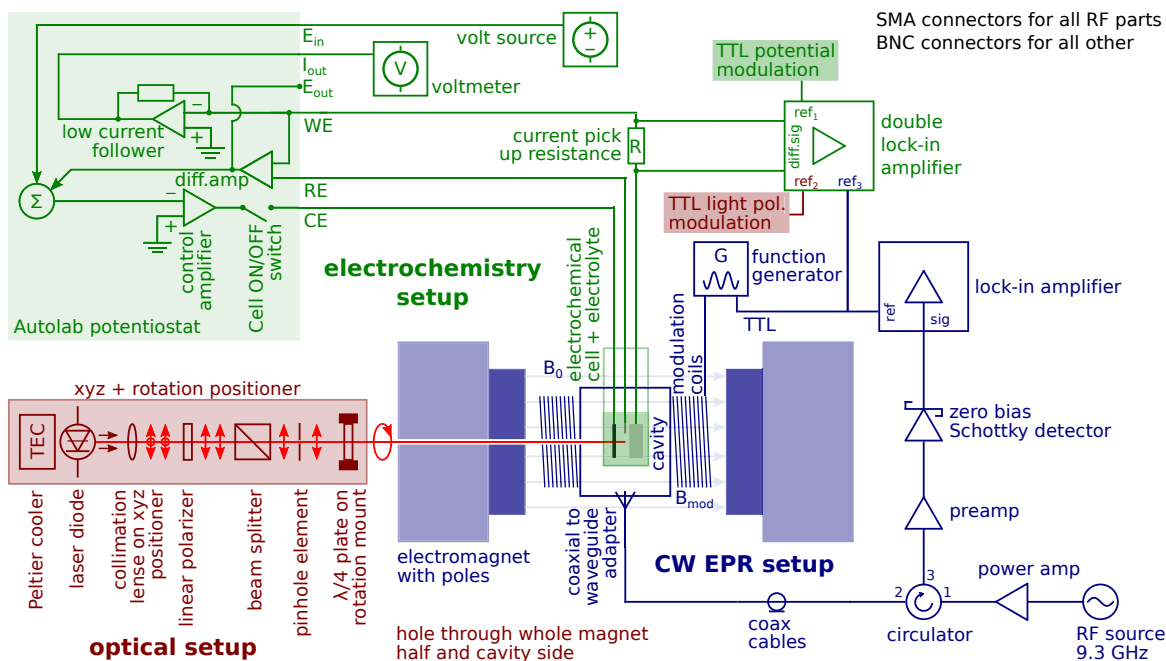
Figure 3.1 – Complete setup schematic with three major parts: CW EPR setup, optical excitation part and electrochemical measuring system for EDMR. The CW EPR setup is a common 9.3 GHz cavity system. The optical set-up is necessary for optical spin pumping of p-GaAs electrodes. A hole through the whole length of the magnets left side and cavity was drilled to ensure spin polarization parallel to B_0. The electrochemical measuring system is driven by a potentiostat system and EDMR measurements are performed quasi independent of the potentiostat using a current pick up resistance.

to the extreme sensitivity of MV$^{+\bullet}$ to oxygen. In the case of an accidental presence of oxygen, the electrolyte changes color, so the problem is readily identified. Already traces below 1 ppm lead to a prompt oxidation of MV$^{+\bullet}$ to MV^0 and therefore loss of the blue color in the MV solution.[54] This also applies to all possible interactions with other chemicals and catalysts. Reported as helpful,[111] I found pump thaw freeze cycles not necessary for degassing regarding radical stability, given preparation is performed inside a well maintained glove box, hardware is well cleaned and all chemicals are of pure and dry standard. Regarding MV$^{+\bullet}$ stability, the electrochemical cells described below are stable for more than three and a half years.

We use a cavity CW EPR system and are therefore limited to electrolyte volumes of some ten microliters. Due to the large sample consumption,[1] I use a rather low cost electrolyte container of standard 5 mm NMR tubes (*Wilmad LabGlass, Economy NMR Sample Tube*, 5mm outer diameter, Class B glass, 400MHz), which shows a good equilibrium between acceptable microwave distortion, volume and price. Everything in contact with the radical solution, especially new NMR tubes, has to be cleaned in an acetone ultrasonic bath of at least 40 °C for at least one hour and immediate subsequently placement inside a glove box (*Jacomex, GP[Campus]*, well maintained such that O_2 and H_2O concentrations are always below 15 ppm). Otherwise, chemicals adsorbed on the surfaces will destroy the MV$^{+\bullet}$ radicals. Further preparation was performed as much as possible inside this glove box.

---

[1] More than 150 fully prepared electrochemical cells after 3.5 years.

[111] C. S. Johnson, and H. S. Gutowsky, "High-Resolution ESR Spectra of Photochemically Generated Free Radicals: The Viologens", The Journal of Chemical Physics **39**, 58–62 (1963).
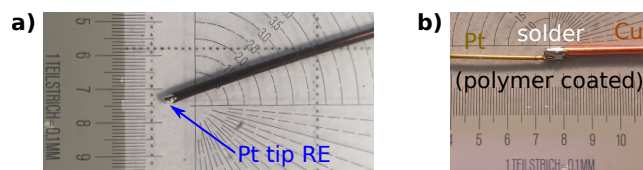
Figure 3.2 – Pt wire tips of 0.125 mm diameter as RE in a) and soldering contact to a Cu cable in b. All cables are polymer coated and their color reflects not the metal. Scale of 0.1 mm per bar.

Standard reference electrodes such as *normal hydrogen electrodes* are in general used in electrochemistry (EC) to allow comparison with literature. However, standard reference electrodes are bulky and therefore not accessible for us. I found the often used Ag/AgCl quasi reference electrode[2] to react with $MV^{+\bullet}$ radicals and therefore unfit as reference electrode, $MV^{+\bullet} \xrightarrow{Ag^+} MV^{2+}$. I settled on polyester coated platinum wire tips of 0.125 mm diameter such as displayed in figure 3.2 a), which proved to influence the system less than silver wires and being chemically more inert.

As counter electrode, a bare $\varnothing = 0.5$ mm Pt rod proved to generate stable and reproducible results. I tried several other CE systems, such as Pt wire wound to a coil, Pt mesh or Pt plates. However, a straight rod has the least influence regarding MHD effects, field induced bending and is most easy to use. With regards to the shape of the electric field lines, the rod should be placed at least partly in front of the WE chemically active face. To be most sensitive to processes at the WE interface, current should be limited if at all by the WE active surface area and not the CE size. The CE surface was therefore always at least double of the WE surface. For large WE surfaces, a single bend was therefore introduced into the Pt rods of the counter electrode. ITO as transparent CE would be a nice option since it would allow the light needed for the optical excitation to go through the CE. In general, ITO gave good results regarding electrochemical measurements. However, a method for ITO coating of the 5 mm NMR tubes inside would need to be developed. Pt as counter electrode has additionally to its inert nature the advantage of acting as catalyst for the MV reduction processes, which reduces the necessary surface area.[112] The adsorption of $MV^{+\bullet}$ and MV^{2+} on Pt could raise problems. However, it has been observed that adlayers of only sub-monolayer thickness form, so that at any time also clean Pt is in contact with the electrolyte.[113]

Both, CE and RE were contacted by soldering to otherwise polyester coated $\varnothing = 0.3$ mm copper cables. Due to the detection using lock-in technique, special care was given to the soldering joints. To avoid Schottky effects (copper(1)oxide Cu_2O) and ensure hot soldering joints, the metals on both sides were sandpaper cleaned, etched and soldered with increased soldering temperature and additional acid to decrease the oxidation prone time. Such as displayed in figure 3.2 b), soldering contacts were kept in sub millimeter size to avoid inductance effects on the modulation signal.

All working electrodes are contacted via $\varnothing = 0.3$ mm copper cables in a three step process (figure

---

[2] Preparation by applying a galvanostatic current of 200 μA between an Ag wire und a Pt counter electrode dipped into an 1 M LiCl solution with nitrogen bubbling.

[112] C. L. Bird, and a. T. Kuhn, "Electrochemistry of the viologens", Chemical Society Reviews **10**, 49 (1981).

[113] B. Beden, et al., "Investigation of the adsorption of methyl viologen on a platinum electrode by voltammetry coupled with "in situ" UV—visible reflectance spectroscopy", Journal of Electroanalytical Chemistry and Interfacial Electrochemistry **170**, 357–361 (1984).
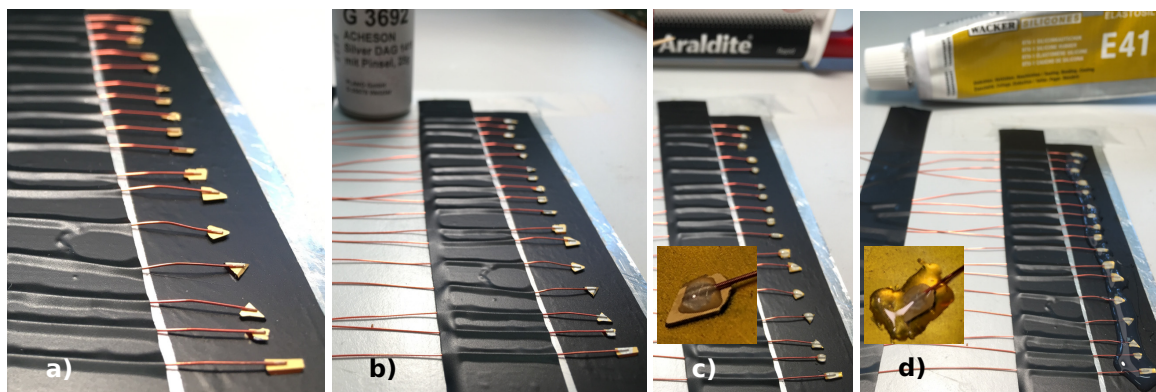
Figure 3.3 – Batch WE ohmic contacting with silver paste on top of a gold contact, a) and b), mechanical stabilization using epoxy glue, c), and protection using silicone glue, d). Presented batch is at the example of p-GaAs/Ti(20 nm)/Au(200 nm) backside contact.

3.3). Silver paste (*Acheson Silver DAG 1415*) is applied on a Cu cable pushing on the WE contacting areas, a) and b). The contact is mechanically stabilized with epoxy glue (*Araldite Rapid*), which therefore should cover much of the WE contact region, c). Drying for two hours is necessary. Epoxy is well suited for mechanical stabilization. However, it reacts with MV when in contact, lowering the MV$^{+\bullet}$ concentration over time and ultimately dissolving parts of its own compounds. Flexible silicone glue (*Wacker Silicones, Elastosil, E41*) on the other hand, is not interacting with any of the MV$^{+\bullet}$ electrolyte compounds. Everything but the active WE surface is therefore covered with a silicone layer to ensure chemical inertness, d). Additionally, all soldering joints are sealed with silicone. The silicone has to dry for at least 24 hours before it can be brought in contact with the electrolyte, otherwise radical loss will happen due to chemicals diffusing out of the glue. Due to the long silicone drying process, preparation was typically done in batches. After drying, the silicone is carved down with a scalpel to its final form. This form is such that half of the NMR tube diameter is filled with the WE in such a way that the WE is almost immobile.

The electrodes and wires connected to them are exposed to an external magnetic field of ≈330 mT. Two equivalent solutions have been found to minimize the noise due to interaction with cables: either twisted cables[66,67,114] or keeping the cables inside the magnetic field as straight as possible, figure 3.4 a) and b). For the latter case, the cables had to be stabilized by wrapping together with teflon tape. In general, the WE and CE are opposing and bend away from each other such that they push against the NMR glass tube walls. This stabilizes the electrode system further inside the NMR tube. The RE is situated between WE and CE so that electric field lines are relatively straight between the three electrodes, and close to the WE to minimize IR drop (figure 3.4 b)). Any RE movement changes the CV, the RE is therefore additionally fixed in silicone or by teflon tape close to the WE.

After cutting the cleaned NMR tubes down to a length of 50 mm to minimize the length of unshielded cables, the electrodes and approximately 10 to 20 µL of electrolyte are inserted. Epoxy glue proved to be quasi impermeable to oxygen, mechanically stable and, unlike silicone, does not diffuse MV$^{+\bullet}$ destructive chemicals while drying. The NMR tube is therefore sealed inside the glove

[114] F. M. F. Rhen, et al., "Influence of a Magnetic Field on the Electrochemical Rest Potential", Journal of The Electrochemical Society **153**, J1–J7 (2006).
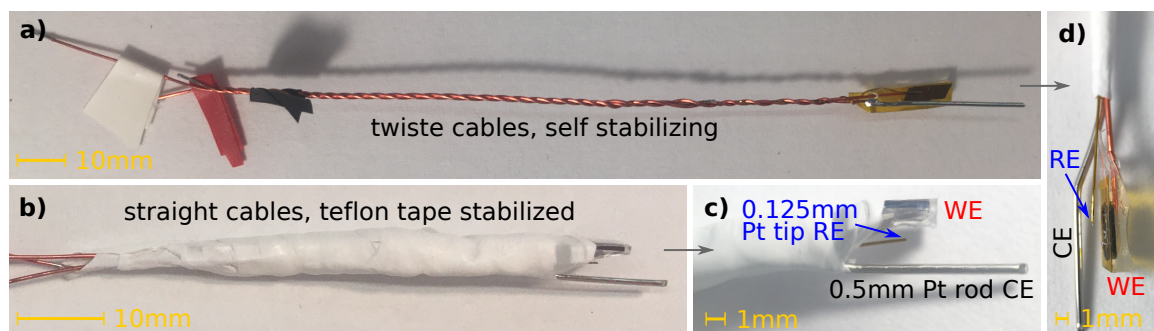
Figure 3.4 – Three electrode system. Magnetic field influence on the cables is decreased by either twisted pair, a), or straight cables, b). Straight cables are stabilized with a thick layer of teflon tape, such that no movement inside the NMR tube is possible. The Pt rod CE is positioned in front of the WE and bent against the NMR tube wall for stabilization, c) and d). A Pt tip RE is situated close (submillimeter) in front of the WE to decrease IR drop.

box with epoxy glue. Two hours of drying is sufficient for oxygen tightness, full manual stability is however only reached after twelve hours. It is necessary to always keep the electrochemical cell upright, since any contact between electrolyte and epoxy can destroy the sample. Additional calcium grains for the purpose of water and oxygen absorbance were used by previous group member working with OLED,[115] but brought in this work no additional advantage. Two typical electrochemical cells are displayed in figure 3.5, a) and b). The described preparation and sealing of electrochemical cells, electrodes and contacts results in a stability regarding oxygen tightness and general stability for at least one year, some samples were still functioning after 3 years outside the glovebox, though they changed their CV due to surface coating. Radical stability is better than 3.5 years. The described electrochemical cell is the result of a three year long process and is still under improvement especially regarding miniaturization and combinability with optical excitation. The present electrochemical cell version is optimized regarding noise and microwave interaction.

The electrochemical measurements, i.e. cyclic voltammograms, chronopotentiometric and chronoamperometric measurements, open circuit potential (OCP) determination and differential methods, are driven by a *Metrohm Autolab PGSTAT302N* Potentiostat/Galvanostat system, additionally equipped with a *FRA32M* module for impedance measurements, a *SCAN250* module to perform true linear sweeps, and a *BA* module for the option of simultaneous measuring and radical
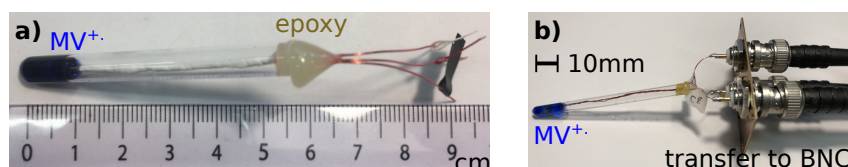
Figure 3.5 – Complete electrochemical cell suitable for simultaneously performed EC and CW EPR. A three electrode system is situated inside a 5 mm NMR tube filled with saturated $MV^{+\bullet}$ radical electrolyte. Presented is a twisted cable and straight cable system, b) and a). Bare copper cables are kept short and transferred to BNC cables. The whole unshielded part is situated inside a faraday cage (not displayed).

[115] F. Comandè, "Spin processes and charge dynamics in organic light emitting diodes", PhD thesis (EPFL, 2014), pp. 1–117.

production with different electrodes. The potentiostat system allows to perform all types of electrochemical measurements in fast sequence without having to change the electronic system nor having to write a driving program for each process as would be necessary for a home built system. All electrochemical measurements are presented as raw, i.e. untreated. This is helpful to visualize possible noise and verify cell stability. Only the presented results in section 4 are treated, which is fully discussed in section 3.2.1 and the results are marked with the specifications of used filtering system.

It is common in electrochemistry to present not the current but current density, i.e. current divided by WE surface area in contact with the electrolyte. However, in this thesis the actual current is of more interest, e.g. for sensitivity and noise range evaluation aspects. All electrochemical measurements are therefore presented with current, not current density, and surface area will be indicated.

3.1.2 Working Electrodes for Spin Dependent Current Change

Within this work, results for the resonant detection of spin dependent current change are presented for three general types of WE, which are called p-GaAs, Al5 and [5]helicene and are fully described below. p-GaAs uses optical spin pumping. This renders these samples most complex. All p-GaAs samples were home built using Zn doped wafers of (111) orientation (*Wafer Technology LTD*, $3 \times 10^{17}\,\mathrm{cm}^{-3}$ doping concentration, DS polished). Backside contacting was performed as described above. To achieve ohmic contact, literature suggests various sophisticated ways via mostly multilayer and different post treatments for interface barrier lowering.[116,117] The following method works sufficiently well to obtain ohmic contact for the purpose of continuous potential sweep and modulation techniques:

1. chemical cleaning

2. oxygen plasma cleaning

3. 20 nm Ti deposition with electron beam physical vapor deposition (EPVD)
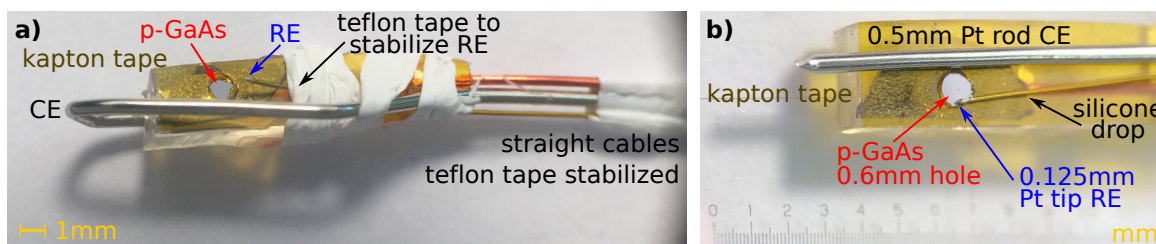
Figure 3.6 – Three electrode system with a p-GaAs WE. Except of a 0.6 mm hole, the p-GaAs is covered with chemically inert kapton tape to avoid currents of not optically pumped regions. The RE electrode in a) is manually stabilized with teflon tape close to the WE interface area. In b) this manual stabilization is achieved with a drop of silicone.

[116] A. Piotrowska, "Ohmic Contacts to GaAs: Fundamentals and Practice", Acta Physica Polonica A **84**, 491–504 (1993).

[117] A. G. Baca, et al., "A survey of ohmic contacts to III-V compound semiconductors", Thin Solid Films **308 - 309**, 599–606 (1997).
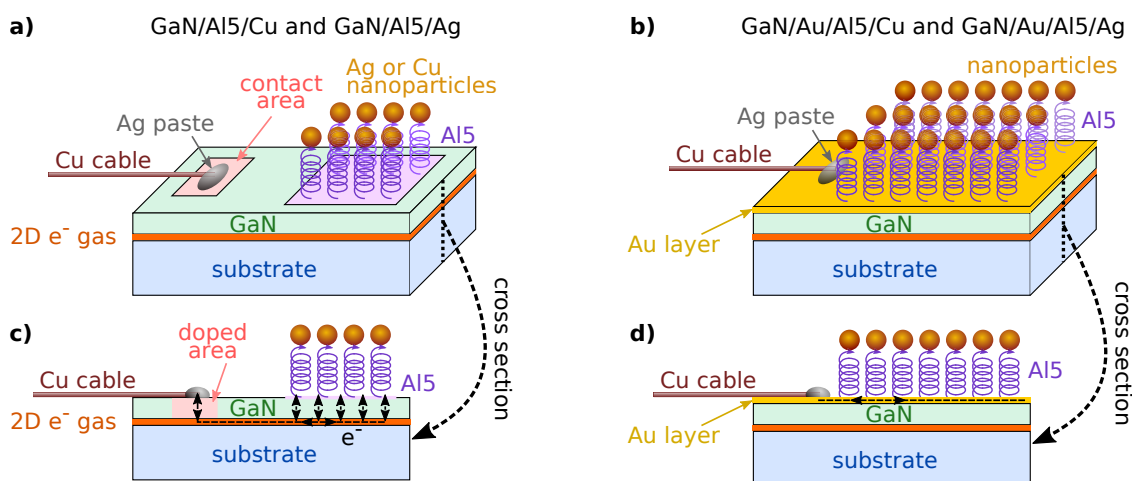
Figure 3.7 – Schematic of five alanine group peptide (Al5) functionalized electrodes. a) displays the structure of Al5 deposited on top of GaN. Current flows through a 2D electron gas, such as depicted in the cross section c). Al5 has nanoparticle endings of either Cu or Ag, in the following described as GaN/Al5/Cu and GaN/Al5/Ag. b) and d) depict the corresponding with an additional Au layer in between Al5 and GaN, in the following called GaN/Au/Al5/Cu and GaN/Au/Al5/Ag. The 2D electron gas is here a residual of other experiments, and for our purpose current flows directly from contact through the gold layer to Al5 which is deposited on the whole surface.

4. 200 nm Au deposited with EPVD

5. silver paste

To avoid currents from regions not optically pumped, the surface has to be partly covered. The beam spot arriving at the sample is of $\varnothing \approx 1\,\mathrm{mm}$. I therefore use a chemical resistant adhesive kapton tape and cover the sides with silicone. A $\varnothing = 0.6\,\mathrm{mm}$ hole is embossed through the kapton at the center of the p-GaAs piece, such as depicted in figure 3.6 a) and b) for two different electrodes. After combining the prepared p-GaAs WE with the CE and RE and fine tuning their relative orientation, the whole three electrode system is etched for 20 s in 6 M aqueous HCl acid followed by rinsing with *milli-Q* water. Etching should not be exaggerated, since arsenide is more actively etched than gallium and the resulting surface and CV are strongly changed. This cleaning technique was developed and tested by Dr. Mika Tamski for the purpose of optical spin pumping and impedance measurements.

Bare p-GaAs is in general not very stable regarding electrochemical experiments, which again is mostly due to the more reactive arsenide. To improve p-GaAs, we are developing functionalized p-GaAs. Functionalization is the process of modifying the surface chemistry by attaching molecules or nanoparticles on the surface. This is further discussed in section 5.

All substrates functionalized with peptides of five alanine groups (Al5) were kindly prepared and provided by Prof. Naaman's group at the Weizmann institute. Four types of samples were provided, Al5 with nano particle ending of either Cu or Ag, deposited on gold or directly on GaN. Multilayers in the GaN substrate create a 2D electron gas, about 20 nm below the surface. The exact construction is to date not fully known to us. however, in essence it is what is represented in figure 3.7, a) without gold and b) with gold. The corresponding cross sections are shown in c) and d). Depicted is also the way of contacting with silver paste. What remained unclear was the
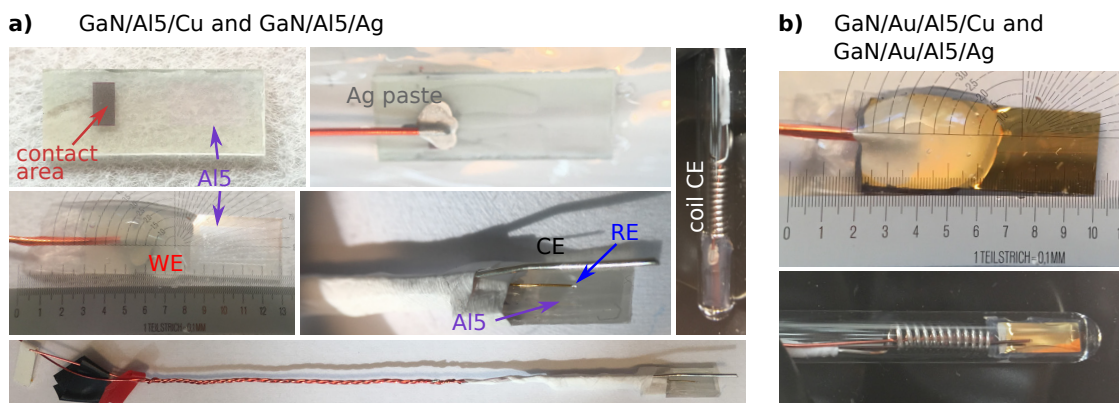
Figure 3.8 – GaN/Al5 and GaN/Au/Al5 WE sample preparation. Contacting with silver paste on the intended contact area in a) and directly on gold in b).

substrate double layer which creates a 2D electron gas. In any case, the contacting area is heavily doped GaN, allowing ohmic contact to the 2D electron gas along which the current flows until below the area of deposited Al5. Current between the 2D electron gas and Al5 takes place through an undoped GaN. The current is therefore in general very low for these samples, i.e. maximum current of typically some 100 nA. Al5 was terminated with nano particle endings of either Cu or Ag. These samples are therefore called GaN/Al5/Cu and GaN/Al5/Ag. Al5 is deposited in the form $SHCH_2CH_2CO(AlaAib)_5COOH$ only on a certain area, hardly, but just visible in figure 3.8 a) as a square of different reflection. Ohmic contact to a copper cable is prepared with silver paste on the contact area and post stabilization as above described for p-GaAs with first epoxy and then silicone. For this and all coming samples, the WE was not etch cleaned with HCl as described above but only CE and RE. The WE was simply rinsed with *milli-Q* water.

Preparation of substrates with a gold layer (unknown thickness) between GaN and Al5 was more straight forward. Al5 is deposited as $NH_2(AlaAib)_5CONH_2CH_2CH_2SH$ on Au covering the whole front side. Small scratches into the gold layer ensures direct ohmic contact of silver paste to gold. The 2D electron gas was therefore not used, such as indicated in figure 3.7 b). Stabilization and protection were done as above.

As visible in figure 3.8 b) for gold and a) without gold, Al5 samples were partly prepared with Pt CE coils. These were the first samples where I observed a resonant resistance change. However, coils produce less stable results compared to straight rods, as will be further discussed in section 5. After this initial trial, experiments showing resistance change were performed with straight Pt rod CEs.

Helicene functionalized substrates were kindly prepared and provided by the LSEN group of Dr. Magali Lingenfelder, Karla Banjac, by depositing thiadiazole-[5]helicene on a mica substrate covered with 200 nm Au (*Phasis*) by dropcasting 7 mM helicene solution in nonanoic acid. Contacting was identical to the GaN/Au/Al5 samples, as depicted in figure 3.9. The samples were photo active, which is why most of the preparation was performed in almost complete darkness with only a small red light lamp. To minimize the effect of mass transport limitation induced problems, the active WE surface area was decreased. However, Au is not very stable on mica and easily peels off. Kapton tape is therefore out of question. Consequently, I used silicone by first covering only the
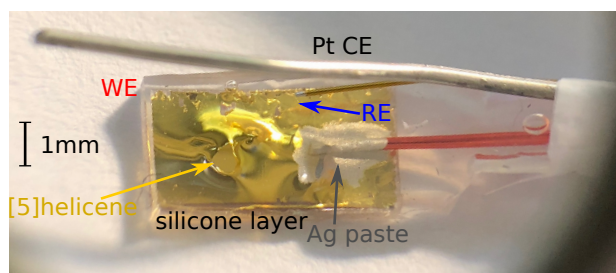
Figure 3.9 – Helicene sample, [5]helicene deposited on a 200 nm Au layer on top of a mica substrate. Chemically active surface area was decreased down to 0.5 mm^2 using silicone to decrease diffusion problems.

edges and subsequent pulling from the edges over the surface to the opposite side, leaving only a small hole open in the middle. This method resulted not in the most beautiful sample but one of the best in terms of clarity of the spin dependent current change. Hole sizes below 0.5 mm^2, i.e. $\varnothing \approx 0.4$ mm) are well possible at a coverage thickness around the hole of less than 0.1 mm, such as depicted in figure 3.9. In comparison to kapton, this hole does not have sharp edges, which is of advantage regarding diffusion. Additionally, silicone has the least side effects, when well dried.

3.1.3 Optical Excitation System

As discussed in section 2.2.3, spin polarization on the electrode side can be achieved by optical spin pumping on p-GaAs with a laser diode (LD) of wavelength 830 nm (*Thorlabs* 50 mW *HL8338MG*). The light is first linearly polarized with a beam splitter and then circularly polarized with a $\lambda/4$ plate, compare figure 3.10. A $\lambda/4$ plate produces circularly polarized light when the incident light is linearly polarization at an angle of 45° relative to the optical $\lambda/4$ plate axis. The circular handedness is inversed for $-45°$. However, the LD light is in reality not monochromatic, therefore the beam splitter emits not perfectly linearly polarized light and the resulting circular polarization is correspondingly imperfect. In this setup the best was elliptically polarized light
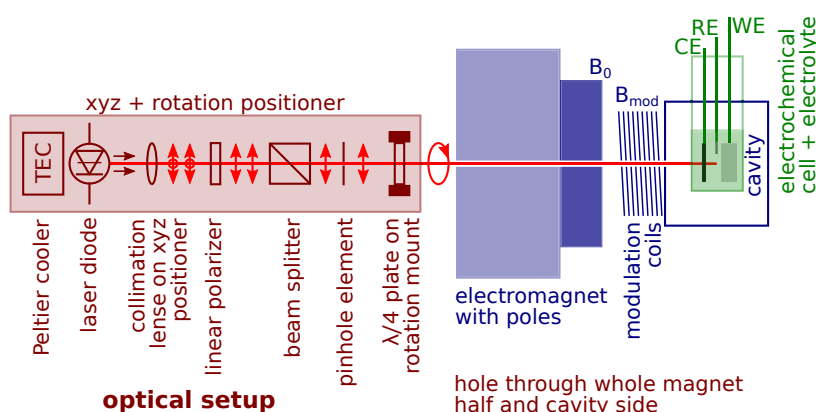
Figure 3.10 – The optical set-up is necessary for optical spin pumping of p-GaAs WEs. A hole through the whole length of the magnets left side and cavity was drilled ($\varnothing = 1mm$ at cavity) to ensure spin polarization parallel to B_0. The laser light power can be adjusted by a rotational linear polarizer in front of a beam splitter, which reduces the laser light power noise in comparison to direct current calibration. The $\lambda/4$ plate responsible for circular polarization is mounted on a motorized rotation mount, allowing automated light polarization switching and modulation at up to 10 Hz for lock-in detection. A pinhole element decreases the rotation induced power modulation.
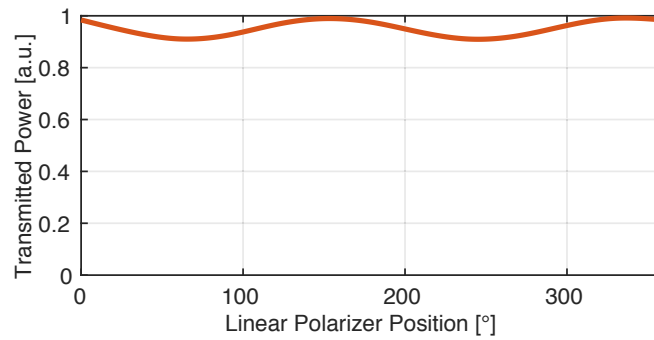
Figure 3.11 – Circularly polarized light characterization for a $\lambda/4$ plate with 830 nm light. For constant $\lambda/4$ plate orientation a behind positioned linear polarizer is rotated continuously between 0° and 360 degres. The presented curve with a transmitted power modulation of 10 % is the best $\lambda/4$ plate rotational position (resolution of 0.25°).

with an imperfection of 10 % from circularly polarized light, such as depicted in figure 3.11.

One possible modulation to be detected by the lock-in would be to switch the circular polarization helicity and observe the effect of helicity, therefore spin polarization, on the electrochemical current. In order to get the modulation, the $\lambda/4$ plate is mounted on a motorized rotation mount (*Thorlabs Brushless Motor DDR15/M, driven by the KBD101*). The rotation mount runs at a maximal speed of $f = 5$ Hz and polarization inversion is every 180°. Rotation at f will therefore switch between parallel and antiparallel spin polarization at $2f = 10$ Hz. As is well visible in plot 3.12 (blue data set) and also described by Chazalviel, this rotation can produce a laser light power modulation at f and its harmonics, if the laser beam is not sufficiently small and perfectly centered in the middle of the $\lambda/4$ plate.[16] This caused a modulation of the electrochemical current which is due to the photoconductivity modulation, not a spin effect. Additional to the general collimation adjustment, I therefore use a $\varnothing = 1$ mm centered pinhole element right in front of the rotation mount, red data set in plot 3.12.

I found in all tested laser diodes having output power of immense noise over some range of the operation parameters, but also some sweet spots with very low power. Because of this, the LD is run continuously at its sweet spot and the light power is adjusted by a rotatable linear polarizer in front of the beam-splitter. For further stability, we use a temperature controlled mount (*Thorlabs TCLDM9* diode mount combined with a *TED200C* temperature controle and *LDC240C* current controller). The yellow line in plot 3.12 is the result using a pin hole element and sweet spot power
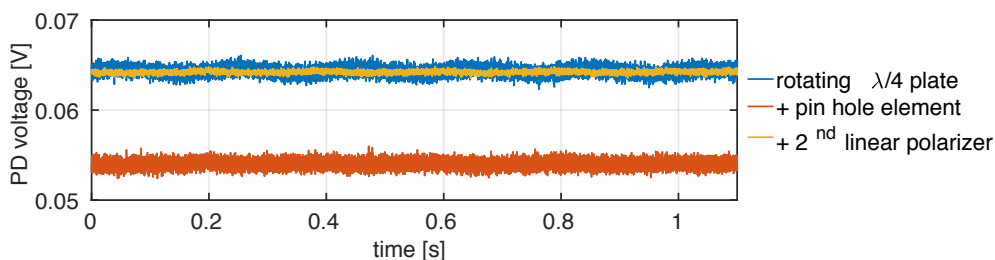
Figure 3.12 – Laser light stabilty and noise. The pinhole element of $\varnothing = 1$ mm eliminates most of the sine like power modulation induced by the rotating $\lambda/4$ plate. The second linear polarizer allows light power adjustment with the laser diode at the point of minimum noise, see main text.

a) optical bench with
   2x three axis positioner
   + rotation positioner

b) magnetic pole
   with 5mm hole

c) 1mm hole through cavity side

1) LD system
4) beam splitter
7) outside of magnetic
   pole with hole

2) lense system
5) 1mm pin hole

3) linear polarizer
6) rotating λ/4 plate
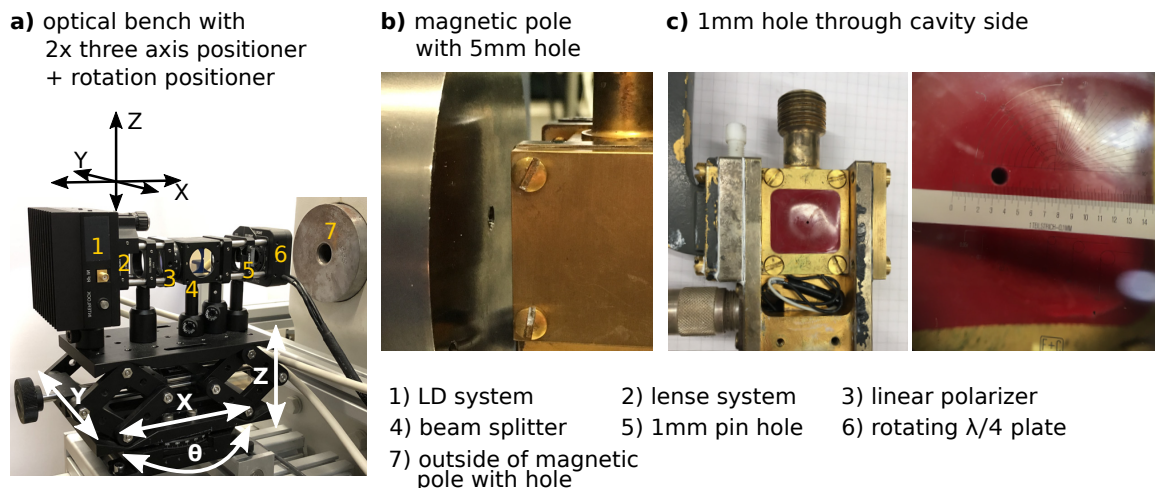
Figure 3.13 – Optical bench, hole through magnetic pole piece and cavity side. The light beam has to be guided through the optical setup, magnet, pole and cavity side onto the WE $\varnothing = 0.6\,\mathrm{mm}$ active surface. All together a length of 60 cm covering 5 holes. The diode lens system is therefore mounted on a three axis positioner and the whole optical bench on a second three axis plus rotational positioner.

calibration.

The resulting spin polarization by optical pumping is parallel to the light wave vector. To reach a maximal current change, it is therefore important to shine the light parallel to the external magnetic field of the EPR setup, i.e. the light has to come from the side of the cavity. As displayed in figure 3.13, the pole piece center screw was removed so that the left hole can be used as light path, a), a $\varnothing = 5\,\mathrm{mm}$ hole was drilled through the left electromagnet pole piece, b), and a $\varnothing = 1\,\mathrm{mm}$ hole through the cavity side, c). The complete optical setup is aligned in four steps. First, the laser light is collimated and centered orthogonally to the $\lambda/4$ plate center using a x, y, z positioner. Second, the laser light has to be aligned along the whole length of the 25 cm long and to $\varnothing = 5\,\mathrm{mm}$ narrowing hole through the electromagnet and its pole piece. For this, the complete optical bench is mounted on an $x, y, z + \Theta$ rotational positioner. Third, the cavity needs to be centered between the pole pieces, such that the light goes through the $\varnothing = 1\,\mathrm{mm}$ hole into the center of the cavity. Fourth, the NMR tube with a p-GaAs WE needs to be inserted, such that the light hits the $\varnothing = 0.6\,\mathrm{mm}$ hole of the capton protection. This is the trickiest part, since one cannot see anything directly but only indirectly. This is done by observing the OCP, which increases by some 10 mV, when light of some 100 μW hits the p-GaAs. To add an additional adaptation possibility, I constructed the NMR tube holder with a small tilt, such that rotation of the holder moves the NMR tube bottom with electrode system in a circle of 2mm diameter inside the cavity center to fine compensate a last mismatch between light and WE. The influence of the cavity side hole on the CW EPR result is discussed in 3.1.5.

3.1.4 Methyl Viologen Electrolyte Preparation and Characterization

Methyl viologen is in literature described as rather difficult to handle. However, I got to appreciate it a lot. The reactivity of $MV^{+\bullet}$ regarding oxygen, water and other chemicals need to be tackled, but chemical changes are indicated thanks to the $MV^{+\bullet}$ blue color. A big advantage of $MV^{+\bullet}$ is the relatively narrow redox potential window and its comproportionation reaction $MV^0 + MV^{2+} \longrightarrow 2MV^{+\bullet}$
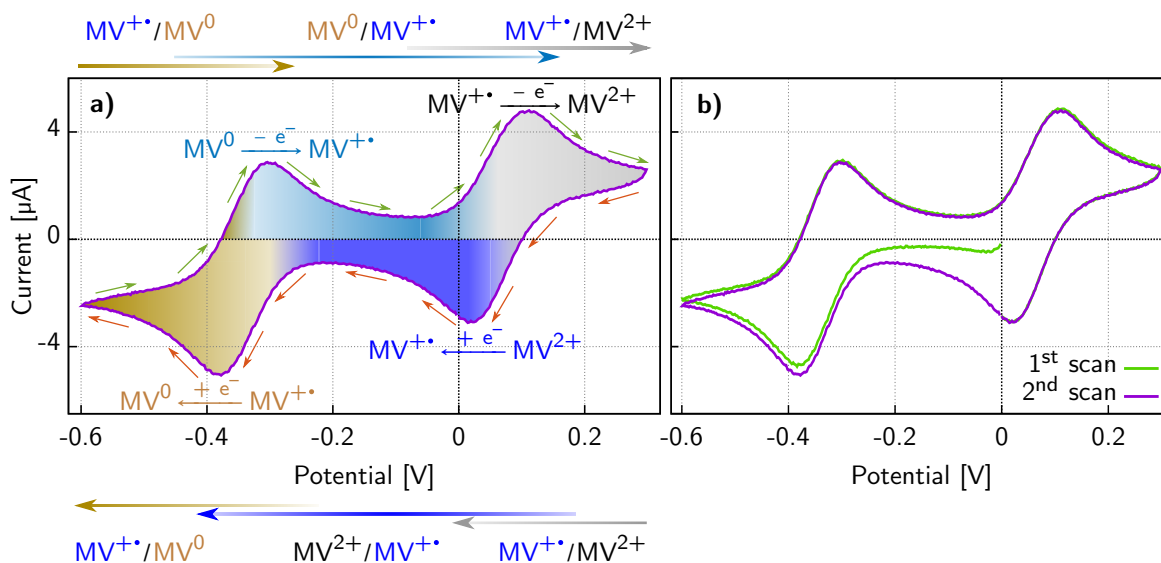
Figure 3.14 – CV of Methyl Viologen in ACN with TBAP and Au/helicene WE with $1\,mm^2$ active surface. The majority processes are indicated at their maximum with the corresponding chemical process in scanning direction. Indicated are also the direction of scanning (orange arrows for reduction and green for oxidation direction), majority process ranges (outside in normal process notion) and strength (color coded arrows and surface color gradients). Subfigure a) shows the second of two consecutive CVs, subfigure b) shows additionally the first CV. b) illustrates the strong CV dependency on the sample history.

(section 2.1.1). The comproportionation process is working in our favor by continuously shifting the concentration to more $MV^{+\bullet}$ radicals. A small potential window is necessary regarding electrolyte and electrode decomposition. A CV covering all methyl viologen redox peaks is presented in figure 3.14 a) for the example of an $MV^{+\bullet}$ saturated electrolyte recorded with a helicene WE. The $MV^{2+}/MV^{+\bullet}$, $MV^{+\bullet}/MV^0$ reduction, and $MV^0/MV^{+\bullet}$, $MV^{+\bullet}/MV^{2+}$ oxidation peaks are indicated in scanning direction, color coded according to the color of the product. The potential scanning direction is also indicated, orange for reduction direction and green for oxidation direction. As discussed in 2.1, each region is not solely governed by one single process, but is a combination of all feasible processes. For example, at the $MV^{+\bullet}/MV^0$ reduction peak, the energy is sufficient for all four redox reactions. However, the $MV^{+\bullet}/MV^0$ process dominates, resulting in a negative net current. Which of the four processes is the majority process depends on the applied potential and the scanning direction, since both together determine the accessible probability distribution (W) and the availability of the species. The majority processes and the progressive transitions from one process to another being the majority process are indicated with color gradients inside the CV and with arrows outside the plot. Figure b) illustrates the concentration dependency of CVs by comparing two consecutive scans for a $MV^{+\bullet}$ saturated electrolyte. The $MV^{2+}/MV^{+\bullet}$ reduction peak is almost not present in the first scan but very present in the subsequent scan. This is due to the $MV^{+\bullet}$ electrolyte saturation and therefore no MV^{2+} being present on the electrode surface at the beginning. However, each redox peak produces the reactants needed for the subsequent peak in the cyclic scanning direction. The $MV^{2+}/MV^{+\bullet}$ reduction peak is therefore the product of the previous full CV sweep going through the $MV^{+\bullet}/MV^{2+}$ oxidation peak and MV^{2+} not having diffused away from the WE yet. Direct CV comparison is also difficult due to this electrode history dependency.

MV has three redox species and one might therefore expect three probability distribution levels,

Figure 3.15 – Derivation for the probability distribution (W) of methyl viologen as consequence of reduction and oxidation energy level correlations, a) and b). $W_{MV^{+\bullet},Red}$ and $W_{MV^{+\bullet},Ox}$ are coupled, i.e. have the same surface area but are only accessible for different potentials.
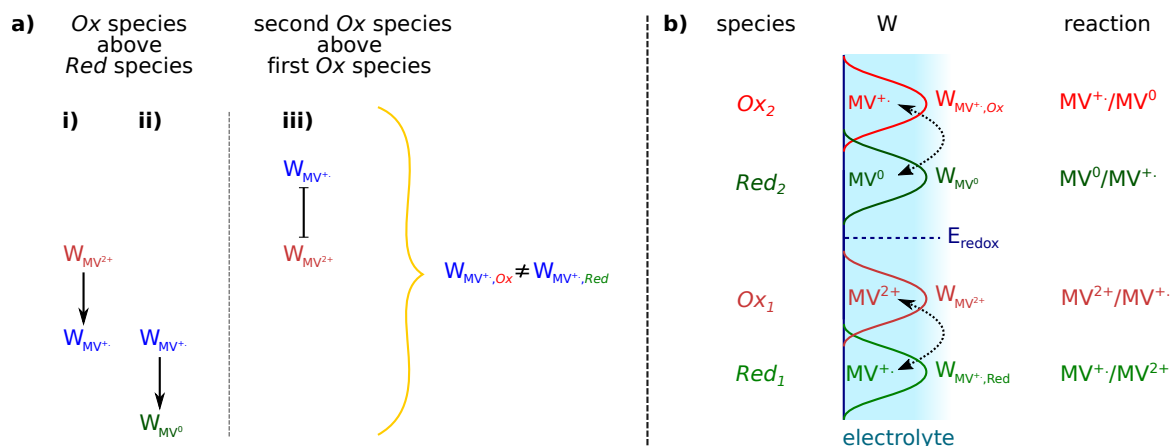
$W_{MV^{2+}}$, $W_{MV^{+\bullet}}$ and W_{MV^0}. However, as discussed in section 2.1, oxidation states are always above reduction states. This implies, that the probability distribution $W_{MV^{2+}}$ of the *Ox* species MV^{2+} has to be above the *Red* level $W_{MV^{+\bullet}}$, such as indicated in figure 3.15 a) i). Also the *Ox* species energy level $W_{MV^{+\bullet}}$ has to be above the *Red* species energy level W_{MV^0}, ii). However, the second *Ox* species energy level $W_{MV^{+\bullet}}$ has to be above the *Ox* species energy level $W_{MV^{2+}}$, otherwise $MV^{+\bullet}/MV^0$ would be reduced at less negative potentials than $MV^{2+}/MV^{+\bullet}$, iii). In other words, $W_{MV^{+\bullet}}$ has to be above and below $W_{MV^{2+}}$, which is necessary due to $MV^{+\bullet}$ being simultaneously *Red* and *Ox* species. It manifests, that the reduction and oxidation probability distribution of $MV^{+\bullet}$ can not be identical, $W_{MV^{+\bullet},Red} \neq W_{MV^{+\bullet},Ox}$. This distinction is further evident when looking at the CV in figure 3.14, where the redox peaks $MV^{+\bullet}/MV^0$ are at a much more negative potentials than those of $MV^{+\bullet}/MV^{2+}$. MV^0 on the other hand is always *Red* and MV^{2+} always *Ox* species. The general methyl viologen probability distributions therefore have to be as in figure 3.15 b). It is obvious that $W_{MV^{+\bullet},Red}$ and $W_{MV^{+\bullet},Ox}$ are coupled, i.e. same size since it is the same reduction state.

At a practical level, the biggest problem with methyl viologen is its solubility and finding the right combination of solvent and supporting electrolyte. The concentration of the supporting electrolyte should be in the 100 mM range and of $MV^{+\bullet}$ in the 1 mM range. Trying a number of solvents, I found the best combination to be with tetrabutylammonium perchlorate (TBAP, $(CH_3CH_2CH_2CH_2)_4N(ClO_4)$, *Sigma Aldrich*, purity ≥ 99.0 %) as supporting electrolyte, dissolved in acetonitrile (ACN, CH_3CN, *AcroSeal*, purity ≥ 99.9 %, extra dry over molecular sieve), which is also confirmed elsewhere.[118] TBAP dissolves well in ACN, however MV^{2+} maximum solubility is somewhere below 0.1 mM range. Literature suggests several anion exchange reactions to increase the MV^{2+} solubility, i.e. $MVCl_2$ chloride exchange to $MV(PF_6)_2$ or $MV(BF_4)_2$ discussed by Peon et al. and Grampp et al..[48,119] However, I considered two other options which avoid possible contamination: solvent combination and concentration shifting. Even though TBAP is insoluble in

[118] Y.-E. Sung, et al., "Demonstration of Electrochemical Generation of Solution-Phase Hot Electrons at Oxide-Covered Tantalum Electrodes by Direct Electrogenerated Chemiluminescence", The Journal of Physical Chemistry B **102**, 9797–9805 (1998).

[119] G. Grampp, et al., "ESR and ENDOR investigations of the degenerate electron exchange reactions of various viologens in solution. Solvent dynamical effects", Applied Magnetic Resonance **30**, 145–164 (2006).
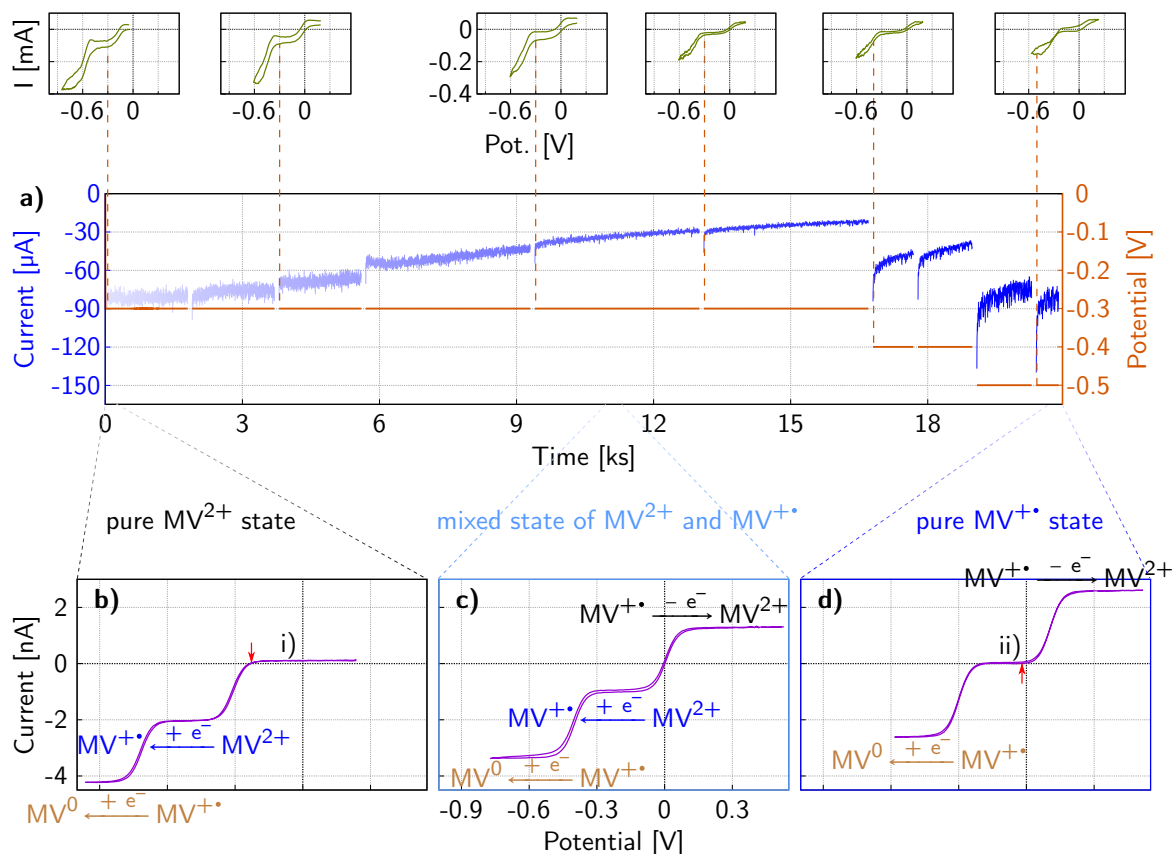
Figure 3.16 – Chronoamperometric and CV measurements for the electrolytic production of $2\,\text{mM}$ $MV^{+\bullet}$ electrolyte with $200\,\text{mM}$ TBAP dissolved in ACN. Start point is a MV^{2+} saturated solution with additional undissolved methyl viologen dichloride as powder dispersion. Subfigure a) shows the current for the chronoamperometric $MV^{+\bullet}$ electrolyte production in blue and the applied potential in orange over time in kiloseconds. The blue color gradient indicates the increasing $MV^{+\bullet}$ concentration. A selection of checkpoint CVs are plotted above a) with corresponding subsequent potential adjustment indicated as orange dashed line. Subfigures b) till d) show CVs recorded with UMEs at the start, middle and end of the process. The potential and current axis of b) till d) are kept constant throughout the plots to emphasize the CV shift horizontal and vertical direction. The underlying raw data set to this specific plot was recorded by Dr. Mika Antero Tamski with a *Gamry Interface1000E* potentiostat. Radical production was performed with large Pt coils as WE and CE and a Pt tip as RE. b), c), d) were recorded with Pt $10\,\mu\text{m}$ Basi UME CE and WE versus Pt at $20\,\text{mV/s}$.

methanol, adding $10\,\%$ of methanol increases the solubility of MV^{2+} by factor 100. Concentration shifting is done by electrolytic production of $MV^{+\bullet}$ in a MV^{2+} saturated solution with additional undissolved methyl viologen dichloride as a powder dispersion stirred and heated to $70\,^\circ\text{C}$ (ACN boiling point is $\approx 81\,^\circ\text{C}$). Applying a potential negative enough to reduce MV^{2+} to $MV^{+\bullet}$ decreases the MV^{2+} concentration and more methyl viologen dichloride can dissolve as MV^{2+}. This method has a limit in the $2\,\text{mM}$ range, however without the disadvantage of a second solvent, which I used henceforth.

Figure 3.16 shows a selection of measurements performed for electrically produced $MV^{+\bullet}$ using the above-described solution/dispersion combination. Subfigure a) shows the chronoamperometric measurement, i.e. current development over time, in blue for the time of the $MV^{+\bullet}$ electrolyte production, time in kiloseconds. The corresponding applied potential is plotted in orange, right
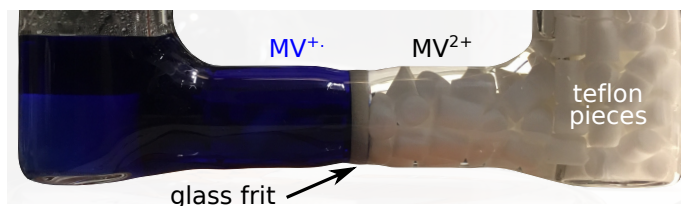
Figure 3.17 – $MV^{+\bullet}$ production using electroreduction. WE and CE are separated by a glass frit. The CE chamber is filled with teflon pieces to avoid large amounts of electrolyte waste.

y-axis. The chronoamperometric measurement was interrupted several times, visible as line breaks in a). At each of the breaks a CV scan was performed to check the electrolyte composition. A selection of these CVs are plotted in green above a). The orange dashed lines indicate not only the time stamp for the recorded CV, but also the position of afterwards applied potential within the CV, i.e. in what redox range the potential lies. Axis scales are the same for all CV inlets. The experiment was conducted with Dr. Mika Tamski. While the electroreduction process, the species concentrations are changed and subsequently the CV shifts. However, we want to stay on the $MV^{2+}/MV^{+\bullet}$ plateau and avoid shifting below nor into the range of $MV^{+\bullet}/MV^0$. At approximately 17 ks the applied potential had to be adapted. The potential increase at 19 s is the last step, when the radical concentration increase started to stagnate. At this point, the potential was adjusted to the $MV^{+\bullet}/MV^0$ plateau with the goal to use the comproportionation reaction $MV^0 + MV^{2+} \longrightarrow 2MV^{+\bullet}$ to push the $MV^{+\bullet}$ concentration one last bit. To ensure control over the products, WE and CE were separated by an ion bridge in this experiment. Figure 3.17 shows a photo of the electroreduction cell. The resulting electrolyte at the WE was dark blue while the electrolyte in the CE chamber stayed clear (pure MV^{2+}). The strong noise visible in the chronoamperometric measurement and the green CV inlets is due to the continuously running magnetic stirrer applied for acceleration of the overall reduction process.

The initial, intermediate and final state of the electrolyte were controlled with ultramicroelectrode (UME) scans, presented in b) and d) with indicated timestamp via dashed lines. The majority redox processes taking place at each plateau are indicated. As discussed in section 2.1, UMEs have the huge advantage of minimizing diffusion limitation, which is the reason for the absence of redox peaks but the presence of plateaus. The original electrolyte only contained MV^{2+}, b). Almost no $MV^{+\bullet}/MV^{2+}$ oxidation current is therefore possible at the corresponding plateau i). For this constellation of highly conducting UME and almost only MV^{2+} in the electrolyte, the point of crossing zero current, indicated with red arrow, coincides with E_{redox} which is located approximately at the center of $W_{MV^{2+}}$ (no $W_{MV^{+\bullet}}$ nor W_{MV^0}, compare figure 2.6).

Subfigure c) shows the UME result for a 50 % mixed state of MV^{2+} and $MV^{+\bullet}$, obtained by mixing the final version of pure $MV^{+\bullet}$ electrolyte and original pure MV^{2+} electrolyte in a 1:1 (v/v) ratio. All four processes are present in this case. The CV is shifted in potential and current, which is mostly due to reduced $W_{MV^{2+}}$ and increased $W_{MV^{+\bullet}}$. Interestingly, the CV shift is to more positive potentials, i.e. E_{redox} shifts up. This is due to $W_{MV^{+\bullet},Red}$ and $W_{MV^{+\bullet},Ox}$ being coupled, since it is the same molecule state. Therefore, $W_{MV^{+\bullet},Red}$ and $W_{MV^{+\bullet},Ox}$ are generated simultaneously, which shifts E_{redox} to the center between them, i.e. above $W_{MV^{2+}}$ in figure 3.15 b).

At the point when all MV^{2+} is reduced to $MV^{+\bullet}$, the current at the corresponding reduction po-

tential drops to zero, as shown in figure 3.16 d). However, alone, plot d) is no proof for a pure $MV^{+\bullet}$ concentration. In fact, it only says that at the center plateau ii) the net current is zero, i.e. $MV^{2+}/MV^{+\bullet}$ reduction happens at the same rate as the $MV^0/MV^{+\bullet}$ oxidation process. However, the combination of graphs a) to d) allows to make the statement of almost pure $MV^{+\bullet}$ concentration. This shows that the procedure as described is perfectly suited to achieve a methyl viologen electrolyte containing almost only $MV^{+\bullet}$, even though at the very end a potential strong enough to reduce $MV^{+\bullet}$ to MV^0 is applied.[3] We can assume at this point that E_{redox} is shifted to the center, the position it has in figure 3.15 b). E_{redox} corresponds to the point of the plateau indicated with a red arrow.

Based on the information collected with Pt UME and helicene/Au electrodes, we can understand also the possible charge transfer processes at GaAs. Figure 3.18 displays the CV of above described p-GaAs sample. Four curves are presented correspondingly to increasing light power. Indicated are the scanning directions and the majority processes in scanning direction. The light arriving behind the magnetic pole piece hole was $300\,\mu W$ for the strongest line. However, the light arriving actually on the p-GaAs is less due to the passing of the $\varnothing 1\,mm$ cavity hole and subsequent $\approx 2\,mm$ thick electrolyte layer covering the WE. The indicated power values are therefore deduced from a calibration procedure, namely $\approx 100\mu W$. A good method for the detection of actual power arriving at the p-GaAs is still pending. It is clearly visible, that the $MV^{+\bullet}/MV^0$ reduction and $MV^0/MV^{+\bullet}$ oxidation peaks are only appearing for increased light power, representing the expected photo cathodic behavior. On the other hand, the $MV^{2+}/MV^{+\bullet}$ reduction and $MV^{+\bullet}/MV^{2+}$ oxidation peaks are also clearly present without light, indicating that these processes occur readily in the dark and that light excitation makes minor changes only (compare figure 2.12). This is surprising, since the $MV^{2+}/MV^{+\bullet}$ reduction peak shows negative current. To fully explain this, the correct combination of p-GaAs band structure and redox species energy level distributions have to be found.

To do so, the following rules have been applied and are visible in the schematics around the CV in figure 3.18. An applied potential shifts E_F and therefore bends conduction and valence bands. Holes (green) can only travel up and electrons (red) only down the bending bands. This is important because the band bending may imply that charge carriers are forced away from the interface. However, inter semiconductor band to molecule tunneling in the fashion of figure 2.13 or vice versa is possible. This possibility is indicated as horizontal arrows. The following oxidation processes can take place:

- electrons from a *Red* species (green) transfer to the conduction band (red),
- holes from the valence band (green) recombine with electrons from a *Red* species (green).

The following reduction processes can take place:

- electrons from the conduction band (red) transfer to an *Ox* species (red),
- *Ox* species (red) capture electrons from the valence band (green), thus creating a hole.

Therefore, conduction and valence band can in principle both oxidize and reduce. The system

---

[3] A corresponding double check using charge calculation results in a produced charge much larger than the available MV molecules, and is therefore not suited as concentration control.
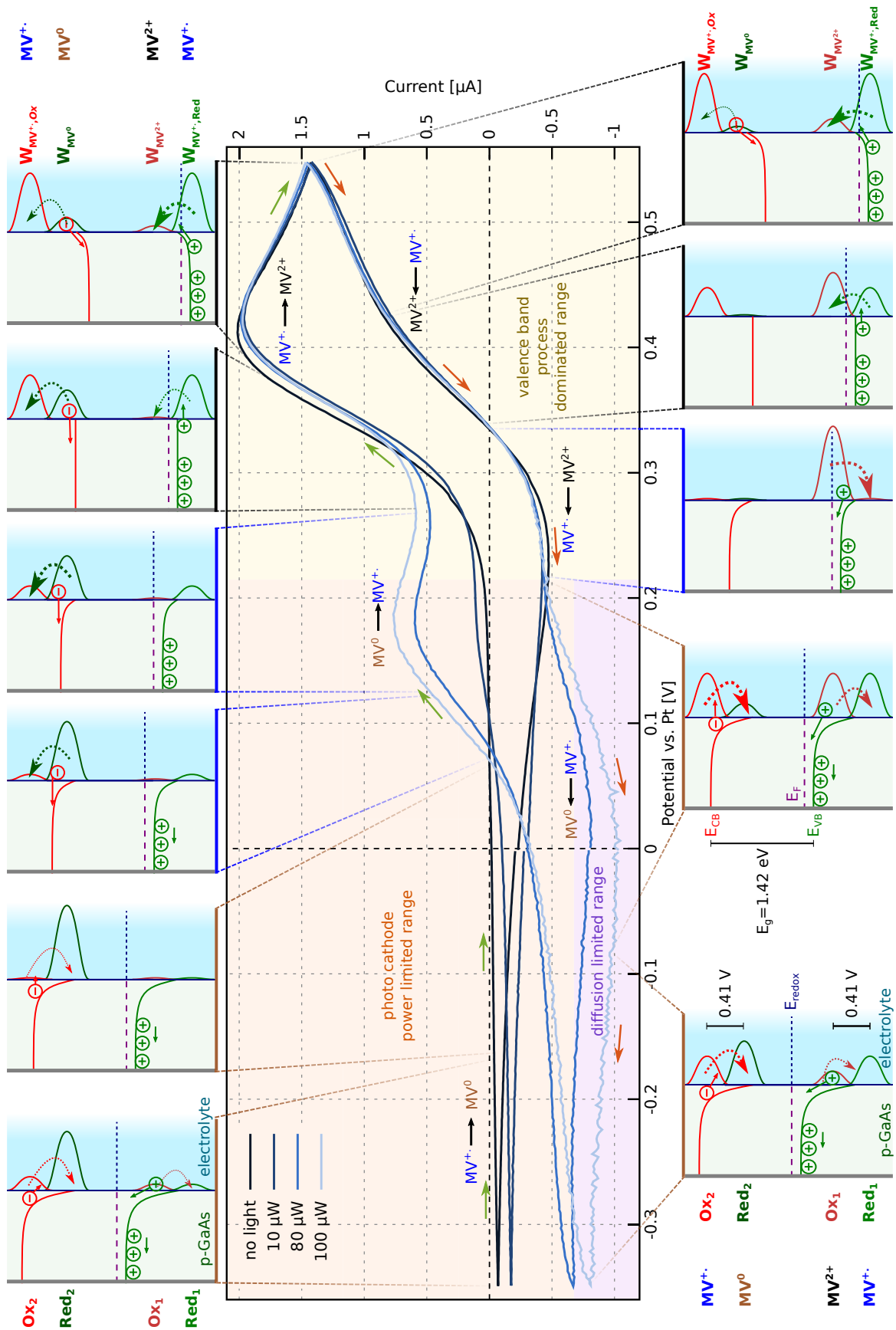
Figure 3.18 – Light dependent CV composition for p-GaAs and graphic interpretation.

is strongly diffusion limited, i.e. reduction or oxidation of a species leads fast to the exhaustion of the reactant and an accumulation of the product in the electrode's vicinity. Correspondingly, this leads to a shrinking $W_{reactant}$ and growing $W_{product}$ in the vicinity of the electrode. E_{redox} is defined by the electrolyte bulk concentration and is therefore not changing. The depletion of one species can lead to a vanishing contribution to the current of a certain reactant. The density distributions are generated with the corresponding species, i.e. they are directly proportional to the specie's concentration. $W_{MV^{+\bullet},Red}$ and $W_{MV^{+\bullet},Ox}$ correspond to the same molecule state and only indicate its two energy barriers. $W_{MV^{+\bullet},Red}$ and $W_{MV^{+\bullet},Ox}$ are therefore coupled and are generated identically. Green dashed arrows indicate oxidation transfer, i.e. positive currents in form of electron conduction to the electrode or electron hole recombination at the interface. Red dashed arrows indicate reduction transfer, i.e. negative current in form of electron conduction from the electrode or hole generation by electron trapping. Dashed arrow thickness indicates the corresponding transfer rate and therefore current strength. The plateau separation in figure 3.16 regarding the points of steepest slope for two consecutive plateaus is approximately $410\,mV$. The maximum of $W_{MV^{+\bullet},Ox}$ therefore has to be at a distance of $410\,mV$ from the maximum of W_{MV^0}, and correspondingly $W_{MV^{+\bullet},Red}$ $410\,mV$ from the maximum of $W_{MV^{2+}}$. Additionally the band gap of p-GaAs of $E_g = 1.42\,eV$ has to be taken into account.

I propose the following transfer processes that provide a consistent picture of the CV, UME voltammograms and light-dependent CVs. Key is the pinning of E_{VB} between $W_{MV^{+\bullet},Red}$ and $W_{MV^{2+}}$, assumption without which the specific positive and negative anode range behavior would not be possible. The resulting band moving when the potential is applied and the redox level distributions as shown in figure 3.18 can explain the CV at every point. In particular, the critical points of the CV are thereby explained. However, the specific pinning could also be compensated by surface states. A modified picture would consist in taking into account surface states near the valence band.

The important message of this graphical derivation is that the $MV^{2+}/MV^{+\bullet}$ reduction and $MV^{+\bullet}/MV^{2+}$ oxidation peaks have to be based on processes involving the valence band. Oxidation of $MV^{+\bullet}/MV^{2+}$ therefore has to be an interfacial electron hole recombination process. This model applies only for the case of an electrolyte saturated with $MV^{+\bullet}$ such as the one I have prepared for which I report EDMR results in the next chapter. In the case of a solution saturated with MV^{2+}, the redox potential is situated further down which means that also the pinning is further down. This change is in fact so strong, that all redox peaks of a MV^{2+} saturated electrolyte are accessed by the photo cathodic range, no redox peaks are visible without light. This has important consequences as discussed in section 2.3, a resistance change at resonance for the $MV^{+\bullet}/MV^{2+}$ oxidation can only be observed for a spin dependent electron hole recombination. For a MV^{2+} saturated electrolyte this is therefore not possible in a direct manner. However, it would be possible by way of in combination with specific surface states as intermediates. It is therefore advantageous to use an $MV^{+\bullet}$ saturated electrolyte, since direct spin dependent valence band recombination is possible. On the other hand, if a spin effect is observed for a MV^{2+} saturated electrolyte, this would be a hint that surface states are involved.

For the execution of experiments using p-GaAs, we need to analyze and understand also the photo cathodic potential range. Figure 3.18 displays clearly the $MV^{+\bullet}/MV^0$ reduction peak increase with increasing light power. In fact, for low powers the whole left region increases simultaneously

and only for stronger powers, a peak emerges. The light power at which the peak emerges is the point of reactant exhaustion onset, i.e. the current is no longer photo excited electron limited but diffusion limited. As discussed, this should be avoided in view of spin relaxation issues. For the sample used to collect the data of figure 3.18, this corresponds to a power just below $80\,\mu W$. Staying below this range is also helpful with respect to noise issues. As seen for the CV taken at $100\,\mu W$, noise is noticeably greater. The source of this noise is unclear, however not important for us.

The characterization of saturated $MV^{+\bullet}$ electrolyte for all Al5 samples follows the discussion of helicene electrodes on figure 3.14 and does not show any significant deviation. It is discussed in section 4 when the EDMR data are presented. These Al5 electrodes present superior stability compared to our bare p-GaAs electrodes.

3.1.5 CW EPR Setup Characterization and Saturation Considerations

The heart of the home built EPR system consists of a *Varian V-4531* microwave cavity situated in the center of a C-shape *LakeShore* water cooled electromagnet with flat magnetic poles driven by a *Bouhnik* $\pm 63\,A$ power supply. A continuous microwave signal produced by an *Agilent Technologies* analog signal generator (*E8257D PSG*) is fed via flexible coax cables with SMA connectors (*Mini-Circuits CBL-3FT-SMSM*+l)[4] through a circulator (*Narda 4925*) and a *Narda* adapter (4601) into the cavity system. The back reflected signal is transformed into a DC signal using a zero bias Schottky detector (*Narda 4503A*) and fed into a lock-in detector, *Zurich Instruments HF2Li* or *Signal Recovery 7225 DSP*, depending on the experiment. The necessary modulation for standard CW EPR is achieved by modulating the magnetic field with two modulation coils mounted at the cavity's sides (part of the *Varian V-4531* cavity module). The modulation signal and TTL reference is driven by a *Tektronix* function generator (ARG 3011). Magnetic field modulation is for all experiments within this thesis performed at a frequency of $1.111\,kHz$ with sinusoidal modulation of peak to
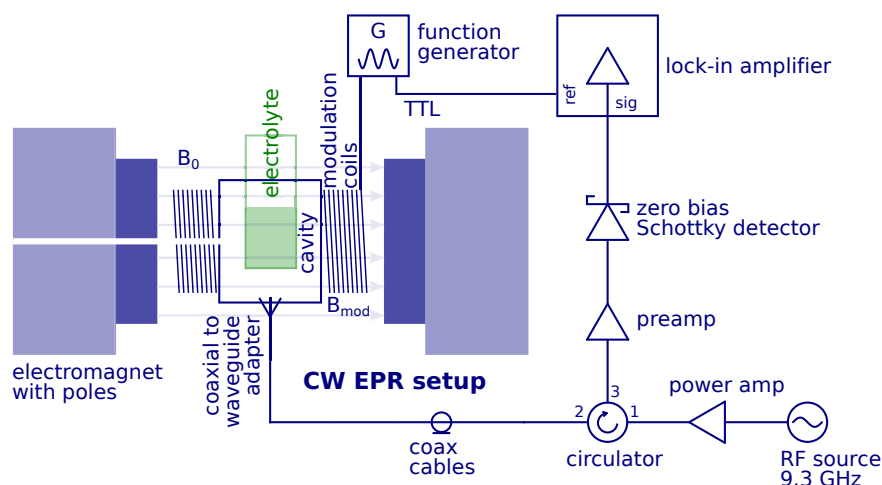

Figure 3.19 – The CW EPR setup is a typical $9.3\,GHz$ cavity system with impedance change induced microwave back-reflectance detection by means of magnetic field modulation based lock-in technique. The magnetic field can be swept from $-850\,mT$ to $850\,mT$.

---

[4] These show less damping than semi rigid coax cables.
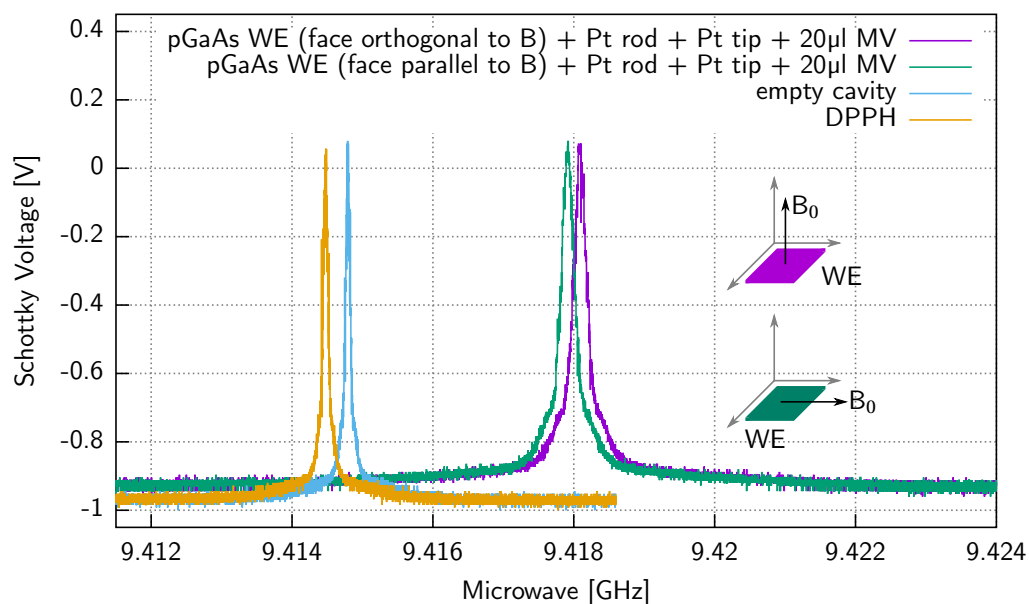
Figure 3.20 – Cavity resonances for different samples, recorded with 12 dBm and preamp. The samples including electrodes and electrolyte strongly disturb the cavity. Part-goal of the sample-production is to minimize this influence, i.e. large Q and small microwave distortion.

peak amplitude $B_{mod,ptp} = 0.52$ mT. This is a sweet spot of this coil set, higher frequencies led to a modulation amplitude decrease and as a consequence, the signal diminishes. Depending on the experiment, a low noise preamp (*Narda-MITEQ AFS5-08001200-10-10P-5*, 32 dB gain but limited to 13 dBm input) or a power amplifier (*Mini circuits ZVE-3W-183+*, 35 dB gain) was used. The calibration for the power amplifier is documented under A.1.1 and correspondingly corrected for every experiment, so that power reported is the actual power arriving at the cavity. In the following, it will become obvious that the setup is far from being a high sensitivity, high resolution, low noise system. However, systems fulfilling these three criteria are usually incapable of measuring comparably large volumes of lossy samples including a three electrode system. In fact, the *Varian V-4531* cavity was the only cavity tested which was capable of coping with the demands necessary to cope with our electrochemical cells.

As discussed in section 2.2.1, the EPR spectrometer sensitivity is directly proportional to the quality factor (Q). The *Varian V-4531* cavity system has a TE 102 mode and a Q between 3400 and 4000 for reasonable samples. Q is dependent on the whole sample-cavity system and is calculated by $Q = \nu_{res}/\Delta\nu$ (equation 2.22, see figure 2.18 for the determination of $\Delta\nu$). For the determination of Q, figure 3.20 shows cavity MW reflection spectra in a 12 MHz window around cavity resonance for a p-GaAs sample used in this thesis and for comparison an empty cavity and a small powder sample, DPPH in a 5 mm NMR tube. Most importantly, the peak-shape is changed for the rather bulky p-GaAs sample. The peak center widening reflects a decrease of Q. However, especially important here is the cavity resonance peak top widening, which is in fact stronger than at the center. This top widening has a huge effect on the sensitivity but is not reflected by *Q*. For a p-GaAs sample orientation with its surface parallel and perpendicular to B_0, *Q* is not changed but the frequency is shifted due to the changed matching and tuning settings of the iris.

Table 3.1 – Quality factors of different samples. For comparison Q of the empty cavity, a DPPH powder sample, 2 mM MV$^{+\bullet}$ solution and an early generation electrochemical cell. The most right two entries are of the newest generation electrochemical p-GaAs sample with the p-GaAs WE parallel to, and facing the external magnetic field. All results recorded are with the hole in the cavity side.

empty cavity	10 mg DPPH	0.25 ml MV$^{+\bullet}$	1st gen. cell	p-GaAs ∥ B	p-GaAs ⊥ B
3692	3677	2060	614	1361	1376

The two major components changing Q of our samples are the polar electrolyte (acetonitrile's polarity index is 5.8) and the electrodes. A comparison of Q values for several samples, including the ones of figure 3.20, is given in table 3.1 (12 dBm, no amplifier). Comparing empty and DPPH, small non-polar media don't change Q by much in general. However, a rather large amount of 250 µl of the polar MV$^{+\bullet}$ electrolyte decreases Q already by almost a factor of two. Electrodes decrease Q further, such that the first generations of built cells[5] had a *Q* six times smaller than non-lossy samples, e.g. DPPH powder. The general conclusion is, that minimizing the amount of polar electrolyte is the most important factor. However, the system is not able to detect small volumes of the 2 mM MV$^{+\bullet}$ electrolyte and also full electrode coverage has to be achieved, i.e. approximately 100 µl are needed with the most recent cells. I usually manage to achieve a just visible EPR signal in combination with a quality factor between 1300 and 2000 (depending on WE size and composition) by minimizing the electrode size, amount of used glue at the electrodes and electrolyte, which is relatively independent of the sample orientation inside the cavity. Also, as discussed in section 3.1.3, a $\varnothing = 1$ mm hole through the cavity side for optical excitation does not influence Q too much, see table 3.1, since the *Q* of an empty cell and DPPH is well between the above mentioned 3400 and 4000 for reasonable samples of the original cavity without a hole in its side.

Regarding the MV$^{+\bullet}$ saturated electrolyte, EPR resonance is barely visible for a single EPR scan at a power below 15 dBm and without pre-amplifier for a typical sample volume of 100 µl containing an electrode system. However, averaging usually reveals the resonance signal. Figure 3.21 shows the CW EPR spectrum of 200 µl sample of 2 mM MV$^{+\bullet}$ recorded with the home-built system at 12 dBm with preamp, a), and without preamp but average of 100, b). However, the preamp is limited to powers below 12 dBm, which is the case for all EDMR experiments below. The summation can introduce a broadening of the resonance peak, which has to be carefully monitored. For many of the experiments below, such a summation was performed and indication of the numbers of summed EPR spectra is given. If this is the case, for the whole experiment the peak positions were monitored and the experiment interrupted as soon as a peak shift occurred. In any case, this averaging does not change the quantitative results.

The absence of the MV$^{+\bullet}$ hyperfine lines is not due to averaging but inhomogeneity broadening, such as discussed in section 3.1.5. The B_0 inhomogeneity due to the distance between the flat magnetic poles which is imposed by the cavity width, i.e. 45 mm, in combination with samples covering a certain inhomogeneity range results in different sample regions reaching resonance at different currents applied to the electromagnet. For comparison the spectrum of a 10 µl 2 mM MV$^{+\bullet}$ sample recorded with a benchtop *Magnettech MS400* at 10 dBm and 0.005 mT modulation

---

[5] Several millimeter large p-GaAs piece with much glue, a coiled Pt-mesh as CE and large volume of MV$^{+\bullet}$ electrolyte.

a) 200 µl 2 mM MV$^{+\bullet}$ with preamp, avg. of 10

b) 200 µl 2 mM MV$^{+\bullet}$, no preamp, avg. of 100

c) 10 µl 2 mM MV$^{+\bullet}$ with *MS400*, avg. of 10
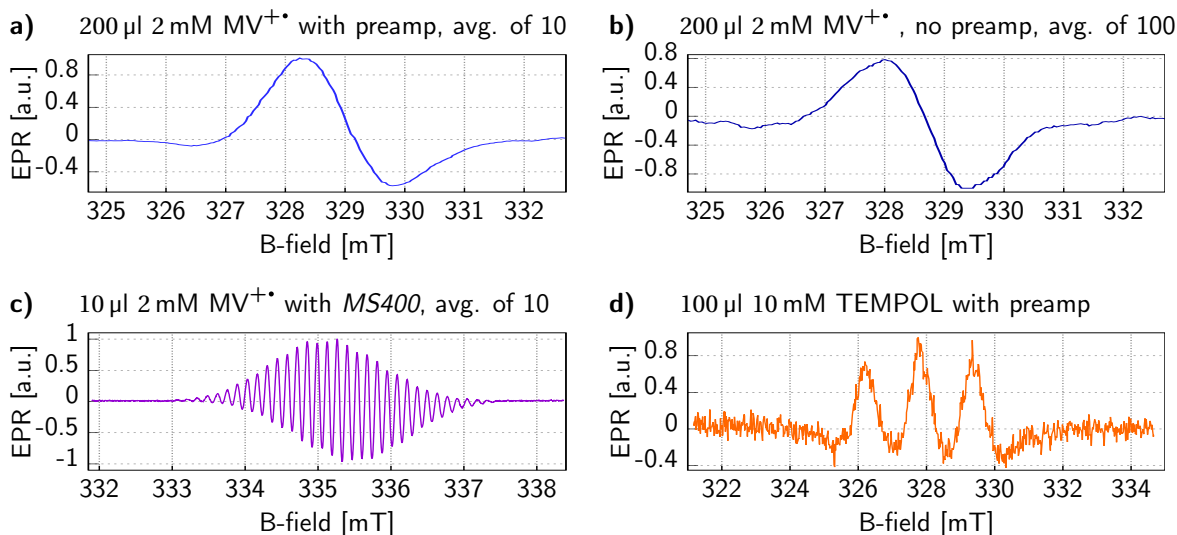
d) 100 µl 10 mM TEMPOL with preamp

Figure 3.21 – EPR spectra comparison for the home-built CW EPR system and a benchtop *Magnettech MS400*. Hyperfine resolution of MV$^{+\bullet}$ is not possible with the home-built setup. The magnetic field homogeneity is however sufficient for TEMPOL hyperfine splitting resolution.

is presented in c). However, also here by far not all hyperfine splittings are resolved.[111,119,120] The best resolution of the home-built setup in combination with a sample inside a 5 mm tube is just enough for resolving TEMPOL hyperfine splitting (4-hydroxy-2,2,6,6-tetramethylpiperidine 1-oxyl, 100 µl 10 mM TEMPOL dissolved in milli-Q water), d). The absence of hyperfine resolution regarding MV$^{+\bullet}$ with the home-built setup is however not important for us, since we only rely on the general resonance effect, i.e. population disturbance. The resonance field, MW frequency and resulting g-values of the home-built system (9.231 GHZ, 329(7) mT, g=2.004(1)) and the MS400 (9.399 GHZ, 335.35(5) mT, g=2.0025(5)) correspond good enough with literature g-value of 2.003.[52,121]

A critical point regarding the general outcome of any experiment using EPR is the matching and tuning described in section 2.2.1. The matching and tuning has a direct outcome on the EPR spectrum signal to noise ratio (SNR). Figure 3.22 was recorded by matching and tuning only to a certain value below 0 V reflectance (compare figure 3.20). This was done by mistuning the MW frequency, while keeping the impedance matching unchanged. An MW shift responsible for an offset of 100 mV changes the SNR from approximately 5 to 50. An offset of 100 mV occurs easily due to e.g. temperature change. In fact, a temperature drift by 7 °C is capable to shift the offset to 500 mV. The SNR change is not due to decreased noise, but due to increased EPR signal strength. It is therefore crucial to keep the temperature stable.

For quantitative EPR experiments it is important to stay far off MW power saturation, i.e. to stay in a power range where the EPR signal increases linearly with B_1, compare to section 2.2.1.[64] We however depend on a resonant spin population change as large as possible to reach strong current changes and are not too much concerned about signal conservation and resolution, see in 2.3

[120] W. Dunham, et al., "Application of fast Fourier transforms to EPR spectra of free radicals in solution", Journal of Magnetic Resonance (1969) **40**, 351–359 (1980).

[121] N. Leblanc, et al., "Unprecedented stacking of MV^{2+} dications and MV$^{+\bullet}$ radical cations in the mixed-valence viologen salt (MV)$_2$(BF$_4$)$_3$(MV=methylviologen) · ", Chemical communications (Cambridge, England) **49**, 10272–4 (2013).
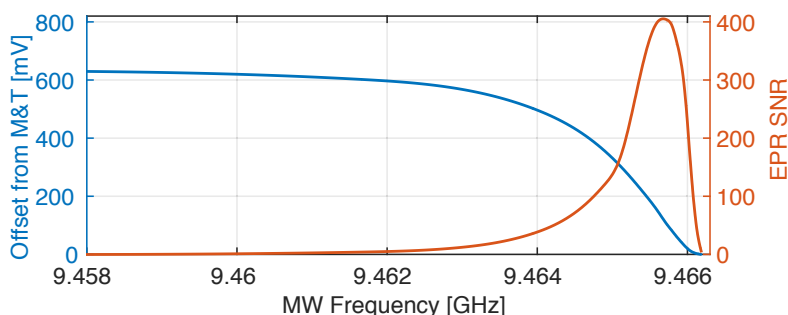
Figure 3.22 – EPR SNR of DPPH for varying matching and tuning (M&T) offset, recorded at 10 dBm. The M&T offset is achieved by reducing the applied MW frequency away from the point of minimal MW reflection from the cavity. The SNR increases massively around this supposedly optimal M&T when varying the frequency by values as small as 0.01 %. This effect can also be produced by varying temperature, i.e. slight changes of cavity, waveguide and sample dimensions or absorbance behavior. SNR is here defined as X lock-in peak to peak height squared divided by the squared noise height in voltage.

the discussion for equation 2.31. For the power saturation evaluation, a list of full EPR scans at increasing MW powers is recorded. The plot of the corresponding signal strengths over the square root of MW power is called saturation curve. I plotted the square root because of equation 2.23 and 2.24. Typically, the second integral of the lock-in signal, i.e. first integral of the absorption peak, is used as signal strength, which is proportional to the absorbed energy within one scan through resonance. However, for samples where *"the peak-to-peak line width is invariant, comparison of peak-to-peak amplitude is a convenient method of quantitating signals."* ([64] p. 44). See figure 3.23 for the *peak-to-peak* signal height and width definition. Within the whole power range used, I found no significant peak to peak broadening within our B_0 resolution, not with the home-built nor with the MS400 EPR spectrometer. Finally, I found the peak-to-peak amplitude evaluation to be much less noisy compared to the second integral, well visible in figure 3.24, a 200 µl sample of 100 mM TEMPONE (4-oxo-TEMPO; *Sigma Aldrich* ≥ 98 %) dissolved in the non-polar solvent toluene (monomethyl benzene, *AnalaR NORMAPUR*, ≥ 99.5 %), i.e. no power absorption loss. This is even the case for experiments with the benchtop MS400.

Depending on the source, saturation is defined as either half the power at which the maximum signal is reached, or as the point where the slope departs from linear behavior. In our case, the second definition is better suited, since we want to push the amount of spin flips. Figure 3.26 shows a selection of recorded saturation curves, b) till g). Subfigure a) is a collection of the three typically occurring saturation types, i.e. no power saturation due to short relaxation times T_1, inhomogeneous saturation with leveling, and homogeneous saturation with signal decrease due to line broadening, see equation 2.21, $\Delta B_{ptp} = \frac{4}{3\gamma^2 T_2^2}(1 + \gamma^2 B_1^2 T_1 T_2)$.
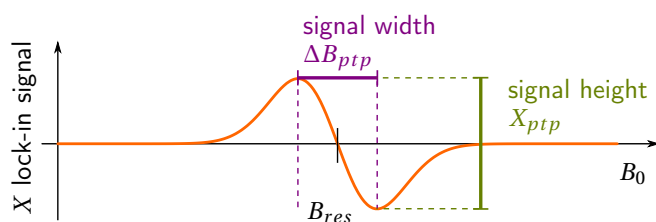
Figure 3.23 – Definition of peak-to-peak height X_{ptp} and width ΔB_{ptp} of the lock-in EPR signal.
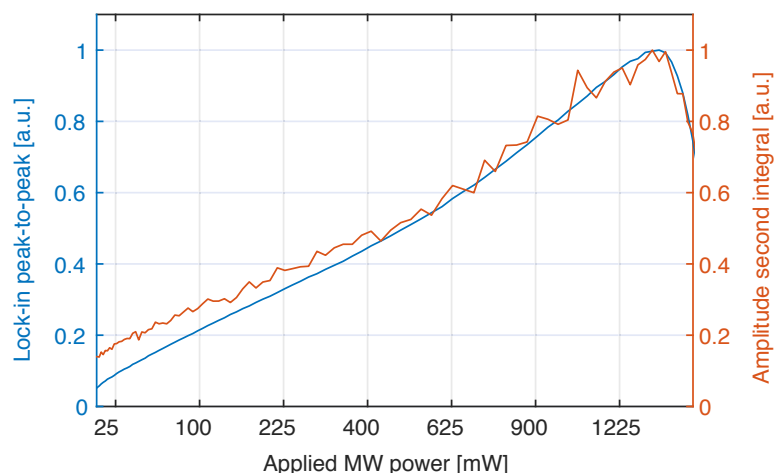
Figure 3.24 – Peak-to-peak amplitude of lock-in signal (blue, left y-axis) in comparison to the second integral amplitude (red, right y-axis) for power saturation. Data points are connected to emphasize noise.

Subfigure 3.26 b) is recorded as reference and displays the saturation of 2 mM MV$^{+\bullet}$ in ACN sample with 200 mM TBAP recorded with the bench-top EPR spectrometer Magnettech MS400, a well defined saturation curve with linear (to the square root of MW power) behavior up to 20 mW and subsequent homogeneous signal amplitude decrease. The linear range is emphasized with a red dashed fitting line. This type of measurement with the MS400 is for lossy samples only possible by confining the sample using capillaries. Otherwise matching and tuning is not possible. However, the same sample recorded with the home-built setup does not show any EPR signal at all for any power nor with a pre-amp and even for summations of more than 100 experiments. However, if we use the same amount of the same solution in a standard 5 mm NMR tube, we get a signal which linearly increases without reaching saturation, c). The extreme noise in c) despite an average of 140 scans illustrates the low SNR with small 2 mM MV$^{+\bullet}$ samples. I found a minimum sample volume of 50 µl to 100 µl necessary for quantifiable EPR results.

Subfigures d) and e) show saturation curves for a round 5 mm NMR tube filled with 100 µl of a 2 mM MV$^{+\bullet}$ and a p-GaAs WE, for an orientation of WE surface parallel to B_0 or perpendicular to B_0. The sample saturation is strongly orientation dependent. For a WE orientation parallel to B_0, ∥ (d)), saturation is reached already around 400 mW compared to 900 mW for an orientation of the WE perpendicular to B_0, ⊥ (e)). This can be explained by comparison with the cavity mode as displayed in figure 3.25. The B_1 inhomogeneity in the cavity center is larger in the direction
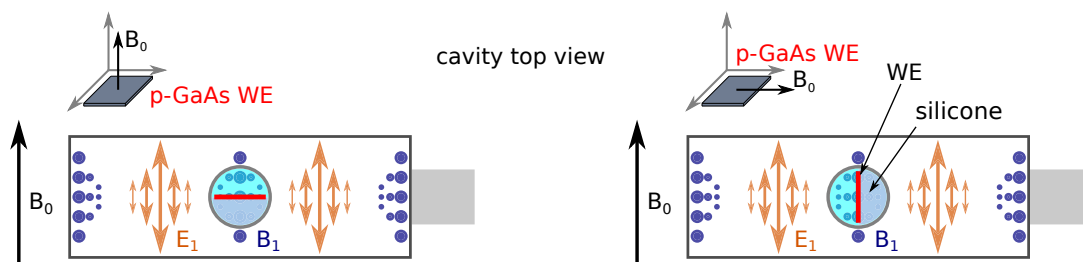
Figure 3.25 – Advanced from figure 2.19, TE$_{102}$ cavity mode with electrolyte (turquoise) and p-GaAs WE (red) inside. The experienced overall power is orientation dependent.
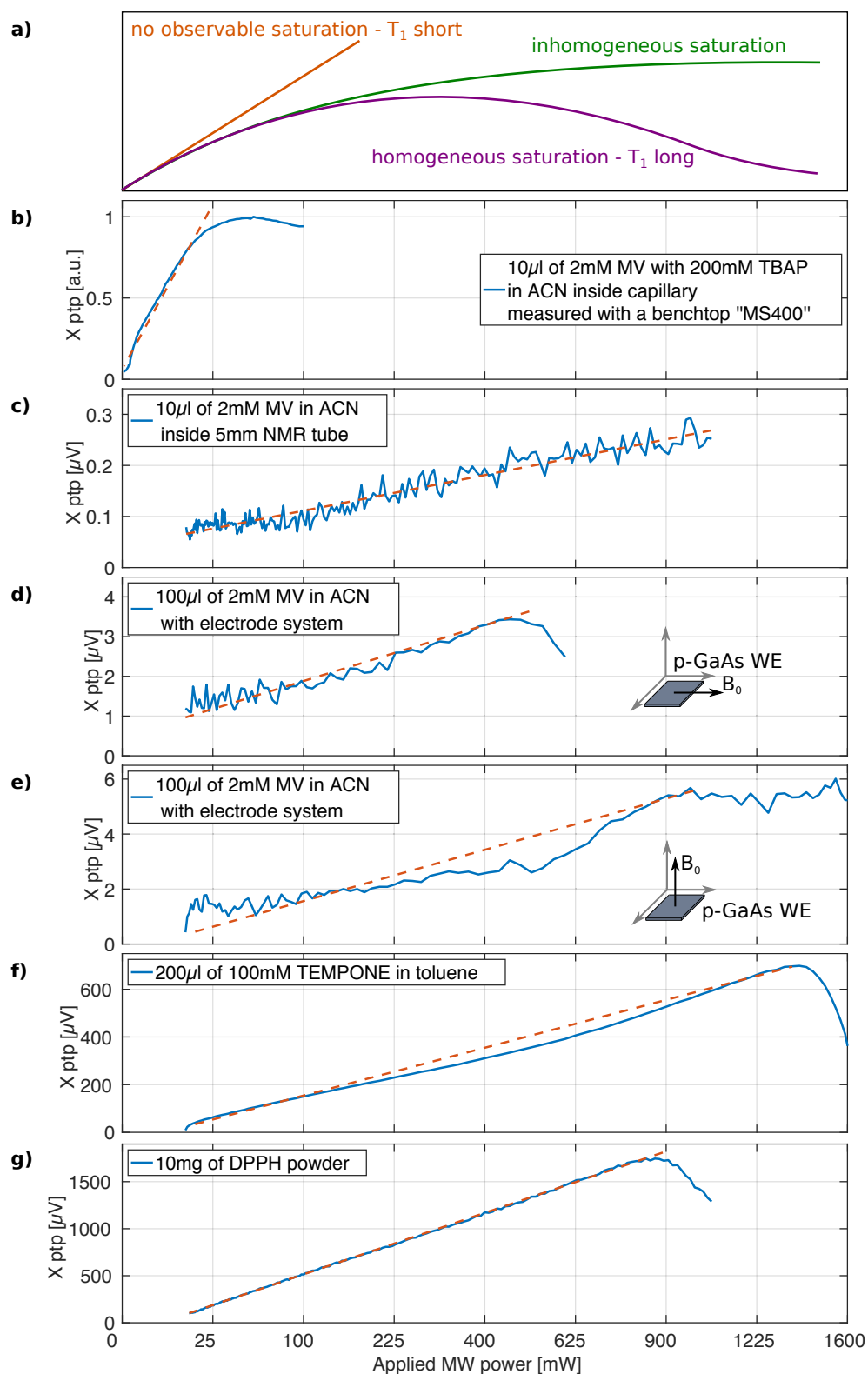
Figure 3.26 – Comparison of MW power saturation curves for different samples. The x axis is scaled as square root but true values indicated. Note also the different y-axis scalings. b) is recorded with the MS400, whil c) till g) are recorded with the home-built EPR set-up. The dashed red lines are linear fits indicating the range of linear behavior. The presented results are raw, no filtering whatsoever was used, to elucidate noise problems. However, averaging was performed, at differing amount, b) no average, c) of 140 scans, d) till g) of 10 scans. Matching and tuning was done at the highest power applied.

orthogonal to B_0 than parallel with B_0. Due to the cell construction, electrolyte is situated mostly in front of the WE and not behind it. In orthogonal orientation the electrolyte therefore covers a larger range of inhomogeneity in comparison to parallel orientation. This results in different spatial regions reaching saturation at different powers. Radicals further away from the cavity center reach saturation only at larger power. Additionally, in the ⊥ configuration the WE sides reach more into the E_1 field and therefore absorb more energy, i.e. heating. It is therefore more MW power necessary to reach the same B_1 for the ⊥ configuration compared to the ∥ configuration. The second difference between d) and e) is their different types of saturation. ∥ orientation appears like a homogeneous saturating sample, while ⊥ appears to behave like an inhomogeneously saturating sample. This is however not the actual radical saturation type changing but again a B_1 effect, radicals further away from the center compensate the typical signal decrease after the maximum.

The SNR for d) and e) is bad. However, they represent typical samples used for EDMR experiments below, for which the sample size nor radical concentration should be increased, as discussed above. Besides the sensitivity problem, also heat is a problem, in fact the sample partly boils off at too much power. Subfigure f) shows the result for a sample which avoids this heating problem by using a non polar electrolyte of 200 µl 100 mM TEMPONE dissolved in toluene. The amount of radicals is therefore 100 times larger compared to d) and e). The homogeneously saturating curve is correspondingly 100 times larger.

Subfigure g) for DPPH powder exemplifies an ideal sample, small and not lossy. This non-liquid sample is the only one showing true linear behavior. It is unclear what causes this non linear behavior of all liquid samples. It is further interesting, that all samples recorded with the home-built setup, including the non lossy samples f) and g), show saturation only at anomalously high powers. This is again the result of combining large samples with a large B_1 inhomogeneity ([64], p.47). The large samples cover a range of different B_1. When the sample at the very center of the cavity experiences already a B_1 large enough to saturate, the sample areas further away from the center (up to 1.5 mm due to the 4 mm inner tube diameter) experience a weaker B_1 strength and therefore saturate only at stronger applied MW powers.

A general B_1 strength can therefore not be defined for this system. Furthermore, the power needed for saturation could not be applied due to the described boiling. I therefore use only a power where the sample is at maximum heated to 35 °C to avoid evaporation, electrode coating and peptide decomposition. This is reached for all samples presented below at approximately 16 dBm, i.e. 40 mW. In fact, the MS400 would show at 40 mW already saturation. Additionally, the EDMR measurement is sensitive only to the processes at the WE/electrolyte interface, see sections 2.2.4 and 2.3. It is therefore sufficient to achieve saturation at the interface, which is located at the tube and cavity center where typically also B_1 is the strongest. It is likely that saturation is partly reached at the interface, when using 16 dBm. This however is not guaranteed. Further effects of these saturation measurements and a more detailed experimental description are discussed in A.1.

In view of equation 2.31, it would be useful to know the relaxation time T_1. However, as discussed at the end of section 2.2.1, Q and C' have to be known to find the actual T_1 using CW EPR and not pulsed techniques. C' is unknown, so that only a T_1 approximation can be performed, using

equation 2.26

$$T_1 \geq \frac{2}{\sqrt{3}\gamma\Delta B_{ptp}}$$
$$\approx \frac{6.56 \times 10^{-7}\,\text{mT}}{\Delta B_{ptp}}. \tag{3.1}$$

Such approximated minimum values for the samples in graph 3.26 are listed in table 3.2 and compared with pulsed EPR literature T_1 values. T_1 is strongly dependent on solvent, concentration, used RF range and temperature. It is therefore partly difficult to find directly comparable experimental situations in literature. The literature value for DPPH is directly comparable with my result, i.e. DPPH powder, measured with pulsed X-band EPR at room temperature.[122,123] However, for 100 mM TEMPONE in toluene no directly comparable literature exists. Therefore the T_1 value of experimental conditions closest to this are noted, i.e. 20 µM TEMPONE in toluene[124] and 500 µM TEMPONE in H_2O.[125] For $MV^{+\bullet}$ only one literature value exists at all, which is for a 1 mM $MV^{+\bullet}$ solution in ethanol with 0.7 mM *coumarin 343* dye molecules.[126]6 The comparison therefore has to be discussed with these experimental condition differences in mind.

Table 3.2 − T_1 minimum value approximation with $T_1 \geq \frac{2}{\sqrt{3}\gamma\Delta B_{ptp}}$ for the samples of figure 3.26 and comparison to pulsed EPR literature value of otherwise similar experimental conditions.

	$MV^{+\bullet}$ radical				TEMPONE	DPPH
T_1 lit.	5.7 µs[126]				0.45(6) µs [124,125]	0.057(2) µs [122,123]
exp. $T_1 \geq$	MS400 - b) 0.48(2) µs	no elect. - c) 0.4(2) µs	‖ - d) 0.5(2) µs	⊥ - e) 0.4(3) µs	f) 0.47(7) µs	g) 1.4(4) µs

Comparing these values, it is clear that equation 3.1 is not suited for an exact T_1 evaluation. However, some conclusions can be made. DPPH should be similar to literature, since the experimental conditions were identical. However, my approximated T_1 is not even in the same range as the literature value. This might be due to the narrow DPPH spectrum, 0.5 mT, which brings the home-built setup at its resolution limit. To the contrary, TEMPONE is surprisingly accurate with literature, even though the concentrations are strongly different. Since the TEMPONE spectrum is rather broad (1.5 mT), one could conclude that the approximation of equation 3.1 is suitable for broad EPR spectra. The literature value for $MV^{+\bullet}$ is hard to compare with my approximation,

---

6 MV^{2+} is reduced by *coumarin 343* dye molecules in combination with TiO_2 nanoparticles and photon excitation at 355 nm.

[122] J. Granwehr, "A New Approach to Longitudinally Detected Electron Paramagnetic Resonance", PhD thesis (ETH Zürich, 2002).

[123] R. Brändle, et al., "Impulsspektroskopische Untersuchungen der Elektronenspinrelaxation in freien Radikalen", Zeitschrift für Naturforschung A **25**, 1–11 (1970).

[124] A. Collauto, et al., "First determination of the spin relaxation properties of a nitronyl nitroxide in solution by electron spin echoes at X-band: A comparison with Tempone", Journal of Magnetic Resonance **223**, 180–186 (2012).

[125] J. S. Hyde, et al., "Spin-label EPR T1values using saturation recovery from 2 to 35 GHz", Journal of Physical Chemistry B **108**, 9524–9529 (2004).

[126] D. M. Martino, et al., " FT-EPR Study of Photoinduced Electron Transfer at the Surface of TiO 2 Nanoparticles ", The Journal of Physical Chemistry B **101**, 8914–8919 (2002).
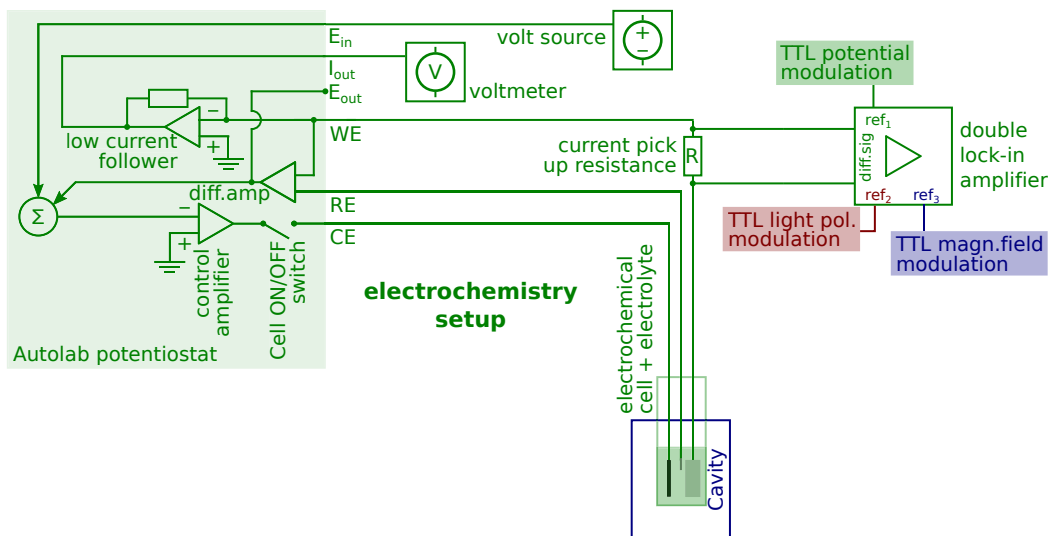
Figure 3.27 – Electrical detection setup including the electrochemical cell, potentiostat, lock-in (Zurich instruments HF2Li) and the various possible read out channels. The electrochemical measuring system is driven by a potentiostat system which allows us to perform CV, chronoamperometry, impedance scans and longtime OCP observation without changing the electronic setup. A lock-in connected around a resistance measures the signal proportional to the current at the WE in means of three possible modulation techniques: light, potential and magnetic field modulation. The lock-in used for EDMR has two signal inputs with each 3 digital channels and can detect on each of these 6 channels independently on one of the two detected modulation reference frequencies. This also facilitates double lock-in detection.

since the solvents used by me and the other authors are completely different and an additional reactant is presented in [126]. The very long T_1 reported by [126] might be due to adsorbed MV$^{+\bullet}$. In conclusion, in certain circumstances equation 3.1 is suitable for an approximation of T_1 for broad spectra, but has to be considered with caution.

3.1.6   EDMR Setup Settings, Characterization and Noise Reduction

The aim of this work is to study processes happening at the working electrode surface. CW EPR is however bulk sensitive. Electrochemical measurements on the other hand are electrode surface sensitive. The obvious solution is their combination to detect magnetic resonance electrically (EDMR), i.e. the detection of resonance while observing the WE current described in section 2.2.4. The electrical detection schematic is depicted in figure 3.27. The obvious way to measure EDMR would be to straightforwardly combine the hardware driving processes regarding magnetic field sweep, MW control and potentiostat control into one program. However, the implementation of Autolab into LabView is quite difficult, as comments Metrohm: "*Regarding SDK, Autolab does not provide full support.*" The only option to include the Autolab software is to run two independent programs simultaneously, one controlling the EPR system, the other controlling the potentiostat. However, this requires a time-stamp method, which is always inconvenient and error-prone. Therefore, I control the potentiostat with the external voltage control E_{in} and use the analog current output port I_{out} to monitor the current at the WE, see figure 3.27. I_{out} hereby delivers the current without intermediate digitization and in voltage form, as $I_{out} = I/(currentrange)$.

As calculated in 2.3, the relative current change is expected in the 10^{-4} range, i.e. 0.1 nA to 1 nA
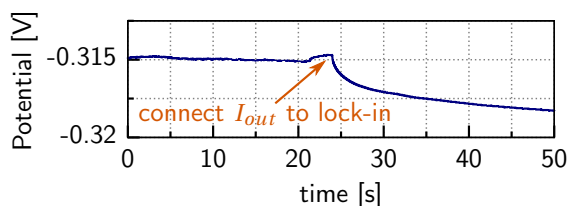
Figure 3.28 – Potentiostat result dependency on connected ports at the example of I_{out} connected to a lock-in while performing a chronopotentiometric measurement for $-0.4\,\mu A$ applied, using the sample of figure 3.30.

for a maximal current of $1\,\mu A$ to $10\,\mu A$. This is fully in the range of the current noise, as will be shown a bit further below. A typical method to increase the signal to noise ratio (SNR) is lock-in amplification, as described in 2.2.1. To do so, the spin dependent signal part has to be modulated. The biggest signal change would appear by changing the spin polarization, either of the radicals in solution, or of the working electrode. Fast magnetic field direction inversion is technically hard to realize and would introduce a whole range of other problems, see e.g. section 3.2.2. The alternative, as described by Chazalviel, is the inversion of the light circular polarization helicity. This can be achieved by e.g. rotating a $\lambda/4$ plate when working with p-GaAs. The lock-in signal will here be proportional to the difference in current of the parallel and anti parallel spin configuration, which will change at resonance due to the electrolyte spin-polarization decrease at resonance. The other obvious modulation technique is EPR related, i.e. magnetic field or microwave modulation. Microwave power directly influences the spin dependent current because it caused the microwave power induced CV shift described in section 3.2.2. Thus, microwave power modulation is not an option. MW frequency modulation is not possible due to the use of a cavity system. Magnetic field modulation is the common CW EPR technique. All of the mentioned techniques were tried. However, the method most effective for spin dependent charge transfer detection at the interface was in my case the potential modulation, in fact the only method so far to show a spin dependent current change at resonance. The potential modulation method is discussed in detail here below and in section 3.2.1.

The Autolab PGSTAT302N potentiostat accuracy is 0.2 % of the current range, e.g. an accuracy of 6 nA for a set current range of $1\,\mu A$ is necessary to not overload while performing a CV reaching up to $3\,\mu A$. Therefore, it was not possible to use the current detectors of the Autolab in the lock-in detection experiment.[7] The potentiostat also shows strong internal cross talk which further prevented the use of the Autolab for the lock-in detection. Figure 3.28 shows as example a chronopotentiometric measurement, with a potential increase when a lock-in is connected to the I_{out} port.[8] The measured voltage should be completely independent of a hardware connected to the I_{out} port. This appears to be a general problem for this type of high sensitivity potentiostats, which are built with the intent as stand-alone measuring systems. This was a major source of problems for me, since within the realm of this work the potentiostat is most often not used as planned by the manufacturer, see appendix A.3 for further discussion. To avoid any possible inter-

---

[7] Metrohm additionally states a current resolution of 0.0003 % of the current range. This is 1000 times better than their stated accuracy and would definitely be sufficient to resolve our sought effect. However, they do not comment on which of their two stated values, "accuracy" and "resolution", is the actual sensitivity. The most likely answer is "absolute" and "relative" accuracy.

[8] The lock-in used was here the Zurich instruments HF2Li, set as float and high impedance.

nal interference of the potentiostat with the modulation induced AC signal, and to be independent of the potentiostat's current range defined maximal sensitivity, I measured the AC signal by means of an additional current pick-up resistance R connected in series with the WE, see figure 3.27. As I was using an external detection of the modualtion current, I was able to measure simultaneously the DC current with a voltmeter connected to the I_{out} port of the potentiostat.[9]

The lock-in actually measures not the current but the voltage around the pick-up resistance R, i.e. indirect current measurement using $U = R \cdot I$. The pick-up resistance has to be carefully chosen, as large as possible to amplify the small current signal, but small enough to not interfere with the actual electrochemical cell impedance R_{cell}. If the used resistance is very similar or larger than the cell impedance, it will start to dominate the measurement completely and alter the result. The cell impedance therefore had to be determined for this reason. It was also necessary to characterize the impedance so as to work at the frequency at which the impedance is predominantly due to the charge transfer process at the electrode, as discussed below.

In section 3.2.1 it will become clear, that the EDMR measurements cover the whole CV potential range and not only a constant potential. However, the impedance changes continuously along the CV. Since the pick-up resistance is not variable but fixed, I have to choose the potential values at which I expect a spin effect to be visible. As discussed in section 2.3, a resonant spin dependent charge transfer is to be expected at the $MV^{+\bullet}/MV^0$ reduction and the $MV^{+\bullet}/MV^{2+}$ oxidation region. The current change is expected to be the strongest in the potential range in which diffusion limitation is minimal, i.e. at the increasing peak slope in scanning direction. Figure 3.29 a) shows CV of a GaN/Au/Al5/Ag sample. By choosing the potentials as indicated with dashed lines, I can actually probe simultaneously reduction and oxidation peaks at both potentials.

The corresponding impedance measurements are presented for the frequency range of 2×10^5 Hz to 0.5 Hz for the first redox peak at 40 mV in e) as Nyquist plot and f) as Bode plot. The corresponding impedance data for the second redox peak at -370 mV are shown in c) and d). The fits, indicated as lines, are the result of the equivalent electric circuit presented in b). Comparing with the introduction of impedance measurement along figure 2.9, it is striking that we have two Randle's circuits in parallel configuration. This double circuit gives the best fit, while a single Randal's circuit is for most measurements completely off. This indicates two surface processes happening simultaneously, which is most likely due to two different surface types being present.[127]

The second question is what modulation frequency to choose. Frequency and resistance are coupled, see d) and f). Ideally we want a pick-up resistance as large as possible, but also want to stay off the diffusion induced part, which is accounted for by the Warburg module and clearly visible as the almost linear range for large Re(Z) in c) and e). We must work at higher frequencies in order to stay away from the frequency range where diffusion limitation dominates the AC current, i.e. to the left the linear region in c) and e). The chosen point is indicated with an arrow in c) and corresponds to 270 Ω. 200 Hz corresponds in e) to 400 Ω, well visible in f). In conclusion, if we use

---

[9] For all measurements it is important to not only observe the lock-in AC signal, but also the DC change over time. However, AC and DC cannot be simultaneously read out with different hardware through the I_{out} port at the potentiostat due to hardware interferences. When e.g. using a voltmeter and lock-in at the same time at I_{out}, part of the AC signal is lost and the read voltage drops, instead of both systems stating to have high impedance.

[127] K. Jüttner, "Electrochemical impedance spectroscopy (EIS) of corrosion processes on inhomogeneous surfaces", Electrochimica Acta **35**, 1501–1508 (1990).
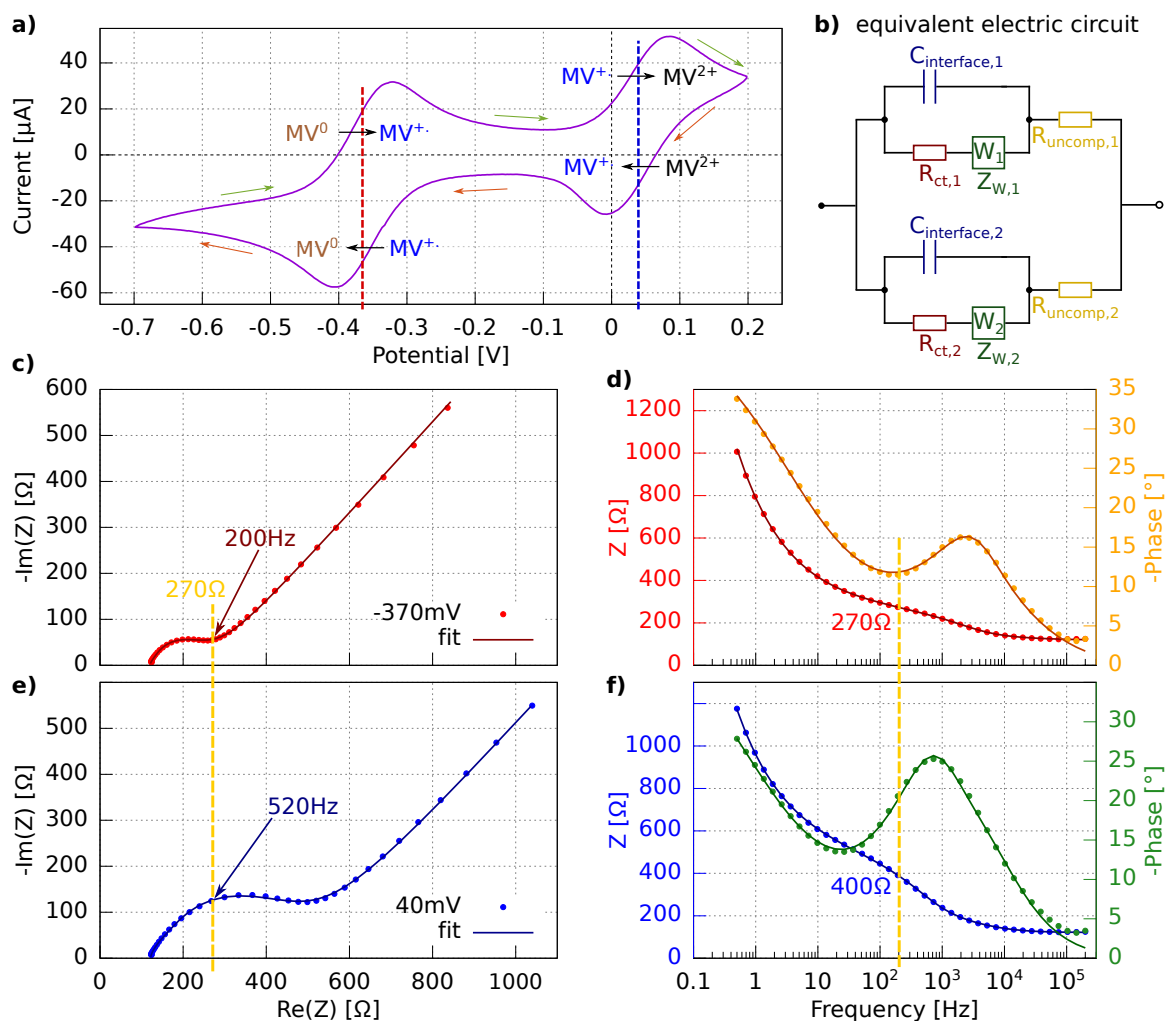
Figure 3.29 – Impedance measurement at the example of a GaN/Au/Al5/Ag with a Pt-tip RE and Pt-rod CE in a 2 mM MV$^{+\bullet}$ ACN electrolyte with 200 mM TBAP sample for the determination of a suitable potential modulation frequency and current pick-up resistance. The two potentials used for impedance measurements are indicated with dashed lines in the CV in a), recorded at 50 mV/s. c) and e) show the corresponding Nyquist plots. d) and f) the corresponding Bode plots. b) shows the equivalent electric circuit used for the fit, i.e. two parallel Randles circuits representing two simultaneous surface processes.

this point before the linear range in c) as defining the modulation frequency.

A pick-up resistance same large or larger than the cell resistance is directly visible in the CV and as SNR increase in the impedance measurements. With this reasoning, I chose for this sample a modulation frequency of 200 Hz and a pick-up resistance of 200 Ω.

Choosing the current pick-up resistance at 3/5 to 2/3 of the cell resistance corresponding to used potential modulation frequency does in fact not influence the result in a measurable way. Figure 3.30 displays this at another sample, helicene, as direct CV comparison with and without resistance in a), and as relative difference in b). Also displayed is the effect of a lock-in connected to the pick-up resistance. For this sample $R = 300\,\Omega$ was chosen. Figure 3.30 demonstrates also, that direct CV comparison for on/off resonance is not sufficient to detect the expected current changes when exciting the spin resonance, which are at the very best in the 0.01 % range. The
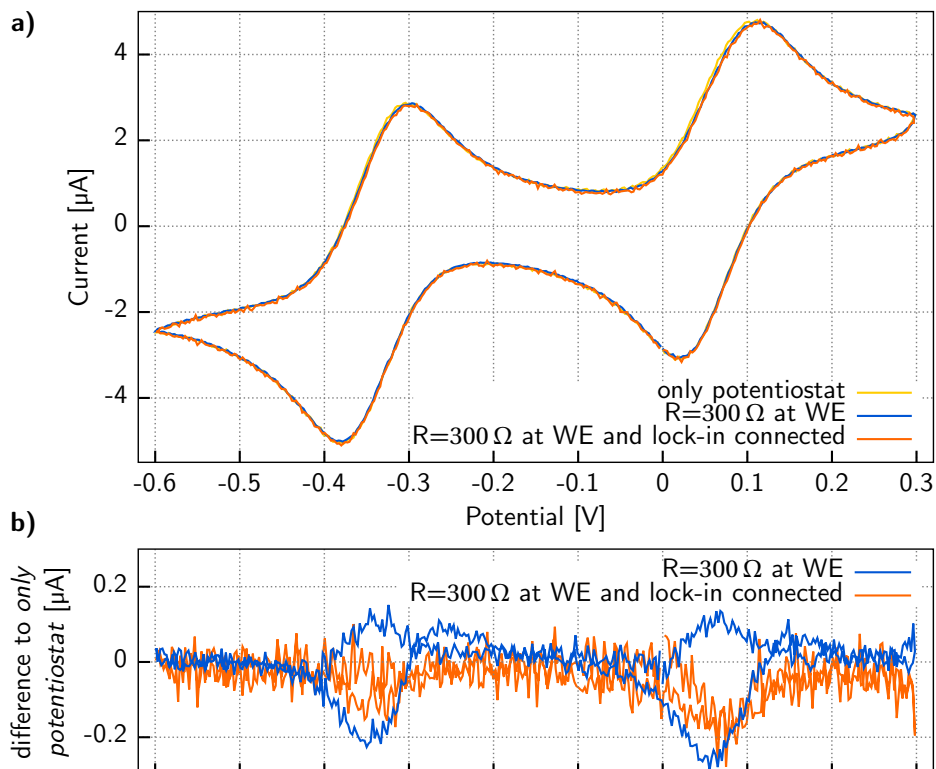
Figure 3.30 – Current pick-up resistance R and lock-in influence on the CV for the case of a helicene sample, a), recorded at 50 mV/s. Difference between with and without additional R or lock-in. The relative current change is of 1 % to 5 %.

lock-in detection is required.

Despite the use of a lock-in technique, one of the biggest problems is noise. Johnson noise scales with the square root of temperature, which is however fixed around room temperature due to the liquid sample state. It is therefore necessary to keep the detection bandwidth low, i.e. large time constant τ of the $R_{lpf} \cdot C_{lpf}$ type lock-in low-pass filter (R_{lpf} low pass resistance, C_{lpf} low pass capacitance)

$$\tau = R_{lpf}C_{lpf} = \frac{1}{2\pi f_c}, \qquad (3.2)$$

to achieve a small filtering *cutoff frequency* f_c.

An important factor for lock-in detection is ground loop induced noise pick up, which could be partly avoided by forcing a *real* float measurement using the differential voltage connection measurements as depicted in figure 2.16.[10] For these differential systems it is of help to use identical cables, cable lengths and keeping them tight together to avoid large loop area magnetic pickup.[67] Grounding was in general a huge problem in this experiment. It helped to set the overall system to one common floating ground which is connected to the power grid ground only through a high impedance and an additional filter. The biggest problem was the computer interface. The Metrohm potentiostat uses USB as interface, which has a ground contact. USB

---

[10] Compared to single ended voltage measurement *quasi* float with high impedance.

ground loop isolated cables were used. The rest of the hardware was connected via ground-less GPIB cables. The complete setup was disconnected from the building ground, but the grounds of individual instruments were connected to each other via e.g. BNC cables. The potentiostat was connected to the ground via a high impedance and plug filter. It is the one device that connects the rest of the setup to the ground.

The connection to the pick-up resistance happens inside a grounded Faraday shield, i.e. a metallic box. Also all inevitable cable transformations (all potentiostats come with banana cables) are done in a metal box. The electrochemical cell is situated inside the cavity, which acts as a Faraday cage. To fully close this shield, I added a metal box on top of the cavity, so that the complete cell and copper cables to BNC transitions are shielded. The electrode copper cables inside the electrochemical cells are exposed to the external magnetic field and are therefore either twisted or kept as straight as possible, as discussed in section 3.1.1. Another most important point is to keep any device using rotating magnets (mostly fans) far away from the EDMR system. Their sine-waves were directly visible in the electrochemical current if they were located at a distance below 30 cm. Combining all described methods with an additional low-pass filter system at the lock-in input port allowed me to decrease the noise amplitude to an equivalent of 1 nA af WE current. This is however for a sample without light-source. Shining light on a p-GaAs WE introduces immense amount of noise due to the distance between light source and sample in combination with vibrations.

Further noise reduction can be obtained with double lock-in detection. This consists in using two different types of modulations, e.g. B_0 and potential, at frequencies f_1 and f_2. In double lock-in detection, the two lock-ins are connected in series. The signal output of the first lock-in (li_1) (filtering for f_1) is fed into the second lock-in (li_2) (filtering for f_2). It is hereby important, that

$$f_2 \ll f_1,$$

so that the f_2 information can pass the li_1 low-pass filter.[128] Also the corresponding time constants τ_i have to be chosen carefully with respect to each other and f_2 to avoid smoothing induced information loss, see equation 3.2,

$$\tau_2^{-1} \ll (2\pi\tau_1)^{-1} \approx f_2.$$

Double lock-in has the advantage, that only information accessible to both modulations passes both lock-ins. Signal sources which are only proportional to one modulation will be filtered by the other lock-in. This method was tried for all experiments of simultaneous EDMR and EPR detection, but did not produce any improvement over the single lock-in, i.e. field modulation for EPR and voltage modualtion for EDMR.

In view of the complexity of the detection scheme, I decided to verify that the EDMR detection scheme worked by measuring a ferromagnetic sample. A 40 nm thick permalloy film (Py, alloy of typically $Ni_{80}Fe_{20}$) of length 10 mm and width 2 mm was mounted at 45° on a holder and situated inside the cavity such that the face was parallel to B_0 (in plane configuration) and tilted by 45° away from the cavity main axes. The in-plane orientation maximized the FMR signal and the 45° tilt

[128] J. Goree, "Double lock-in detection for recovering weak coherent radio frequency signals", Review of Scientific Instruments **56**, 1662–1664 (1985).
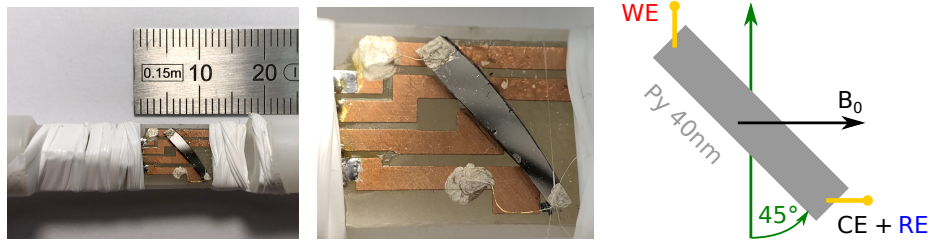
Figure 3.31 – Permalloy sample film of 40 nm thickness, 10 mm × 2 mm. Contacting with gold wires ⌀ = 0.02 mm and silver paste is well visible in the middle. The sample orientation and potentiostat electrode contacting for FMR respectively EDMR is indicated on the right.

maximizes the EDMR signal (see [129] section 5.3 and 6.3).[129] Using magnetic field modulation and MW at 9.4 GHz, the Py sample gives a large CW ferromagnetic resonance (FMR) signal as displayed in figure 3.32 a), b) and c), which are in agreement with the field to frequency relation found for 20 nm to 40 nm Py films in literature.[129,130] d) shows the signal obtained when the Schottky diode was directly connected to the potentiostat (WE core BNC, CE and RE at shield BNC) and the lock-in to the E_{out} port. The direct lock-in, a), and passed-through-the-potentiostat signal, d), show a similar SNR. For d) the E_{out} port was used, which does not include a scaling but transfers the analog signal directly. This is why a) and d) are directly comparable and in fact show almost the identical signal size. This indicates that the potentiostat transfers measured signals to the analog output ports without noise nor filtering. A similar FMR signal was obtained when using the I_{out} port, though less intuitive, since the Schottky diode delivers voltage and not current. I also found a crosstalk to E_{in} so strong that the resonance can even be detected at the E_{in}, however 1000 times smaller.

Additionally electrical contacts where prepared at the ends of the Py sample with Au wires and silver paste. I connected the WE to one end and RE+CE to the other end of the Py sample. The lock-in is connected to the I_{out} port and measures the current change around resonance at OCP. The resulting lock-in EDMR signal in e) has a far smaller SNR than the corresponding CW FMR signal in b). EDMR in this case is based on the anisotropic magnetoresistance (AMR) of the Py film, which is at best about 4 %. AMR may be much smaller in this film grown without any attempt to optimize the AMR effect. Also, the contacts were by far not optimal for sensitive electric measurements. Finally, it should be pointed out that conduction in the sample is not a resonant circuit. In EDMR, the excitation benefits from the Q of the resonator, but the precession of the magnetization as detected by AMR does not benefit from the Q of the resonator. I have also tried to use the potentiostat to impose a constant voltage. This gives the same spectrum without changing the SNR significantly. In any case, this shows the general functionality of using a combination of potentiostat and lock-in to electrically detect magnetic resonance using the current.

To avoid the crosstalk that is internal to the Metrohm potentiostat, an additional voltage pick up resistance R_{pu} was put in series with the WE. The current is therefore measured indirectly by measuring the voltage U_{pu} around R_{pu}, such that $I = U_{pu}/R_{pu}$. Again, R_{pu} should be as large as possible, to maximize U_{pu}, however small enough such the the electrochemical cell resistance R_{sample} is dominant. The sample resistance is 25 Ω, such that I chose $R_{pu} = 10$ Ω. The WE is

---

[130] K. J. Kennewell, et al., "Magnetization pinning at a Py/Co interface measured using broadband inductive magnetometry", Journal of Applied Physics **108** (2010) 10.1063/1.3488618.

Figure 3.32 – Proof of EDMR functionality using a potentiostat with a Permalloy sample rotated by 45° and with its surface aligned with B_0. d) shows the result of the Schottky diode directly connected to the potentiostat (WE to core BNC, CE and Re at shield BNC). e) is the result of measuring the current at OCP between the long Py ends with a potentiostat and feeding this signal through the I_{out} port to a lock-in. f) uses an additional voltage pickup resistance $R_{pu} = 10\,\Omega$ at the WE instead of I_{out}. a), b) and c) show the standard CW FMR of Py recorded simultaneously and correspondingly with d), e) and f). Measured at 30 dBm and 9.4 GHz.

connected to R_{pu} which is connected to one Py contact while CE+RE are connected to the second contact. The lock-in is connected around R_{pu}. The resulting lock-in signal is shown in f) with corresponding CW FMR in c). f) is basically identical to e), thus proving EDMR using an additional resistance to avoid in-potentiostat cross talk.

3.2 Simultaneously Performed EDMR, EC and EPR

The goal is to see resonance in the current signal at certain potential ranges. To do so, the above discussed electrochemical (EC), EPR and EDMR are now combined. However, as will be shown, EDMR measurements at constant potential are troublesome. I therefore developed a measuring system, allowing simultaneous continuous potential sweep and quasi-continuous magnetic field sweep, which is discussed in 3.2.1. Regarding the combined electrochemistry, EPR and EDMR, the dependencies of microwave, magnetic field, measured/applied potential and measured current on each other is discussed in 3.2.2.

3.2.1 Rational for Matrix Scans

The most natural method to do EDMR would be to sweep the magnetic field through resonance as in CW EPR, while sitting at one potential. However, this has a striking problem, the exponential current decay as shown at the example of figure 3.33. When turning on the potential, the reactant accumulated on the WE surface is exhausted and the product accumulates. As discussed in section 2.1 a), this corresponds at the beginning to the discharging of a capacitance C of an $R_S C$ series

Figure 3.33 – Chronoamperometric exponential current decay for an applied voltage of $-0.4\,V$ on a GaN/Au/Al5/Ag sample in a) (potential step coming from OCP). Constant potential EDMR by potential modulation in b).

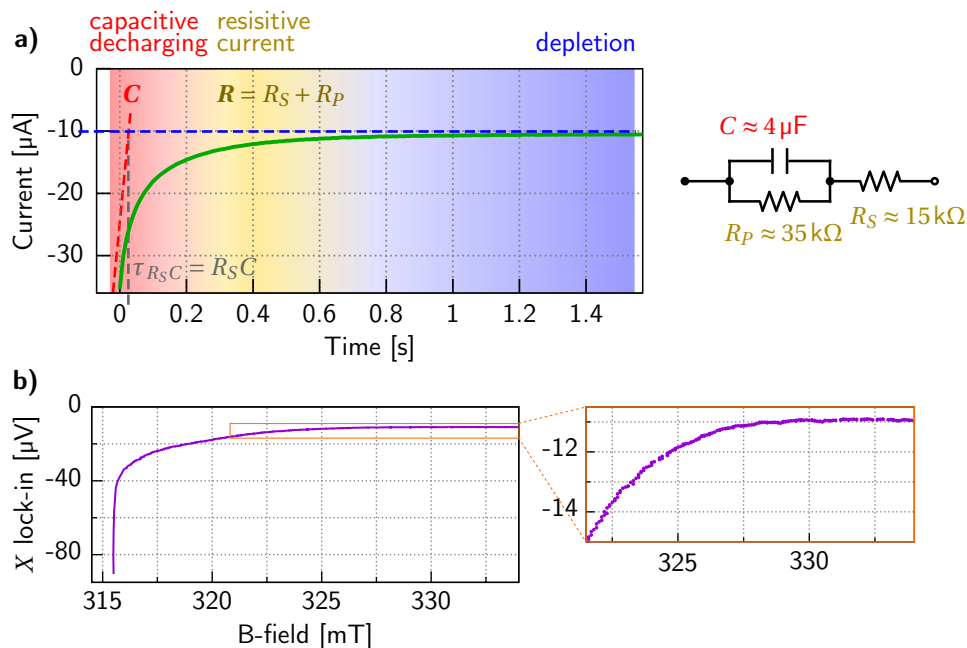circuit, seamlessly going into resistive current with $R = R_S + R_P$, until depletion of the reactant prevails, i.e. diffusion limited current. The charging time constant $\tau_{R_SC} = R_SC$ defines the time until $e^{-t/\tau_{R_SC}}$ of the final current is reached. In electrochemistry, the capacitance influence is assumed sufficiently vanished at $5 \cdot \tau_{R_SC}$. Almost directly afterwards reactant exhaustion at the WE surface prevails. Even for this sample of huge τ_{R_SC}, $5 \cdot \tau_{R_SC}$ is reached at the latest at 0.5 s. Which is by far not sufficient for a magnetic field sweep through resonance.

The exponential decay proved to introduce a continuing lock-in offset drift, such as displayed in b). These lock-in drifts make long-time sweeps less meaningful, since also the contained signal scales with this drift. To achieve a constant current to circumvent such drift, potential adaptation can be used. Hereby, the potential is continuously shifted, yet should stay in the desired potential range. In the example of figure 3.34 a), I applied three different constant currents, indicated in a color coded way in a) and respectively in the resulting chronopotentiometric measurement b). The solid lines in a) indicate the potential range swept with the aim to keep the current constant. It is obvious, that for this specific example no current exists for which the potential does not exceed the $MV^{+\bullet}/MV^0$ reduction range. To improve on the diffusion limitation, the WE surface was decreased from $1.1\,mm^2$ to $0.5\,mm^2$, c). This allowed remarkably long measurements at constant currents and requiring relatively small potential changes. The current decrease from a) to c) corresponds well to the decreased surface area. Interesting is the increased noise in d) compared to b) due to the longer experiment time, which also reflects in the strong CV change in c) comparing the CV before the application of $-0.2\,\mu A$ and CV 30 minutes after. This change is far more severe than with the matrix scan method described below, where such strong change appears after continuous scans for one or two days. Using reduced surface areas, the potentials are stable and do not exceed the second reduction peak for more than 3 hours. This is by far enough time to perform averaged EDMR scans. However, neither single EDMR nor summations up to 200 consecutive scans (2 h)
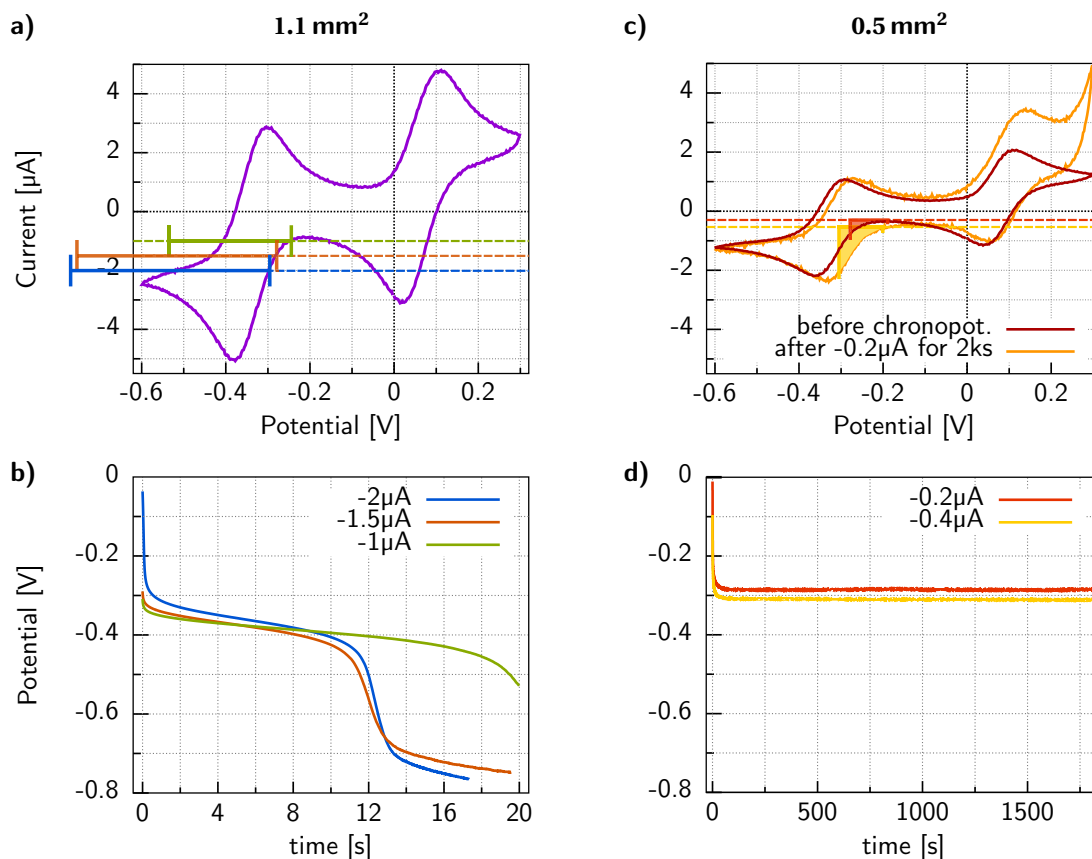
Figure 3.34 – Chronopotentiometric EDMR method without flow device for the case of a helicene sample. The potential adaptation responsible for the current in b) and d) are indicated in the CVs in a), respectively c). For ease of comparison, the current and potential ranges are kept constant.

showed any current change nor EDMR effect around resonance. This is a clear indication that reactant diffusion limitation has to be minimized as much as possible.

To circumvent diffusion and reactant exhaustion problems, two possibilities exist. Either avoiding diffusion or diminishing the diffusion influence by use of dynamic experimental methods. The former approach requires either electrolyte stirring or a constant electrolyte flow. Stirring introduces in any case vibrations and is complex to implement into a cavity system and limited cell size. A flow device, such as used by Chazalviel, has two major problems. Regarding a combination with cavity systems it introduces additional electrolyte into the cavity, making adequate matching and tuning probably impossible. However, this has been tried by others, though for UME systems in combination with loop-gap resonators.[25] The second problem is oxygen tightness regarding MV$^{+\bullet}$ stability, which is rather complicated for large systems. Chazalviel had less space limitations (no cavity) and placed his whole electrolyte system in nitrogen atmosphere. Regarding the dynamic diffusion limitation circumvention, I developed two different approaches,

1. potential jumping between desired potential $E_{measure}$ and a defined rest potential,

2. continuous CV sweeps combined with stepwise magnetic field sweep , thus collecting data in a matrix of data points taken around resonance.
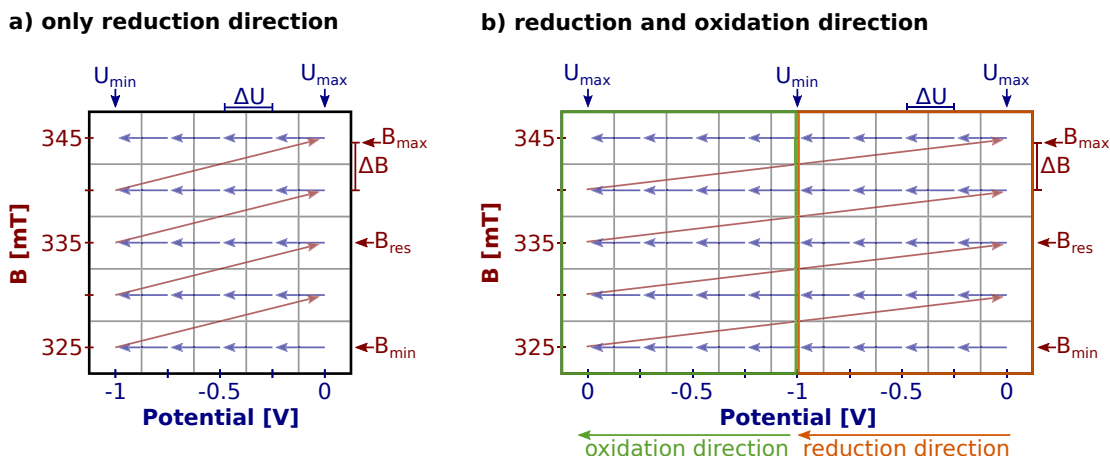
Figure 3.35 – Code basis illustration for the matrix scanning scheme with row major order. In a) for only reduction direction matrix scans, in b) for a full CV. b) shows the measuring concept and not the representation concept, for which the plots are split into only reduction direction part and only oxidation direction part, with the latter also mirrored, see figure 3.36.

The potential jump method, documented in appendix A.4, does so far not work due to timing and phase continuity problems.

The second dynamic approach is potential sweep at constant magnetic field. In other words, I perform CV scans and change the magnetic field for every CV by a small amount ΔB, thus sweeping B_0 through resonance. The sample history dependent change from CV to CV is hereby continuous and can be distinguished from a resonance change. The magnetic field is only after every CV stepwise increased. However, due to the small step size of $\Delta B \approx 0.02\,\text{mT}$ in combination with the electromagnet's hysteresis this compares to a quasi continuous B_0 sweep. This method is therefore a combination of simultaneous continuously swept potential and quasi continuously swept magnetic field. The data are recorded in a matrix of data points, where each data point records the value of the lock-in response at a certain voltage and a set field voltage value. Once the matrix scan is finished, spectra are extracted from the matrix scan by plotting lock-in data at set voltage value as a function of field.

Initially, only the reduction direction was scanned, such as depicted in figure 3.35 a). This was partly to save time, partly due to code and evaluation technical problems. Therefore, part of the results presented in section 4, are only presented for voltage scans in reduction direction. The LabVIEW program therefore sweeps the applied potential with step size ΔU of typically 3 mV to 4 mV, while the magnetic field is kept constant. It is obvious, that this is no linear CV but an approximation using a staircase sweep. After each potential sweep, the magnetic field is increased by ΔB. Due to the specific appearance, I ended up calling the resulting plots matrix scans. To see possible effects in the whole CV range, the potential is first scanned from maximal value of the potential down to the minimal value and then back up again, covering the whole reduction and oxidation range. This appears trivial, is however programmatical realized in a way such as depicted in figure 3.35 b).To acquire a matrix of reduction scans takes 3 to 12 hours depending on the potential and field window sizes and resolution, and consequently a combined reduction+oxidation matrix scan takes between 6 and 24 hours. The resolution is defined by ΔU and ΔB. The recorded single direction matrices were of size 200×200 up to 600×600. The
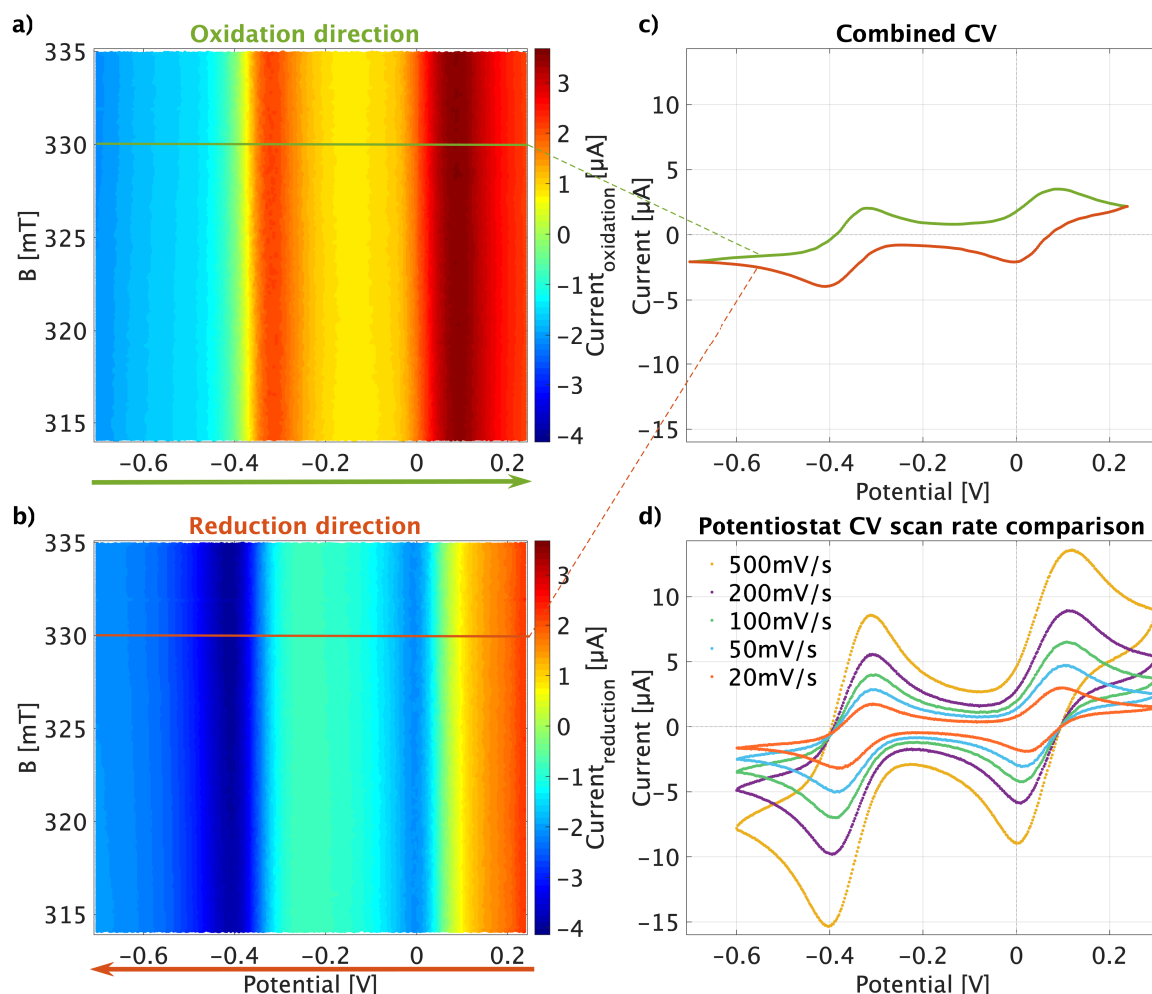
Figure 3.36 – Current matrix scan, b) reduction direction, a) oxidation direction for a helicene sample. d) shows a linear CV performed directly with the potentiostat for a collection of scan rates. The matrix potential scan rate was approximately 40 mV/s, average of 7 scans, potential step size was 3 mV and magnetic field step size 0.05 mT. The color coding for the reduction direction is orange, and green for the oxidation direction, and is kept throughout the whole thesis.

scanning speed is ultimately limited by the program delay time. The scan rate is therefore defined by the program quality, computer calculation speed, hardware feedback lag and step size ΔU, see appendix A.3 for further information. In my most recent LabVIEW program, a potential step size of $\Delta U = 1$ mV results in a scan rate of approximately 9 mV/s, i.e. 30 mV/s to 40 mV/s for most of my measurements.

Measured and recorded are simultaneously the electrochemical current using the I_{out} port, EDMR lock-in signal, CW EPR lock-in signal, applied potential and magnetic field. The scan for continuously swept full CVs over a range of quasi-continuously swept B_0 therefore leads to a data set of at least two sets of three 3D (3D = signal × potential × field) matrices with linked entries, i.e. one set of three 3D matrices for reduction and one for oxidation direction. Regarding the EDMR lock-in signal, also the lock-in Y has to be evaluated and controlled to ensure full signal on X without phase information loss. For additional $2f$ detection, double lock-in or simultaneous lock-in detection of several parallel performed modulation techniques the number of matrices to evaluate

increases correspondingly. I found the top-view of the 3D matrix plots to be the most convenient for interpretation. As example, figure 3.36 shows such a surface plot with the measured current in color coded form as surface with corresponding potential value on the x-axis and corresponding magnetic field value on the y-axis. The matrix is already split into only reduction direction, b), and only-oxidation-direction scan, a), which combine together to the typical CV, such as indicated with a row cut of a) and b) put together in c). To show the consistency of these recordings with normally acquired CVs, subplot d) shows a collection of CVs at increasing scan rate recorded independently from a) and b) directly with the potentiostat in a separate experiment on the same helicene sample. The matrix potential scan rate was approximately 40 mV/s when accumulating the data shown in a) and b). Subfigure c) compares correspondingly well to its closest relative in d), the light blue line recorded at 50 mV/s. The code related staircase approximation is therefore sufficiently close to a linear CV result. This is however not necessarily the case. If the potential steps are chosen too large or the program delay is too big, e.g. a constant-potential like current overshoot is observable for every step.

The consecutive CV sweeps in figure 3.36 are only slightly but most importantly continuously changing along the stepwise increased magnetic field. The regularity of this plot attests to the chemical stability of the electrochemical cell. The lock-in result evaluation is not the most straight forward, which is best discussed taking as an example potential modulation. Figure 3.37 shows the lock-in result for potential modulation recorded simultaneously with figure 3.36, helicene. The matrix was recorded using a modulation of 200 Hz with an amplitude of 3 mV. 3.37 a) is the lock-in result for reduction direction and b) oxidation direction. The signal was measured differentially around a pick-up resistance of $R_{pu} = 300\,\Omega$ situated between the WE and potentiostat.

To see what the lock-in signal corresponds to, I do an short approximation in the following, which follows mostly unit considerations. The lock-in input signal is a potential difference U_{pu} measured around the pick-up resistance R_{pu} and proportional to the current at the WE,

$$\frac{U_{pu}}{R_{pu}} = I_{WE}. \tag{3.3}$$

The differential current is proportional to the differential voltage U_{WE} at the WE, and the sample impedance R_{sample},

$$\mathrm{d}I_{WE} = \frac{\mathrm{d}U_{WE}}{R_{sample}}. \tag{3.4}$$

The lock-in output signal U_{output} in volts can be approximated with the potential modulation $\Delta U_{WE,mod}$ as

$$U_{output} = \frac{\Delta U_{pu}}{\Delta U_{WE,mod}}.$$

Obviously this is not correct regarding units. This is due to the lock-in read out, which is for any measurement in volts. The ZI HF2LI lock-in uses hereby a digital, non-scaling conversion, such that a unit conversion factor of $C_V = 1\,\mathrm{V}^{-1}$ is necessary, i.e. $U_{output} \cdot C_V = \Delta U_{pu}/\Delta U_{WE,mod}$.
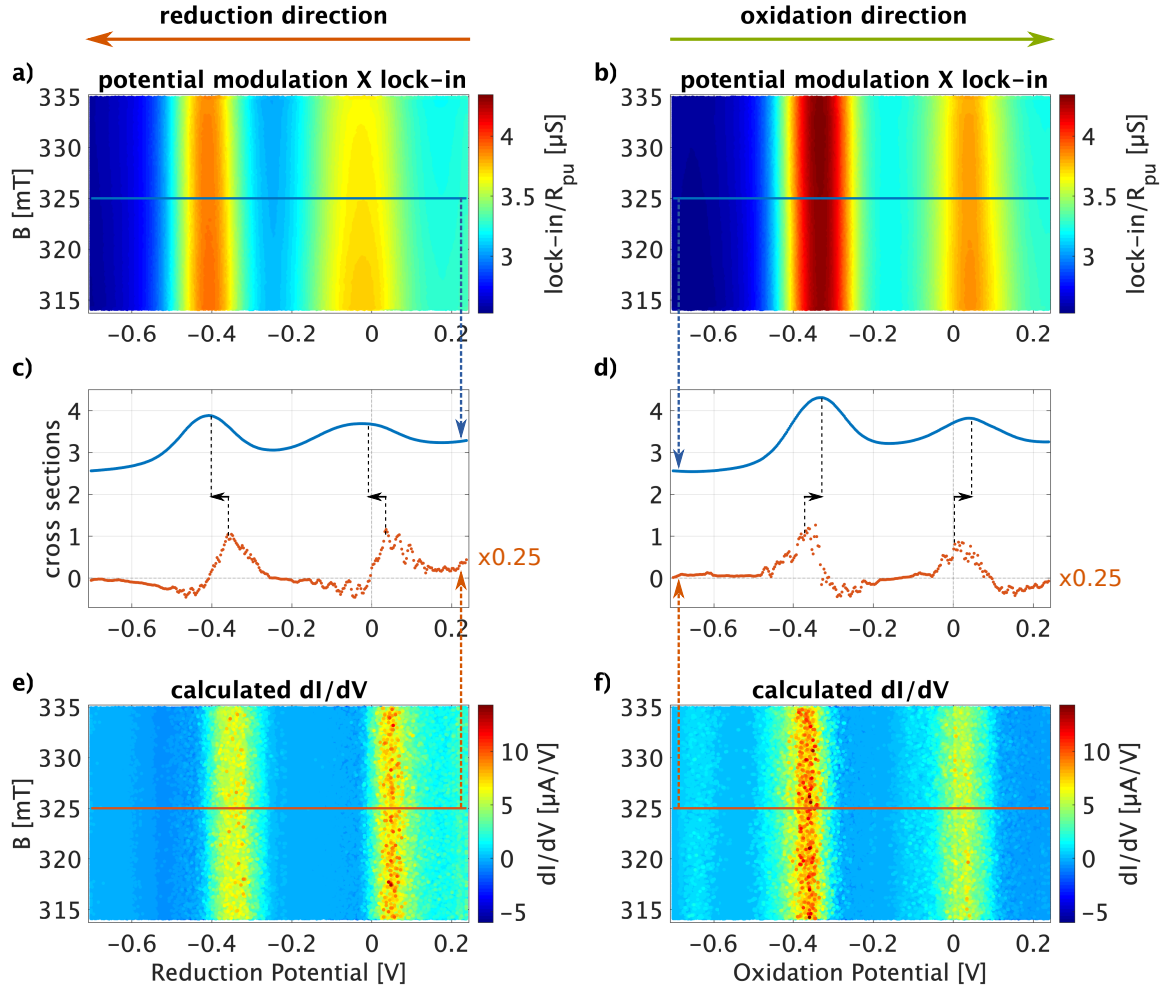
Figure 3.37 – Potential modulation lock-in matrix scan simultaneously performed with figure 3.36 in a) and b). e) and f) are calculated from figure 3.36 a) and b) using $1/R = dI/dU$. c) and d) compare row cross sections of a) and e), respectively b) and f).

Dividing $U_{output}C_V$ by R_{pu}, we therefore get

$$\frac{U_{output}C_V}{R_{pu}} = \frac{\Delta\left(U_{pu}/R_{pu}\right)}{\Delta U_{WE,mod}} \qquad | \text{ eq. 3.3}$$

$$= \frac{\Delta I_{WE}}{\Delta U_{WE,mod}} \qquad | \text{ eq. 3.4}$$

$$= \frac{1}{R_{sample}}. \qquad (3.5)$$

Dividing the lock-in output by the pickup resistance R_{pu} therefore delivers a result proportional to the reciprocal sample resistance, i.e. electrical admittance. To mark these results clearly as potential modulation results, they will be presented below in this conductance form, i.e. in Siemens [S]. Subfigures a) and b) in figure 3.37 are already presented as lock-in result divided by R_{pu}.

In figure 3.37, I compare the matrix of lock-in data ($1/R_{sample}$), a) and b), with admittance data dI/dV ($V \equiv U_{WE}$) calculated from the matrix data of figure 3.36, e) and f). Subfigures c) and d) in figure 3.37 are row cross sections along the potential of a) and e) in c), and of b) and f) in d). The

91

cross sections in a) and b) (lock-in data) can be compared with the cross-sections in e) and f) of dI/dV deduced from I vs. V and B data. Well visible is the lock-in reduced noise level but also a potential shift, indicated with arrows. The shift of the lock-in signal compared to the dI/dV signal to later times is the result of a combination of scanning speed and lock-in integration time. The scanning speed was here approximately 30 mV/s and the time constant 200 ms, i.e. a theoretical delay of 6 mV. However, it is known that the actual lock-in time delay is in general a manifold of the actual time constant. The actual shift of 30(8) mV/s is in fact 5 times longer. For the results part we can therefore assume a shift in scanning direction of $5 \cdot scanrate \cdot \tau$ in comparison to the non-time delayed current signal. The visible broadening is also due to τ. This time delay that amounts to an apparent voltage shift is a correction that needs to be applied in the detailed analysis of the EDMR spectra presented in chapter 4.

The calculated $1/R = dI/dV$ signal is four times larger than the lock-in result, which is why the row cross sections of e) and f) are multiplied with 0.25. This is due to equation 3.5 being an approximation, and due to the integration time induced broadening.

For direct comparison with equation 2.31, the natural procedure would be to further integrate the lock-in signal with over the applied potential U_{WE}, equation 3.4, to have the noise filtered current signal and see actual current changes along resonance and not $1/R_{sample}$. However, this multiplication artificially reduces noise for small $|U_{WE}|$, while amplifying for large $|U_{WE}|$. Therefore, multiplication with U_{WE} is only done for final quantification of the current change around resonance ΔI_{res}, while matrices and line cuts are presented unchanged as $1/R_{sample}$.

In the raw data of course no small change can be visible due to color bar range defined by the change of the conductance $1/R_{sample}$ along the potential. A soft detrend, in the form of averaging the potential scans and subtracting them from each line, levels the raw data without altering the contained information, such as presented in figure 3.38 c). Here already, the practiced eye can recognize a change in the red color in the region around -0.4 V and 327 mT. This is EDMR detection of a spin signal, which is as expected faint. For comparison, subfigure b) shows the average of 100 columns of the CW EPR matrix, and in a) a current matrix row averaging for the oxidation direction potential sweep. The faint color change is in the range of EPR resonance and can therefore be ascribed to resonance. However, the human eye is extremely adapted to recognize local color and shape changes in continuous surfaces. In fact, when simply using column cross sections, only noise is visible, such as in d) for the cross section along the blue line in c). In fact, due to this specific scanning method, fluctuations from CV to CV are larger than the described color change, such that the latter is mostly visible as a change in noise. To evaluate the cross section, I developed the following system. First an average including typically 5-20 column cross sections in both potential directions is performed, range indicated with dashed lines in c). This suppresses single point patterns, reduces noise and increases patterns, e). We can now see a kink at 327 mT. This is best visible at the envelope. The major step is therefore the calculation of the difference between upper and lower noise envelope. This purifies the signal further, however only in combination with the previous steps. The envelope difference is filtered using a moving average filter based on a one dimensional rational transfer function and denominator at approximately one.[11] A final detrend levels the column cross sections to zero, such as displayed in figure 3.38 f). A peak is now visible at the field range corresponding to resonance. The envelope difference step

---

[11] See https://www.mathworks.com/help/matlab/ref/filter.html#buagwwg-2.

introduces a factor 2, which has to be withdrawn. The Matlab code part for this evaluation is:

```
1  Pot=load(...);                               % Matrix with pot. values
2  data=load(...);                              % Matrix mod. raw ('B'x'E')
3  PotCrossS=...;                               % Pot. for row cross section
4
5  dataDiff=data-mean(data);                    % Data diff. to column mean
6
7  [~ IndCS] = min(abs(Pot(1,:)-PotCrossS));    % Find index of PotCrossS
8
9  avg=5;                                        % Amount of averaging
10 avgRowCS=mean(data(:,IndCS-avg:IndCS+avg)');
11
12 [envUp,envLo]=envelope(avgRowCS);            % Envelope calculation
13
14 width=10;   movAvg=(1/width)*ones(1,width);  % Def. moving average filter
15 finalCS=detrend(filter(movAvg,1,envUp-envLo))./2;
```

The averaging introduces a broadening in potential direction. A step size of e.g. 3 mV and an averaging of ten lines in positive and negative direction would introduce a broadening of 30 mV in both directions, i.e. 63 mV in total. This has to be kept in mind. The filtering and envelope process introduce an additional broadening in field direction and the moving average filtering method can additionally introduce a shift in field direction. It is therefore of utmost importance to choose averaging range and moving average filter width as small as possible and to fine tune the moving average filter and envelope type for each evaluation again.

Moving average filter systems introduce in general distortions at the edges, which is why cross sections covering only a field range around resonance are presented. Moving average filters also tend to introduce distortions in the center of the line along which it is performed, which is why all my matrix scans are performed with the resonance not in the center but after 3/5 to 3/4 of the field sweep range is already passed.

At this point it is important to remember that in reality the potential direction is scanned and only after every full scan the magnetic field is changed by one step. The presented column cross section along the magnetic field is no real magnetic field sweep, even though it is presented as such. Nearest neighbor data points are not nearest neighbors regarding the time of data collection. A lot can happen between two neighboring data points on these magnetic field line-cuts. Overall, this type of evaluation is well suited to extremely enhance local variations in an otherwise relatively flat surface. This also means, that local variations due to temperature change,[12] light power changes,[13] vibrations,[14] power grid fluctuations,[15] bubbles in the liquid,[16] abrupt electrode surface changes,[17] or computer delay,[18] can appear at resonance and have to be distinguished manually. Almost all good results are from weekend scans, with locked door, closed curtains and locked out computer, or holidays when most in-house heavy duty machines are constantly turned off.

---

[12] Sunrise, sunset, non-constant heater or air conditioner, door opening, all show strong non abrupt change from row to row.

[13] For example dust flying through the beam, visible as extremely local changes.

[14] In-row change, mostly not visible in the rows before and after.

[15] Heavy duty machines turned on/off introduce very local or almost abrupt and then constant changes within one row and continuing through coming rows.

[16] Mostly local changes over few potential steps.

[17] For example, peeling leads to an abrupt change, which is then constant for some time.

[18] Using other software parallel leads to a slowed down LabVIEW run time, which ends in a reduced potential scan rate, visible as current overshoot due to lag.
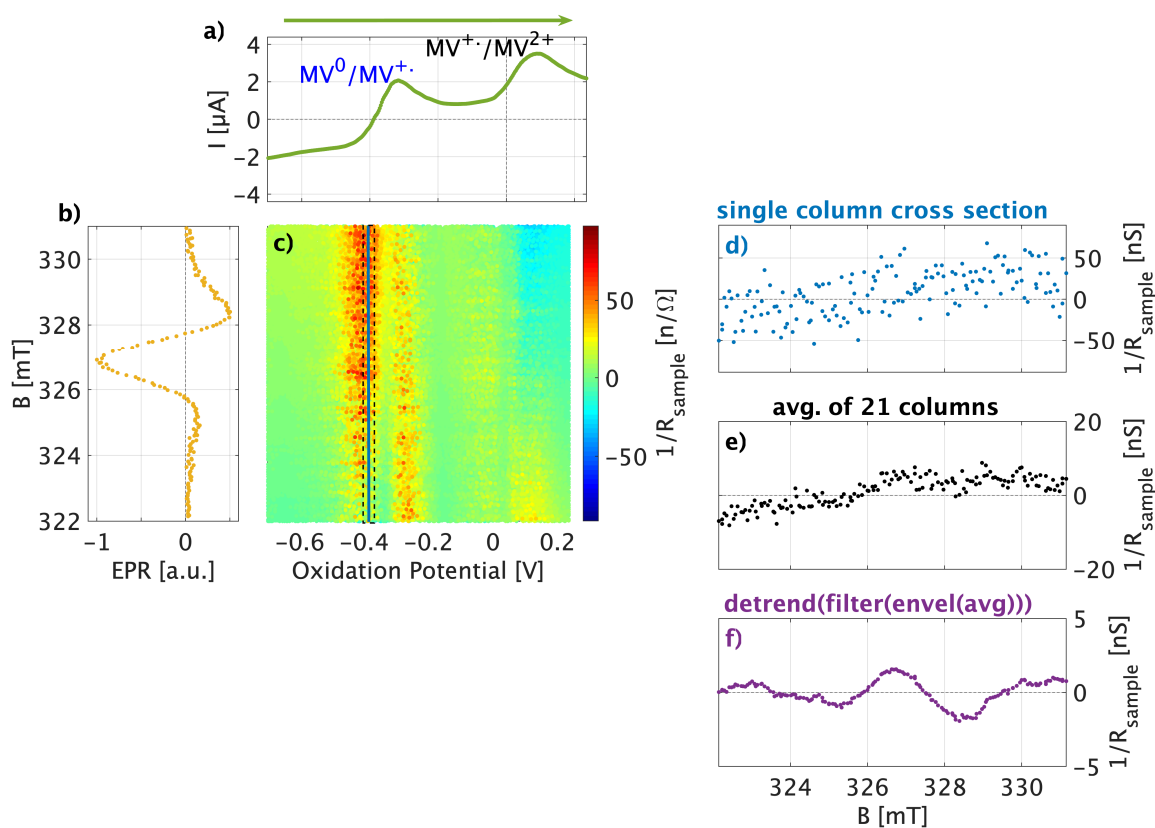
Figure 3.38 – llustration of data evaluation process at the hand of the oxidation direction scan in figure 3.37. a) shows the corresponding current, b) a column cross section of the corresponding simultaneous CW EPR matrix. c) is the difference to its mean, derived of figure 3.37 b). d) till f) displays the used evaluation algorithm, note the different y-axis scalings.

In section 4, cross section lines with obvious local variations which are not repeatable are therefore suppressed. Only samples showing repeatable patterns within several full matrix scans for the same sample and for different samples of same type are presented. Samples showing patterns around resonance only for one single matrix scan are not considered as actual signal and therefore not presented.

To perform a thorough EDMR measurement, several parts have to be calibrated and characterized for each sample again. The general setup calibration and adjustment consists in any case of the sample positioning such that the working electrode is situated in the cavity center, i.e. where the magnetic field of the microwave mode has its maximum, and subsequent matching and tuning of the cavity and microwave system as described in 2.2.1 and 3.1.5. For photo active working electrodes, also the laser light has to be calibrated as described in 3.1.3. After this, the CV has to be characterized so that the optimal potential range, and for photo active electrodes also the optimal light power, is known. The impedance characterization is important for the choice of the best potential modulation settings and the choice of resistance for the current pickup, see section 3.1.6. Potentiostat current range and lock-in sensitivity, phasing and time constant settings are self-evident. The sample resonance and maximal possible microwave power have to be determined. Only after such full calibration and characterization, a simultaneous electrochemical, EPR and EDMR measurement can be successfully performed. The time to build a good cell is at least one

and a half day. Full calibration, measurement and evaluation lasts at least two days and up to two weeks, depending on the chemical stability and inertness of the electrochemical cell.

3.2.2 Inter Measuring-System Interferences and Dependencies

Three systems are combined into one setup, electrochmical, CW EPR and EDMR. Interferences and dependencies on each other therefore must be examined. This concern mostly current induced resonance changes, magneto hydrodynamic effects on the electrochemical current and microwave induced CV shifts. Possible ways to minimize these effects are discussed. Ultimately, for each of these points, I will describe whether they could be spurious signals looking like resonance be the source of the observed resonant charge transfer change observed in section 4.

Electrochemical Current Effect on CW EPR

The general influence of an electrode system on the CW EPR result was illustrated on figure 3.26. Not only the presence of an electrode but also its orientation relative to B_0 strongly influence the EPR signal strength and MW power saturation behavior. This is potential independent and therefore not important for the EDMR discussion. However, the electrochemical process itself influences the EPR signal, as presented in figure 3.39. Subfigure a) shows the current recorded simultaneously with the EPR signal magnitude in c). The potential was scanned at $40\,\mathrm{mV/s}$ in the reduction direction i.e. positive to negative potential scanning direction without oxidation direction sweep. An average of several cross sections along the potential of a) is plotted in b). To actually see the EPR signal strength change, an average of all columns in c) was subtracted from each column, and d) shows the difference of each data point from the average as a function of the potential. The EPR signal strength increases to more negative potentials away from the center with a maximum at $-0.65\,\mathrm{V}$ vs. Pt, while it slightly decreases to more positive potentials with a minimum at approximately $0.15\,\mathrm{V}$ vs. Pt. This change of 4 % appears clearly, but it is not significantly larger than the actual noise level. This can be interpreted as a direct influence of the radical production and consumption. Beyond $-0.65\,\mathrm{V}$ vs. Pt the signal decreases, which is due to the domination of the $MV^{+\bullet}/MV^0$ process. This is an indication for how long $MV^{2+}/MV^{+\bullet}$and $MV^{+\bullet}/MV^0$are running parallel, before actual MV^{2+} diffusion limitation sets in.

A similar type of potential dependent resonance experiments on liquid samples was tried by other, using NMR.[131] Chazalviel suggested this in a similar manner to be used for producing highly spin polarized EPR samples. With respect to the resonant spin charge transfer detection, the effect shown in figure 3.39 is not very significant, since it affects mostly the CW EPR result. The production is proportional to the sweeping and not modulation at several 100 Hz, such that the lock-in signal is not probing this as modulation.

Magnetic Field Effects on Electrochemical Current

Figure 3.40 is a good example for a magneto hydrodynamic (MHD) effect. Subfigure a) shows the current for a scan from $-700\,\mathrm{mT}$ to $+700\,\mathrm{mT}$, while b) shows scanning from $+700\,\mathrm{mT}$ to $-700\,\mathrm{mT}$,

[131] S.-H. Cao, et al., "In Situ Monitoring Potential-Dependent Electrochemical Process by Liquid NMR Spectroelectrochemical Determination: A Proof-of-Concept Study", Analytical Chemistry **89**, 3810–3813 (2017).
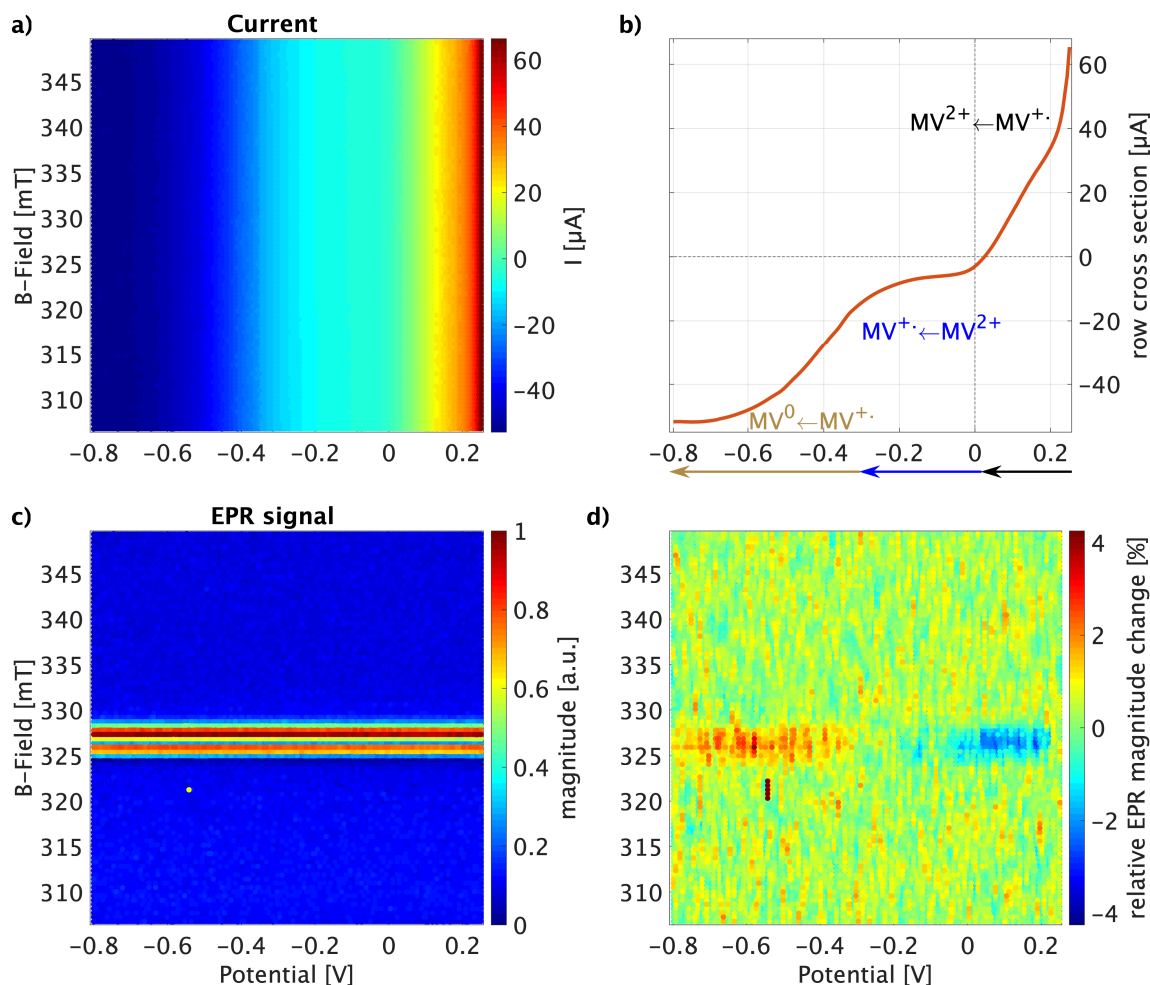
Figure 3.39 – EPR signal strength dependency on the electrochemical process at the example of p-GaAs. Subfigure a) shows the current recorded simultaneously with the EPR signal magnitude in c). b) is an average of several cross sections along the potential in a) with corresponding majority processes indicated. d) shows the difference of each data point from the average along the potential at same B_0 as relative EPR magnitude strength change c).

recorded with a coil type CE. Looking at a single color in a) or b), especially the light blue describes a curved shape, though it should be either relatively constant at the same potential for very stable samples or experience a current decrease at constant potential along the magnetic field scanning direction due to aging. The color change is due to stronger currents for increasing B_0 in absolute value at constant potential. It is most likely that this field dependency is due to magneto hydrodynamic effects (MHD) as described by Monzon and Coey and discussed in section 1. The curve shape is almost a semi circle, however not centered fully around 0 mT but with an offset, i.e. moved in magnetic field scanning direction such that for a) the semi circle maximum is at approximately +300 mT and for b) at −300 mT. This appears almost as a hysteresis effect, is however mostly due to moving electrodes, since no ferromagnetic elements are part of the sample. Also sample aging could explain this. However due to the way of suppressing the effect, I can conclude that cell aging was not the source: I am able to suppress both effects almost completely by spatially confining the liquid, using a straight rod as CE in front of the WE surface, keeping the quasi RE tip in front of the WE, and fixing all three electrodes against movement from each
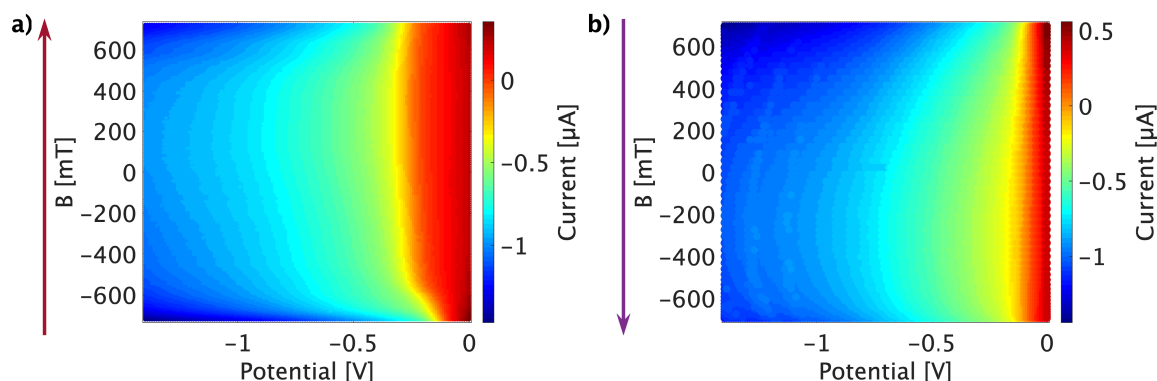
Figure 3.40 – Current dependency on magnetic field strength. Subfigure a) shows the current for a scan from $-700\,\text{mT}$ to $700\,\text{mT}$, while b) shows scanning from $700\,\text{mT}$ to $-700\,\text{mT}$. The electrode system was a Pt tip RE, Pt coil CE and p-GaAs WE with low light power to stay far below diffusion limitation.

other and in relation to the electrochemical cell. Up to fields of $5\,\text{T}$, my most recent cells do not show MHD larger than typical CV-to-CV change. However, EDMR confines the magnetic field range on a range of typically $320\,\text{mT}$ to $335\,\text{mT}$. The residual MHD is unimportant due to the use of resonance.

Another effect of the magnetic field can be seen looking at the MW reflected from the cavity. As visible in figure 3.41, the reflection shows an antisymmetric change around $0\,\text{mT}$. The lock-in offset change is several times larger than the actual EPR signal magnitude. The effect can be avoided by renewing matching and tuning. For some samples no such change along B_0 is visible. For other samples the symmetry is different. This effect can only be explained with impedance change due to a change in the matching condition caused by a shift in the position of the electrodes in the sample induced by the B_0 field. This again can not be the source for spin dependent current change since it is a non-resonant feature. Practically, this is important, because the changing MW reflection is ultimately a changed MW power at the sample. It is therefore essential to redo matching and tuning if swapping the B_0 direction.
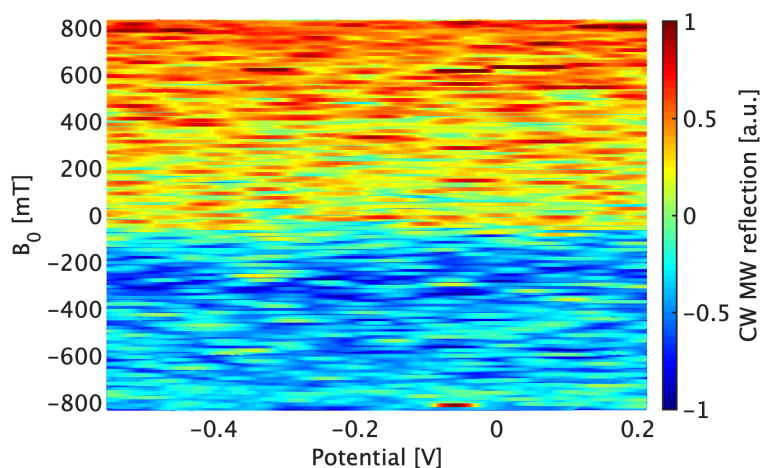
Figure 3.41 – B_0 dependent MW reflection at the example of Au/Al5/Cu. Visible is an offset change around $0\,\text{mT}$, which is potential independent.
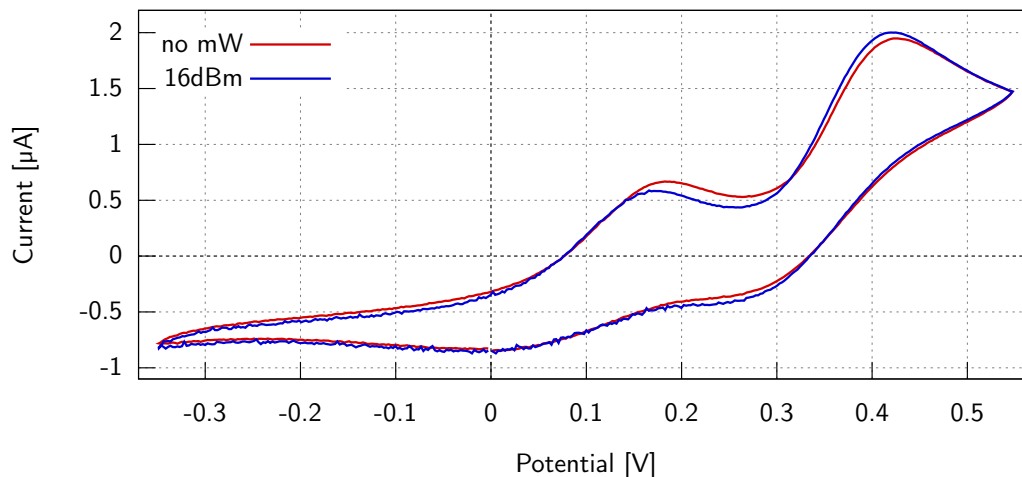
Figure 3.42 – Microwave induced CV change at the example of p-GaAs.

Microwave Induced Electrochemical Changes

Performing a CV before and after turning on the MW shows differences, such as those visible in figure 3.42. The shift is different for different CV regions and different samples. Microwave power has influence on the magnitude of this shift. Figure 3.42 presents a shift mostly visible at the oxidation peaks. This is the effect seen in most samples. However, some samples experienced shifts by up to 500 mV. The shifting is fast. Back shifting after turning off MW on the other hand is slow, taking some minutes. This can only be explained with a temperature change. If a CV is performed at 16 dBm it shows stronger noise, which is due to a heating process. Once a new equilibrium is reached, this noise disappears. Thus, the change is in any case constant, once the MW power is fixed. MW induced CV changes are therefore not relevant for resonance.

4 Resonantly Detected Spin-Dependent Electrode Processes

The combination of electrochemistry, EPR and EDMR into simultaneous measurements was performed on several samples with the aim to resonantly detect a spin dependent current change at the electrode/electrolyte interface. Only results which were repeatably reproduced with the same sample and with at least two different electrodes of the same type are presented in the following. This was the case for working electrodes of helicene, p-GaAs in combination with optical pumping, GaN/Au/Al5/Ag and GaN/Al5/Ag. For each type of sample only the best result is presented as example. All measurements presented in this chapter were performed with 2 mM $MV^{+\bullet}$ produced by electrolysis in a solution with 200 mM TBAP as supporting electrolyte dissolved in ACN. The RE was for all samples a Pt tip of 0.1 mm diameter and 0.5 mm length and the CE were either a Pt rod of 20 mm length or Pt coil (based rod of length 100 mm), both of diameter 0.5 mm.

The continuous potential sweep and stepwise B_0 sweep method of acquiring data, the resulting matrix representation and subsequent evaluation scheme which lead to the results presented below are discussed in section 3.2.1. The results are presented in the reverse chronological order in which they were obtained. The first sample, helicene, was the last one recorded. I show it first because it is the clearest and nicely readable result. The last presented sample, GaN/Al5/Ag, is a high-impedance sample. However, it was the first sample in which I observed a spin dependent current change at resonance using EDMR.

4.1 Helicene

The EDMR spectra, which are actually cross sections along the magnetic field at fixed potential are presented here for a helicene WE sample, following the evaluation system explained on figure 3.38. Thanks to my data accumulation method, I can generate EDMR spectra at various points on the cyclic voltammogram. I therefore chose the representation such as displayed in figure 4.1. The actual CV of the electrochemical cell is placed in the figure center, d), however turned by 90° counterclockwise, i.e. potential on the right y-axis and current on the x-axis. The corresponding majority processes are indicated as chemical reaction formulas close to the redox peaks and arrows outside the plot, color coded according to the product and pointing in scanning direction. The CV is the result of five averaged row cross sections of the reduction and oxidation direction current matrices. The corresponding CW EPR X lock-in results are presented in a) and b) and are the result
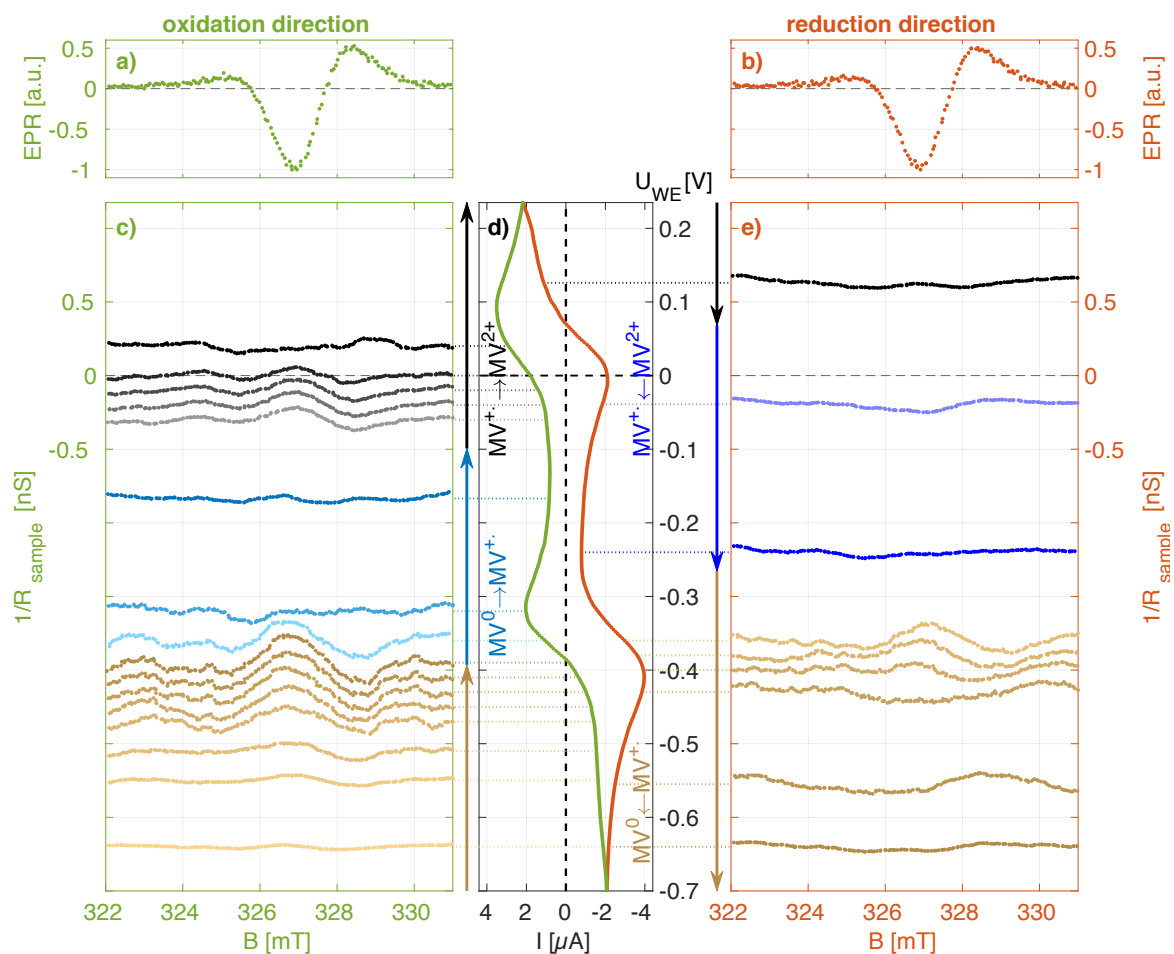
Figure 4.1 – Cross sections of the potential modulation EDMR result of helicene for the oxidation direction in c) and for the reduction direction in d). Figure a) and b) show the CW EPR average of 100 matrix columns, and d) an average of five rows of the current matrix. The dashed lines indicate the baseline, corresponding potential, and position in the CV. The CV reduction and oxidation peaks are labeled with the corresponding majority redox process. Arrows in scanning direction additionally indicate the majority process range in product color. The evaluation based matrix system is the result of an average of 7 consecutive matrix scans.

of an average over 100 column cross sections from the corresponding oxidation and reduction direction CW EPR matrices. Thus, as explained in chapter 3.2.1, they are not mere EPR spectra but reconstructed from the matrix of microwave reflection data. Subfigure c) and e) represent the EDMR spectra. They are not obtained as in normal spectroscopy. They are reconstructed from potential modulations EDMR X lock-in data matrices, expressed in conductance units. The spectra are shifted vertically, so that their baseline is aligned with the actual potential at which the cross section is taken in the lock-in data matrix.

The following color codings are used in this and all other figures: red stands for reduction direction potential sweep, green for oxidation direction, black corresponds to the majority MV^{2+} production range, blue for $MV^{+\bullet}$ production range, and brown for MV^0 production range. $MV^{+\bullet}$ blue color coding is further split into two nuances of blue to distinguish reduction and oxidation directions. The EDMR cross sections are additionally color coded with a color gradient in potential scanning direction to distinguish them more easily.

In the data representation of figure 4.1, every conductance cross section line is clearly affiliated with its corresponding potential position along the CV and with the CW EPR, which helps locate the field at which the resonance occurs. A complete set of equidistantly distributed conductance cross sections would be quite confusing. Focus was therefore given on cross sections where $1/R_{sample}$ changes around resonance. For potential ranges where no resonance was detected, only a few additional cross section lines are presented as representative of null result.

For this first type of sample, I will discuss the cross section patterns along the complete CV in full length. Let us start at approximately +0.7 V vs. Pt, i.e. 0 μA, and proceed in negative potential sweep direction, i.e. reduction direction. At 0 V vs. Pt the $MV^{2+}/MV^{+\bullet}$ reduction peak reaches its maximum strength. The $MV^{2+}/MV^{+\bullet}$ majority process continues until approximately −0.26 V vs. Pt, indicated with a blue arrow on the right. In this whole range, no consistent peak structure around the resonance range is visible on the cross section lines. We don't expect an EDMR signal, i.e. a spin effect, since here a diamagnetic molecule is reduced, i.e. electron tunneling to MV^{2+}, which is able to accept electrons with spins of either polarization.

At −0.26 V vs. Pt the current strength increases slowly again, indicating the beginning of the $MV^{+\bullet}/MV^0$ majority range, with its reduction peak maximum strength at −0.4 V vs. Pt and continuing until the most negative potential applied, −0.7 V vs. Pt. Just before the peak maximum, a peak appears in the EDMR spectrum, with its maximum at 327 mT, i.e. at resonance. This is also the region, where we expected a spin dependent current change due to the reduction of a paramagnetic molecule, i.e. tunneling of electrons which are spin polarized by the CISS effect to a spin polarized radical which is able to accept only electrons of opposite spin polarization. At resonance the radical spin polarization is disturbed. This is also the region where Chazalviel observed a spin dependent current change using his non-resonant method.[16] This pattern disappears again after the $MV^{+\bullet}/MV^0$ peak is passed, which is the diffusion limited depletion range. At −0.7 V vs. Pt we inverse the potential scanning direction, i.e. scan in oxidation direction. The region until −0.39 V vs. Pt is still of negative current, i.e. still majority $MV^{+\bullet}/MV^0$ reduction range, even though in the oxidation direction. Here again a pronounced peak in the EDMR spectra is observed, as it should, that confirms what had been observed in the reduction sweep. In fact, this resonance appears more pronounced than that in reduction direction. This might be due to a current noise decrease for small currents, which is typical for this type of electrochemical cell.

At −0.39 V vs. Pt the current goes through zero again, such that the last spectrum showing resonance corresponds clearly to the $MV^0/MV^{+\bullet}$ oxidation majority range. The $MV^0/MV^{+\bullet}$ majority range continues until approximately −0.1 V vs. Pt with an oxidation peak maximum strength at −0.33 V vs. Pt. Other than at the very onset of this part, this potential range does not show resonance. We do not expect any resonance in this $MV^0/MV^{+\bullet}$ oxidation range, since a diamagnetic molecule transfers an electron of either spin polarization to the electrode. From −0.1 V vs. Pt onward, the current increases, indicating the start of the $MV^{+\bullet}/MV^{2+}$ oxidation range with its maximum at +0.09 V vs. Pt and continuing until the upper end of the CV at +0.23 V vs. Pt. Resonance is here pronounced at the beginning of the $MV^{+\bullet}/MV^{2+}$ oxidation peak. For chiral molecules this is expected due to the CISS effect, according to which only spin polarized electrons coming from the paramagnetic radical of a certain spin polarization are accepted. However, this resonance pattern disappears already before the actual $MV^{+\bullet}/MV^{2+}$ oxidation peak slope starts. At +0.23 V vs. Pt we inverse the scanning direction again and scan in reduction direction. We are however still in the
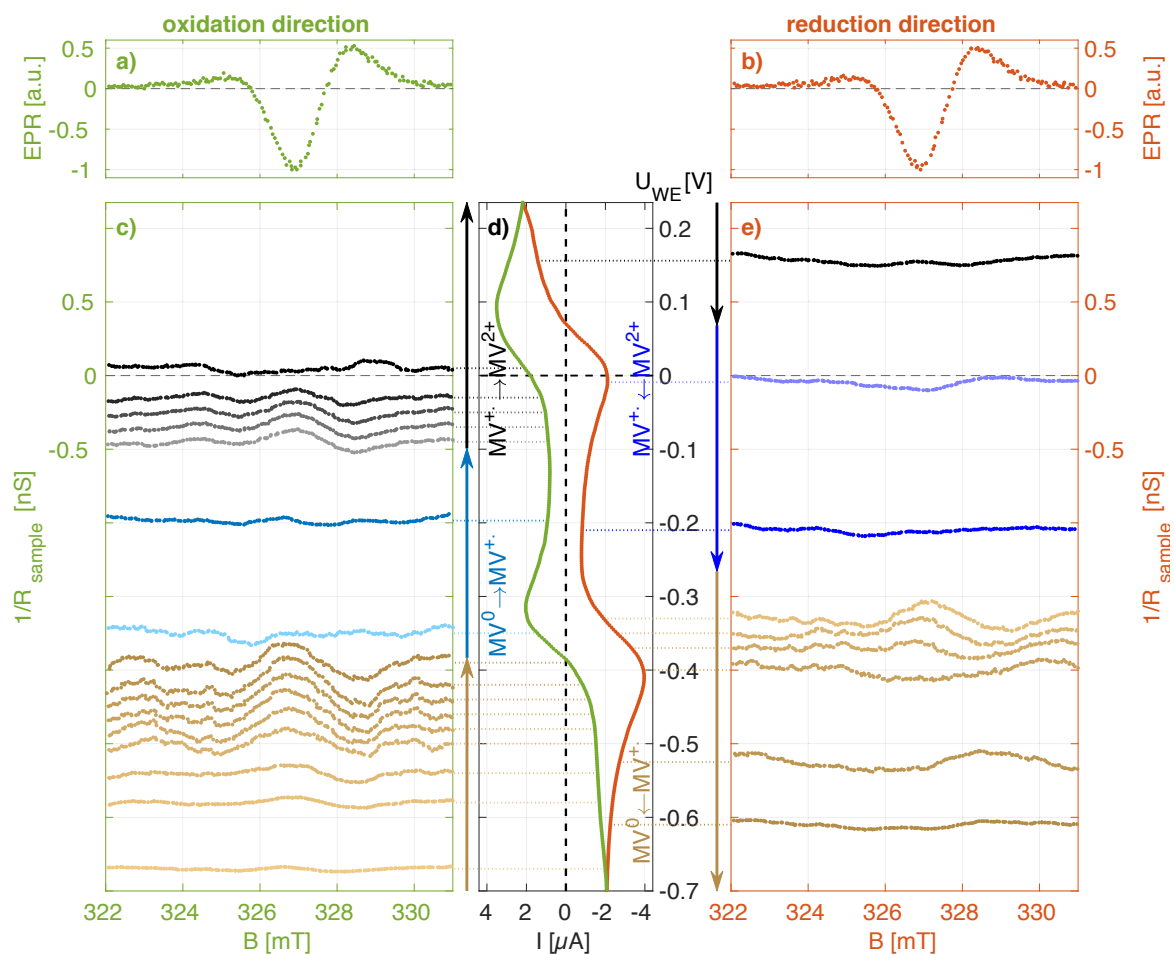
Figure 4.2 – Cross sections of the potential modulation EDMR result for helicene, including a 30 mV potential-shift against the scanning direction.

$MV^{+\bullet}/MV^{2+}$ majority oxidation range, which continues without showing resonance until +0.7 V vs. Pt, from where this result discussion along the CV started.

Apart from the first EDMR spectrum in oxidation direction at the $MV^0/MV^{+\bullet}$ oxidation range, all appearing or not appearing resonant conductance changes are compatible with the model presented in section 2.3. The appearance of resonance at the beginning of the $MV^0/MV^{+\bullet}$ oxidation range can be explained, once we include the potential shift correction described alongside figure 3.37 in section 3.2.1, which was described as induced by a combined effect of potential scan rate and lock-in integration time. As discussed there, for the used scan rate of 30 mV/s and integration time of 200 ms the appearing shift is of 30 mV in scanning direction. To account for this, I therefore replotted figure 4.1 with EDMR spectra moved by 30 mV to more positive potentials for the reduction direction, and by 30 mV to more negative potentials for the oxidation direction, as shown in figure 4.2. In this representation, the first cross section of the $MV^0/MV^{+\bullet}$ oxidation range is now situated just at the end of the $MV^{+\bullet}/MV^0$ reduction range, in which resonance is expected. Thus, in this corrected representation, all patterns of this helicene sample can be accounted for. Results presented below are directly potential-shift corrected and the applied shift is indicated.

Of course, the process majority regions have no abrupt beginning and ending, so that a resonance

can appear in between the regions I have marked.

Let us now proceed to a quantitative estimate of the effect. In view of equation 3.4, the relative current change at resonance is given by

$$\left(\frac{\Delta I_{WE}}{I_{WE}}\right)_{res} = \left(\frac{\Delta\left(\frac{1}{R_{sample}}\right)}{\frac{1}{R_{sample}}}\right)_{res},$$

since U_{WE} is resonance-independent. The conductance change at resonance has a maximal amplitude of approximately $\Delta\left(1/R_{sample}\right)_{res} \approx 0.25\,\text{nS}$ at approximately $-0.4\,\text{V}$ vs. Pt in oxidation direction. Due to lock-in offset considerations, the absolute conductance should not be taken directly from the lock-in signal (in contrast to difference values). Therefore, we calculate the conductance directly from the cyclic voltammograms. Thus, the conductance at $-0.4\,\text{V}$ vs. Pt is estimated as

$$\left(\frac{1}{R_{sample}}\right)_{res} = \left(\frac{dI_{WE}}{dU_{WE}}\right)_{res} \approx 24.5\,\mu\text{A}.$$

The maximal relative current change at resonance is therefore of

$$\left|\frac{\Delta I_{WE}}{I_{WE}}\right|_{res} = \left|\frac{\Delta\left(\frac{1}{R_{sample}}\right)}{\frac{dI_{WE}}{dU_{WE}}}\right|_{res} \approx \frac{0.25\,\text{nS}}{24.5\,\mu\text{S}} \approx 1.0 \cdot 10^{-5}.$$

Due to the used envelope-difference evaluation scheme, the sign of the current change can not be defined. Therefore, the values discussed must be understood as absolute value. As derived in section 2.3, we expect the relative spin dependent current change at resonance to be of at maximum of $1 \cdot 10^{-4}$ at most. There are two main artifacts that may explain why we did not reach this maximum effect: MW power saturation was not fully reached and spin relaxation takes place. This will be further discussed in section 4.5.

This is by far the best sample in terms of effect clarity. The quality of this sample is probably a combination of the stability intrinsic to helicene on gold, and of the experience gathered over the years as to how to produce a reliable sample, i.e. an electrochemical cell that fits in the microwave cavity. The resonance patterns of the samples discussed below are more elusive, and we will be guided in their evaluation by the present analysis. In view of the rather complex data treatment, an error propagation discussion would be difficult. What confirms us that we have indeed detected the spin effect is what we have observed it when the potential is right and not elsewhere. Furthermore, the data presented in figures 4.1 and 4.2 result from 7 consecutive matrix scans which are superposed. Resonance was visible in every one of those 7 scans. Averaging simply improved the SNR. The fact that we can superpose these matrix scans and enhance the SNR indicates that we have indeed detected a signal which adds up coherently when adding the matrix scans. This also illustrates the outstanding stability of this sample, which still showed a resonance in the EDMR spectra after 7 scans, i.e. after $7 \times 9\,\text{h} = 63\,\text{h}$ and therefore more than 2000 full CVs.

4.2 p-GaAs

The p-doped GaAs WE sample is more complex to discuss than the CISS samples because of the additional optical pumping process. Furthermore, bare p-GaAs is less stable than functionalized electrodes. This leads to larger CV changes over time. Averaging of whole matrices is due to this continuously changing experimental situation less effective. The light excitation and also the lower overall current increase the relative importance of the noise. As a consequence, the EDMR results are more broadened for p-GaAs electrodes than for the other electrodes I studied.

The CV presents broader features in the case of p-GaAs electrodes than for helicene on gold. The result in figure 4.3 includes the correction for the potential shift by 30 mV (data acquired with 30 mV/s and 200 ms time constant).

Change at resonance is pronounced in the EDMR cross sections in the reduction direction at the $MV^{+\bullet}/MV^0$ reduction range, and in the oxidation direction mostly at the $MV^{+\bullet}/MV^0$ reduction range and $MV^{+\bullet}/MV^{2+}$ oxidation range. This is very similar to the results obtained with helicene-functionalized Au electrodes. However, the regions are broader. An overlap of the $MV^{+\bullet}/MV^0$ reduction resonance signal into the $MV^0/MV^{+\bullet}$ oxidation range is visible. If we assume the helicene
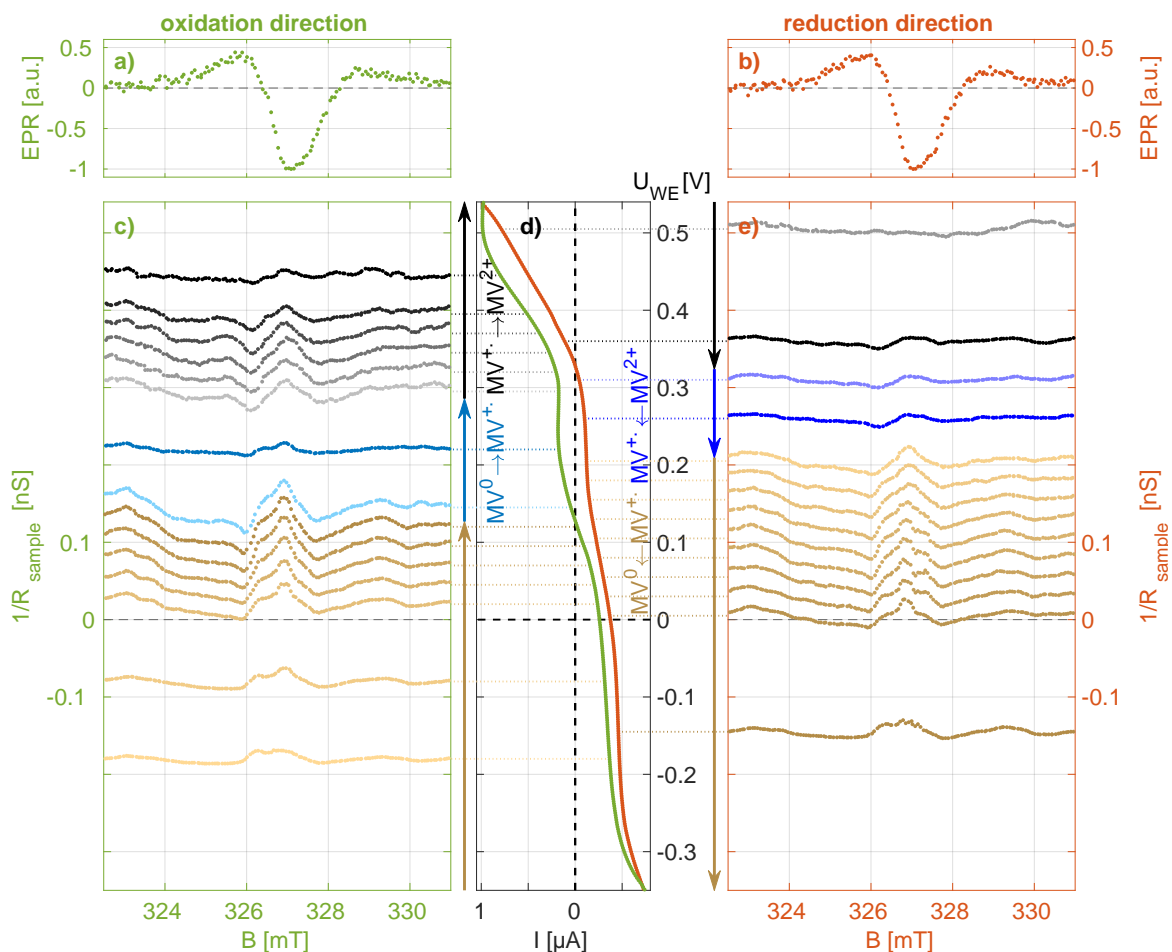

Figure 4.3 – Cross sections of the potential modulation EDMR result of p-GaAs including a 30 mV shift against the scanning direction.

result to be more reliable, such that a conductance change at resonance should only appear for the oxidation range of MV$^{+\bullet}$/MV^{2+} and the reduction range of MV$^{+\bullet}$/MV^0, we could conclude that the majority process ranges are for this p-GaAs sample overlapping over a much larger potential window. This could explain the extreme distortion of the CV, i.e. the fact that it is very tilted and the reduction peaks are not at all below the oxidation peaks.

The spin dependendent current change for optically pumped p-GaAs at resonance in reduction direction underlays the same argumentation as for chiral molecules, i.e. the spin polarized MV$^{+\bullet}$ radical is only able to accept electrons of opposite spin polarization and at resonance the radical spin-polarization is disturbed. However, during an oxidation process the explanation is different. As described in section 2.3, a current of electrons going directly into the electrode conduction band would most likely not, because the weak optical pumping we apply cannot be expected to fill the conduction band. To the contrary, in order to avoid spin relaxation of electrons in the conduction band, we have applied a weak optical pumping (below the CV limitation due to electrolyte diffusion sets on). Spin dependence can only be ascribed to optically pumped, spin polarized, electrons tunneling to a surface state, which can undergo a charge transfer with the ions at the electrode. The alternative would be an electron-hole recombination process. These holes can only be spin polarized from optical spin pumping. Therefore, only at potentials more negative than flat band potential, i.e. band down bending to the p-GaAs surface, we can expect majority wise spin polarized holes at the p-GaAs surface. As discussed in section 3.1.4 along figure 3.18, this is most likely not the case for the MV$^{+\bullet}$/MV^{2+} oxidation potential. Therefore, the detection of the EDMR spectrum under oxidation of MV$^{+\bullet}$/MV^{2+} implies that partially filled surface states or holes in the vicinity of the surface are responsible for this process.

Let us now consider the relative magnitude of the spin dependence in the case of p-GaAs. The maximum conductance change is for this sample in the order of $\Delta\left(1/R_{sample}\right)_{res} \approx 0.05\,\text{nS}$ at $U_{WE} \approx -0.1\,\text{V}$ vs. Pt in reduction direction, with a corresponding conductance of $(dI_{WE}/dU_{WE})_{res} = 3.6\,\mu\text{S}$, i.e.

$$\left|\frac{\Delta I_{WE}}{I_{WE}}\right|_{res} = \left|\frac{\Delta\left(\frac{1}{R_{sample}}\right)}{\frac{dI_{WE}}{dU_{WE}}}\right|_{res} \approx \frac{0.05\,\text{nS}}{3.6\,\mu\text{S}} \approx 1.4\cdot10^{-5}.$$

This is in the same range as helicene, which is surprising because the charge transfer process of the p-GaAs electrode is likely involving surface states.

4.3 GaN/Au/Al5/Ag

The GaN/Au/Al5/Ag samples was solely studied in reduction direction, see discussion in connection with figure 3.35. As no light excitation is needed, the sample orientation can be chosen freely to examine the influence of the WE orientation relative to B_0. I carried out my measurements for two directions, WE facing B_0 in a) to c) of figure 4.4, and the WE surface aligned with B_0 in d) to f). The molecules are presumed to be pointing away from the surface, though not perfectly orthogonal to it. The electrode orientation in which B_0 is normal to the surface is expected to be one of maximum spin dependence effects.
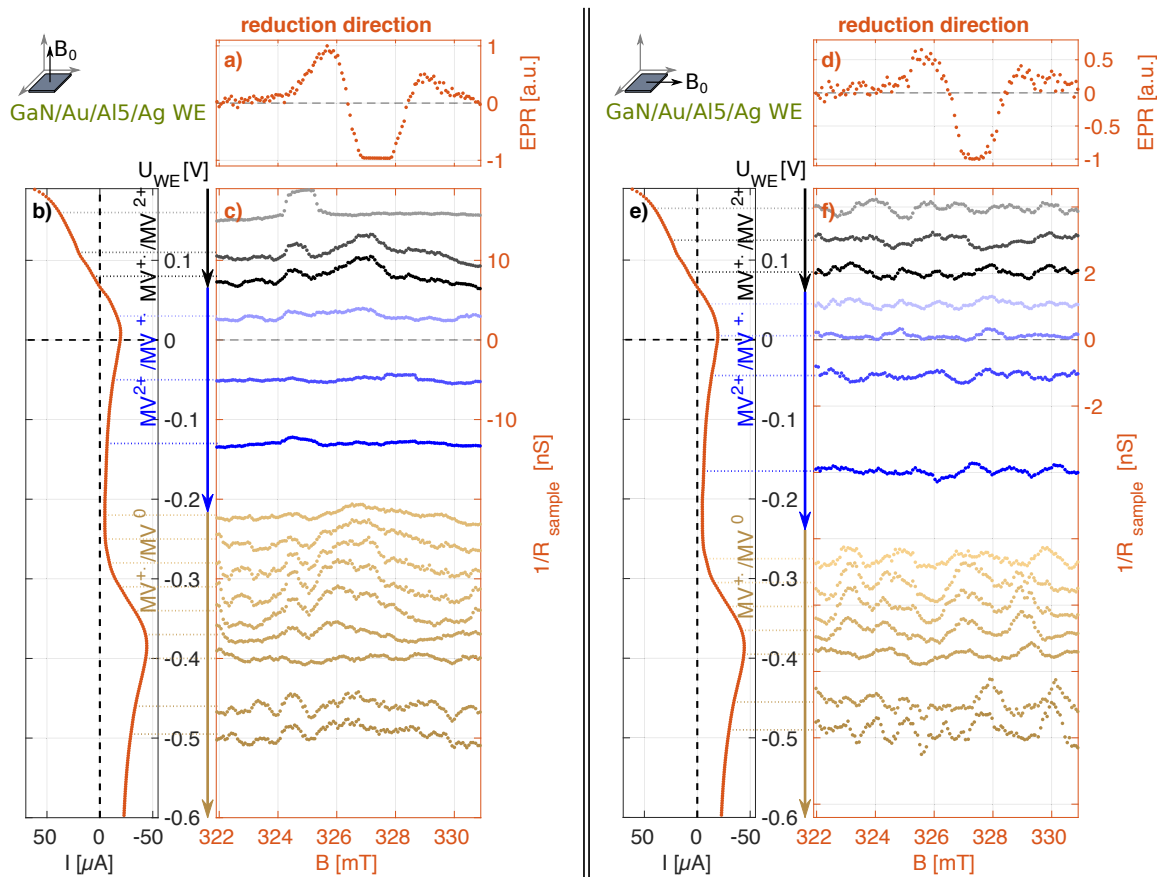
Figure 4.4 – Cross sections of the potential modulation EDMR result of GaN/Au/Al5/Ag including a 75 mV shift against the scanning direction. Only the reduction direction was recorded. Subfigures a) till c) represent an orientation of the WE facing B_0, showing an average of two scans with 10 s waiting time between the potential scans. Presented is an average of two consecutive scans. Subfigures d) till f) are for an orientation of the WE parallel with B_0, showing an average of four consecutive scans with 10 s waiting time between the potential scans.

The potential shift correction is here of 75 mV (500 mV/s integration time and 30 mV/s scan rate). As for helicene in reduction direction, a spin dependent current change at resonance appears mostly in front of the $MV^{+\bullet}/MV^0$ reduction peak. Resonance for this sample is also visible before the $MV^{2+}/MV^{+\bullet}$ reduction peak. This potential range is in fact the $MV^{+\bullet}/MV^{2+}$ majority oxidation range, for which a resonance effect on the current can be expected. Indeed, it is observed for helicene and p-GaAs, though in the oxidation direction. For the helicene and p-GaAs resonance, it was not observed in the reduction scanning direction. This can be explained based on the different scanning potential patterns that I used. For this sample only the reduction direction was scanned. The $MV^{+\bullet}/MV^{2+}$ oxidation peak is therefore not passed. Diffusion limitation has not set in yet when the potential scanning is done this way.

Let us now turn to the relative size of the effect. The maximum effect for WE orientation facing B_0 is here in the order of $\Delta\left(1/R_{sample}\right)_{\perp res} \approx 5\,\mathrm{nS}$ at $U_{WE} \approx -0.25\,\mathrm{V}$ vs. Pt, with a corresponding

conductance of $(dI_{WE}/dU_{WE})_{\perp res} = 100\,\mu S$, i.e.

$$\left|\frac{\Delta I_{WE}}{I_{WE}}\right|_{\perp res} = \left|\frac{\Delta\left(\frac{1}{R_{sample}}\right)}{\frac{dI_{WE}}{dU_{WE}}}\right|_{\perp res} \approx \frac{5\,\text{nS}}{100\,\mu S} \approx 5.0\cdot 10^{-5}.$$

For the electrode orientation where B_0 is in plane, f), the current change at resonance is extremely weak and only slightly visible before and after the $MV^{+\bullet}/MV^0$ reduction peak. The maximum effect is here of the order of $\Delta\left(1/R_{sample}\right)_{\parallel res} \approx 1\,\text{nS}$ at $U_{WE} \approx -0.37\,\text{V}$ vs. Pt, with a corresponding conductance of $(dI_{WE}/dU_{WE})_{\parallel res} = 180\,\mu S$, i.e.

$$\left|\frac{\Delta I_{WE}}{I_{WE}}\right|_{\parallel res} = \left|\frac{\Delta\left(\frac{1}{R_{sample}}\right)}{\frac{dI_{WE}}{dU_{WE}}}\right|_{\parallel res} \approx \frac{1\,\text{nS}}{180\,\mu S} \approx 5.6\cdot 10^{-6}.$$

The current change observed at an orientation of the WE normal to B_0 is according to this approximation almost ten times larger than for the WE with in plane B_0. This large difference is expected, since the spin polarization of electrode and electrolyte are orthogonal to each other when the WE is in plane with B_0.
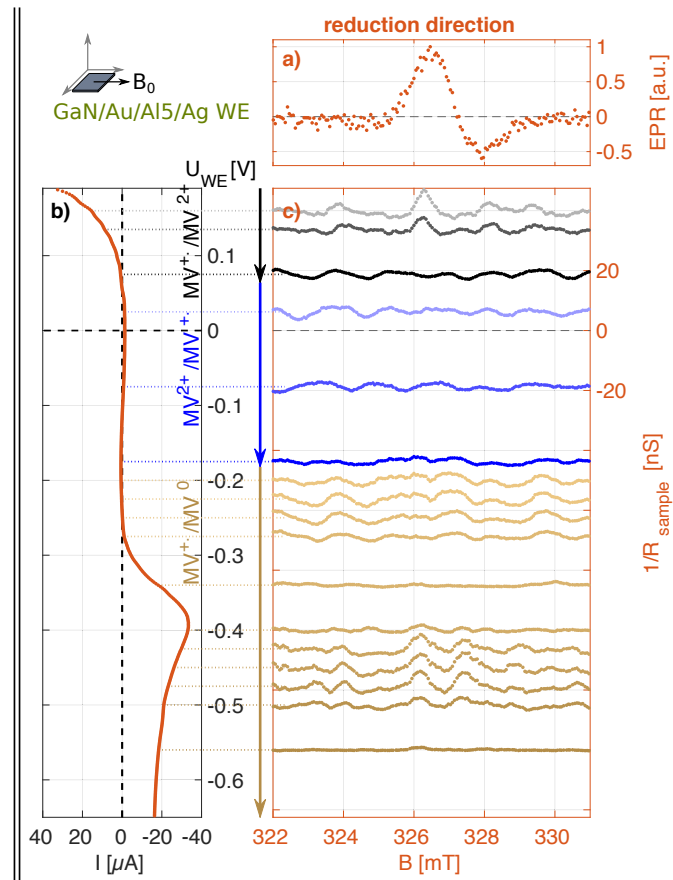

Figure 4.5 – Cross sections of the potential modulation EDMR result of GaN/Au/Al5/Ag for an orientation of the WE surface parallel to B_0 with 30 mV shift against the scanning direction. Here, only the reduction direction was recorded.

These results were obtained with a coil as CE. For this sample type, a cell with straight Pt rod CE was built. The result presented in figure 4.5 was the first recorded sample with a straight CE and it was used for in-plane orientation. Unfortunately, this sample turned out to be less stable, so that no measurement in perpendicular orientation could be performed. However, the result is less noisy and well pronounced conductance changes at resonance are visible in the $MV^{+\bullet}/MV^{2+}$ oxidation range and the $MV^{+\bullet}/MV^0$ reduction range. This clear improvement speaks in favor of using Pt rods rather than coils as CE. It is surprising, that the $MV^{+\bullet}/MV^0$ pattern at resonance only appears behind the corresponding reduction peak and not at the increasing slope of the $MV^{+\bullet}/MV^0$ reduction peak as is the case for helicene and p-GaAs in 4.1 and 4.2. Looking at the current, this is a range of 10 to 40 times the current as in 4.1 and 4.2. Strong currents usually showed stronger noise most likely induced by turbulences, such that the disappearance might be due to SNR decrease. In any case, a resonance detected by EDMR in this sample orientation can only be interpreted as a molecule orientation partly not perpendicular to the surface.

The maximal effect is here in the order of $\Delta\left(1/R_{sample}\right)_{\parallel res} \approx 0.5\,\mathrm{nS}$ at $U_{WE} \approx -0.49\,\mathrm{V}$ vs. Pt, with a corresponding conductance of $(dI_{WE}/dU_{WE})_{\parallel res} = 90\,\mu\mathrm{S}$, i.e.

$$\left|\frac{\Delta I_{WE}}{I_{WE}}\right|_{\parallel res} = \left|\frac{\Delta\left(\frac{1}{R_{sample}}\right)}{\frac{dI_{WE}}{dU_{WE}}}\right|_{\parallel res} \approx \frac{0.5\,\mathrm{nS}}{90\,\mu\mathrm{S}} \approx 5.6 \cdot 10^{-6}.$$

This is the same result as for the sample in figure 4.4 but with increased SNR from using the Pt rod CE.

4.4   GaN/Al5/Ag

This electrode type has no gold at the surface. However, the GaN substrate contains a 2D electron gas which determines the electrode conductance. The measurements were performed in the same manner as for GaN/Au/Al5/Ag, i.e. only reduction direction for WE normal to B_0, a) to c), and for the WE with B_0 in plane, d) to f) in figure 4.6.

The resonance was located near the matrix edge. The WE orientation with B_0 in plane was recorded first and is the result of an average of four matrices. The WE orientation normal to B_0 was recorded afterwards and unfortunately the electrochemical cell stopped working after this first scan, which explains its higher noise level in e.g. the CW EPR line cut (lack of averaging). For both orientations only a small conductance change at resonance is visible, which is for c), before the $MV^{+\bullet}/MV^0$ reduction peak and for f), after it. The pattern in f) appears larger than in c), however it is only the SNR which is different.

The maximum effect for the GaN/Al5/Ag WE orientation normal to B_0 is here in the order of $\Delta\left(1/R_{sample}\right)_{\perp res} \approx 2\,\mathrm{pS}$ at $U_{WE} \approx -0.38\,\mathrm{V}$ vs. Pt, with a conductance of $(dI_{WE}/dU_{WE})_{\perp res} = 160\,\mathrm{nS}$, i.e.

$$\left|\frac{\Delta I_{WE}}{I_{WE}}\right|_{\perp res} = \left|\frac{\Delta\left(\frac{1}{R_{sample}}\right)}{\frac{dI_{WE}}{dU_{WE}}}\right|_{\perp res} \approx \frac{2\,\mathrm{pS}}{160\,\mathrm{nS}} \approx 1.2 \cdot 10^{-5}.$$
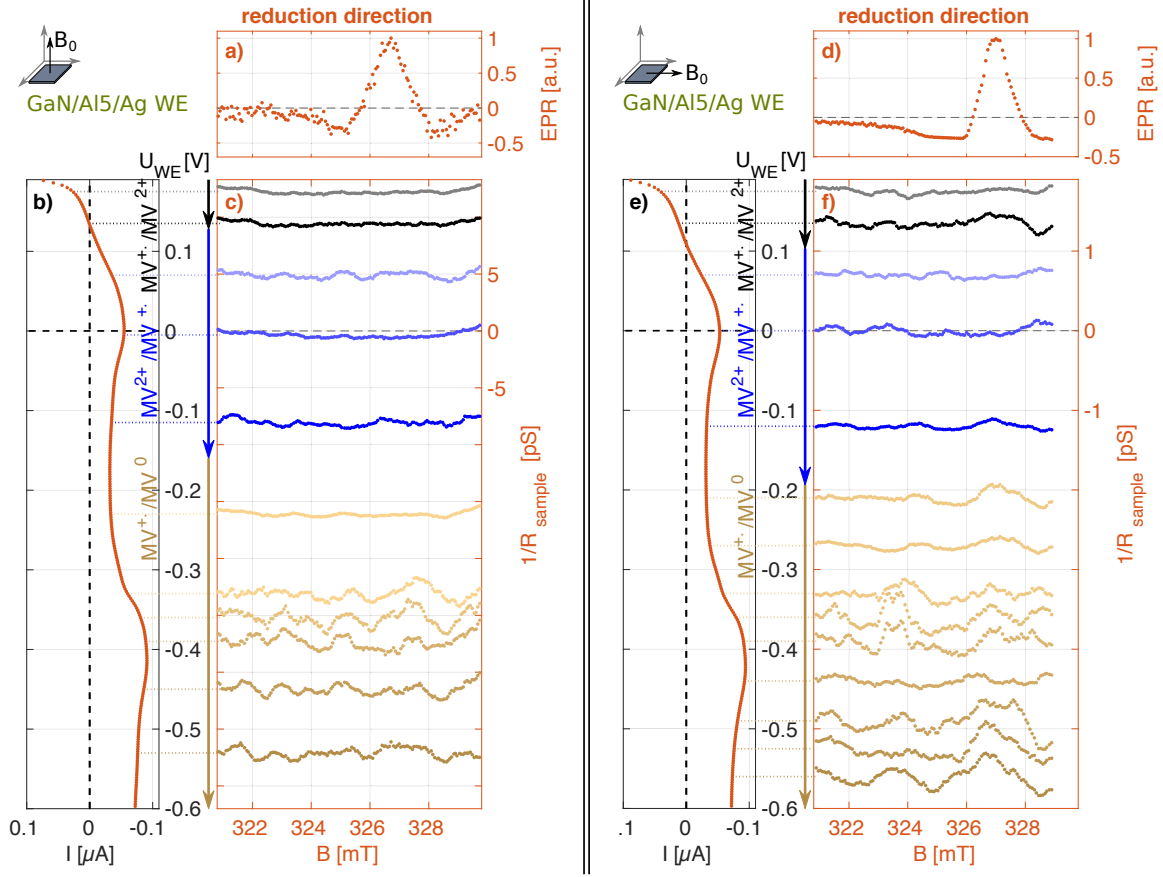
Figure 4.6 – Cross sections of the potential modulation EDMR result of GaN/Al5/Ag including a 30 mV shift against the scanning direction. Here, only the reduction direction was recorded. Subfigures a) till c) are for an orientation of the WE facing B_0, showing a single scan with 120 s waiting time between the potential scans. Subfigures d) till f) are for an orientation of the WE parallel with B_0, showing an average of four consecutive scans with 10 s waiting time between the potential scans.

The maximum effect of this GaN/Al5/Ag WE for an orientation with B_0 in plane is here of the order of $\Delta\left(1/R_{sample}\right)_{\parallel res} \approx 0.5\,\text{pS}$ at $U_{WE} \approx -0.48\,\text{V}$ vs. Pt, with a corresponding conductance of $(dI_{WE}/dU_{WE})_{\parallel res} = 210\,\text{nS}$, i.e.

$$\left|\frac{\Delta I_{WE}}{I_{WE}}\right|_{\parallel res} = \left|\frac{\Delta\left(\frac{1}{R_{sample}}\right)}{\frac{dI_{WE}}{dU_{WE}}}\right|_{\parallel res} \approx \frac{0.5\,\text{pS}}{210\,\mu\text{S}} \approx 2.3\cdot10^{-6}.$$

The effect at an orientation of the WE normal to B_0 is according to this approximation 5 times larger than for the WE with B_0 in-plane, which is in agreement with the result of GaN/Au/Al5/Ag. Because there is no gold on this electrode, the electrochemical current is much smaller than when GaN is covered with gold. As a consequence, the SNR is quite low in this case.

4.5 Result Comparison

Figure 4.7 and table 4.1 sum up the results presented in section 4 and compare the different samples and orientation. Table 4.1 also includes all experimental conditions which could affect the result. On the left in figure 4.7 the examined samples are named. Next to their names, color coded bars are drawn, which indicate with their thickness how strong a current change at resonance was observed at the potential below or above which they are drawn. The bars below the CV correspond to reduction direction, the ones above the CV to the oxidation direction. It appears, that for all samples a current change at resonance occurs when the $MV^{+\bullet}$ radical is the reactant, i.e. in the $MV^{+\bullet}/MV^0$ reduction majority range in both scanning directions. No current change occurs for the $MV^{+\bullet}$ production, neither in reduction nor oxidation direction. For the oxidation of $MV^{+\bullet}/MV^{2+}$, an effect is clearly visible in the oxidation direction, however only in reduction direction when not a full CV is performed but only reduction sweeps without long waiting time between the CV. This is in stark contrast to the $MV^{+\bullet}/MV^0$ behavior, which is better visible in the
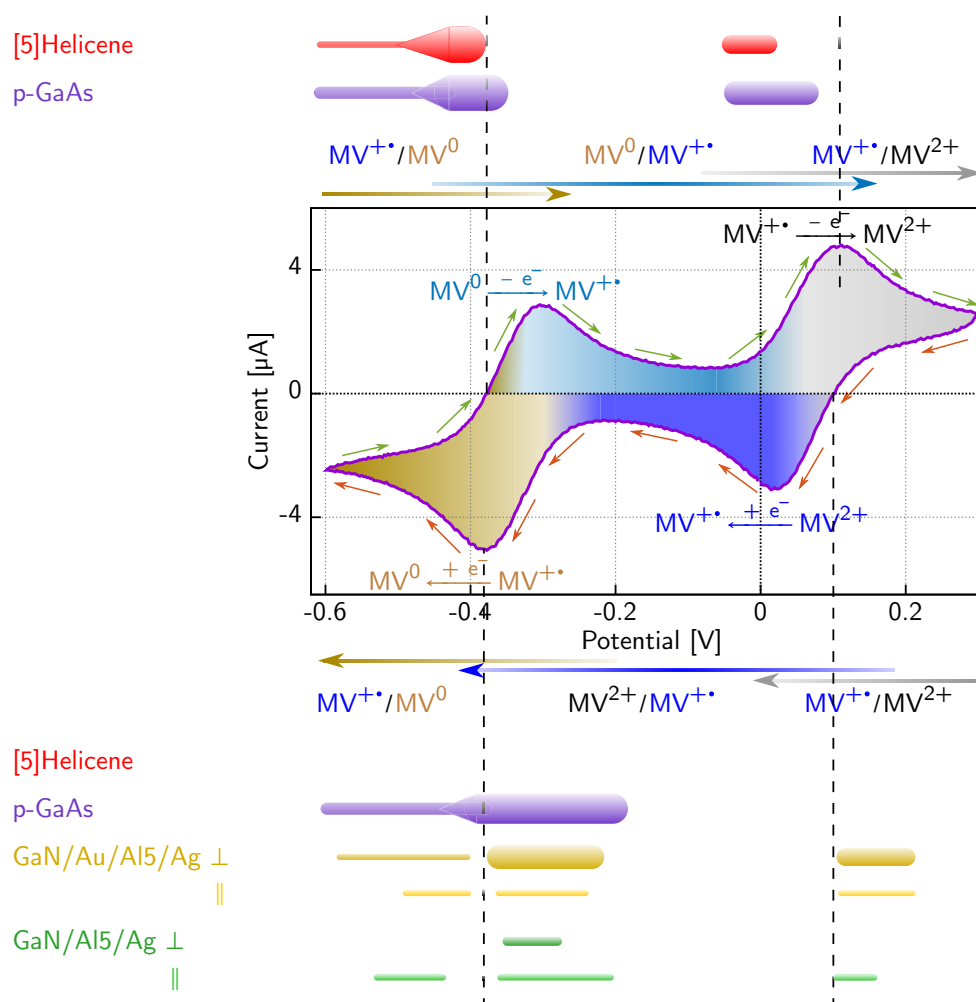
Figure 4.7 – Comparison of current change potential range and in-sample relative strength. The CV has all appearing ranges and overlapping regions indicated. Above (below) of the CV, the sample types measured for the oxidation (reduction) direction are indicated. The corresponding, color coded bars indicate at what potential the current change at resonance was observed, and the effect strength is indicated with the thickness of the bar.

Table 4.1 – EDMR result comparison for all samples.

$\left|\frac{\Delta I_{WE,res}}{I_{WE,res}}\right|$ indicates the maximal current change at resonance.

$I_{WE,res}$ - Corresponding current.

"WE surface" - WE surface area taking part in electrochemical processes.

"WE contacting " - "f_{Cu}" contact with copper cable front side, "b_{Cu}" contact on back side (current goes though substrate), "f_{Au}/b_{Cu}" contact with gold wire at front leading to backside for copper contact.

"Pt CE" indicates the type of Pt CE, i.e. rod or coil.

"break' - delay time between two consecutive CV.

"E_{mod} ptp" - Peak to peak potential modulation amplitude.

"scan rate" - Potential staircase sweep scan rate.

"int. time" - Integration time.

"pot. shift" - Applied potential shift, except figure 4.1.

"sample age" - age of the sample in amount of full CV, respectively amount of half CV at the beginning of the evaluated matrix scan (rounded).

"average of" - indicates if the presented result is from a single matrix scan or an average of matrices.

"quality" - quality of the final plot as presented in section 4, reaching from excellent (++), good (+), bad (−+) till hardly evaluable (−).

"effect visible" - in-sample and overall comparison of effect strength at the indicated reduction / oxidation region and direction, reaching from not measured ( ), no resonance effect (−), hardly visible (−+), visible (+) till very strong and clear (++).

"?" indicates a questionable result.

	5Helicene	p-GaAs	AuAl5Ag ⊥	∥	∥ #2	Al5Ag ⊥	∥
$\left\|\frac{\Delta I_{WE}}{I_{WE}}\right\|_{res}$	$1\cdot10^{-5}$	$1\cdot10^{-5}$	$5\cdot10^{-5}$	$6\cdot10^{-6}$	$6\cdot10^{-6}$	$1\cdot10^{-5}$	$2\cdot10^{-6}$
$I_{WE,res}$	0.5 µA	1 µA	6 µA	40 µA	22 µA	0.08 µA	0.07 µA
WE surface	1 mm²	1 mm²	10 mm²		9 mm²	6 mm²	
WE contact	f_{Cu}	b_{Cu}	f_{Au}/b_{Cu}		f_{Cu}	f_{Au}/b_{Cu}	
Pt CE	rod	rod	coil		rod	coil	
break	0 s	10 s	10 s		10 s	120 s	10 s
E_{mod} ptp	8 V	3.5 V	7 V		3.5 V	7 V	
scan rate	30 $\frac{mV}{s}$	30 $\frac{mV}{s}$	30 $\frac{mV}{s}$		20 $\frac{mV}{s}$	30 $\frac{mV}{s}$	
int. time	200 ms	200 ms	500 ms		500 ms	200 ms	
pot. shift	30 mV	30 mV	75 mV		50 mV	30 mV	
sample age	10	10	$\frac{1}{2}$ 500	$\frac{1}{2}$ 1250	$\frac{1}{2}$ 20	$\frac{1}{2}$ 10	$\frac{1}{2}$ 650
average of	7	3	2	1	1	1	4
quality	++	+	+	−	+	−+	−
effect visible							
reduction dir.							
MV$^{+\bullet}$/MV^{2+}	−	?	+	−	+	−	−+
MV^{2+}/MV$^{+\bullet}$	−	?	−	−	−	−	−
MV$^{+\bullet}$/MV^{0}	+	++	++	−+	+	−+	+
oxidation dir.							
MV$^{+\bullet}$/MV^{0}	++	++					
MV^{0}/MV$^{+\bullet}$	−	?					
MV$^{+\bullet}$/MV^{2+}	+	++					

"wrong" direction.

Looking closer, the signals are strongest before diffusion limitation sets in, i.e. at the increasing redox peak slopes, which correspond to the kinetically dominated regions for the $MV^{+\bullet}/MV^0$ reduction in reduction direction and $MV^{+\bullet}/MV^{2+}$oxidation in oxidation direction. The current change at resonance almost always disappears at the current peak maxima. In the diffusion limited regions a current change is observable, but mostly diminished. However, after inverting the scanning direction, i.e. $MV^{+\bullet}/MV^0$ reduction in the oxidation direction and $MV^{+\bullet}/MV^{2+}$oxidation in the reduction direction, the current change at resonance is more clearly visible. This is most likely due to a SNR increase as result from a more stable current.

The clearest results are achieved with small WE surfaces of good conductance. The small surface area reduces the diffusion limitation, see figure 3.34. Also the use of a straight CE in front of the WE results in more stable currents compared to coils. This might be not so much because of the potential modulation and vibration-induced induction currents and voltages, but rather from the positioning of the CE directly in front of the WE.

The orientation of the WE facing B_0 shows as expected a larger spin dependent current change at resonance than the orientation of the WE surface with B_0 in plane. Long helical molecules typically do not attach to a surface in an orthogonal manner but are rather connected at some angle.

Resonance was also tested for inverted field direction. One would expect opposing $\left(\frac{\Delta I_{WE}}{I_{WE}}\right)_{res}$ sign values for $+B_{res}$ and $-B_{res}$. This also applies to opposing light and helicity. However, so far this is not detectable due to the use of envelopes in the evaluations.

The Al5 functionalized samples with Cu nano particle endings showed only extremely blurry patterns at resonance in the conductance matrix. These electrodes were also far less stable than GaN/Al5/Ag and GaN/Au/Al5/Ag. The result for copper nano particle endings is not presentable in the manner of section 4 and a quantitative evaluation is not possible. The instability is either due to less chemical stability of the Cu nano particle, more chemisorption of MV at the fucntionalized WE surface or worse bonding of the chiral molecules to the substrate. Due to the lower sample stability, it is not possible to state whether the weakness of the signal can be attributed to a shorter spin diffusion length in Cu than in Ag.

The most stable sample, Au/Al5/Ag, lost its resonance sensitivity only after more than 6000 reduction direction sweeps, though the last results were extremely weak. Also the helicene samples show similar stability. The CV typically change within the first 50 to 100 scans, after which the sample were in general stable for several thousand CV. The only exception is bare p-GaAs, which typically is not functioning in a normal manner anymore after already approximately 500 CVs.

Only at the end of this thesis, we found the helicene samples not being actually enantiopure. Assuming actual racemic mixture, one could not expect a spin filtering effect. However, due to the natural predominance of one helicity one can assume an imperfect racemic state and therefore in average only a decreased and not net zero spin selectivity. The detected spin effect could also has its origin in a preferred adsorption of one helicity. If the WE coating was however actually racemic, then the observation of a spin dependent current change at resonance could only be explained by

methyl viologen being pro-chiral and becoming chiral by adsorption.[132]

For direct comparison with literature, it is useful to also calculate the relative spin dependent charge transfer rate difference using equation 2.31,

$$\frac{k_{+\frac{1}{2}} - k_{-\frac{1}{2}}}{k_{+\frac{1}{2}} + k_{-\frac{1}{2}}} \approx \frac{\left(\frac{\Delta I_{WE}}{I_{WE}}\right)_{res}}{2W^{MW}T_1 \frac{\Delta N^0}{N^0}}.$$

As discussed in section 2.3, the radical spin polarization at room temperature and 335 mT is of $\frac{\Delta N^0}{N^0} \approx 8 \cdot 10^{-4}$, and at MW power saturation we have $2W^{MW}T_1 \approx \frac{1}{3} \ldots 1$. Using the above values for $\left(\frac{\Delta I_{WE}}{I_{WE}}\right)_{res}$, we get for Al5 a maximal relative spin dependent charge transfer rate difference of

$$\left(\frac{k_{+\frac{1}{2}} - k_{-\frac{1}{2}}}{k_{+\frac{1}{2}} + k_{-\frac{1}{2}}}\right)_{Al5} \approx 6 \ldots 19\,\%.$$

Literature states in this case a spin polarization of 8 %,[90] which lays well in our range. For p-GaAs, we have

$$\left(\frac{k_{+\frac{1}{2}} - k_{-\frac{1}{2}}}{k_{+\frac{1}{2}} + k_{-\frac{1}{2}}}\right)_{p-GaAs} \approx 2 \ldots 5\,\%,$$

while literature suggests 10 %.[95] Our value is hereby in a region less than half of the literature value. This can be explained with the different nature of experimental situation. The literature value is found as value inside a solid state system, while our value corresponds to the spin polarization after passing the interface, i.e. including the spin relaxation time, which may occur during a surface-state-mediated transport. For [5]helicene, we have

$$\left(\frac{k_{+\frac{1}{2}} - k_{-\frac{1}{2}}}{k_{+\frac{1}{2}} + k_{-\frac{1}{2}}}\right)_{[5]helicene} \approx 1 \ldots 4\,\%.$$

No literature value for [5]helicene exists. However, the spin filtering efficiency of [4]helicene was found to be 4 %,[92] and for [7]helicene of around 6 … 8 %.[91] We can therefore assume that the spin filtering efficiency of [5]helicene should be somewhat larger than 4 %. Our value is hereby just at the lower limit of this estimate. A discrepancy can be expected since our [5]helicene was not enantiopure.

[132] F. Zaera, "Chirality in adsorption on solid surfaces", Chemical Society Reviews **46**, 7374–7398 (2017).

5 Outcome Discussion and Prospects

Within this thesis I developed a system to produce a stable $MV^{+\bullet}$ radical-rich electrolyte and perform electrochemical measurements using electrodes functionalized with chiral molecules or optically pumped p-GaAs electrodes. The measurements consisted of simultaneously performed CW EPR and EDMR measurements for at least several days in normal laboratory conditions. The results show a sensitivity down to at least picoamps. With this system, I could show a spin dependent charge transfer. The spin dependence was demonstrated by exciting the spin resonance of radicals in the electrolyte.

The spin dependent current change at resonance was manifested on the $MV^{+\bullet}/MV^0$ reduction majority potential range and the $MV^{+\bullet}/MV^{2+}$ oxidation majority potential range, i.e. processes which consume the paramagnetic methyl viologen state. The relative current change for the reduction of $MV^{+\bullet}$ to MV^0 was most pronounced at the increasing reduction peak. This result confirms Chazalviel's results.[16] This effect is evidenced for both types of electrodes, i.e. optical
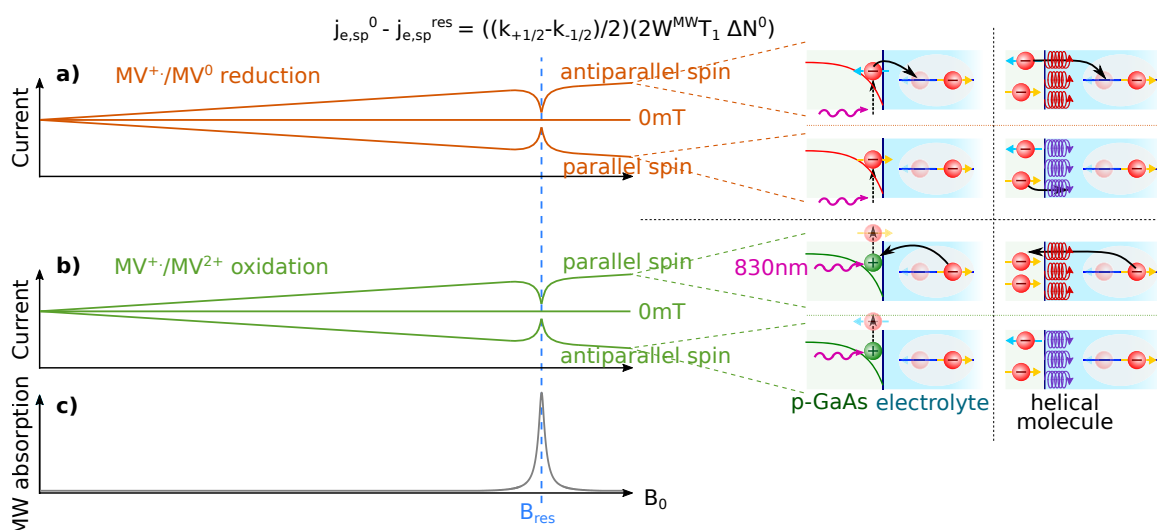

Figure 5.1 – Spin dependent current change sign at resonance. a) depicts the increasing and decreasing current along B_0 depending on the relative spin polarization of electrode and radical for p-GaAs and helicene and corresponding current change direction at resonance. b) depicts the same for the oxidation. c) depicts the radical's MW absorption.

spin pumping on p-GaAs and covered with chiral molecules. The spin dependence in this process is the acceptance of a spin polarized electron on the spin polarized radical which excludes parallel electron spins (triplet state). At resonance, the radical spin polarization is disturbed. To the extend that the exitation of the spin resonance would be at saturation, the current at resonance should be equal to the current in the absence of magnetic field, as depicted in figure 5.1 a).

The current change at resonance in the opposite scanning direction, i.e. a spin dependent charge transfer effect for the oxidation of $MV^{+\bullet}$ to MV^{2+}, occurs also on the increasing slope of the oxidation peak. For CISS this spin dependence is due to the fact that only one type of spin polarized electrons can tunnel through, as depicted in figure 5.1 b). This graph also shows, that oxidation using CISS could be used to spin polarize the substrate. For p-GaAs the spin dependency for oxidation is based on either spin dependent electron pair building at a surface state or spin dependent electron hole recombination at the valence band. If fully confirmed, this would be the first time a charge transfer dependency on spin dependent electron hole recombination at an electrode/electrolyte interface has been observed using resonance.

The uncertainty, whether the charge recombination in the oxidation direction at the p-GaAs / electrolyte interface is at surface states or via direct recombination in the valence band, could be cleared by another resonance experiment. Surface states such as dangling bonds can act as paramagnetic centers and are in this case accessible for resonance. This resonance is at a different field than that of $MV^{+\bullet}$, such that they should be distinguishable, see Stutzmann et al. p. 6.[70] However, if no such resonance can be found, this does not necessary exclude surface state recombination, since also unfavorable relaxation times of these could be the source of missing resonance.

Our measurements regarding the interfacial current change are confirmed by an order of magnitude approximation, i.e. relative current change below 10^{-4}. The model developed in section 2.3 also predicts a current increase at resonance for parallel spin orientation at the $MV^{+\bullet}/MV^0$ reduction majority range for both, CISS and optical spin pumping, and a current decrease at resonance for antiparallel spin orientation, see figure 2.31 (also figure 2.25 and 2.26). For the $MV^{+\bullet}/MV^{2+}$ oxidation majority range this is inversed, i.e. decreased current at resonance for parallel and increased current at resonance for antiparallel spin orientation for both, CISS and optical spin pumping. To fully confirm this model, the sign of the current change at resonance has to be known. However, the result is at the moment too smeared to distinguish between current increase or decrease at resonance. Furthermore, due to the used envelope difference evaluation scheme, the direction of current change is lost. The proof of reversing the effect by reversing either the electrode or radical spin polarization therefore is yet to be done.

Simultaneous to this work, we were therefore working at various fronts to improve the signal, which split into two categories: stabilizing the electrode and increasing the signal strength. As stated in section 3.1.5, MW power is limited so that the sample is not heated above 35 °C, which is reached at 16 dBm. A check experiment showed that by increasing the MW power to a maximum sample heating to 50 °C is reached at 26 dBm. A higher power should lead to an increased current change at resonance due to being closer to saturation of the resonance.

Double lock-in detection using simultaneously potential and field modulation did so far not show an improvement of the EDMR signal. However, this will be further pursued, as the detection

of signals only proportional to both modulation types is a promising feature, compare section 3.1.6. Another idea is here the simultaneous modulation of field and potential, driven by a single generator at frequency f. The combined modulation signal is here be expected at $2f$.

For a direct magnetic field sweep at constant potential through resonance, the sole solution appears to be a flow-through electrochemical cell such as used by Chazalviel. If going in this direction, the additional problems such as sealing, manual electrode stability, setup integration, flow induced noise reduction and the increased electrolyte volume inside the cavity would have to be tackled. However, the outcome will be well worth the trouble. A flow device not only avoids reactant depletion limitation and allows constant potential lock-in measurements, but also constant potential measurements in combination with different methyl viologen oxidation state species concentrations.

Optical modulation for lock-in detection of the current difference of opposing light helicity was tried by me in two ways already, a $\lambda/4$ plate rotation mount for up to $2f = 10\,\text{Hz}$ modulation and a liquid crystal variable retarder (LCVR). The rotation mount power stability is much better than a liquid crystal variable retarder (LCVR) because the retarder shows a power modulation of several percent between left and right circular polarization. LCVR are additionally extremely temperature sensitive, so that the applied voltages to achieve the right retardance for left or right circularly polarized light changes continuously. Moreover, a $10\,\text{Hz}$ lock-in detection proved to be not sufficiently fast. I worked on a home built $1\,\text{kHz}$ rotation mount for a $\lambda/4$ plate. The big problem was the current driver for the motor, which introduces such strong current peaks into the power grid, that the lock-in safety module caused a crash. This can only be resolved by using high end variable power modulation converters. The next trouble with this mechanical approach would be to solve the vibration problem. In the same price category, but without vibration problems are Pockels cells.

Dr. Mika Tamski and I are performing experiments with functionalized p-GaAs for better chemical stability and inertness using organic molecules or deposition of a thin inert metal. The biggest question is in that case the spin conservation, i.e. spin diffusion length at room temperature. Au has a spin diffusion length of $\approx 32\,\text{nm}$ and Pt of $\approx 2\,\text{nm}$ at room temperature.[133] It is however not clear, if the photo cathodic effect can be preserved. CISS and optical pumping could probably be combined if the molecules used for functionalization are additionally helical. The combination of optical spin pumping and CISS to sum their effect would open the way to several experiments such as direct current increase or decrease by switching the light helicity.

I have developed ferromagnetic electrodes of Ni and permalloy, which would possibly allow us an added spin polarization effect and therefore low cost easy to use electrodes with decreased surface state induced spin polarization loss problems. The surface protection using Ag is however not yet optimized.

Another concept to explore would be the use of tellurium (Te) electrodes. Te semiconductor grow under certain conditions in a chiral structure could therefore be used as electrode of defined spin polarization. The helicity is here due to a crystal structure of each layer slightly turned

[133] M. Isasa, et al., "Temperature dependence of spin diffusion length and spin Hall angle in Au and Pt", Physical Review B **91**, 024402 (2015).

against the previous, called screw dislocation, and is assumed to spin polarize similar to molecular helicity.[134,135] It has been shown, that helically structured Te shows current induced bulk magnetization.[136] It is however still unclear if the reason for the spin polarization in screw dislocated solids is identical to spiral molecules. For electrochemistry mostly the question of effective spin polarized interface charge transfer possibility is raised. However, an electrode with such a chiral surface morphology may cause an enantioselective adsorption of methyl viologen, which could possibly also show CISS and would not necessarily be distinguishable from an actual Te spin filtering effect.[137]

The options are numerous and promising, especially regarding combined systems with CISS.

[134] O. Gomonay, "Crystals with Defects May Be Good for Spintronics", Physics **11**, 78 (2018).

[135] L. Hu, et al., "Ubiquitous Spin-Orbit Coupling in a Screw Dislocation with High Spin Coherency", Physical Review Letters **121**, 66401 (2018).

[136] T. Furukawa, et al., "Observation of current-induced bulk magnetization in elemental tellurium", Nature Communications **8**, 1–5 (2017).

[137] A. Ahmadi, et al., "Surface Reactivity at "Chiral" Platinum Surfaces", Langmuir **15**, 2420–2424 (1999).

A Appendix

A.1 Microwave Power Saturation

In section 3.1.5 the power saturation is determined to approximate the relaxation times and to determine the best measurement settings. Additional observations within these measurements are presented here below.

A.1.1 Power Calibration at Cavity

For microwave power amplification a 35 dB *Mini-Circuits ZVE-3W-183+* amplifier was used (3 W maximal output). In general, the amplifier appears to be rather of 32 dB. The damping of the system between amplifier and cavity was approximately of 1 dB power loss for the linear range (measured with a *Hewlett-Packard '436A' Power Meter* plus *8481H Power Sensor*). The power arriving at the cavity is displayed in figure A.1 and compares to a 30.8 dB amplification versus set power at the source. At approximately 0 dBm of source power, the power arriving at the cavity is saturating, even though this is still well in the limit of all used parts and measuring parts.
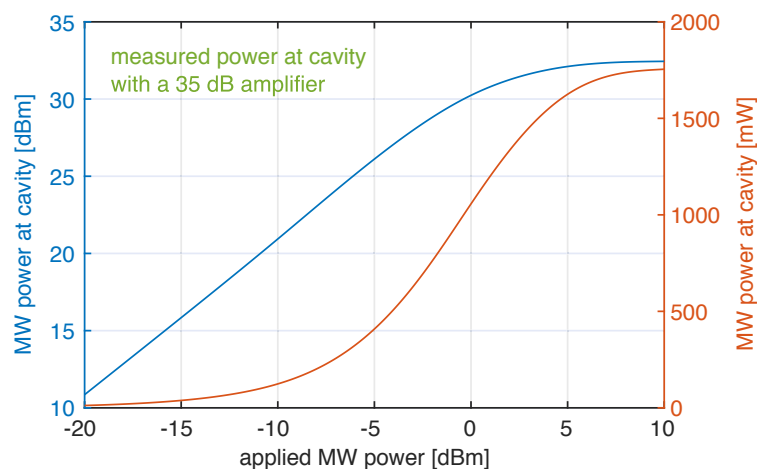
Figure A.1 – Microwave power calibration (fit) at the cavity for a 35 dB amplifier.

119

A.1.2 MS400 Benchtop Measurement of $10\,\mu l$ of $2\,mM$ $MV^{+\bullet}$ inside a capillary

The two following figures are for the completion of section 3.1.5. Figure A.2 shows the result of a microwave power saturation measurement for a $10\,\mu l$ sample of $2\,mM$ $MV^{+\bullet}$ with $200\,mM$ TBAP in
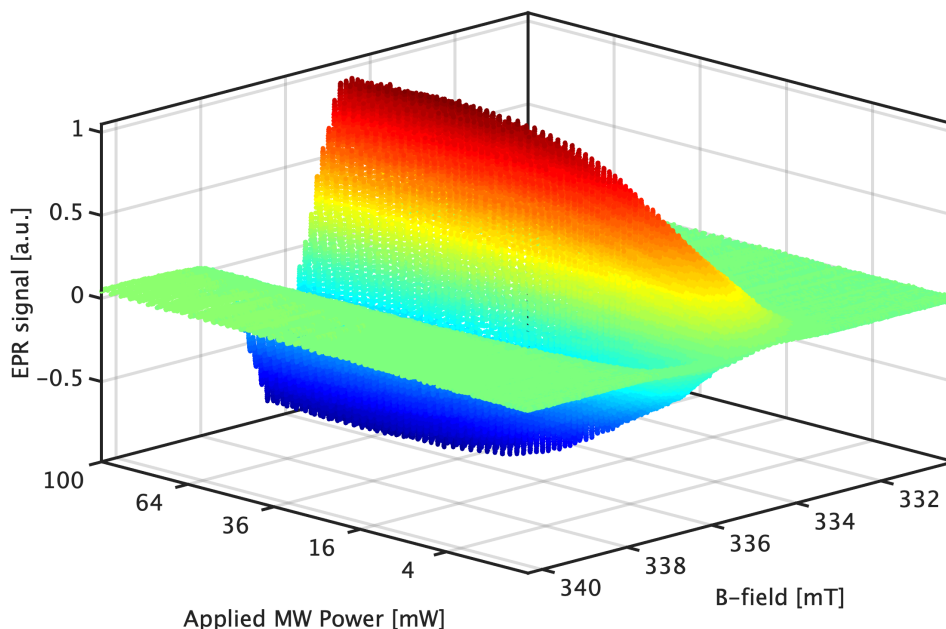

Figure A.2 – Microwave power saturation curve for a $10\,\mu l$ sample of $2\,mM$ $MV^{+\bullet}$ inside a capillary with a benchtop MS400 EPR spectrometer at $9.398\,GHz$. The color code is proportional to the EPR signal and illustrates the increase linear to the square root of the power until saturation is reached.
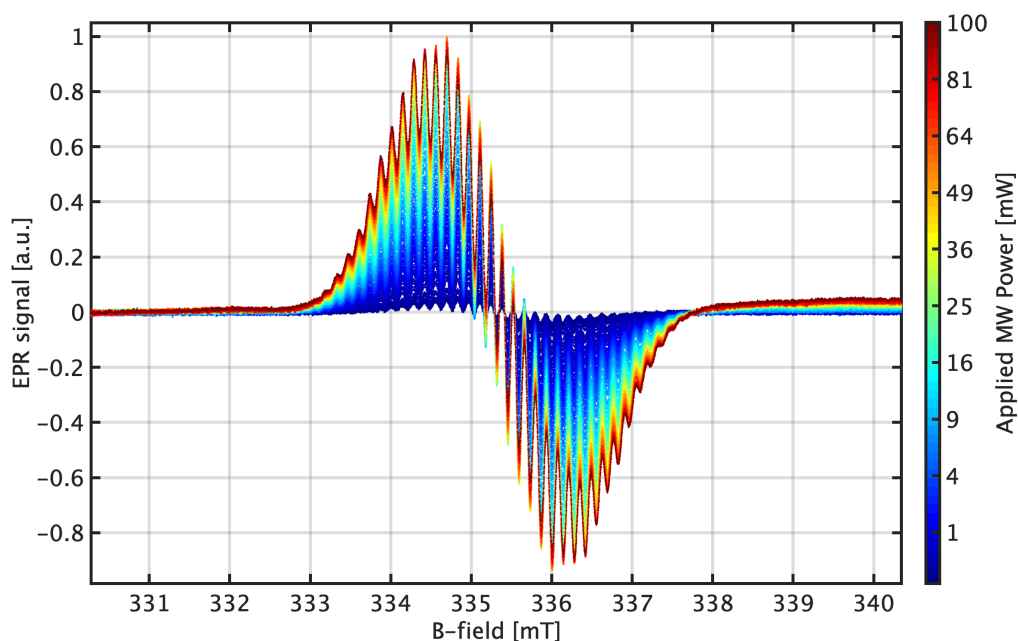

Figure A.3 – Front view (along the power axis) of figure A.2.

acetonitrile inside a capillary (1 mm inner diameter) measured with a benchtop EPR spectrometer (*Magnettech MS400*). The axis for the microwave power is scaled with the square root of the power but true value indication. The color code is proportional to the EPR signal and illustrates its increase linear to the square root of power until saturation is reached.

Figure A.3 is a front view (along the power axis) of figure A.2 to illustrate the continuity of hyperfine splitting through all applied microwave powers (different color code, representing here the applied power). The hyperfine splitting line positions are unchanged for the whole power range of almost 100 mW, while the overall EPR signal width is increasing.

A.1.3 Power Dependent EPR On-Channel Phase Inversion and Resonance Shift

Within the scope of looking for a microwave power saturation of the EPR signal using the home-built setup, I observed two unexplained behaviors, an on-channel phase inversion at high MW power (negative sign to positive and vice versa) and for other samples a resonance shift. For both observations I have no explanation, though I want to document these for possible similar observations of other researchers.

Figures A.5 and A.6 show the MW power saturation curves for the sample of 100 mM TEMPONE in toluene, i.e. non lossy sample. After reaching saturation, the EPR signal suddenly decreases, vanishes and reappeares with phase inversion. The phase inversion is within one channel, here X, and not a phase shift between two channels, such as emphasized with corresponding cross sections in figure A.4 (line in figure A.4 is multiplied by 1000 to make Y visible at all).

The signal decrease could in general be explained by a signal broadening, however not the disappearance. The complete disappearance might be explained by hardware not able to cope with high powers (this should not be the case, all used hardware is well within their power ranges). However, both hypotheses cannot explain the signal reappearance nor the sign inversion. This behavior is reproducible for different samples of lossy and non lossy nature.
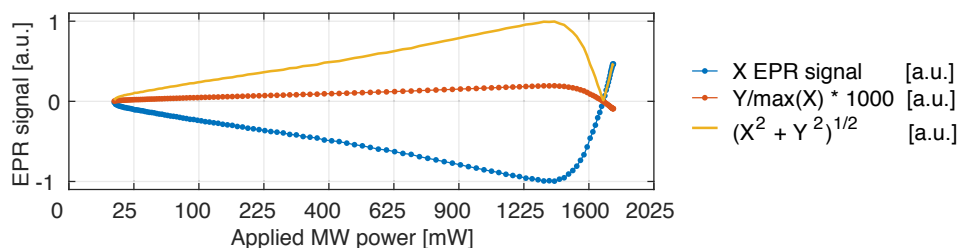

Figure A.4 – Cross section along the MW power axis in figure A.6 at 326.8 mT for the comparison of the lock-in X-, Y-, and magnitude- signal ($\sqrt{X^2 + Y^2}$). Y is multiplied with 1000 to make it visible. The EPR signal vanishing and reappearance is also well visible in the magnitude, however with phase-inversion information loss.
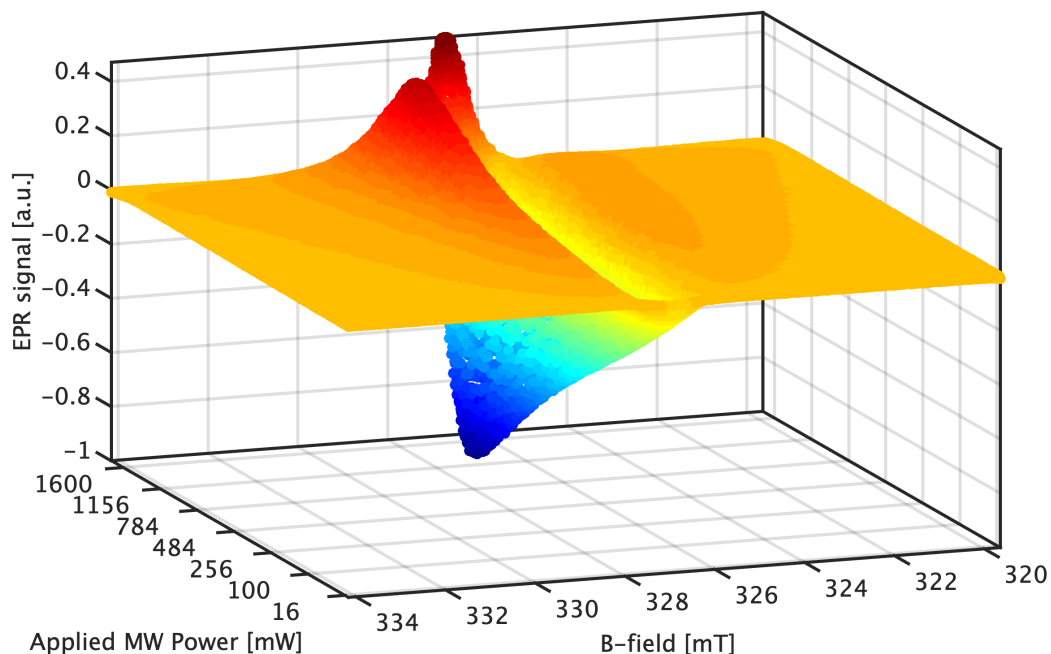
Figure A.5 – Power dependent EPR phase inversion for a 100 mM TEMPONE sample dissolved in toluene, diagonal view. The plot is a normalized average of seven consecutive scans (no smoothing nor fitting). The color code depicts the EPR lock-in signal strength and is identical to figure A.6. The MW power axis is scaled as square root.

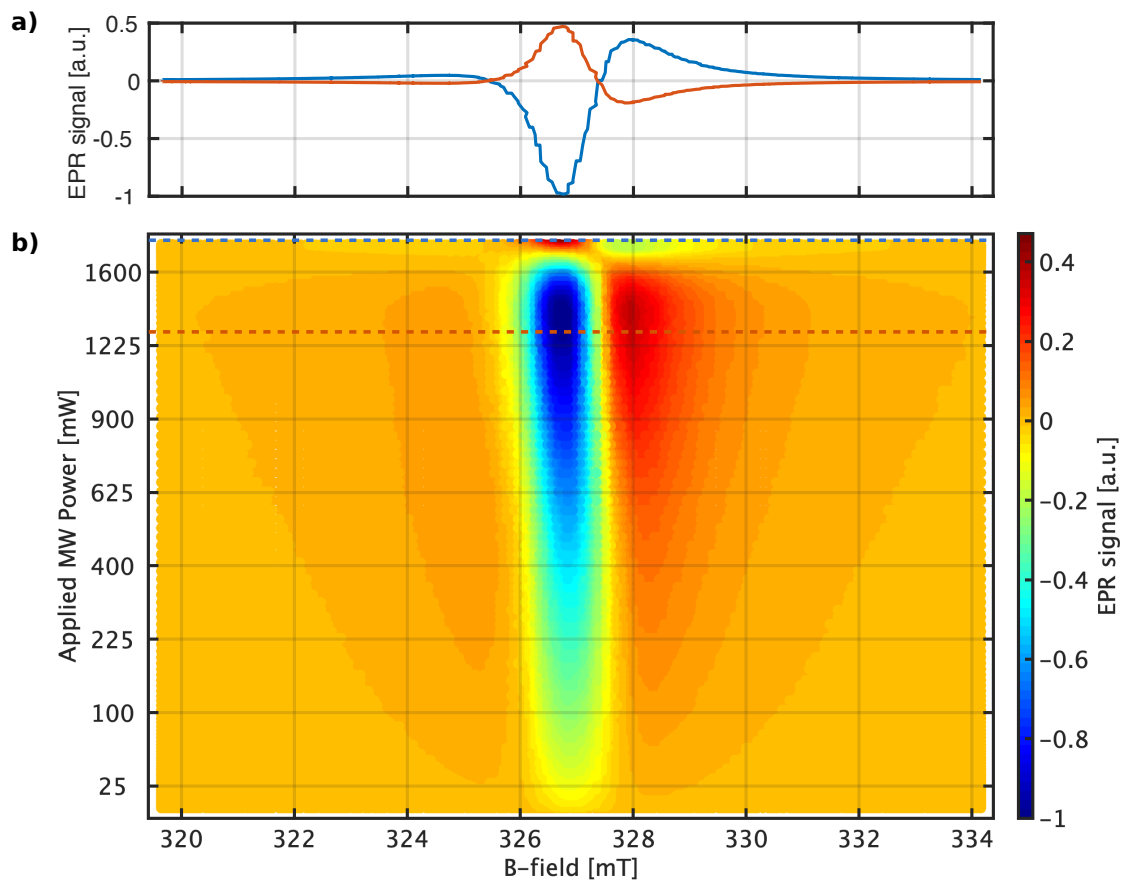**Figure A.6** – MW power dependent EPR phase inversion for a 100 mM TEMPONE sample dissolved in toluene. Top view of figure A.5 in b) and dashed lines indicated cross sections in a).
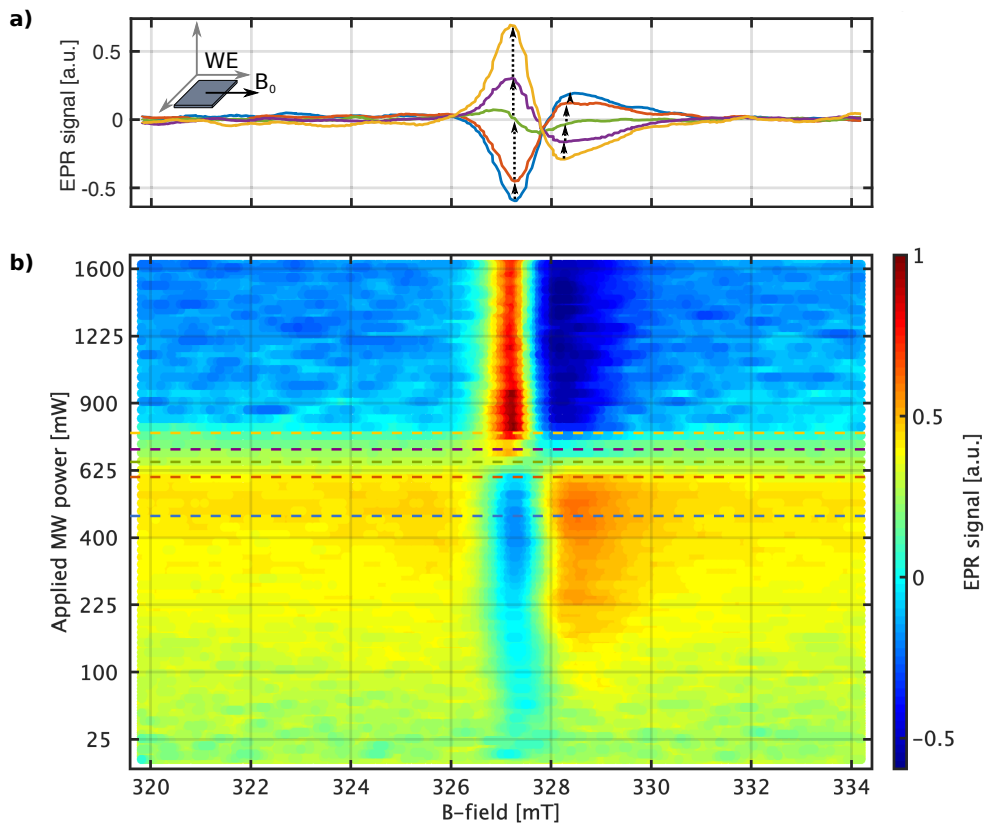
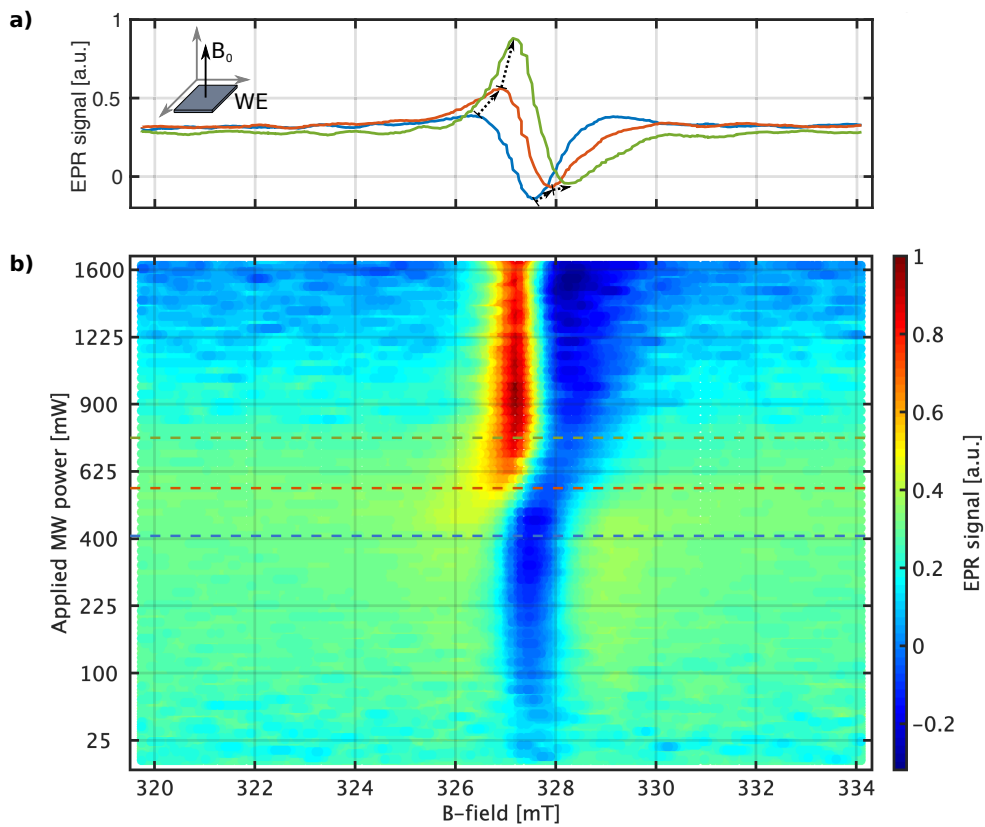**Figure A.7** – MW power dependent EPR resonance shift for a 2 mM MV$^{+\bullet}$ with a p-GaAs WE $\parallel$ B_0.

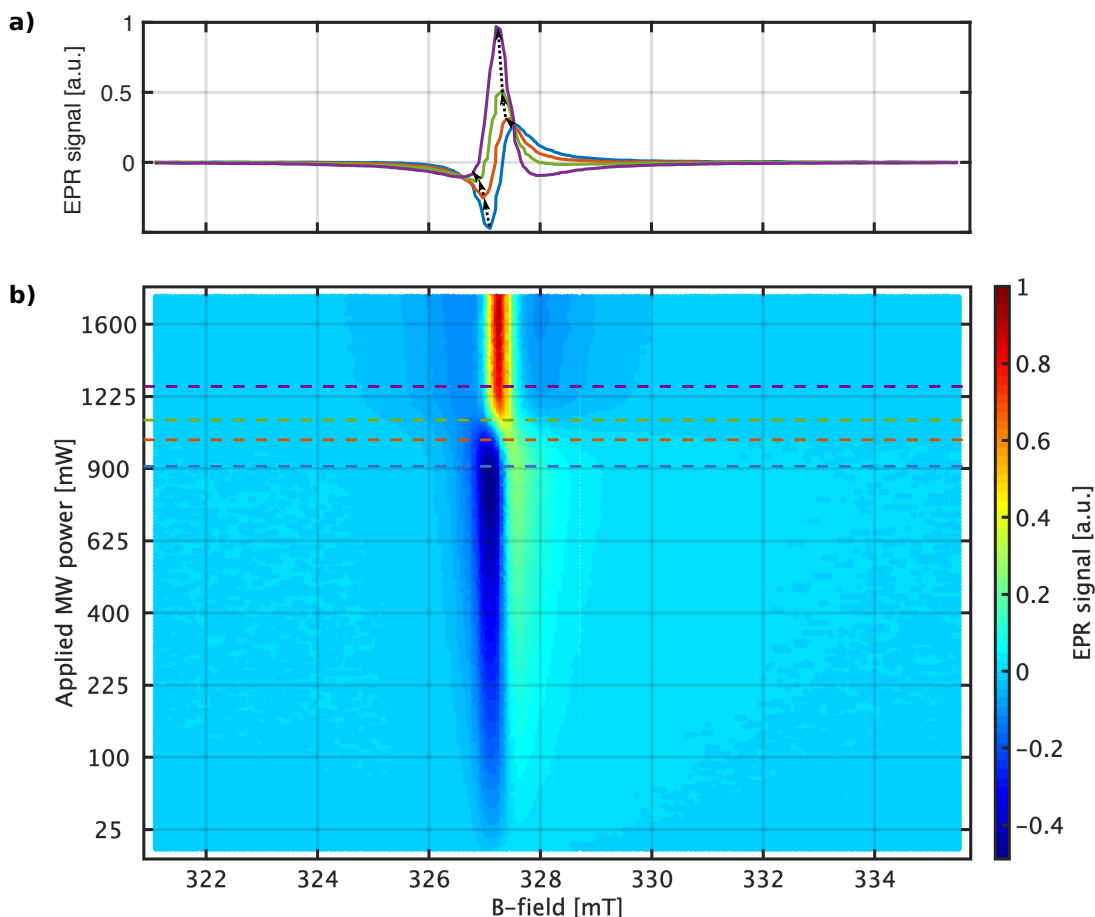**Figure A.8** – MW power dependent EPR resonance shift for a 2 mM MV$^{+\bullet}$ with a p-GaAs WE $\perp$ B_0.

Figure A.9 – Top view of MW power dependent EPR resonance shift for a DPPH powder sample.

For a sample of 2 mM MV$^{+\bullet}$ dissolved in ACN with 200 mM TBAP with a p-GaAs WE, Pt rod CE and Pt wire-tip RE inside a 5 mm NMR tube, the saturation curve measurement was sample-to-B_0 orientation dependent. For an orientation of the WE face aligned with B_0, the result is structurally the same as for TEMPONE, see figure A.7 (average of 11 scans). The vanishing is complete at approximately 660 mW compared to 1600 mW for TEMPONE in toluene, even though the ACN solution is lossy and toluene is not. The cross sections in a) are vertically aligned for better comparability. However, the baseline actually drops relatively abrupt by approximately 50 % of the overall signal range (also around 570 mW). This sudden baseline drop is very unusual and was not observed with any other experiment. However, it appeared identically for all 11 scans of this sample in this p-GaAs WE orientation. A general source of baseline shift is usually a temperature change. This might be the case here at high powers due to MW-heating. This is supported by a pattern change when turning the sample by 90°, presented in figure A.8. MW heating is electric field driven, which is not homogeneously distributed such as discussed in section 3.1.5. In this orientation no sudden baseline drop, nor signal vanishing nor sign inversion is observed. However, in this orientation of the p-GaAs facing B_0, the resonance is shifted to a larger field. Additionally, the process appears to be here centered around 570 mW, compared to 660 mW of parallel alignment. Figure A.9 shows the MW saturation curve of DPPH powder, which shows a shift less pronounced as in figure A.8 and to smaller magnetic fields.

A.2 Light Filter Induced Light Power Noise

I noticed a strong dependency of the laser power stability on the applied current, i.e. partly heavily increased noise, partly laser power jumps such as depicted in figure A.10. It turned out, that a band pass filter (*Thorlabs FB830-10*) was the source for this. The band-pass filter is a space separated dielectric-stack type, functioning on constructive interference at the center frequency. The most likely explanation is, that at increasing applied currents more laser diode surface area is activated, leading to differently sized laser spot on the filter and hence different interference patterns. This also explains a noise increase when cables where touched: laser source moving in comparison to the band pass filter with subsequently different interference patterns.

A.3 Experiment Control Software and Data Evaluation

I designed and wrote all LabVIEW programs myself. Focus was given on minimizing delays induced by respond times and computer calculation delays. Emphasis was given on fully automated measurement schematics with programmatically or partly self adjusting parameters such as e.g. MW power. Two main programs were designed, one for mostly standard CW EPR line scans, integrated EPR and automated power saturation measurements such as presented e.g. in figure A.5. The second program is mostly programmed for simultaneous CW EPR, EDMR and potentiostat measurements. Recorded are six digital lock-in channels for EDMR, one analog lock-in channel for CW EPR, gaussmeter measured B_0 at cavity height, Bouhnik current, potentiostat current, applied
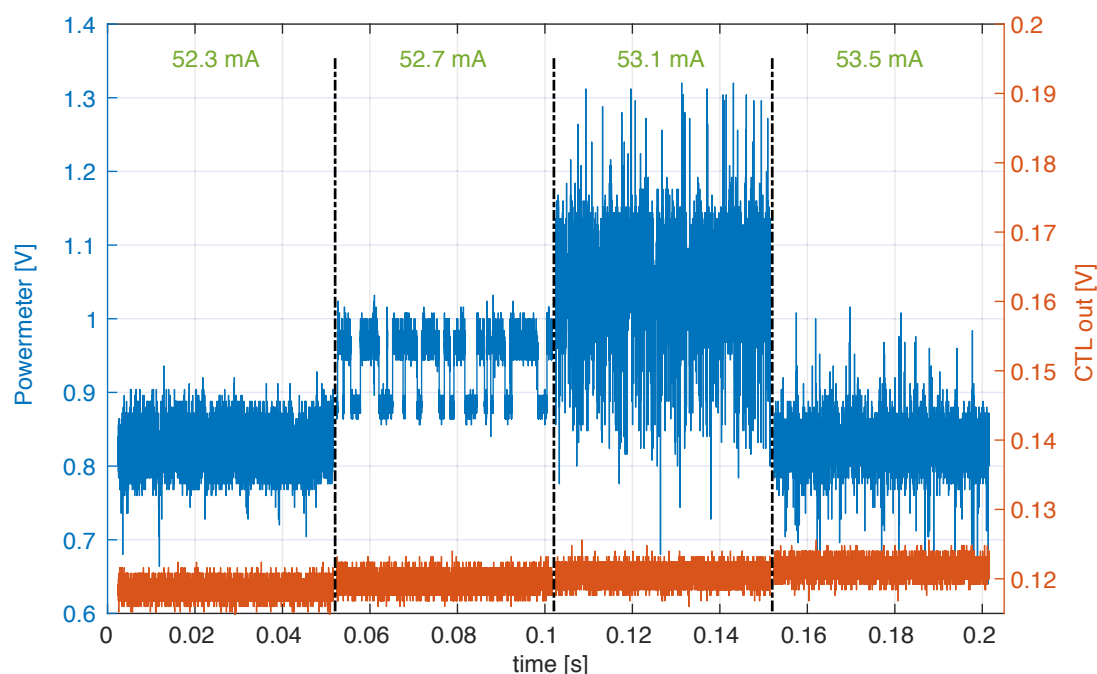

Figure A.10 – Laser power stability and noise over applied current. The red data shows the control current (*CTL out* is the monitor current output), over time stepwise increased with corresponding output current noted in green above. The resulting laser light power was measured with a Si amplified detector (*Thorlabs, PDA36A-EC* with 0 dB amplification).

potential and MW source parameters.

A huge problem was the implementation of the Metrohm potentiostat. Section 3.1.6 discusses the software implementation and hardware interferences. Another problem was the potential modulation, which should be driven by the current driving source, i.e. the potentiostat. This is not straight forward with Metrohm due to a missing control interface regarding this aspect and also regarding external voltage control enabling. These settings can be applied using the Autolab software, are however automatically disabled otherwise. Additionally, Autolab crashes after run times longer than some hours. I found the easiest workaround to be an Autolab program which first enables external voltage control, and then starts an impedance measurement for single frequency. This program has to be interrupted and not stopped in the normal manner. The interruption leaves the settings enabled, allowing full external control and constant potential modulation.

Due to the specific measuring method and weak signal, I developed a method to visualize and evaluate all possible signal channels in a simple and fast way such as described in section 3.2.1. Due to the matrix based data set I used Matlab for this, as Matlab works especially well in combination with matrices.

A.4   Potential Jump Chronoamperometric EDMR

The potential jump schematic for chronoamperometric EDMR is illustrated in figure A.11. At every field step the potential is first applied on a defined rest potential, e.g. OCP, and after a certain resting time the desired potential for EDMR is applied. Figure A.12 shows three example measurements performed on GaN/Au/Al5/Ag. Subplots a) to c) show the applied potential (orange), resulting current (blue) and the magnetic field steps at the same time (purple). The delay time after applying $-0.4\,\mathrm{V}$ and the integration time itself define the region of measurement along the exponential current decay such as discussed on figure 3.33, i.e. predominantly capacitive, resistive or in the depletion range, compare figure 3.33 a). Depletion range, a), should be avoided due to just described reactant exhaustion. The re-accumulation of reactants in the resting phase happens in this example at the original OCP. Due to concentration changing induced OCP change, the current is here also exponential, though of opposite current sign.
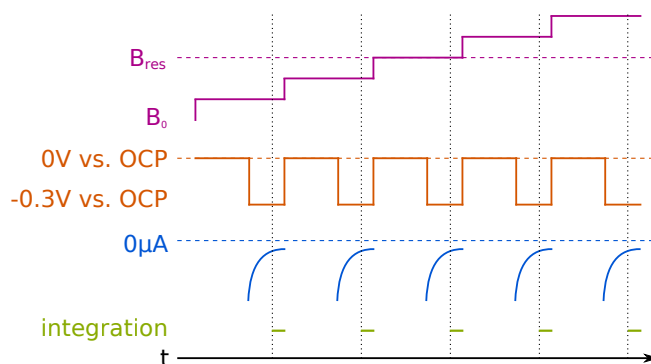

Figure A.11 − EDMR with potential jumping, code concept illustration. The potential is in this example jumped between OCP and $-0.3\,\mathrm{V}$ vs. OCP.
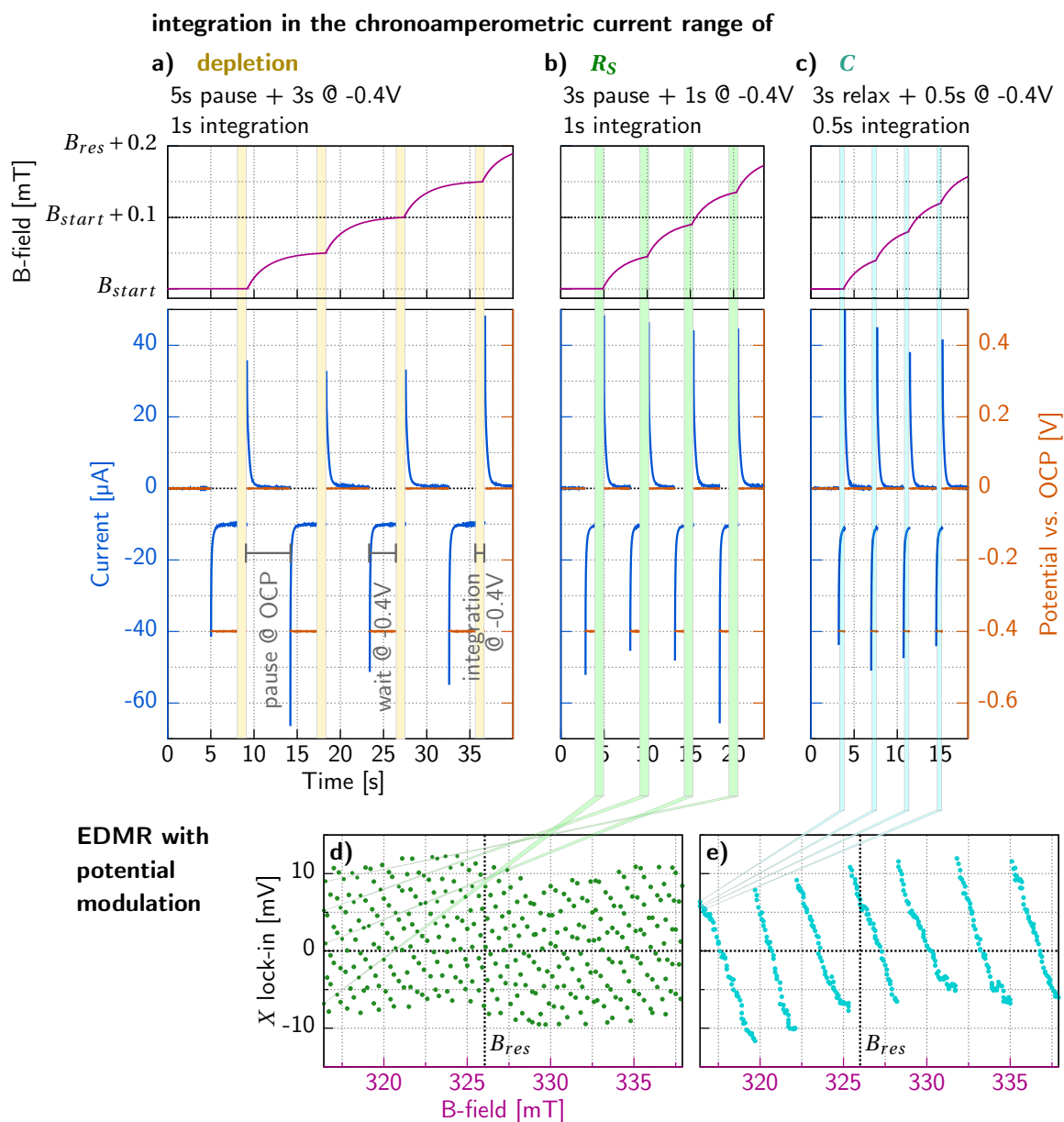
Figure A.12 – EDMR by jumping the potential between 0 V and −0.4 V vs. OCP at the example of GaN/Au/Al5/Ag. Shown are applied potential (orange), resulting current (blue) and the magnetic field swept at the same time (purple) in a) till c) exemplified for the three different ranges along the exponential current decay.

Figures d) and e) are the EDMR results obtained by potential modulation of 2 mV at 880 Hz for the corresponding examples b) and c). Every integration time in b) (c)) leads to a single data point in d) (e)), illustrated with the colored stripes. The extremely different appearance of d) as extreme noise and saw-tooth type pattern in e) examplifies the big problem of this method which is based on the discontinuous input signal at the lock-in. Any modulation superimposed with this type of extreme *on/off* input signal happens, makes lock-in detection extremely hard to handle. With local detrending and filtering techniques figure e) can be brought to a flat line, however, in comparison to below described matrix method, the noise is approximately 100 times larger.

Bibliography

[1] M. I. Dyakonov, "Current-induced-spin-orientation-of-electrons-in-semiconductors_1971_Physics-Letters-A.pdf", Phys. Lett. A **35**, 459–460 (1971) (cit. on p. 1).

[2] A. Fert, "Origin, development, and future of spintronics (Nobel lecture)", Angewandte Chemie - International Edition **47**, 5956–5967 (2008) (cit. on p. 1).

[3] M. N. Baibich, J. M. Broto, A. Fert, F. N. Van Dau, F. Petroff, P. Etienne, G. Creuzet, A. Friederich, and J. Chazelas, "Giant Magnetoresistance of (001)Fe/(001)Cr Magnetic Superlattices", Physical Review Letters **61**, 2472–2475 (1988) (cit. on p. 1).

[4] G. Binasch, P. Grünberg, F. Saurenbach, and W. Zinn, "Enhanced magnetoresistance in layered magnetic structures with antiferromagnetic interlayer exchange", Physical Review B **39**, 4828–4830 (1989) (cit. on p. 1).

[5] Y. Ando, "Spintronics technology and device development", Japanese Journal of Applied Physics **54**, 070101 (2015) (cit. on p. 1).

[6] V. K. Joshi, "Spintronics: A contemporary review of emerging electronics devices", Engineering Science and Technology, an International Journal **19**, 1503–1513 (2016) (cit. on p. 1).

[7] T. Takui, L. Berliner, and G. Hanson, eds., *Electron Spin Resonance (ESR) Based Quantum Computing*, Vol. 31, Biological Magnetic Resonance (Springer New York, New York, NY, 2016) (cit. on p. 1).

[8] F. Comandè, and J. P. Ansermet, "Pulsed magnetic resonance of Alq3 OLED detected by electroluminescence", Synthetic Metals **173**, 40–42 (2013) (cit. on pp. 1, 4, 41).

[9] C. Caspers, D. Yoon, M. Soundararajan, and J. P. Ansermet, "Opto-spintronics in InP using ferromagnetic tunnel spin filters", New Journal of Physics **17** (2015) 10.1088/1367-2630/17/2/022004 (cit. on p. 1).

[10] D. Yoon, M. Soundararajan, and J. P. Ansermet, "Nuclear polarization by optical pumping in InP:Fe above liquid nitrogen temperature", Solid State Nuclear Magnetic Resonance **70**, 48–52 (2015) (cit. on p. 1).

[11] J. Fabian, and S. D. Sarma, "Spin relaxation of conduction electrons", 1708–1715 (1999) (cit. on p. 2).

[12]   I. Žutić, J. Fabian, and S. D. Sarma, "Spintronics: Fundamentals and applications", Reviews of Modern Physics **76**, 323–410 (2004) (cit. on p. 2).

[13]   M. Galbiati, S. Tatay, C. Barraud, A. V. Dediu, F. Petroff, R. Mattana, and P. Seneor, "Spinterface: Crafting spintronics at the molecular scale", MRS Bulletin **39**, 602–607 (2014) (cit. on p. 2).

[14]   W. Mtangi, V. Kiran, C. Fontanesi, and R. Naaman, "Role of the Electron Spin Polarization in Water Splitting", The Journal of Physical Chemistry Letters **6**, 4916–4922 (2015) (cit. on pp. 2, 6).

[15]   C. Fontanesi, "Spin-dependent electrochemistry: A novel paradigm", Current Opinion in Electrochemistry **7**, 36–41 (2018) (cit. on pp. 2, 4, 46).

[16]   J. Chazalviel, "Spin-dependent electrochemical kinetics at a semiconducting photocathode", Journal of Chemical Physics **83**, 149–156 (1985) (cit. on pp. 2, 3, 19, 26, 39, 43, 60, 79, 87, 101, 115, 117).

[17]   L. M. Monzon, and J. Coey, "Magnetic fields in electrochemistry: The Lorentz force. A mini-review", Electrochemistry Communications **42**, 38–41 (2014) (cit. on p. 2).

[18]   L. M. Monzon, and J. Coey, "Magnetic fields in electrochemistry: The Kelvin force. A mini-review", Electrochemistry Communications **42**, 42–45 (2014) (cit. on pp. 2, 96).

[19]   B. Ferreira Gomes, P. Ferreira da Silva, C. M. Silva Lobo, M. da Silva Santos, and L. A. Colnago, "Strong magnetoelectrolysis effect during electrochemical reaction monitored in situ by high-resolution NMR spectroscopy", Analytica Chimica Acta **983**, 91–95 (2017) (cit. on p. 2).

[20]   G. Saravanan, and S. Ozeki, "Magnetic field control of electron tunneling pathways in the monolayer of (ferrocenylmethyl)dodecyldimethylammonium bromide on a gold electrode", Journal of Physical Chemistry B **112**, 3–6 (2008) (cit. on pp. 2, 3).

[21]   A. Modestov, and V. Kazarinov, "Electrochemical reduction of 2,6-diphenylpyrylium cations by spin-polarized electrons. The Hedvall effect", Chemical Physics Letters **206**, 401–404 (1993) (cit. on p. 3).

[22]   L. H. Piette, P. Ludwig, and R. N. Adams, "Electron Paramagnetic Resonance and Electrochemistry. Studies of Electrochemically Generated Radical Ions in Aqueous Solution.", Analytical Chemistry **34**, 916–921 (1962) (cit. on p. 3).

[23]   I. B. Goldberg, D. Boyd, R. Hirasawa, and A. J. Bard, "Simultaneous electrochemical-electron spin resonance measurements. III. Determination of rate constants for second-order radical anion dimerization", Journal of Physical Chemistry **78**, 295–299 (1974) (cit. on p. 3).

[24]   K. R. Fernando, A. J. McQuillan, B. M. Peake, and J. Wells, "Cell for combined electrochemistry and ESR measurements at variable temperatures in a varian TE102 microwave cavity", Journal of Magnetic Resonance (1969) **68**, 551–555 (1986) (cit. on p. 3).

[25]   M. A. Tamski, J. V. Macpherson, P. R. Unwin, and M. E. Newton, "Electrochemical electron paramagnetic resonance utilizing loop gap resonators and micro-electrochemical cells", Phys. Chem. Chem. Phys. **17**, 23438–23447 (2015) (cit. on pp. 3, 87).

[26]   P. C. Mondal, N. Kantor-Uriel, S. P. Mathew, F. Tassinari, C. Fontanesi, and R. Naaman, "Chiral Conductive Polymers as Spin Filters", Advanced Materials **27**, 1924–1927 (2015) (cit. on p. 4).

[27] P. C. Mondal, C. Fontanesi, D. H. Waldeck, and R. Naaman, "Field and chirality effects on electrochemical charge transfer rates: Spin dependent electrochemistry", ACS Nano **9**, 3377–3384 (2015) (cit. on p. 4).

[28] T. J. Zwang, S. Hürlimann, M. G. Hill, and J. K. Barton, "Helix-Dependent Spin Filtering through the DNA Duplex", Journal of the American Chemical Society **138**, 15551–15554 (2016) (cit. on p. 4).

[29] A. Kumar, E. Capua, M. K. Kesharwani, J. M. L. Martin, E. Sitbon, D. H. Waldeck, and R. Naaman, "Chirality-induced spin polarization places symmetry constraints on biomolecular interactions", Proceedings of the National Academy of Sciences **114**, 2474–2478 (2017) (cit. on pp. 4, 6).

[30] W. Mtangi, F. Tassinari, K. Vankayala, A. Vargas Jentzsch, B. Adelizzi, A. R. A. Palmans, C. Fontanesi, E. W. Meijer, and R. Naaman, "Control of Electrons' Spin Eliminates Hydrogen Peroxide Formation During Water Splitting", Journal of the American Chemical Society **139**, 2794–2798 (2017) (cit. on p. 4).

[31] R. Naaman, Y. Paltiel, and D. H. Waldeck, "Chiral molecules and the electron spin", Nature Reviews Chemistry **3** (2019) 10.1038/s41570-019-0087-1 (cit. on p. 4).

[32] D. Mandler, "Chiral self-assembled monolayers in electrochemistry", Current Opinion in Electrochemistry **7**, 42–47 (2018) (cit. on p. 4).

[33] S. Steil, N. Großmann, M. Laux, A. Ruffing, D. Steil, M. Wiesenmayer, S. Mathias, O. L. A. Monti, M. Cinchetti, and M. Aeschlimann, "Spin-dependent trapping of electrons at spinterfaces", Nature Physics **9**, 242–247 (2013) (cit. on p. 4).

[34] R. A. Rosenberg, D. Mishra, and R. Naaman, "Chiral Selective Chemistry Induced by Natural Selection of Spin-Polarized Electrons", Angewandte Chemie - International Edition **54**, 7295–7298 (2015) (cit. on p. 6).

[35] D. Qi, A. Kenaan, D. Cui, and J. Song, "Novel insights into the selection to electron's spin of chiral structure", Nano Energy **52**, 142–152 (2018) (cit. on p. 6).

[36] G. Pályi, C. Zucchi, and L. Caglioti, eds., *Progress in Biological Chirality* (Elsevier, 2004) (cit. on p. 6).

[37] G. Hayashi, M. Hagihara, and K. Nakatani, "Application of L-DNA as a molecular tag", Nucleic Acids Symposium Series **49**, 261–262 (2005) (cit. on p. 6).

[38] W. Zhang, K. Banerjee-Ghosh, F. Tassinari, and R. Naaman, "Enhanced Electrochemical Water Splitting with Chiral Molecule-Coated Fe3O4Nanoparticles", ACS Energy Letters, 2308–2313 (2018) (cit. on p. 6).

[39] D. A. Brownson, and C. E. Banks, *Interpreting Electrochemistry* (2014), pp. 1–201 (cit. on pp. 8, 15).

[40] Metrohm Autolab B.V., *Autolab Application Note* (https://www.ecochemie.nl/download/Applicationnotes/, 2011) (cit. on p. 10).

[41] Gamry Instruments Inc., *Application Note* (https://www.gamry.com/application-notes/, 2012) (cit. on p. 10).

[42]   N. Elgrishi, K. J. Rountree, B. D. McCarthy, E. S. Rountree, T. T. Eisenhart, and J. L. Dempsey, "A Practical Beginner's Guide to Cyclic Voltammetry", Journal of Chemical Education **95**, 197–206 (2018) (cit. on p. 12).

[43]   S. Creager, *Handbook of Electrochemistry - Chapter: Solvents and Supporting Electrolytes* (Elsevier, 2007), pp. 57–72 (cit. on p. 12).

[44]   J. E. B. Randles, "Kinetics of rapid electrode reactions", Discussions of the Faraday Society **1**, 11 (1947) (cit. on p. 17).

[45]   A. J. Bard, and L. R. Faulkner, *Electrochemical Methods: Fundamentals and Applications*, Vol. 2 (Wiley, New York, 2001), p. 864 (cit. on pp. 18, 21).

[46]   T. E. Keyes, and R. J. Forster, *Handbook of Electrochemistry* (Elsevier, 2007), pp. 591–635 (cit. on p. 18).

[47]   P. M. S. Monk, *The Viologens: Physicochemical Properties, Synthesis, and Applications of the Salts of 4,4'-Bipyridine* (Wiley, Manchester, 1998), p. 311 (cit. on p. 19).

[48]   J. Peon, X. Tan, J. D. Hoerner, C. Xia, Y. F. Luk, and B. Kohler, "Excited State Dynamics of Methyl Viologen. Ultrafast Photoreduction in Methanol and Fluorescence in Acetonitrile", The Journal of Physical Chemistry A **105**, 5768–5777 (2001) (cit. on pp. 19, 63).

[49]   T. W. Ebbesen, G. Levey, and L. K. Patterson, "Photoreduction of methyl viologen in aqueous neutral solution without additives", Nature **298**, 545–548 (1982) (cit. on p. 19).

[50]   M. Suzuki, N. D. Morris, and T. E. Mallouk, "Photosensitized production of doubly reduced methylviologen followed by highly efficient methylviologen radical formation using self-assembling ruthenium(ii) complexes", Chemical Communications **1**, 1534–1535 (2002) (cit. on p. 19).

[51]   H. Yoshikawa, and S.-i. Nishikiori, "Photoinduced Color Change of Methylviologen in Polycyano-Polycadmate Host Clathrates.", Chemistry Letters **5**, 142–143 (2000) (cit. on p. 19).

[52]   T. M. Bockman, and J. K. Kochi, "Isolation and Oxidation-Reduction of Methylviologen Cation Radicals. Novel Disproportionation in Charge-Transfer Salts by X-ray Crystallography", Journal of Organic Chemistry **55**, 4127–4135 (1990) (cit. on pp. 20, 72).

[53]   P. M. S. Monk, R. D. Fairweather, M. D. Ingram, and J. A. Duffy, "Evidence for the Product of the Viologen Comproportionation Reaction being a Spin-paired Radical Cation Dimer", J. Chem. Soc. Perkin Trans. II **1**, 2039–2041 (1992) (cit. on p. 20).

[54]   P. B. Sweetser, "Colorimetric determination of trace levels of oxygen in gases with the photochemically generated methyl viologen radical-cation", Analytical Chemistry **39**, 979–982 (1967) (cit. on pp. 20, 52).

[55]   C. Stradowski, "Methylviologen cation radical as probe of oxygen diffusion through polymer", Journal of Applied Polymer Science **41**, 2511–2512 (1990) (cit. on pp. 20, 51).

[56]   N. Chitose, J. A. LaVerne, and Y. Katsumura, "Effect of Formate Concentration on Radical Formation in the Radiolysis of Aqueous Methyl Viologen Solutions", The Journal of Physical Chemistry A **102**, 2087–2090 (1998) (cit. on pp. 20, 51).

[57]   N. Sato, *Electrochemistry at Metal and Semiconductor Electrodes* (Elsevier Science, Hokkaido, 1998), p. 412 (cit. on p. 22).

[58]   A. W. Bott, "Electrochemistry of semiconductors", Current Separations **17**, 87–92 (1998) (cit. on p. 22).

[59]   A. J. Bard, "Photoelectrochemistry and heterogeneous photo-catalysis at semiconductors", Journal of Photochemistry **10**, 59–75 (1979) (cit. on p. 22).

[60]   J. Li, and L. Peter, "Surface recombination at semiconductor electrodes", Journal of Electroanalytical Chemistry and Interfacial Electrochemistry **193**, 27–47 (1985) (cit. on p. 23).

[61]   R. Memming, *Semiconductor Electrochemistry 3. Electrochemical Systems* (Wiley-VCH Verlag GmbH & Co. KGaA, Weinheim, Germany, Apr. 2000) (cit. on pp. 23–25).

[62]   J. E. Wertz, and J. R. Bolton, *Electron Spin Resonance: Elementary Theory and Practical Applications* (Springer Netherlands, Dordrecht, 1972), p. 497 (cit. on pp. 25, 34).

[63]   D. M. Murphy, *Metal Oxide Catalysis - Chapter - EPR Spectroscopy of Polycrystalline Oxide Systems*, Vol. 1 (Wiley-VCH Verlag GmbH & Co. KGaA, Weinheim, Germany, 2009), pp. 1–50 (cit. on p. 25).

[64]   G. R. Eaton, S. S. Eaton, D. P. Barr, and R. T. Weber, *Quantitative EPR* (Springer Vienna, 2010), pp. 1–185 (cit. on pp. 25, 32–34, 72, 73, 76).

[65]   C. P. Slichter, *Principles of Magnetic Resonance*, Third Enlarged and Updated Edition, Springer Series in Solid-State Sciences (Springer Berlin Heidelberg, 1990), pp. 1–655 (cit. on pp. 25, 29, 32).

[66]   P. Horowitz, and W. Hill, *The Art of Electronics*, 3rd edition (Cambridge University Press, 1989) (cit. on pp. 28, 54).

[67]   Stanford Research Systems, *About Lock-In Amplifiers* (www.thinkSRS.com, 2011), pp. 1–9 (cit. on pp. 28, 54, 82).

[68]   Scientific Instrument Group, *Explore the Lock-in Amplifier* (www.signalrecovery.com, 1983), pp. 1–4 (cit. on p. 28).

[69]   J. S. Hyde, W. Froncisz, J. W. Sidabras, T. G. Camenisch, J. R. Anderson, and R. A. Strangeway, "Microwave frequency modulation in CW EPR at W-band using a loop-gap resonator", Journal of Magnetic Resonance **185**, 259–263 (2007) (cit. on p. 29).

[70]   M. Stutzmann, M. S. Brandt, and M. W. Bayerl, "Spin-dependent processes in amorphous and microcrystalline silicon: a survey", Journal of Non-Crystalline Solids **266-269**, 1–22 (2000) (cit. on pp. 30, 39, 41, 45, 116).

[71]   Bruker, *EPR resonators* (https://www.bruker.com/, 2009), pp. 1–26 (cit. on p. 33).

[72]   A. Lund, E. Sagstuen, A. Sanderud, and J. Maruani, "Relaxation-Time Determination from Continuous-Microwave Saturation of EPR Spectra", Radiation Research **172**, 753–760 (2009) (cit. on p. 34).

[73]   F. K. Kneubühl, "Line Shapes of Electron Paramagnetic Resonance Signals Produced by Powders, Glasses, and Viscous Liquids", The Journal of Chemical Physics **33**, 1074–1078 (1960) (cit. on p. 35).

[74]   D. Freude, *Spectroscopy for Physicists - Chapter 3 - Paramagnetic Electron Resonance* (Uni Leipzig, 2006), pp. 1–14 (cit. on p. 35).

[75] K. Ray, S. P. Ananthavel, D. H. Waldeck, and R. Naaman, "Asymmetric scattering of polarized electrons by organized organic films of chiral molecules", Science **283**, 814–816 (1999) (cit. on p. 35).

[76] S. G. Ray, S. S. Daube, G. Leitus, Z. Vager, and R. Naaman, "Chirality-induced spin-selective properties of self-assembled monolayers of DNA on gold", Physical Review Letters **96**, 1–4 (2006) (cit. on p. 35).

[77] M. Gazzotti, S. Arnaboldi, S. Grecchi, R. Giovanardi, M. Cannio, L. Pasquali, A. Giacomino, O. Abollino, and C. Fontanesi, "Spin-dependent electrochemistry: Enantio-selectivity driven by chiral-induced spin selectivity effect", Electrochimica Acta **286**, 271–278 (2018) (cit. on p. 35).

[78] P. C. Mondal, C. Fontanesi, D. H. Waldeck, and R. Naaman, "Spin-Dependent Transport through Chiral Molecules Studied by Spin-Dependent Electrochemistry", Accounts of Chemical Research **49**, 2560–2568 (2016) (cit. on p. 35).

[79] B. Gohler, V. Hamelbeck, T. Z. Markus, M. Kettner, G. F. Hanne, Z. Vager, R. Naaman, and H. Zacharias, "Spin Selectivity in Electron Transmission Through Self-Assembled Monolayers of Double-Stranded DNA", Science **331**, 894–897 (2011) (cit. on p. 35).

[80] W. T. Baron Kelvin, "The molecular tactics of a crystal", Oxford: Clarendon Press, 74 (1894) (cit. on p. 36).

[81] S. Yeganeh, M. A. Ratner, E. Medina, and V. Mujica, "Chiral electron transport: Scattering through helical potentials", Journal of Chemical Physics **131** (2009) 10.1063/1.3167404 (cit. on p. 36).

[82] J. Gersten, K. Kaasbjerg, and A. Nitzan, "Induced spin filtering in electron transmission through chiral molecular layers adsorbed on metals with strong spin-orbit coupling", The Journal of Chemical Physics **139**, 114111 (2013) (cit. on p. 36).

[83] R. Gutierrez, E. D?az, C. Gaul, T. Brumme, F. Dom?nguez-Adame, and G. Cuniberti, "Modeling Spin Transport in Helical Fields: Derivation of an Effective Low-Dimensional Hamiltonian", The Journal of Physical Chemistry C **117**, 22276–22284 (2013) (cit. on p. 36).

[84] S. Matityahu, Y. Utsumi, A. Aharony, O. Entin-Wohlman, and C. A. Balseiro, "Spin-dependent transport through a chiral molecule in the presence of spin-orbit interaction and nonunitary effects", Physical Review B **93**, 1–10 (2016) (cit. on p. 36).

[85] E. Díaz, R. Gutiérrez, C. Gaul, G. Cuniberti, and F. Domínguez-Adame, "Coherent spin dynamics in a helical arrangement of molecular dipoles", AIMS Materials Science **4**, 1052–1061 (2017) (cit. on p. 36).

[86] V. V. Maslyuk, R. Gutierrez, A. Dianat, V. Mujica, and G. Cuniberti, "Enhanced Magnetoresistance in Chiral Molecular Junctions", The Journal of Physical Chemistry Letters **9**, 5453–5459 (2018) (cit. on p. 36).

[87] X. Yang, C. H. van der Wal, and B. J. van Wees, "Spin-dependent electron transmission model for chiral molecules in mesoscopic devices", Physical Review B **99**, 024418 (2019) (cit. on p. 36).

[88] S. Varela, V. Mujica, and E. Medina, "Effective spin-orbit couplings in an analytical tight-binding model of DNA: Spin filtering and chiral spin transport", Physical Review B **93**, 1–16 (2016) (cit. on p. 36).

[89]   T. Ando, "Spin-orbit interaction in carbon nanotubes", Journal of the Physical Society of Japan **69**, 1757–1763 (2000) (cit. on p. 36).

[90]   M. Kettner, B. Göhler, H. Zacharias, D. Mishra, V. Kiran, R. Naaman, C. Fontanesi, D. H. Waldeck, S. Sek, J. Pawłowski, and J. Juhaniewicz, "Spin Filtering in Electron Transport Through Chiral Oligopeptides", The Journal of Physical Chemistry C **119**, 14542–14547 (2015) (cit. on pp. 37, 113).

[91]   M. Kettner, V. V. Maslyuk, D. Nürenberg, J. Seibel, R. Gutierrez, G. Cuniberti, K. H. Ernst, and H. Zacharias, "Chirality-Dependent Electron Spin Filtering by Molecular Monolayers of Helicenes", Journal of Physical Chemistry Letters **9**, 2025–2030 (2018) (cit. on pp. 37, 113).

[92]   V. Kiran, S. P. Mathew, S. R. Cohen, I. Hernández Delgado, J. Lacour, and R. Naaman, "Helicenes - A New Class of Organic Spin Filter", Advanced Materials **28**, 1957–1962 (2016) (cit. on pp. 37, 113).

[93]   J. S. Blakemore, "Semiconducting and other major properties of gallium arsenide", Journal of Applied Physics **53**, R123 (1982) (cit. on pp. 37, 39).

[94]   F. Meier, and B. Zakharchenya, *Optical Orientation - Modern Problems in Condensed Matter Sciences*, Vol. 8 (1984) (cit. on p. 38).

[95]   C. Weisbuch, and C. Hermann, "Optical detection of conduction-electron spin resonance in GaAs, Ga1-xInxAs, and Ga1-xAlxAs", Physical Review B **15**, 816–822 (1977) (cit. on pp. 39, 113).

[96]   G. Lampel, "Nuclear dynamic polarization by optical electronic saturation and optical pumping in semiconductors", Physical Review Letters **20**, 491–493 (1968) (cit. on p. 39).

[97]   D. J. Lepine, "Spin-Dependent Recombination on Silicon Surface", Physical Review B **6**, edited by Intergovernmental Panel on Climate Change, 436–441 (1972) (cit. on pp. 39, 40).

[98]   A. K. Fumani, and J. Berezovsky, "Spin-Pumping Efficiency in Room-Temperature CdSe Nanocrystal Quantum Dots", The Journal of Physical Chemistry C **118**, 28202–28206 (2014) (cit. on p. 39).

[99]   H. Dersch, L. Schweitzer, and J. Stuke, "Recombination processes in a-Si:H: Spin-dependent photoconductivity", Physical Review B **28**, 4678–4684 (1983) (cit. on p. 39).

[100]   I. Solomon, "Spin-dependent recombination in a silicon p-n junction", Solid State Communications **20**, 215–217 (1976) (cit. on p. 40).

[101]   F. C. Rong, G. J. Gerardi, W. R. Buchwald, E. H. Poindexter, M. T. Umlor, D. J. Keeble, and W. L. Warren, "Electrically detected magnetic resonance of a transition metal related recombination center in Si $p-n$ diodes", Applied Physics Letters **60**, 610–612 (1992) (cit. on pp. 40, 41).

[102]   S. T. Goennenwein, S. W. Schink, A. Brandlmaier, A. Boger, M. Opel, R. Gross, R. S. Keizer, T. M. Klapwijk, A. Gupta, H. Huebl, C. Bihler, and M. S. Brandt, "Electrically detected ferromagnetic resonance", Applied Physics Letters **90**, 3–5 (2007) (cit. on p. 41).

[103]   W. Harneit, C. Boehme, S. Schaefer, K. Huebener, K. Fostiropoulos, and K. Lips, "Room temperature electrical detection of spin coherence in C60", Physical Review Letters **98**, 1–4 (2007) (cit. on p. 41).

Bibliography

[104] T. Eickelkamp, "Electrically detected magnetic resonance in photoexcited fullerenes", Molecular Physics **95**, 967–972 (1998) (cit. on p. 41).

[105] J. A. Gómez, F. A. Castro, F. Nüesch, L. Zuppiroli, and C. F. O. Graeff, "On the origin of exciton formation in dye doped Alq3 OLEDs", Applied Physics A **108**, 727–731 (2012) (cit. on p. 41).

[106] F. Comandè, and J.-P. Ansermet, "Time-resolved spin processes in Alq3 light-emitting diodes", Physical Review B **90**, 201201–1 –4 (2014) (cit. on p. 41).

[107] F. C. Rong, W. R. Buchwald, E. H. Poindexter, W. L. Warren, and D. J. Keeble, "Spin-dependent Shockley-read recombination of electrons and holes in indirect-band-gap semiconductor p-n junction diodes", Solid State Electronics **34**, 835–841 (1991) (cit. on p. 41).

[108] M. Xiao, I. Martin, E. Yablonovitch, and H. W. Jiang, "Electrical detection of the spin resonance of a single electron in a silicon field-effect transistor", Nature **430**, 435–439 (2004) (cit. on p. 41).

[109] T. Aichinger, and P. M. Lenahan, "Giant amplification of spin dependent recombination at heterojunctions through a gate controlled bipolar effect", Applied Physics Letters **101**, 1–5 (2012) (cit. on p. 41).

[110] D. M. G. Leite, A. Batagin-Neto, O. Nunes-Neto, J. A. Gómez, and C. F. O. Graeff, "Electrically detected magnetic resonance modeling and fitting: An equivalent circuit approach", Journal of Applied Physics **115**, 034510 (2014) (cit. on p. 41).

[111] C. S. Johnson, and H. S. Gutowsky, "High-Resolution ESR Spectra of Photochemically Generated Free Radicals: The Viologens", The Journal of Chemical Physics **39**, 58–62 (1963) (cit. on pp. 52, 72).

[112] C. L. Bird, and a. T. Kuhn, "Electrochemistry of the viologens", Chemical Society Reviews **10**, 49 (1981) (cit. on p. 53).

[113] B. Beden, O. Enea, F. Hahn, and C. Lamy, "Investigation of the adsorption of methyl viologen on a platinum electrode by voltammetry coupled with "in situ" UV—visible reflectance spectroscopy", Journal of Electroanalytical Chemistry and Interfacial Electrochemistry **170**, 357–361 (1984) (cit. on p. 53).

[114] F. M. F. Rhen, D. Fernandez, G. Hinds, and J. M. D. Coey, "Influence of a Magnetic Field on the Electrochemical Rest Potential", Journal of The Electrochemical Society **153**, J1–J7 (2006) (cit. on p. 54).

[115] F. Comandè, "Spin processes and charge dynamics in organic light emitting diodes", PhD thesis (EPFL, 2014), pp. 1–117 (cit. on p. 55).

[116] A. Piotrowska, "Ohmic Contacts to GaAs: Fundamentals and Practice", Acta Physica Polonica A **84**, 491–504 (1993) (cit. on p. 56).

[117] A. G. Baca, F. Ren, J. C. Zolper, R. D. Briggs, and S. J. Pearton, "A survey of ohmic contacts to III-V compound semiconductors", Thin Solid Films **308 - 309**, 599–606 (1997) (cit. on p. 56).

[118] Y.-E. Sung, F. Gaillard, and A. J. Bard, "Demonstration of Electrochemical Generation of Solution-Phase Hot Electrons at Oxide-Covered Tantalum Electrodes by Direct Electrogenerated Chemiluminescence", The Journal of Physical Chemistry B **102**, 9797–9805 (1998) (cit. on p. 63).

[119] G. Grampp, B. Y. Mladenova, D. R. Kattnig, and S. Landgraf, "ESR and ENDOR investigations of the degenerate electron exchange reactions of various viologens in solution. Solvent dynamical effects", Applied Magnetic Resonance **30**, 145–164 (2006) (cit. on pp. 63, 72).

[120] W. Dunham, J. Fee, L. Harding, and H. Grande, "Application of fast Fourier transforms to EPR spectra of free radicals in solution", Journal of Magnetic Resonance (1969) **40**, 351–359 (1980) (cit. on p. 72).

[121] N. Leblanc, N. Mercier, O. Toma, A. H. Kassiba, L. Zorina, P. Auban-Senzier, and C. Pasquier, "Unprecedented stacking of MV^{2+} dications and $MV^{+\bullet}$ radical cations in the mixed-valence viologen salt $(MV)_2(BF_4)_3(MV=methylviologen)\cdot$", Chemical communications (Cambridge, England) **49**, 10272–4 (2013) (cit. on p. 72).

[122] J. Granwehr, "A New Approach to Longitudinally Detected Electron Paramagnetic Resonance", PhD thesis (ETH Zürich, 2002) (cit. on p. 77).

[123] R. Brändle, G. Krüger, and W. Müller-Warmuth, "Impulsspektroskopische Untersuchungen der Elektronenspinrelaxation in freien Radikalen", Zeitschrift für Naturforschung A **25**, 1–11 (1970) (cit. on p. 77).

[124] A. Collauto, A. Barbon, and M. Brustolon, "First determination of the spin relaxation properties of a nitronyl nitroxide in solution by electron spin echoes at X-band: A comparison with Tempone", Journal of Magnetic Resonance **223**, 180–186 (2012) (cit. on p. 77).

[125] J. S. Hyde, J. J. Yin, W. K. Subczynski, T. G. Camenisch, J. J. Ratke, and W. Froncisz, "Spin-label EPR T1values using saturation recovery from 2 to 35 GHz", Journal of Physical Chemistry B **108**, 9524–9529 (2004) (cit. on p. 77).

[126] D. M. Martino, H. van Willigen, and M. T. Spitler, " FT-EPR Study of Photoinduced Electron Transfer at the Surface of TiO 2 Nanoparticles ", The Journal of Physical Chemistry B **101**, 8914–8919 (2002) (cit. on pp. 77, 78).

[127] K. Jüttner, "Electrochemical impedance spectroscopy (EIS) of corrosion processes on inhomogeneous surfaces", Electrochimica Acta **35**, 1501–1508 (1990) (cit. on p. 80).

[128] J. Goree, "Double lock-in detection for recovering weak coherent radio frequency signals", Review of Scientific Instruments **56**, 1662–1664 (1985) (cit. on p. 83).

[129] A. C. Von Bieren, "Spin and Heat Currents in Magnetic Nanostructures", PhD thesis (EPFL, 2013), p. 153 (cit. on p. 84).

[130] K. J. Kennewell, M. Kostylev, N. Ross, R. Magaraggia, R. L. Stamps, M. Ali, A. A. Stashkevich, D. Greig, and B. J. Hickey, "Magnetization pinning at a Py/Co interface measured using broadband inductive magnetometry", Journal of Applied Physics **108** (2010) 10.1063/1. 3488618 (cit. on p. 84).

[131] S.-H. Cao, Z.-R. Ni, L. Huang, H.-J. Sun, B. Tang, L.-J. Lin, Y.-Q. Huang, Z.-Y. Zhou, S.-G. Sun, and Z. Chen, "In Situ Monitoring Potential-Dependent Electrochemical Process by Liquid NMR Spectroelectrochemical Determination: A Proof-of-Concept Study", Analytical Chemistry **89**, 3810–3813 (2017) (cit. on p. 95).

[132] F. Zaera, "Chirality in adsorption on solid surfaces", Chemical Society Reviews **46**, 7374–7398 (2017) (cit. on p. 113).

[133]   M. Isasa, E. Villamor, L. E. Hueso, M. Gradhand, and F. Casanova, "Temperature dependence of spin diffusion length and spin Hall angle in Au and Pt", Physical Review B **91**, 024402 (2015) (cit. on p. 117).

[134]   O. Gomonay, "Crystals with Defects May Be Good for Spintronics", Physics **11**, 78 (2018) (cit. on p. 118).

[135]   L. Hu, H. Huang, Z. Wang, W. Jiang, X. Ni, Y. Zhou, V. Zielasek, M. G. Lagally, B. Huang, and F. Liu, "Ubiquitous Spin-Orbit Coupling in a Screw Dislocation with High Spin Coherency", Physical Review Letters **121**, 66401 (2018) (cit. on p. 118).

[136]   T. Furukawa, Y. Shimokawa, K. Kobayashi, and T. Itou, "Observation of current-induced bulk magnetization in elemental tellurium", Nature Communications **8**, 1–5 (2017) (cit. on p. 118).

[137]   A. Ahmadi, G. Attard, J. Feliu, and A. Rodes, "Surface Reactivity at "Chiral" Platinum Surfaces", Langmuir **15**, 2420–2424 (1999) (cit. on p. 118).

B Curriculum Vitae

Felix Blumenschein, M.Sc.

Chem. de Veilloud 54 • 1024 Ecublens • Switzerland

Tel: +41 767 47 91 18 • felix.blumenschein@gmail.com

Citizenship: German • Civil status: partnership, one child

Date / place of birth: 4th July, 1987, Bad Saulgau, Germany

Experiences and Qualifications

- **Experimental**: CW EPR, EDMR, lock-in amplification, double lock-in, electrochemistry, impedance electrochemistry, room temperature low current measurements, STM, STS, LEED, EBPVD, CVD, TPG, glovebox, clean room, low temperature physics, UHV, signal processing

- **Scientific**: spintronics, electrode/electrolyte interface, chirality, CISS, optical spin pumping, surface physics, solid state physics, quantum mechanics, methyl viologen, helicene, alanine peptide, self-assembled monolayers, p-GaAs electrode, surface functionalization, graphene

- **IT:** Matlab, LabVIEW, Gnuplot, Inkscape, LaTeX, MS Office, Lightroom, FCPX, SPIP, Mac, Windows, Linux, Python, C/C++, Fortran, Octave

- **Languages:**
  German: *native*
  English: *excellent*
  French: *good*

PhD at the EPFL

Conference Contribution

- Spin Chemistry Meeting 2017: Poster "EPR study of spin dependent charge transfer processes at electrodes"

- SpinOS Conference 2018: Poster "EPR Study of Spin Dependent Charge Transfer Processes at Functionalized Electrodes"

- SPS Lausanne 2018: Poster "EPR Study of Spin Dependent Charge Transfer Processes at Functionalized Electrodes"

Teaching

- WS 2015/2016: Physique Avancée I (Mécanique)

- WS 2015/2016: Supervision and managing of a TP IV student

- SS 2016: Formation of guidelines, including theory and experiments for CW EPR TP III

- SS 2016: TP III EPR teaching

- WS 2016/2017: TP III EPR and NMR

- SS 2017: TP III EPR and NMR

- WS 2017/2018: TP III EPR and NMR

- SS 2018: Physique Avancée II (Thermodynamique)

- SS 2018: Supervision and managing of a master student for four months

- WS 2018/2019: Physique Générale (Mécanique)

Courses Attended

- Electrochemistry for materials technology (2 credits)

- Magnetic materials in modern technologies - from concepts to real devices (2 credits)

- International Physics Summer School "The principles of dynamic nuclear polarization"

- Interfacial Electrochemistry of Metals and Semiconductors for Energy Conversion and Storage (2 credits)

- Advanced experimental methods in condensed matter and nanophysics (2 credits)

- New Trends in Chiral Magnetism (2 credits)

- Spin Dynamics (4 credits)

Publications

- M. Tamski, **F. Blumenschein**, C. Roussel, J.P. Ansermet "Probing charge transfer processes at p-GaAs electrodes under weak optical excitation", *J. Photoch. Photobio. A: Chem., 382* (2019)

- J. Tesch, P. Leicht, **F. Blumenschein**, L. Gragnaniello, A. Bergvall, T. Löfwander and M. Fonin, "Impurity scattering and size quantization effects in a single graphene nanoflake", *Phy. Rev. B 95, 7, 075429* (2017)

- J. Tesch, P. Leicht, **F. Blumenschein**, L. Gragnaniello, M. Fonin, L. Eugen M. Steinkasserer, B. Paulus, E. Voloshina and Y. Dedkov, "Structural and electronic properties of graphene nanoflakes on Au(111) and Ag(111)", *Nat. Scient. Rep. 6, 23439* (2016).

- P. Leicht, J. Tesch, S. Bouvron, **F. Blumenschein**, P. Erler, L. Gragnaniello, and M. Fonin, Rashba splitting of graphene-covered Au(111) revealed by quasiparticle interference mapping. *Phys. Rev. B 90, 241406(R)* (2014)

- Three further papers under preparation for submission, two as first author

Educational Background

- **Aug. 2015 - Jul. 2019**   **PhD Physics**, *EPFL Lausanne, Switzerland.* Passed without reserve. Thesis: 'Spin-Dependent Processes at Electrodes Detected by Simultaneously Performed EPR, Electrochemistry and EDMR', Porf. J.P. Ansermet, Dr. HDR C. Roussel

- **Oct. 2011 - Nov. 2014**   **M.Sc. Physics**, *University of Konstanz, Germany.* Grade: 1.4 Master Thesis: 'Epitaxial Graphene Flakes on h-BN and Ag(111)', Apl. Prof. Dr. M. Fonin, Prof. Dr. G. Burkard (Konstanz). Thesis grade: 1.3

- **Sept. 2012 - Feb. 2013**   **ERASMUS scholarship**, *Université Joseph Fourier, Grenoble, France*

- **Oct. 2008 - Sept. 2011**   **B.Sc. Physics**, *University of Konstanz, Germany.* Grade: 2.1 Bachelor Thesis: 'Spatially Resolved Characterization of RF QPDs', *Astrium GmbH, Friedrichshafen, Germany*, Supervisor Dr. Dennis Weise, Examiner Prof. Dr. A. Leitenstorfer. Thesis grade: 1.0

- **1994-2007**   **Primary & secondary school**, *Bad Schussenried and Aulendorf, Germany.*

Work

- **2015 - 2019** Teaching: Physique Générale, Physique Avancée I, II and TP3 (EPR, NMR)

- **Apr. 2015 - Jul. 2015** Carpentering, building of a lodge and various renovation works, Germany

- **Dec. 2014 - Apr. 2015** Research assistant in the Magnetic Materials and Spintronics Group (Apl. Prof. Dr. Fonin), *University of Konstanz, Germany*
  Evaluation of experimental data and evaluation program development and part-automation (Matlab), introduction of new group members

- **2013 - 2014** Student assistant, tutoring of bachelor students at the physical practical course (Dr. Runge), *University of Konstanz, Germany*

- **2009 - 2014** Student assistant, HCI Group (Prof. Dr. Reiterer), *University of Konstanz, Germany*
  Building and supporting of a workshop; development and building of electronic parts, e.g. for the exhibition 'Fernbeziehung' (Konstanz)

- **2007 - 2008** Scaffolding work, *Bad Schussenried, Germany*

- **2007 - 2008** Social service as ambulance man at the german red cross (DRK; instead of military service), *Biberach, Germany*

- **2004 - 2008** Saxophone teacher at the MKO, *Otterswang, Germany*